Intermetallics 2025





Educational Center Kloster Banz • Germany

ABSTRACTS

www.intermetallics-conference.de

Table of Contents

Table of 0	Contents	1
Authors		2
Organisa	tion and Imprint	9
Opening	Talk: Wherefore intermetallic and high-entropy alloys?	.10
SCP 1:	Functional intermetallics11-	-22
SCP 1.1:	Thermoelectric Materials Design based-on Solid Solution Formation Substituting for Atomic- an Vacancy-site in Half-Heusler ZrNiSn Alloy Systems	d
SCP 1.2:	Investigation of Phase Transformations for the Formation of Nb ₃ Sn-Superconductors	. 15
SCP 1.3:	Investigation of the β-U phase in U-0.5Ti and U-2Zr	. 17
SCP 1.4:	Handedness resolved studies of the structural and physical properties of the chiral, semiconducting phase LaRhC2	. 20
SCP 2:	Additive manufacturing23-	-30
SCP 2.2:	Laser powder bed fusion of Laves phase-reinforced Fe-25Al-1.5Ta iron aluminide	
SCP 2.3:	Microstructure and mechanical properties of Mo-Si-B alloy processed using electron beam pow bed fusion	der
SCP 2.4:	Application of Thermo-Calc's Additive Manufacturing Module for LPBF of Intermetallics-based Materials	. 30
SCP 3:	Modelling and thermodynamics31-	-40
SCP 3.1:	Data to Aid Materials Design and Process Optimization of Molybdenum- and Niobium-based Refractory Alloys	
SCP 3.2:	Prediction of G-phase precipitation under irradiation by thermodynamic calculation	
SCP 3.3:	Influence of partial occupancy on the elastic tensor of the FeCr σ phase	
SCP 3.4:	Challenges in predicting trends of structural and mechanical properties of refractory CCAs	
SCP 4:	Complex intermetallic phases I41-	-52
SCP 4.1:	Point defect concentration and atomic diffusion in Laves phases: high-throughput atomistic	_
	simulations with universal machine-learning interatomic model	. 41
SCP 4.2:	Highly deformable Laves phase in a high entropy alloy	
SCP 4.3:	A New Family of Ternary Intermetallic Compounds with Two Structural Variants – The ZIP Phase	s45
SCP 4.4:	Crystal structure and peritectoid reaction temperature of Ta ₂ Co ₇ in the Co-Ta binary system	. 48
SCP 4.5:	An overview of intermediate phases in metal-zinc systems	. 51
SCP 5:	Superalloys and related53-	-61
SCP 5.1:	Microstructure-Based Modeling of Temperature-Dependent Yield Strength in	
	Polycrystalline Ni-Based Superalloys	. 53
SCP 5.2:	Deformation-induced transformation of intermetallic phases and their impact on strength	. 54
SCP 5.3:	Grain size effects on interdiffusion in complex concentrated alloys	. 57
SCP 5.4:	Diffusion-induced phase growth kinetics in CoNi/Al and CoCrNi/Al diffusion couples	. 59
SCP 6:	Titanium aluminides I	-71
SCP 6.1:	Additive manufacturing of β-containing TiAl alloys	. 62
SCP 6.2:	Deformation mechanisms at high temperatures in TiAl alloys - Role of addition elements	
SCP 6.3:	Three-dimensional Characterization of the β-Ti Phase in γ-TiAl Base Alloy	
SCP 6.4:	Principle of Novel Alloy Development for Thermal Power Generation toward Carbon Neutrality	
SCP 7:	Titanium aluminides II72-	-82
SCP 7.1:	A journey through TiAl development in IHI Corporation- from alloy design to advanced	
	manufacturing	. 72
SCP 7.2:	Systematic evaluation of load partitioning and deformation mechanisms in a multi-phase	
	intermetallic γ-TiAl based alloy: A synchrotron-based approach	
SCP 7.3:	Reversible stress-induced orthorhombic O phase in TiAl alloys	. 77

SCP 7.4:	Effect of Initial Lamellar Microstructure on Formation Kinetics of Grain Boundary Cellular Microstructure in γ-TiAl Alloys	80
SCP 8:	Iron aluminides83	
SCP 8.1: SCP 8.2:	Microstructure and Mechanical Behavior at High Temperatures of Multi-Phase Iron-Aluminides Re-Assessing the Mechanical Properties of Iron Aluminides: Deformation Behavior and Brittle- Ductile Transition	83 to-
SCP 8.3:	The effect of vacancy concentration on the micromechanical behaviour of B2 FeAl diffusion couples covering a wide range of compositions	
SCP 8.4:	The structure and properties of Fe-28Al powdered iron aluminide strengthened by the MeB bor phase produced by DPF technology under dynamic recrystallization conditions	ide
SCP 9:	BCC-based and constitutionally complex alloys95-	-103
SCP 9.2:	Effects of Aluminium and Tantalum addition on the mechanical behaviour of multicomponent alloys	95
SCP 9.3: SCP 9.4:	Precipitation in Ti-Fe-Mo-Al alloysMechanical Properties and Deformation Mechanism of Additively Manufactured	
	NiAl-CrMo in-situ Composites	. 101
SCP 10:	Silicides104-	·113
SCP 10.1:	Strategies to improve oxidation resistance of Mo-Si-B based intermetallic alloys	
SCP 10.2: SCP 10.3: SCP 10.4:	Development of Mo-Si-B Alloys for Additive Manufacturing	108
	Solidification Technique	. 111
SCP 11:	Complex intermetallic phases I114-	
SCP 11.1:	Phase Equilibria in the V-Rich Region of the V-Si-B System at 1400 °C	
SCP 11.2:	Solid solution strengthening in V-9Si-6.5B-xCr alloys: Role of Cr and Si in the BCC phase	. 117
SCP 11.3:	Grain refinement and interfacial IMCs suppression via Zn addition to enhance the mechanical properties of Cu/Sn-58Bi/Cu microbump	119
SCP 11.4:	Liquidus projection of the Fe-Nb-Si system	
SCP 11.5:	Implications for the homogeneity range of the α_c -Al–Si–Mn phase with the 3d-transition metal	
	elements V, Cr, Fe, Co, Ni, Cu, Zn	
SCP 11.6:	Crystallography and mechanical properties of τ_2 -Al $_3$ FeSi	. 128
Doctor Dr	esentations 130	101

Authors

Name	IDs
A – Be	
Hiroshi Abe	SCP 3.2
Annie M. L. Andersson	SCP 9.3
Thomas Antretter	SCP 7.2
Ingrid Beatriz Araújo de Oliveira	P 010
Gennadii Bagliuk	SCP 8.4
Varun A. Baheti	SCP 4.5
Jakob Bandorf	SCP 2.3
Hanka Becker	SCP 11.5
Klaus Beier	P 006
James P. Best	SCP 8.2, SCP 8.3
Andreas Bezold	SCP 5.2, SCP 9.4

Bh - Gö	
Pinaki Prasad Bhattacharjee	SCP 4.2
Anton Bochkarev	SCP 4.1
Sabine Bodner	SCP 7.2
Jakob Braun	P 016
Christoph Breuner	SCP 8.1
Enrico Bruder	P 012
Ulrich Burkhardt	SCP 1.4
Mustafa Carrion Saldana	SCP 11.1
Ankur Chauhan	P 013
Qing Chen	SCP 3.1
Yong Chen	SCP 10.3, SCP 2.3
Alexander Chizhik	P 002
Ken Cho	SCP 6.1, SCP 7.4
Stavros-Richard Christopoulos	SCP 4.3
Nicole Church	SCP 9.3
Giovanni Brandi Cirillo Yazigi	P 011
Helmut Clemens	SCP 3.4, SCP 6.2, SCP 7.2
Hannah C. Cole	SCP 9.3
Isolda Costa	P 011
Alain Couret	SCP 6.2
Gerhard Dehm	P 014, SCP 8.3
Benedikt Distl	P 016
Ralf Drautz	SCP 4.1
Sylvain Dubois	SCP 4.3
Jenq-Gong Duh	P 008, SCP 11.3
Ashton Egan	SCP 5.2
Alexander Egeberg	P 006
Yolita Eggeler	P 005
Aliakbar Emdadi	SCP 2.2
Anders Engström	P 020, SCP 2.4, SCP 3.1
Lara-Pauline Faden	P 006
Michael Farle	P 012
Claus Feldmann	P 005, P 006
Mariano Forti	SCP 3.3
Mathias Galetz	P 018
Enrique Galindo-Nava	SCP 5.1
Angelika Gedsun	SCP 8.1
Easo George	OT 1
Michael Ghosh	SCP 8.1
Uwe Glatzel	SCP 5.1
Bilal Gökce	P 012
Mathias Göken	SCP 5.2, SCP 9.4

Go – Kn	
Nick Goossens	SCP 4.3
Bronislava Gorr	P 009, SCP 11.1
Yuri Grin	SCP 1.4
Tim Groten	SCP 8.1
Ping Guan	SCP 10.4
Roman Gumeniuk	SCP 1.4
Haisheng Guo	SCP 10.4
Xiping Guo	SCP 10.4
Stefan Guth	SCP 8.2, SCP 8.3
Frederic Habiyaremye	P 004
Thomas Hammerschmidt	SCP 3.3
Marcus Hans	SCP 4.3
Pavel Hanus	P 022, P 023
Liangyan Hao	SCP 3.1
Sebastian Härtel	SCP 2.2
Georg Hasemann	P 003, P 009, P 018, P 019
	SCP 10.3, SCP 11.1, SCP 11.2
Martin Heilmaier	P 013, SCP 8.1, SCP 8.2, SCP 8.3
James M. Hogg	SCP 9.3
David Holec	SCP 3.4
Toshiaki Horiuchi	SCP 3.2, SCP 4.4
Adam Hotař	P 022
Owain S. Houghton	SCP 9.3
Shuigen Huang	SCP 4.3
Shuntaro Ida	SCP 11.2
Takaomi Itoi	SCP 7.4
Aurélie Jacob	SCP 11.4
Anna Sophie Jelinek	SCP 3.4
Rachel Jennings	SCP 7.1
Felix Jensch	SCP 2.2
Johan Jeppsson	SCP 2.4
Nicholas G. Jones	SCP 9.3
Elisabeth Kammermeier	SCP 2.3
Taro Kanda	SCP 7.4
Takahiro Kaneko	P 015
Anwesha Kanjilal	SCP 8.2, SCP 8.3
Nicolas Karpstein	SCP 5.2
Lukas Kaserer	P 016
Alexander Kauffmann	P 013, SCP 8.1, SCP 8.2, SCP 8.3
Amit Keren	SCP 4.3
Yoshisato Kimura	SCP 1.1
Wolfram Knabl	SCP 3.4

Kö – Me	
Markus König	SCP 1.4
Rajesh Korla	SCP 9.2
Carolin Körner	SCP 10.3, SCP 2.3, SCP 9.4
Roja Rani Korrayi	P 019
Guido Kreiner	P 001
Mario J. Kriegel	P 021
Manja Krüger	P 003, P 009, P 018
	SCP 10.3, SCP 11.1, SCP 11.2
Daiki Kubota	P 015
Sharvan Kumar	P 014
Michal Kuris	P 004
Ana Karolina Gratz Lagares de Oliveira	P 010
Ramya Lakshmi	SCP 5.4
Konstantina Lambrinou	SCP 4.3
Giulio I. Lampronti	SCP 9.3
Carl-Magnus Lancelot	SCP 2.4
Fabian Lanoy	P 018
Guillaume Laplanche	SCP 3.3
Stephan Laube	P 013, SCP 8.1
Klemens Lechner	SCP 3.4
Jung Soo Lee	SCP 8.2, SCP 8.3
Sang-Hyeok Lee	SCP 4.1
Yin-Ku Lee	P 008
Williams Lefebvre	P 004
Gerhard Leichtfried	P 016
Andreas Leineweber	P 001, P 021, SCP 1.2, SCP 11.5, SCP 11.6
Volodymyr Levytskyi	SCP 1.4
Christian H. Liebscher	P 014
Pin-Ling Lin	P 008, SCP 11.3
Gang Liu	P 014
Longfei Liu	SCP 10.2
Xu Liu	SCP 7.3
Yury Lysogorskiy	SCP 4.1
Rui Ma	SCP 10.4
Emad Maawad	SCP 7.2
Amer Malik	SCP 2.4
Stuart Maloy	SCP 4.3
Andreas Markström	SCP 2.4
Bernhard Mayr-Schmölzer	P 016
Bharat Mehta	SCP 3.1
Rosie F. L. Mellor	SCP 9.3

Mi – R	
Heiner Michels	SCP 8.1
Michael Mills	SCP 5.2, SCP 9.4
Satoshi Minamoto	SCP 3.2
Rahul Mitra	SCP 10.1
Shota Miyazaki	SCP 4.4
Takamichi Miyazaki	SCP 3.2
Guy Molénat	SCP 6.2
Marco Molinari	SCP 4.3
Daniel Monceau	P 004
Jean-Philippe Monchoux	P 004, SCP 6.2
Moritz Müller	SCP 5.1
Marcel Münch	SCP 8.2
Michael Musi	SCP 6.2, SCP 7.2
Takayoshi Nakano	SCP 6.1, SCP 7.4
Reza Naraghi	P 020
Ganesh Nayak	SCP 4.3
Steffen Neumeier	P 013, SCP 2.3, SCP 5.2 , SCP 9.4
Sarper Nizamoglu	SCP 8.1
Pankaj Kumar Ojha	SCP 4.2
Yotaro Okada	SCP 6.3
Martin Palm	SCP 8.1
Tamanna Panigrahi	SCP 5.4
Gajendra Patel	SCP 9.2
Petra Pazourková Prokopčáková	P 022, P 023
John Perepezko	SCP 10.2
Per Persson	SCP 4.3
Asaf Pesach	SCP 4.3
Yurii Podrezov	SCP 8.4
Radian Popescu	P 005
Aparajita Pramanik	P 013
Florian Pyczak	P 003, P 017, P 019
Yanqiang Qiao	SCP 10.4
Minh-Do Quang	SCP 2.4
Marcus W. Rackel	P 017
Roja Rani Korrayi	P 003
Buzz Rankouhi	SCP 10.2
Lukas Richter	SCP 11.6
Jan Lars Riedel	SCP 8.2, SCP 8.3
Christian Ritschel	P 005
Silja-Katharina Rittinghaus	P 012, SCP 2.1
Sven P. Rudin	SCP 1.3

S-Tr	
Zahra Sabeti	P 003 , P 019
Tarik Saleh	SCP 4.3
Nathanael Wagner Sales de Morais	P 010, P 011
Pierre Sallot	P 004
Daniel Schliephake	P 013, SCP 8.1
Clemens Schmetterer	SCP 11.4
Christopher Schmidt	SCP 10.3
Andre Schneider	SCP 2.4
Jochen Schneider	SCP 4.3
Claudio Geraldo Schön	P 010, P 011, SCP 4.3
Camelia Schulz	SCP 8.1
Ruth Schwaiger	P 009, SCP 11.1, SCP 11.2
Sascha Seils	SCP 8.1
Nobuaki Sekido	P 015
Benjamin Seligmann	SCP 7.2
Sandipan Sen	P 013, SCP 8.2
Natalia Shkodich	P 012
Hamed Shokri	P 012
Peter Singer	P 016
Daria Smirnova	SCP 4.1
levgen Solodkyi	P 018
Erdmann Spiecker	SCP 5.2
Petra Spoerk-Erdely	SCP 3.4, SCP 6.2, SCP 7.2
Sergei Starikov	SCP 4.1
Andreas Stark	P 003, P 017 , P 019
Frank Stein	P 014, SCP 11.4, SCP 4.4, SCP 8.2, SCP 8.3
Howard J. Stone	SCP 5.1, SCP 9.3
Upender Sunkari	SCP 4.2
Eteri Svanidze	SCP 1.4
Martin Švec	P 022, P 023
Joanna Szyndler	SCP 2.2
Masao Takeyama	SCP 6.1, SCP 6.3, SCP 6.4, SCP 7.4
Damien Texier	P 004
Lars Thielemann	P 009
Dan Thoma	SCP 10.2
Marc Thomas	P 004
Katharina Titz	SCP 9.4
Oleksandr Tolochyn	SCP 8.4
Oleksandra Tolochyna	SCP 8.4
Michael Tovar	SCP 2.2
Bikash Tripathy	SCP 4.2

Ts-Z	
Maria Tsoutsouva	P 004
Nobuhiro Tsuji	SCP 4.2
Matheus Tunes	SCP 4.3
Mayur Vaidya	SCP 5.3, SCP 5.4, SCP 9.2
Thomas Vaubois	P 004
Šárka Vávrová	P 022
Raja J. Vikram	P 013
Jozef Vleugels	SCP 4.3
Věra Vodičková	P 022, P 023
Sven C. Vogel	SCP 1.3
Julian Völkl	SCP 5.2
Jan Vollhüter	SCP 9.4
Peter Wagatha	SCP 3.4
Benjamin Wahlmann	SCP 10.3, SCP 2.3, SCP 9.4
Alexander Walnsch	P 021
Simon Waschull	SCP 1.2
Sabine Weiß	SCP 2.2
Liam Wood	SCP 10.2
Zhuocheng Xie	SCP 4.1
Martin Xing	P 020
Bhawna Yadav	SCP 5.4
Shubhangini Yadav	SCP 4.5
Konatsu Yamada	SCP 4.4
Ryosuke Yamagata	SCP 6.3, SCP 7.4
Xinyu Yan	P 015
Liu Yang	P 013
Weiguang Yang	P 009, SCP 11.1, SCP 11.2
Yang Yang	P 020
Yitong Yang	SCP 2.2
Hiroyuki Yasuda	SCP 6.1, SCP 7.4
Thais Kaori Yazawa Ito	P 010
Shuhei Yoshida	SCP 4.2
Kyosuke Yoshimi	P 015, SCP 11.2
Aidar Zakirov	P 004
Christopher Zenk	SCP 2.3, SCP 9.1
Jiyao Zhang	SCP 3.4
Song Zhang	SCP 10.4
Weiwei Zhang	SCP 3.1
Arcady Zhukov	P 002

Organisation and imprint

Venue Date

Educational Center Kloster Banz 29 September – 02 October 2025

Hans-Seidel-Stiftung e.V.

96231 Bad Staffelstein, Germany

Conference Chair

Prof. Dr.-Ing. Manja Krüger Otto-von-Guericke University Institute of Materials and joining Technology (IWF) Universitätsplatz 2 39106 Magdeburg, Germany

Scientific organisers and programme committee

Prof. Dr.-Ing. Martin Heilmaier Karlsruhe Institute of Technology /

Karlsruhe, Germany

Prof. Dr. Florian Pyczak Helmholtz-Zentrum Hereon / Geesthacht, Germany

Dr. Martin Schloffer MTU Aero Engines AG / Munich, Germany
PD Dr. Andre Schneider Thermo-Calc Software AB / Solna, Sweden
Dr. Frank Stein Max-Planck-Institut für Nachhaltige Materialien /

Düsseldorf, Germany

International advisory board

Bernard Bewlay GE Aerospace / Niskayuna, NY, US
Gabriele Cacciamani University of Genova / Genova, Italy
Nathalie Dupin Thermo Calcul / Orcet, France

Martin Friák Institute of Physics and Materials / Brno, Czech Rep.
Easo George Oak Ridge National Laboratory / Oak Ridge, TN, US
Juri Grin Max-Planck-Institut für Chemische Physik fester

Stoffe / Dresden, Germany

Haruyuki Inui Kyoto University / Kyoto, Japan

John Perepezko University of Wisconsin-Madison / Madison, WI / US

Cláudio Schön University São Paulo / São Paulo, Brazil
Masao Takeyama Tokyo Institute of Technology / Tokyo, Japan
Michel Vilasi University of Lorraine / Nancy, France

Conference organization

Conventus Congressmanagement & Marketing GmbH Carl-Pulfrich-Strasse 1 07745 Jena, Germany

www.conventus.de

Online programme for your mobile device

You want to have all programme details at a glance? Just scan the QR-code and be up to date during your time at Kloster Banz.

ISBN - 978-3-948023-57-7



Opening Talk:

Wherefore intermetallic and high-entropy alloys?

Easo P. George^{1,2}

¹University of Tennessee, Materials Science and Engineering Department, Knoxville, TN 37931, USA, egeorge@utk.edu

Intermetallics and high-entropy alloys (HEAs) emerged from different starting points and rationales to evolve and ultimately reach similar end points. The former began as strong compounds with high formation-enthalpies and the latter as solid solutions with high configurational-entropies. However, the ideal microstructure that both systems have converged to seems to be a composite of intermetallics dispersed in a solid solution — at least for certain applications. At different stages of their evolution, intermetallics and HEAs targeted structural or functional applications. My focus here will be on mechanical properties relevant for structural applications. Some of what I will cover is summarized below.

High-temperature properties will be addressed, since that was the original opportunity for intermetallics and is also now the case for the newer refractory HEAs. But so will low-temperature properties, since even materials meant for high-temperature applications require some threshold levels of room-temperature ductility and fracture toughness to withstand routine handling, assembly, accidental drops, and cycling from low to high temperatures. Additionally, HEAs have so far been shown to excel only at low temperatures and not at high temperatures (when compared to existing state-of-the-art competitors).

An early justification for HEAs was that, among the millions of possibilities, a few may turn out to be useful. Intermetallic Laves phases because of their abundance were also once thought to be promising; however, that did not quite pan out. It remains to be seen whether HEAs will fare much better. Research on intermetallics initially focused on stoichiometric ordered compounds. Over time, evidence showed such compounds lacked a proper balance of properties. Focus then shifted to off-stoichiometric compositions and later to two-phase microstructures consisting of ordered precipitates in a solid solution matrix. A similar evolution has occurred in HEAs, first from equiatomic solid solutions to off-equiatomic compositions, and later to two-phase microstructures of ordered intermetallic compounds in a solid solution HEA matrix. With the benefit of hindsight, it appears inevitable that intermetallics and HEAs would both converge to such a well-known earlier microstructure, namely, that of the highly optimized Ni-base superalloys consisting of a high volume-fraction of intermetallic precipitates in a solid solution matrix.

After summarizing the current status of both classes of materials, I will conclude with some thoughts on where future opportunities for HEAs may lie. Mistakes made during the heyday of intermetallics are now being repeated in the field of HEAs. I have my own personal views of why this is so, and I will mention a few of those in my presentation. Additionally, I will point out the pitfalls to avoid and what the issues are that need to be successfully addressed (and solved) if research on HEAs is to be sustained at current levels for more than just a few more years.

²Ruhr Universitität Bochum, Institut für Werkstoffe, Universitätsstr. 150, D-44780 Bochum, Germany

SCP 1.1:

Thermoelectric Materials Design based-on Solid Solution Formation Substituting for Atomic- and Vacancy-site in Half-Heusler ZrNiSn Alloy Systems

Yoshisato Kimura

Institute of Science Tokyo (Former Tokyo Institute of Technology), School of Materials and Chemical Technology, Department of Materials Science and Engineering, Energy Science and Informatics Course, Mail-Box J3-19, Bldg. J3-1516, 4259 Nagatsuta-cho, Midori-ku, Yokohama, Kanagawa 226-8502, Japan, kimura.y.ac@m.titech.ac.jp (kimura.y.83c5@m.isct.ac.jp)

Introduction

Serious natural disasters caused by intensifying abnormal weather have increased all over the world in recent years, making it an urgent task to suppress the global warming via reducing greenhouse gas emission. Thermoelectric power generation is an appealing approach for achieving the carbon neutrality and preserving the global environment, as well as conserving energy. Half-Heusler compounds, such as ZrNiSn, TiNiSn, and so forth [1], are well-known as excellent n-type thermoelectric materials which can be used at around 1000 K to directly convert high temperature waste heat into clean electrical energy. Recently, aiming to utilize waste heat lower than 500 K, thermoelectric power generation module is expected to be used for battery-free IoT application such as data sensing and data transmission system. The ordered structure of the half-Heusler compound ZrNiSn consists of four interpenetrating fcc sub-lattices of Zr, Ni, Sn and a vacancy (see Fig. 2). It can be regarded as if a half of Ni-site in the Heusler ZrNi₂Sn is replaced by vacancy-site in the Half-Heusler ZrNiSn. Conventional approaches to improve thermoelectric properties of half-Heusler would be the electrical tuning by dopig elements, and the reduction of lattice thermal conductivity by solid solution effect according to the substitution of homologous elements with the same number of valence electrons, e.g., (Ti,Zr,Hf)NiSn. The present Author's group found that the thermoelectric properties of ZrNiSn can completely be converted from n-type to p-type due to the electronic structure change caused by the solid solution formation substituting Co and Ir for the vacancy-site in the Zr(Ni,Mx)1+xSn (M = Ir, Co) system [2]. The understanding for this still remains phenomenological, and it is necessary to elucidate mechanistically, for achieving the new thermoelectric materials design concept. Additionally, it was elucidated that lattice thermal conductivity can effectively be reduced according to the solid solution effect substituting for the vacancy-site, owing to the enhancement of phonon scattering. On the other hand, the present author is always interested in that solid solution formation used for optimizing thermoelectric performance should strongly affect mechanical properties, resulting in solid solution hardening or softening, depending on the vacancy-site substitution with different solute atoms. For a desirable thermoelectric module design, it is advantageous to fabricate both n- and p-type materials based on the same compound since physical and chemical properties are expected to be similar each other. For example, a possibility of damaging from thermal stress could be reduce by closer thermal expansion coefficients of both n- and p-type materials. Objective of the present research is to understand the effects of solid solution substitution for the atomic-site and vacancy-site on thermoelectric as well as mechanical properties in order to establish the thermoelectric materials design based on the half-Heusler ZrNiSn alloy systems.

Materials and Methods

Various half-Heusler alloys, $Zr(Ni,M_x)_{1+x}Sn$ (M = Ir, Co, Fe), were firstly prepared by Arcmelting. Nearly single-phase half-Heusler were fabricated by the directional solidification using optical floating zone melting method. Microstructure observation was conducted using scanning electron microscopy of back-scattered electron images and transmission electron microscopy. Chemical compositions of alloys were quantitatively measured using electron probe microanalysis, and lattice parameters were measured by powder x-ray diffractometry. The Seebeck coefficient was measured in a temperature range from 300 K to 1073 K using steady-state method under the condition applying the temperature differences of 5, 10, and 20 K over a length of 6 mm between two R-type thermocouple probes. The Electrical resistivity were measured using the DC four-probe method. The thermal conductivity of the alloy was evaluated on the basis of its density, thermal diffusivity, and heat capacity, which were measured using the Archimedes method, laser-flash method, and differential scanning calorimetry. The first principle calculation using the akai-KKR package was performed to discuss the effects of solutes site-occupation on Seebeck coefficient due to the electronic structure change. Mechanical properties on localized atomic scale were measured using nanoindentation method at ambient temperature after being examined the crystallographic orientation using the electron backscatter diffraction method.

Results and Discussion

Temperature dependence of the Seebeck coefficient measured for nearly single phase Half-Heusler $Zr(Ni,M_x)_{1+x}Sn$ (M: Ir, Co, Fe) alloys is shown in Fig. 1, where x varies with M depending on its solubility. Note that selected previous data [2] are plotted together to see the tendency of M concentration effect. The base material ZrNiSn shows excellent ntype properties, the maximum absolute value is about -200 µV/K at 670 K. Substitution of Ir and Co for the vacancy-site leads to the conduction type conversion from n- to p-type, where Ir is more effective than Co in enhancing p-type positive values of Seebeck coefficient at a given amount of substitution. Note that atomic shuffle may be allowed between Ir, Co, and Ni in vacancy-site and partly in Ni-site. As focusing on transition behavior in the range of Ir substitution fraction x from 0.01 to 0.10, the conversion starts from a low temperature range at small x and proceeds toward a higher temperature range with further increase in x. Consequently, a peak temperature showing the maximum value of Seebeck coefficient shifts from about 380 K up to 1000 K as the Ir substitution increases (x from 0.04 to 0.25), while the maximum Seebeck coefficient increases from 95 to 115 µV/K. This propensity was predicted by the calculation. These results are attributed to the change of electronic structure regarding the Fermi level position shift in a narrow band gap. The electrical resistivity shows a remarkably high value on the transition at x = 0.04, since a major carrier drastically changes from electron to hole. In the case of Fe, the tendency of p-type conversion from n-type due to the substitution for the vacancy-site was predicted based on the calculation, however, the solubility in ZrNiSn was found to be limited small, less than 1 at%. The maximum absolute value of Seebeck coefficient of $Zr(Ni,Fe_x)_{1+x}Sn$ with x = 0.024, is higher than the base ZrNiSn, about -240 µV/K at 450 K. It can be explained as the optimization of n-type property by the ptype doping effect. Provided that n-type carrier electron concentration is slightly higher in ZrNiSn, it can be decreased and optimised by a slight increase of p-type carrier hole concentration according to the Fe substitution, and thereby Seebeck coefficient increases. Even though the solubility is quite small, the tendency of vacancy-site occupancy of Fe can be indirectly supported by microstructure observation and chemical composition analysis. Further addition of Fe slightly beyond the solubility limit, $Zr(Ni,Fe_x)_{1+x}Sn$ alloys have nearly single-phase half-Heusler and its volume fraction is much higher than that in $Zr(Ni_{1-x},Fe_x)$ Sn two-phase alloys (prepared under the assumption Fe substitutes for Ni) at the same x.

On the other hand, the evaluation of mechanical properties for thermoelectric materials is quite important inthe view point of the durability and liability in practical application. Like other typical intermetallic compounds, half-Heusler compounds tend to be extremely hard and brittle. Nanoindentation method was selected to measure mecanical properties of Half-Heusler $Zr(Ni,M_x)_{1+x}Sn$ (M: Ir, Co). Figure 2 represents the dependence of nanohardness on the M atom fraction substituting for the vacancy-site. The present author previously examined mecanical properties of half-Heusler ZrNiSn and Heusler ZrN₂Sn [3]. Nanohardness value is much higher in ZrNiSn than in ZrNi₂Sn (on (121)). Sort of softening behavior is clearly observed according to the substituion of Ir and Co for the vacancy site in ZrNiSn, and Co (atomic radius 0.126 nm) is more effective than Ir (0.136 nm) to lower the hardness. The active slip system of ZrNiSn is not determined yet, and it is suggested as {110}<110> by deducing from the slip systems reported for Heusler phases [4]. On the load-displacement (P-h) curves, so-called pop-in events [5,6] are observed, which is supposed to correspond to the onset of plastic deformation. Critical pop-in load P_c has linear relationship with burst displacement Δh , indicating dislocation generation and glides depends on release of stored elastic energy. Note that pop-in is correctly observed only in OFZ-DS alloys, while multiple pop-in at low stress level is observed probably due to cracking in arc-melt alloys. It is beneficial if the optimization of thermoelectric properties could result in moderating brittleness due to softening.

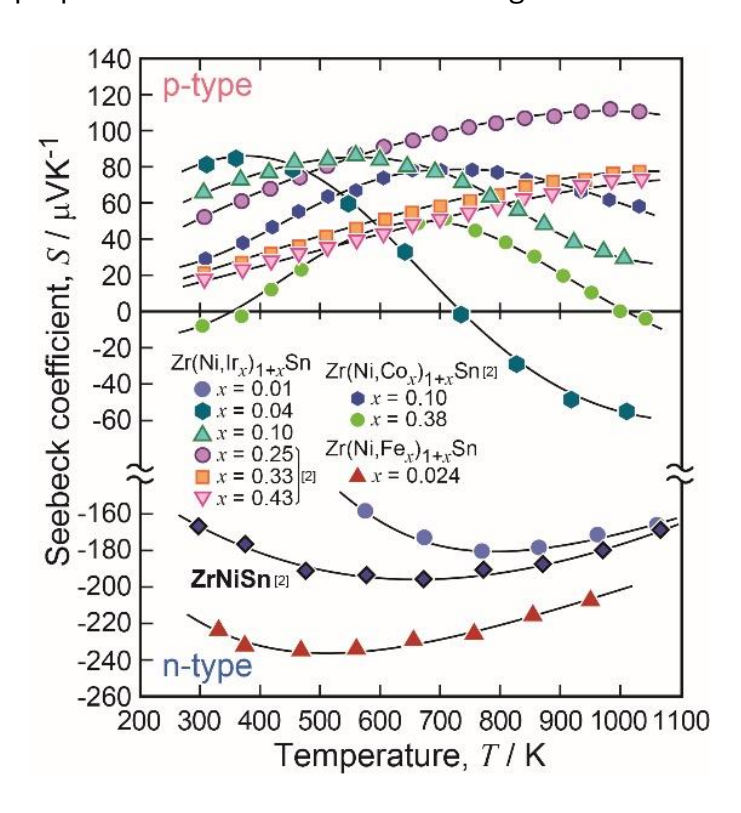


Fig. 1: Temperature dependence of Seebeck coefficient for various half-Heusler $Zr(Ni, M_x)_{1+x}Sn$ alloys (M = Ir, Co, Fe) alloys.

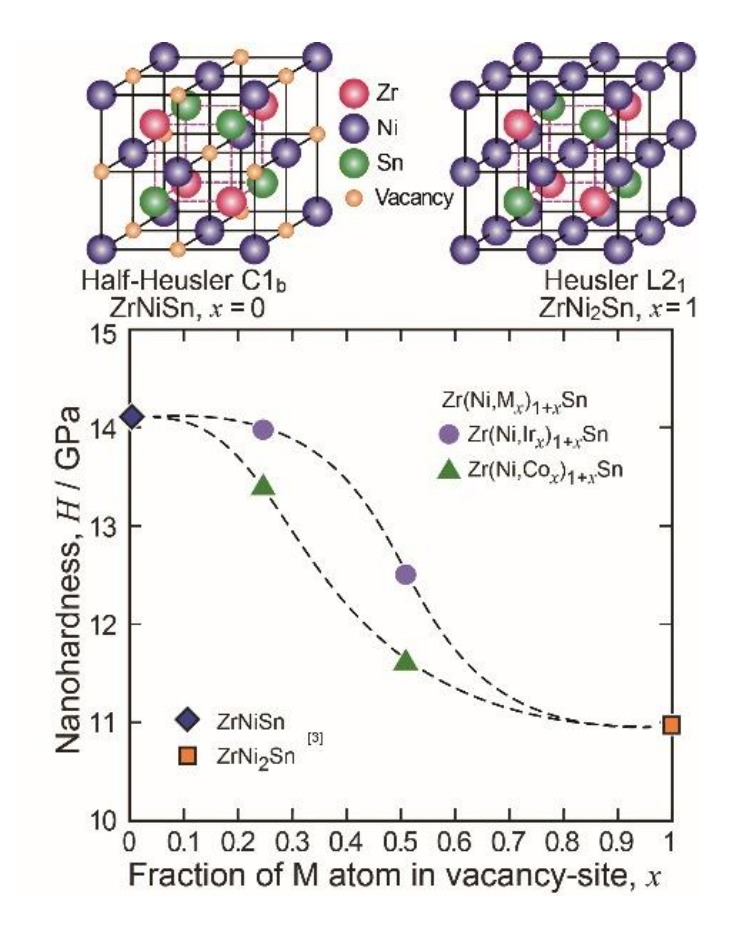


Fig. 2: The dependence of nanohardness measured for $Zr(Ni,M_x)_{1+x}Sn$ alloys (M = Ir, Co) alloys on the fraction of substituting M for the vacancy-site.

- [1] Y. Kimura and Y. W. Chai, JOM. 2015, 67, 233–245.
- [2] Y. Kimura, T. Tanoguchi, and T. Kita, Acta Materialia. **2010**, *58*, 4354–4361.
- [3] Y. Kimura, Y. Tsubono, Y. W. Chai, and T. Ohmura, Intermetallics 2019, Proceedings. **2019**, 47-48.
- [4] P. R. Strutt, R. S. Polvani, and J. C. Ingram, Metallurgical Transactions A. **1976**, *7A*, 23–31.
- [5] T. Ohmura, L. Zhang, N. Sekido, and K. Tsuzaki, Journal of Materials Research. **2012**, 27, 1742–1749.
- [6] T. L. Li, Y. F. Gao, H. Bei, and E. P. George, Journal of the Mechanics and Physics of Solids. **2011**, *59*, 1147–1162.

SCP 1.2:

Investigation of Phase Transformations for the Formation of Nb₃Sn-Superconductors

Simon Waschull¹, Andreas Leineweber¹

¹Institute of Materials Science, TU Bergakademie Freiberg, Gustav-Zeuner-Straße 5, 09599 Freiberg, Germany, <u>simon.waschull@iww.tu-freiberg.de</u>

Introduction

Nb₃Sn is a type II superconductor having the A15 structure in Strukturbericht notation and a homogeneity range of 18 to 25 at.% Sn [1]. As such it is already used in magnets in particle accelerators and a possible candidate for future applications (most notably the future circular collider, FCC) [2].

For the application in FCC, certain specifications have to be met, specifically the critical current density J_c of the current state-of-the-art Nb₃Sn is lower than needed. In order to increase this parameter, flux pinning can be utilized, meaning that the flux line lattice, penetrating the material, is interacting with pinning centers. Grain boundaries as well as nano-precipitates can act as such, the latter being also called artificial pinning centers when they have been introduced on purpose [2].

In the last few years, the so-called internal oxidation has gained some attention as a technology to do exactly that. Here, an oxygen source (for example SnO_2) is incorporated, as well as an additional element with higher affinity to O than Nb (e.g., Hf, Ti, Zr). That way, the additional element forms oxides that are included within the growing Nb₃Sn layer and increase J_c via flux pinning, acting as pinning centers themselves as well as decreasing the grain size (i.e., introducing more grain boundaries) via Zener pinning [3, 4].

Materials and Methods

In order to examine the processes involved in internal oxidation (decomposition of the oxygen source, diffusion of the different species and formation of the intermetallic phases and oxides), model diffusion samples of different geometries are used.

The materials used are Nb and Nb-alloys (Nb-Hf and Nb-Ta-Hf), Sn and Cu (the latter facilitating the formation of Nb $_3$ Sn, [3]) while SnO $_2$ acts as an oxygen source. These are arranged in different diffusion samples with and without an oxygen source and in different setups, which have in common that there is a substrate that is being coated using magnetron sputtering. For certain coatings a structured layer is utilized.

The obtained samples undergo a heat treatment and are then analysed using XRD and SEM (SE- and BSE-imaging, EDS and EBSD).

Results and Discussion

The executed experiments provide insights into the systems relevant for internal oxidation in Nb₃Sn. These include the Cu-rich side of the Cu-Sn system in combination with Nb or Nb-alloy (i.e., with Hf or Ta and Hf), both with and without SnO₂.

The influence of the different elements present, the reaction temperature and the initial microstructure on the formation of the reaction layer, mainly Nb₃Sn, is investigated. An exemplary image of such a sample is depicted in Figure 1 (Nb sheet coated with Cu and Sn without an oxygen source).

With the use of the aforementioned structured layer, it is possible to introduce areas of different local conditions within one sample.

Particular interest in the analysis is put on the thickness, homogeneity and grain size of the Nb₃Sn layer (see Figure 2).

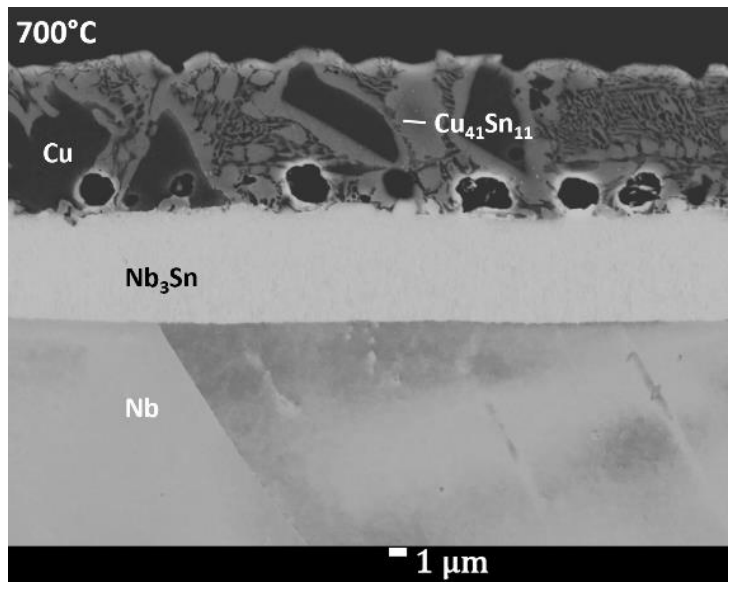


Fig. 1: BSE image of the reaction zone of a Nb sheet coated with Cu and Sn after a final heat treatment step of 72 h at 700°C; visible are the Nb substrate, Nb₃Sn layer and δ -phase (Cu₄₁Sn₁₁), as well as Cu solid solution.

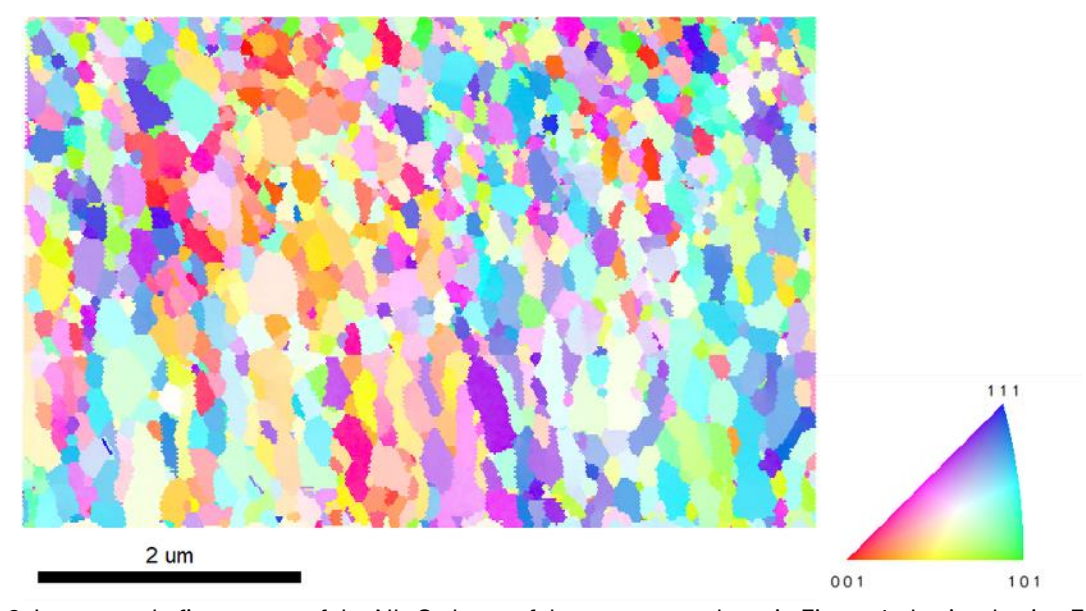


Fig. 2: Inverse pole figure map of the Nb_3Sn layer of the same sample as in Figure 1 obtained using EBSD, showing the fine-grained structure of the A15 phase.

- [1] A. Godeke, Superconductor Science and Technology. **2006**, 19, R68-R80.
- [2] X. Xu, Superconductor Science and Technology. 2017, 30, 093001.
- [3] N. Banno, Superconductivity, **2023**. 6, 100047.
- [4] X. Xu, X. Peng, J. Rochester, M.D. Sumption, J. Lee, G.A. Calderon Ortiz, J. Hwang, Journal of Alloys and Compounds, **2021**. 857, 158270.

SCP 1.3:

Investigation of the β-U phase in U-0.5Ti and U-2Zr

Sven C. Vogel, Sven P. Rudin
Los Alamos National Laboratory, Los Alamos, NM 87545, U.S.A., sven@lanl.gov

The crystal structure of β-U is stable from 935 to 1045 K in pure uranium and is also reported in the uranium-rich parts of binary uranium alloys such as U-Zr or U-Ti. The tetragonal unit-cell with lattice parameters of a=10.759Å and c=5.653Å contains 30 atoms per unit cell. Since the phase is not quenchable, experimental determination of the complex structure must occur in situ. Due to substantial grain growth in especially pure uranium combined with the strong attenuation of even synchrotron X-rays by uranium, neutron diffraction is a suitable probe for such investigations. The most recent determination of the crystal structure of β-U was by Lawson et al. [1] in 1988 from neutron diffraction data, identifying the P4₂/mnm space group rather than the previously proposed P-4n2 and P42nm space groups. Discrepancies in published phase diagrams of the U-Zr system (Figure 1 (a)), including in the uranium-rich region, motivated the present study during which the formation of β-U in a U-2wt.%Zr sample was studied in temperature profiles also applied to several other compositions in this phase diagram [2-5]. The U-Zr system is considered as base alloy for metallic nuclear fuels in transmutation nuclear reactors, therefore resolving discrepancies has practical implications. Additionally, the kinetics of the formation of β-U as well as its crystal structure was studied in U-0.5wt.%Ti exposed to ramp rates of 2K/min and 20K/min temperature ramp rates while several longer holds in the stability field of β-U provided additional crystal structure data. Neutron diffraction data was analyzed with the Rietveld method (Fig. 1 (b)) with all three proposed space groups, providing the crystal structure evolution with lattice parameters, atom positions and atomic displacement parameters to re-evaluate the assessment by Lawson et al. The β-U structure is also of interest to benchmark DFT and MD simulations of uranium [6] and we will report such comparisons here.

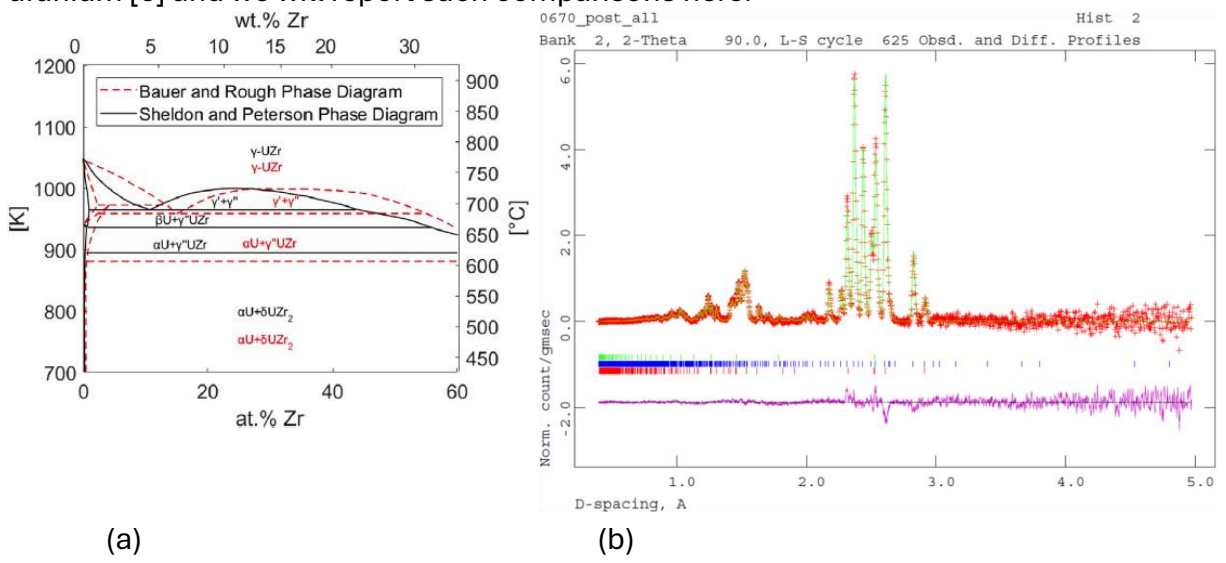


Fig 1: (a) Phase diagrams of the uranium-rich section of the U-Zr system published by Bauer & Rough (red) and Sheldon & Peterson (black) showing discrepancies including related to the formation of the β -U phase (from [3]). (b) Rietveld analysis of neutron diffraction data of a U-2wt.%Zr sample at 943 K showing β -U as the dominant phase with calculated peak positions indicated by blue tick-marks. Red tick marks are intermetallic UZr₂ and green tick marks are γ -U.

Materials and Methods

The U alloy samples considered here were obtained from LANL (U-0.5 wt.% Ti) and INL (U-2 wt.% Zr) and sample preparation and previous characterization can be found in [4,5].

Results and Discussion

The in situ heating of the U-2 wt.% Zr and U-0.5wt.% Ti samples showed the coexistence of UZr $_2$ and U $_2$ Ti intermetallic phases with the β -U phase. This indicates that in both cases the β -U structure was predominantly free of atoms of the alloying elements, allowing to compare the structural parameters obtained as a function of temperature for the two samples. During cooling from the bcc γ -U phase, in which the alloying elements can be readily accommodated and thus redistribute in the uranium matrix, effects of initial super-saturation of the β -U lattice with alloying elements are observed, Fig. 2 (a), which resolve during further cooling. We will compare kinetics of the repartitioning of the atoms of the alloying element into the UZr $_2$ and U $_2$ Ti intermetallic phases. We will present crystal structure results also in the context of the discussion of which of the proposed space groups for β -U describes our data best.

Since experimental data to benchmark e.g. DFT or MD predictions of this system [6] are sparse, our experimental dataset provides a unique opportunity to compare e.g. MD predicted values for the atomic displacement parameters as a function of temperature. Atomic displacement parameters derive from the lattice vibrations, i.e. phonon density of states, of the material from which in turn other thermophysical material parameters can be predicted. Hence, experimental verification of predictions of the phonon spectra are of great value. Fig. 2 (b) shows experimental isotropic displacement parameters for β -U determined from the neutron diffraction experiments during heating (dark blue) and cooling (orange). In both heating and cooling, close to the β/γ transition an increase of the atomic displacement relative to the slope at lower temperatures is observed. MD predicted isotropic atomic displacement parameters for different temperatures are shown in red and generally agree well with experimental values. The increase relative to the slope at lower temperatures is also observed in these predictions. For reference, the slightly higher atomic displacement parameters reported by Lawson et al. [1] are also shown (light blue).

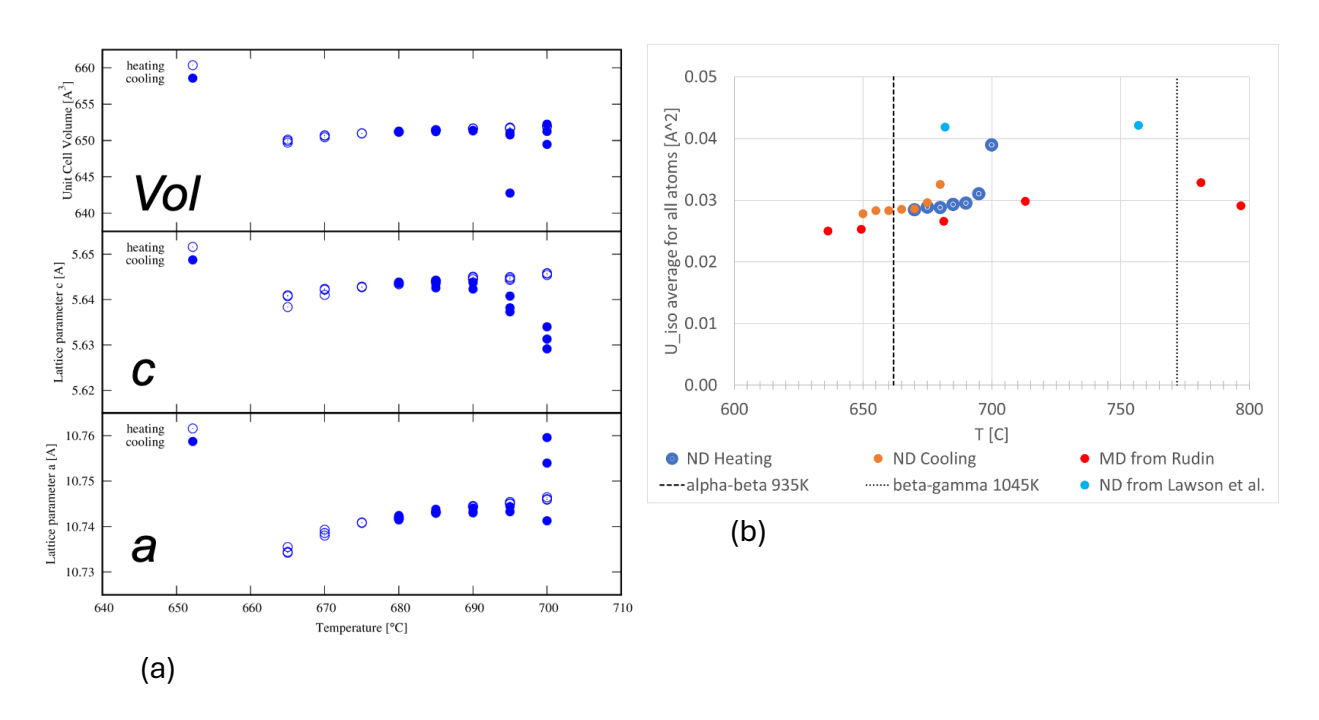


Fig 2: (a) Unit cell parameters in U-2 wt.%Zr as a function of temperature during heating (open symbols) and cooling (closed symbols), showing deviations from linearity as a function of time e.g. during several datasets collected at the same temperature during cooling.

References

- A.C. Lawson, C.E. Olsen, J.W. Richardson, M.H. Mueller, G.H. Lander, Acta Cryst. Section B. **1988**, 44, 89-96.
- W.J. Williams, M.A. Okuniewski, S.C. Vogel, J. Zhang, JOM. 2020, 72, 2042-50.
- W.J. Williams, M.A. Okuniewski, S.C. Vogel, Journal of Nuclear Materials. **2023**, 579, 154380
- Y. Xie, S.C. Vogel, J.M. Harp, M.T. Benson, L. Capriotti, Journal of Nuclear Materials. **2021**, 544, 152665.
- Y. Xie, S.C. Vogel, M.T. Benson, J.M. Harp, Journal of Nuclear Materials. 2022, 564, 153681. S.P. Rudin, Physical Review B. **2018**, 97(13), 134114.

LA-UR-25-23731

SCP 1.4:

Handedness resolved studies of the structural and physical properties of the chiral, semiconducting phase LaRhC₂

Ulrich Burkhardt¹, Yuri Grin¹, Markus König¹, Eteri Svanidze¹, Volodymyr Levytskyi², and Roman Gumeniuk²

¹Max Planck Institut für Chemische Physik fester Stoffe, Nöthnitzer Straße 40, 01187 Dresden, Germany ²Institut für Experimentelle Physik, TU Bergakademie Freiberg, Leipziger Str. 23, 09599 Freiberg, Germany Ulrich.Burkhardt@cpfs.mpg.de; Juri.Grin@cpfs.mpg.de, Markus.Koenig@cpfs.mpg.de,

Eteri.Svanidze@cpfs.mpg.de, Volodymyr.Levytskyi@physik.tu-freiberg.de, Roman.Gumeniuk@physik.tu-freiberg.de

Introduction

Materials with a non-centrosymmetric crystal structure have always played a special role, as technically relevant properties such as optical birefringence, ferroelectricity or pyroelectricity require the absence of an inversion center. More recently, topological materials and especially materials with non-centrosymmetric crystal structures have been the focus of many investigations. Non-centrosymmetric, topological materials like the phase CoSi and other Weyl semimetals exhibit unusual spin arrangements up to localized, helical spin textures (skyrmions) and magneto-transport phenomena including spin Hall effect and chiral anomaly [1, 2]. Another related example is the catalytic behavior of PdGa which is discussed to be influenced by topological, spin-polarized electron surface states [3]. The chirality dependence of chemical or physical properties are often weak and the superposition of contributions from domains with different chirality and crystallographic orientation can reduce or cancel the effect. So, the preparation of well-defined specimens is essential for the systematic investigations of chirality dependent properties.

Combining EBSD based chirality assignment and FIB micropreparation method allows the preparation of suitable specimens from poly crystalline materials. In our recent project we have applied these combined methods to extract mono-chiral single crystals of the phase CoSi suitable for x-ray diffraction experiments or TEM lamellae of the same phase with twin interface between domains of different chirality [4, 5]. These and other analysis on FeSi, FeGe, PdGa (all: SG $P2_13$, FeSi type (B20)),as well as on the chiral elements γ -Se, Te (SG: $P3_121$ / $P3_221$) and β -Mn (SG: $P4_132$ / $P4_322$) [6] show the reliability of the method. Important precondition is the high quality of the experimental pattern. In many cases, the suitable surface quality can be achieved by standard metallographic sample preparation.

In our actual project we apply this method to the preparation of microdevices suitable for the temperature dependent measurements of the electrical conductivity of the chiral phase LaRhC₂ (CeRhC₂ structure type, Pearson code tP16). LaRhC₂ has a series of structurally strongly related phases RTC_2 (R = rare earth, T = transition metal) with various topological properties in their electronic band structures. The tetragonal crystal structure of LaRhC₂ shows the symmetry of the space group $P4_1$ or $P4_3$ with the lattice parameter a = 3.9697(5) Å, c = 15.333(4) Å [7]. It is a semiconductor with a topological trivial band gap according to band structure calculations [8]. The aim of the investigations is to determine the influence of handedness and structural anisotropy on the physical properties of this topologically trivial material.

Materials and Methods

The sample with the overall composition of $La_{25}Rh_{25}C_{50}$ and the total mass of 0.5g were prepared from the elements by arc melting and subsequent annealing for 7 days at 1520 K. The phase analyses by powder X-ray diffraction and metallographic methods revealed the majority phase $LaRhC_2$ with small amounts of the minority phase $LaRh_2$.and LaC_2 . EBSD measurements have been performed on metallographically prepared polycrystalline materials (Bruker CrystAlign EBSD system). The handedness is assigned by the EBSD pattern evaluation using the full pattern matching approach [3] implemented in the mapsweeper software package (AZtecCrystal, Oxford instruments). The mapsweeper EBSD pattern simulation software takes in account dynamic electron scattering which results chirality dependent pattern contributions. FIB sections were realized on a Xe- FIB (FEI Helios G4 PFIB machine Quanta 200 3D ion/electron dual beam; FEI Company).

Results and Discussion

The microstructure of the polycrystalline material shows grains with a diameter up to several 100 μ m, whose different orientations are clearly visible in the polarised light of the optical microscope. The EBSD analyses confirmed the different crystallographic orientation of the grains. The handedness sensitivity evaluation of the EBSD pattern reveal that almost all grains are twinned and formed by several domains with different handedness. The enantiomorph distribution map show an almost equal contribution of both enantiomorph in the microstructure and were used to localize domains suitable for the microdevice preparation. A subset of grains with orientation of the fourfold screw axis perpendicular to the surface normal (s. Fig. 1) were defined by using the [001] pole figure presentation. Within these grains, slices of 200 x 200 μ m² perpendicular to the sample surface were cut from mono-chiral domains.

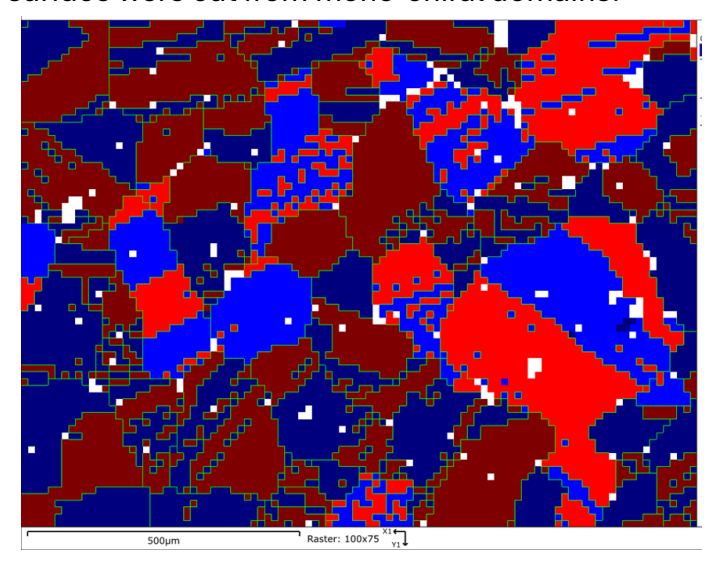


Fig. 1: LaRhC $_2$ - enantiomorph distribution map (red..P4 $_1$ / blue .. P4 $_3$). In the bright areas, the fourfold screw axis aligned almost perpendicular to the surface normal

After the lift-out and FIB polishing the EBSD analysis were used to define the handedness and the orientation of the fourfold screw axis. The final shape was realized by the FIB method which result a microdevice of series-connected bars to measure the electrical resistivity parallel and perpendicular to the fourfold screw axis (s. Fig. 2).

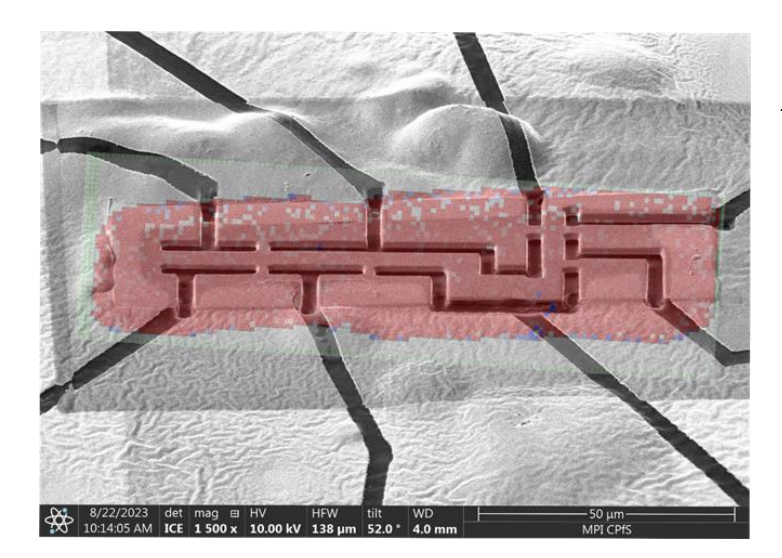


Fig. 2: $LaRhC_2$ – mono-chiral microdevice (red.. $P4_1$) with the fourfold screw axis aligned to the horizontal, long bar (left).

The increase in electrical conductivity with increasing temperature (100 K < T < 300 K) results in band gaps of 20 meV and 32 meV parallel and perpendicular to [001], reflecting the anisotropy of the crystal structure. Both enantiomorphs show the same physical properties with small sample dependent variations without systematic relation to the handedness of the specimens [9].

Acknowledgment

We thank Aimo Winkelmann for advice and discussion on the EBSD pattern analysis.

- [1] B. Yan, C. Felser, Topological Materials: Weyl Semimetals; Annu. Rev. Condens. Matter Phys. **2017**, *8*, 337–54
- [2] L. Schoop, F. Pielnhofer, B. Lotsch, Chemical Principles of Topological Semimetals; Chem.Mater. **2018**, *30*, 3155-76.
- [3] X. Wang, M. Peralta, X. Li, P. Möllers, D Zhoue, P. Merz, U. Burkhardt, H. Borrmann, I. Robredo, C. Shekhar, H. Zacharias, X. Feng, C. Felser; Direct control of electron spin at an intrinsically chiral surface for highly efficient oxygen reduction reaction; PNAS. **2025**, *122*, e2413609122.
- [4] U. Burkhardt, H. Borrmann, P. Moll, M. Schmidt, Yu. Grin, A. Winkelmann, Absolute Structure from Scanning Electron Microscopy; Scientific Report. **2020**, *10*, 4065
- [5] W. Carrillo-Cabrera, P. Simon, M. Schmidt, M. König, H. Borrmann, A. Winkelmann, U. Burkhardt, Yu Grin; Enantiomorph conversion in single crystals of the Weyl semimetal CoSi; Commun. Mater. **2023**, *4*, 109.
- [6] A. Winkelmann, G. Cios, T. Tokarski, P. Bała, Y. Grin, U. Burkhardt; Assignment of chiral elemental crystal structures using Kikuchi diffraction; Materials Characterisation. **2023**, *126*, 112633.
- [7] R. D. Hoffmann, W. Jeitschko and L. Boonk, Structural, chemical, and physical properties of rare-earth metal rhodium carbides LnRhC₂ (Ln = La, Ce, Pr, Nd, Sm); Chemistry of Materials. **1989**, *1*, 580-586.
- [8] R. Ray, B. Sadhukhan, M. Richter, J. I. Facio, J. van den Brink; Tunable chirality of non-centrosymmetric magnetic Weyl semimetals in rare-earth carbides, npj Quantum Materials **2022**, *7*, 19.
- [9] V. Levytskyi, U. Burkhardt, M. König, C. Hennig, E. Svanidze, Yu. Grin, R. Gumeniuk. submitted.

SCP 2.2:

Laser powder bed fusion of Laves phase-reinforced Fe-25Al-1.5Ta iron aluminide

Aliakbar Emdadi¹, Yitong Yang¹, Felix Jensch², Joanna Szyndler², Michael Tovar³, Sebastian Härtel² and Sabine Weiß¹

¹Chair of Physical Metallurgy and Materials Technology, Brandenburg University of Technology Cottbus-Senftenberg, Cottbus, Germany, emdadi@b-tu.de, yang@b-tu.de, weiss@b-tu.de ²Helmholtz-Zentrum Berlin für Materialien und Energie GmbH, Berlin, Germany, tovar@helmholtzberlin.de

³Chair of Hybrid Manufacturing, Brandenburg University of Technology Cottbus-Senftenberg, Cottbus, Germany, jenscfel@b-tu.de, haertel@b-tu.de

Introduction

Intermetallic iron aluminide alloys, based on the Fe₃Al composition, may address a key challenge in the aviation and power generation industries to develop more creepresistant and lightweight alloys as a replacement for heavy and partly expensive conventional superalloys and high-alloy steels. They offer excellent oxidation and corrosion resistance, better strength-to-weight ratios, lower material costs, and lower human toxicity and eco-toxicity than the common high-temperature Ni- and Co-based superalloys [1]. Nonetheless, low strength and creep resistance at temperatures above 650-700 °C have limited their potential application. Numerous strengthening strategies including solid-solution hardening, precipitation hardening, and ordering have been developed to improve the strength and creep resistance at higher temperatures. Among the strategies developed, strengthening by intermetallic Laves phase is one of the most effective concepts for improving the high-temperature mechanical properties of iron aluminides. Tantalum (Ta) has been shown to be an effective alloying element for Fe-Al alloys, which can form the hard and brittle ternary Laves phase (Fe, Al)₂Ta with hexagonal crystal structure (C14, P6₃/mmc, hP12) [2]. Iron aluminides based on Fe-25Al-2Ta (at. %) reinforced with an incoherent (Fe, Al)₂Ta Laves phase revealed higher (creep) strengths at 650 °C than high-alloy P92 steel [3]. The main objective of this work is to investigate the feasibility of printing dense and crack-free bulk Fe₃Al-Ta samples containing (Fe, Al)₂Ta Laves phase precipitates by the laser powder bed fusion (LPBF) process, also known as selective laser melting (SLM). The fundamentals of the process-microstructure relationships governing the as-built LPBF alloy are provided by a detailed microstructural characterization and comparison with those of the as-cast reference material. Such knowledge is essential but limited in the literature given the current interest in the use of advanced aluminides in high temperature structural applications.

Materials and Methods

Gas atomized powder material with a nominal composition of Fe-25Al-1.5Ta (at. %), a fraction size of $+10/-65~\mu m$ and an average particle size of d_{50} = 28.6 μm was supplied by Nanoval GmbH & Co. KG, Berlin. The LPBF experiments were performed using an AconityMIDI laser source equipped with a 400 W single-mode laser with a spot diameter of 80 μm and a wavelength of 1070 nm. The process was conducted in a chamber under argon atmosphere. All samples were exposed using a bidirectional stripe strategy. After each layer, the strips were rotated by 67° so that the exposure vectors in successive layers were not superimposed. The cubic samples were printed with a laser power of 200 W, a scan speed of 750 mm/s, a layer thickness of 0.05 mm, and a hatch distance of 0.1

mm corresponding to a volumetric energy density of 53.33 J/mm³. A stainless-steel plate preheated to 650 °C was used as the substrate.

The microstructures of the as-built LPBF samples were characterized by scanning electron microscopy (SEM) on a TESCAN AMBER equipped with energy-dispersive X-ray spectroscopy (EDX; Oxford Instruments) and high-resolution electron backscatter diffraction (EBSD; Oxford Instruments Aztec system) detectors. The SEM was operated with a beam current of 100 nA and an accelerating voltage of 15 kV. The EBSD data were recorded and analyzed using the AZtecCrystal software (Oxford Instruments). Inverse pole figure (IPF) maps parallel to the building direction (BD) were recorded to study the crystallographic orientations. The low-angle grain boundaries (LAGBs) and high-angle grain boundaries (HAGBs) were identified with misorientations (θ) of $2^{\circ} \le \theta < 15^{\circ}$ and $\theta \ge 15^{\circ}$, respectively. The phase identification was performed at room temperature with a Bruker D8 ADVANCE X-ray diffractometer using Cu-K_{α1+2} radiation ($\lambda \approx 0.15418$ nm).

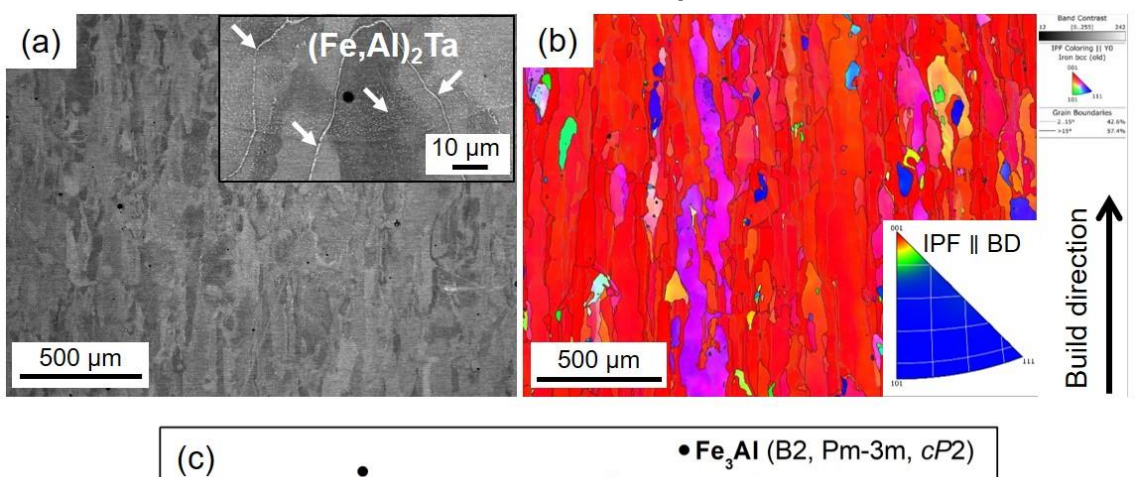
Results and Discussion

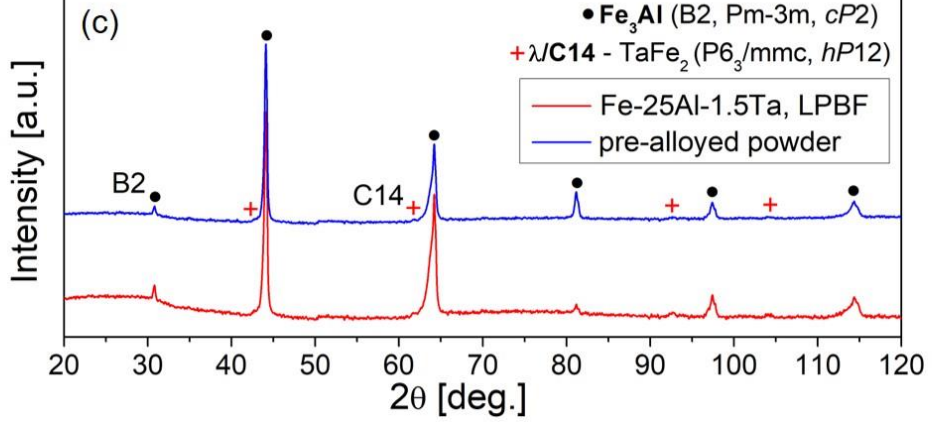
The LPBF-built samples showed no microcracking with a relative density of approximately 99.5% as calculated by X-ray micro-computed tomography (micro-CT). Macrocracks occasionally formed at the substrate-sample interface in a few samples despite the build temperature of 650 °C. Fine spherical pores were observed in the samples, suggesting that these were gas pores formed during the laser processing or inherited from the powder feedstock.

EDX measurements gave an average composition of 75.4Fe-22.9Al-1.7Ta (at.%), indicating a loss of approximately 2 at.% for Al during laser processing. The microstructure was characterized by coarse and columnar grains that grew epitaxially from the substrate, were several millimeters long, and extended over several layers along the BD as shown in Figure 1a. The grain size distribution was inhomogeneous throughout the sample, ranging from 7 to 948 µm. The high magnification SEM-BSE micrograph in the inset of Figure 1a shows that the matrix grains are decorated with a network of fine precipitates. In addition, the precipitates were often observed in the interior of the grains. Compositional analysis of these precipitates by SEM-EDX could not be performed due to their small size. However, the qualitative analysis and previous research indicated that the precipitates were significantly enriched in Ta relative to the matrix [4]. The XRD phase identification diagram in Figure 1c shows that the fine precipitates were (Fe, Al)2Ta Laves phase dispersed in a D0₃-type ordered Fe₃Al matrix. The EBSD inverse pole figure (IPF) maps in Figure 1b show that the microstructure consists of several large and columnar grains elongated along the BD, which are predominantly oriented close to <0 0 1> (red colour) with respect to the BD. A few smaller grains, also elongated along the BD, with different crystallographic orientations can also be observed. Some small grains were oriented in the dominant orientation (red colour) at several locations.

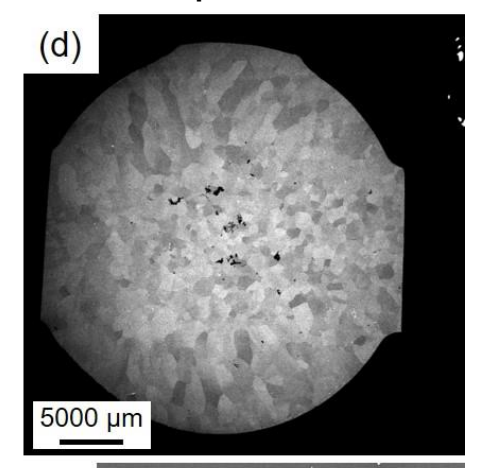
For comparison purposes, the microstructure of the as-cast sample is presented in Figure 1d. The cast sample showed a typical cast microstructure consisting of a columnar zone and equiaxed grains in the center of the cylindrical ingot [5]. Similar to the as-built LPBF sample, the Laves phase precipitates were observed at the boundaries of the matrix grains in the as-cast sample as shown in Figure 1e. However, the amount of fine precipitates dispersed within the matrix grains was significantly lower in the as-cast sample than in the as-built LPBF sample (see inset in Figure 1a).

As-built LPBF sample





As-cast sample



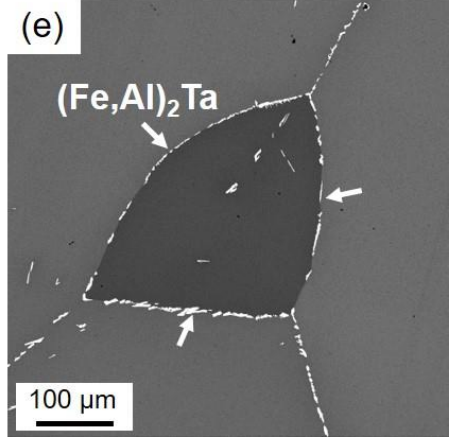


Figure 1. Typical SEM-BSE micrographs of the Fe-25Al-1.5Ta (at.%) as-built LPBF specimen in the BD-SD cross-section taken from the centre of the specimen (a), EBSD orientation map and associated inverse pole figure, IPF, map parallel to the BD overlaid with grain boundary misorientations showing a preferential orientation close to the <0 0 1> direction (red color) with respect to the BD (b), XRD pattern at room temperature (c) showing the characteristic reflections of Fe₃Al phase with D0₃ structure and C14-TaFe₂ Laves phase for both pre-alloyed powder and as-built LPBF sample, and typical SEM-BSE micrographs of the Fe-25Al-1.5Ta as-cast specimen (d and e). The arrows in high magnification images in (a) and (e) refer to several (Fe, Al)2Ta Laves phase precipitates located mainly at grain boundaries and often within the matrix grains. The BD and SD refer to the build and scan directions, respectively.

Conclusions

The present study shows that crack-free and dense samples of Fe $_3$ Al-based iron aluminide alloys reinforced with Laves phase precipitates can be printed by LPBF. The microstructure consists mainly of columnar grains elongated over the build height with a relatively strong <0 0 1> texture and a non-uniform grain size distribution. It can therefore be concluded that the post-treatment after LPBF is required for grain refinement.

Acknowledgements

The present work was funded by the German Research Foundation (Deutsche Forschungsgemeinschaft, DFG) as a part of the project "Post-processing metallurgy of additively manufactured iron aluminides" (project number 528361532).

- [1] M. Palm, F. Stein, G. Dehm, Iron aluminides, Annu. Rev. Mater. Res. **2019**, *49*, 297-326
- [2] G. Sauthoff, Multiphase intermetallic alloys for structural applications, Intermetallics **2000**, *8*, 1101-1109.
- [3] D.D. Risanti, G. Sauthoff, Microstructures and mechanical properties of Fe–Al–Ta alloys with strengthening Laves phase, Intermetallics **2011**, *19*, 1727-1736
- [4] A. Emdadi, S. Bolz, J. Buhl, S. Weiß, M. Bambach, Laser Powder Bed Fusion Additive Manufacturing of Fe3Al-1.5Ta Iron Aluminide with Strengthening Laves Phase, Metals **2022**, *12*, 997.
- [5] A. Emdadi, Y. Yang, S. Bolz, O. Stryzhyboroda, M. Tovar, S. Gein, U. Hecht, S. Weiß, Mechanisms of necklace recrystallization in a BCC Fe-Al-Ta alloy with strengthening Laves phase precipitates, Scripta Mater. **2023**, *237*, 115705.

SCP 2.3:

Microstructure and mechanical properties of Mo-Si-B alloy processed using electron beam powder bed fusion

Yong Chen¹, Elisabeth Kammermeier³, Jakob Bandorf², Steffen Neumeier², Benjamin Wahlmann¹ and Carolin Körner³

¹Center of Advanced Materials and Processes, Friedrich-Alexander Universität Erlangen-Nürnberg, Dr.-Mack-Str. 77, 90762 Fürth, Germany, yong.chen@fau.de, benjamin.wahlmann@fau.de

²Materials and Engineering Institute I, Friedrich-Alexander Universität Erlangen-Nürnberg, Martensstr. 5, 91058 Erlangen, Germany, jakob.bandorf@fau.de, steffen.neumeier@fau.de

³Materials Science and Engineering for Metal, Friedrich-Alexander Universität Erlangen-Nürnberg, Martensstr. 5, 91058 Erlangen, Germany, elisabeth.kammermeier@fau.de, carolin.koerner@fau.de

Introduction

The multiphase alloy Mo-9Si-8B (at.%) exhibits excellent thermal and mechanical properties at temperatures above 1200 °C, making it a promising refractory material for advanced turbine engines [1]. The combination of Mo-Si-B with additive manufacturing (AM) enables the single-step fabrication of complex, near-net-shape components. However, the inherently high brittle-to-ductile transition temperature (BDTT >1000 °C) of Mo-Si-B poses challenges for fabricating crack-free parts. Electron beam powder bed fusion (PBF-EB), characterized by high energy input, enables high powder bed temperatures (i.e., above the BDTT of Mo-Si-B) [2]. This significantly reduces thermal stresses and cracking risk, facilitating the fabrication of crack-free refractory components with complex geometries.

The mechanical and oxidation properties of Mo-Si-B alloys are determined by their multiphase microstructure, including the volume fraction, morphology, and spatial distribution of phases, such as ${\rm Mo_{SS}}$, ${\rm Mo_{3}Si}$, and ${\rm Mo_{5}SiB_{2}}$. An optimal microstructure necessitates a minimized yet continuous ${\rm Mo_{SS}}$ phase distribution: the interconnected ${\rm Mo_{SS}}$ provides crack bridging for damage tolerance while limiting its volume fraction to ensure oxidation resistance [1,3]. Additionally, the crystallographic texture of as-built components influences their mechanical performance. The texture is dependent on the evolution of grain structure which is affected by the shape and size of the melt pool that is determined by the processing parameters [4]. The influence of processing parameters (e.g., lateral velocity, area energy) on the microstructure and texture of as-built Mo-Si-B samples was analyzed within the established processing window. Mechanical properties were characterized using nanoindentation and high-temperature compression tests. This study aims to establish a processing-microstructure-property relationship for PBF-EB fabricated Mo-Si-B alloys.

Materials and Methods

Gas-atomized pre-alloyed Mo-9Si-8B (at.%) powder (GfE GmbH, Nürnberg, Germany) was used and characterized by scanning electron microscopy (SEM, NanoLab 600, FEI, USA) and electron probe microanalysis (EPMA, JXA 8100, Jeol, Tokyo, Japan). The particle size distribution was determined by laser diffraction (Mastersizer 3000, Malvern GmbH, Kassel, Germany). The processing window was predicted through high-throughput thermal simulations employing a semi-analytical temperature model derived from Fourier's heat conduction equation [5]. PBF-EB processes were carried out on a Freemelt One (Freemelt AB, Mölndal, Sweden), equipped with an in-house developed electron optics (ELO) system. Topographical information of the build surface was obtained via

differencing images from opposing ELO detectors. These difference images enabled immediate classification of the surface as porous, good (dense and uniform), or uneven. Dense cuboidal specimens (~15 × 15 × 15 mm³) were fabricated using varied parameters within the established processing window. The specimens were sectioned parallel to the build direction by wire electrical discharge machining, followed by grinding and polishing. Microstructure and crystallographic texture were characterized using an SEM equipped with an electron backscatter diffraction (EBSD) detector.

The mechanical properties of individual phases were characterized by nanoindentation (Nano Indenter XP, KLA) using a diamond CubeCorner indenter tip in displacement-control mode. A constant indentation depth of 80 nm, a strain rate of 0.025 s⁻¹ and an indent spacing of 2 µm were applied. The evaluation was carried out within the indentation depth of 60-75 nm, using the Oliver-Pharr method and assuming a Poisson's ratio of 0.3. A 10 × 10 indentation grid was conducted at the center of the sample. To reflect the intended high-temperature applications, compression tests were conducted on an Instron 4505 universal testing machine (Instron, Norwood, MA, USA) at 800 °C, 1000 °C, and 1200 °C. For each temperature, constant strain rates of 10⁻³ s⁻¹, 10⁻⁴ s⁻¹, and 10⁻⁵ s⁻¹ were applied. Cylindrical specimens (4.5 mm height, 3 mm diameter) were prepared by wire electrical discharge machining.

Results and Discussion

The processing window of Mo-9Si-8B (at.%) was rapidly established by combining highthroughput thermal simulations with ELO monitoring (see Fig.1). A qualitative comparison revealed a strong agreement between the two approaches, enabling accurate processing window identification while significantly reducing the required experimental effort to a single build. High-density Mo-9Si-8B (at.%) samples were successfully fabricated within the established processing window, featuring a typical dendritic microstructure with coarse Moss dendrites and fine interdendritic Mo₅SiB₂ and Mo₃Si phases. EBSD analysis revealed a strong [111] texture in the build direction or a near-isotropic texture, depending on the imposed area energy. Similar behavior has been reported in PBF-EB of pure Mo and pure W, where fiber texture switching was observed with varying process conditions [6,7]. This fiber texture switching can be controlled and potentially exploited to tailor the mechanical performance of components. In addition, intragranular lattice distortions are evident, seen as sub-grain boundaries and orientation gradients within individual grains (see Fig. 2), indicating a thermal-mechanical effect during PBF-EB processing. Moreover, dynamic recovery and recrystallization were observed and attributed to processing-induced mechanical deformation during the PBF-EB process. Nanoindentation tests were conducted to evaluate the influence of area energy on the mechanical properties. A pronounced increase in Young's modulus of the Moss phase was observed with increasing area energy, rising from 427.87 GPa to 480.29 GPa. Fig. 3 shows the high-temperature compression behavior of the PBF-EB processed Mo-9Si-8B (at.%) alloy, revealing excellent compressive strength comparable to that of powder metallurgical counterparts [1]. Specifically, yield stress reached 1350 MPa at 1000 °C (10^{-4} s⁻¹), higher than that of HIPed Mo-6.1Si-7.9B (1150 MPa) [8]. In general, the flow stress decreased with increasing temperature and decreasing strain rate. Three types of stress-strain responses, including work hardening, steady-state flow, and softening, were observed, depending on the deformation conditions. These findings highlight the potential of PBF-EB processing to fabricate high-performance Mo-Si-B alloys with tailored microstructures, competitive mechanical properties, and the ability to fabricate complex geometries.

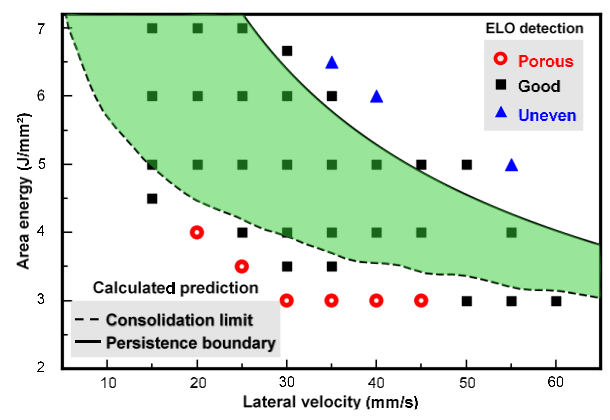


Fig. 1: Processing window of Mo-9Si-8B (at.%) using PBF-EB, derived from a combination of thermal simulations and ELO monitoring.

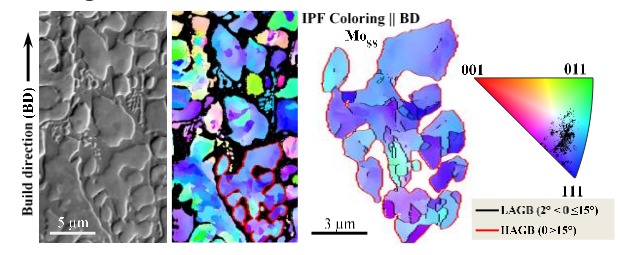


Fig. 2: Cross-sectional SEM image and EBSD IPF map along the build direction. A highlighted grain is shown on the right with its corresponding IPF map, grain boundaries, and IPF color key.

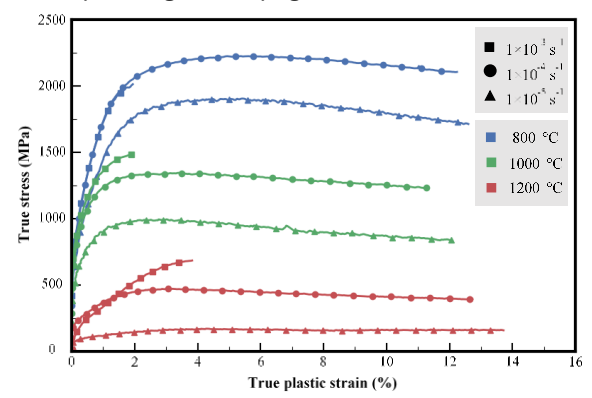


Fig. 3: Stress-strain curves obtained from the compression testing of the as-built Mo-9Si-8B at different temperatures.

- [1] M. Krüger, P. Jain, K.S. Kumar, M. Heilmaier; Intermetallics, **2014**, 48, 10–18.
- [2] Z. Fu, C. Körner; European Journal of Materials, **2022**, *2*(*1*), 54–116.
- [3] Lemberg J A, Ritchie R O; Advanced Materials, **2012**, *24*(26), 3445-3480.
- [4] Breuning C, Böhm J, Markl M, et al; Modelling, **2023**, *4*(3), 336-350.
- [5] DebRoy T, Wei H L, Zuback J S, et al; Progress in materials science, **2018**, 92, 112-224.
- [6] Fernandez-Zelaia P, Ledford C, Ellis E A I, et al; Materials & Design, **2021**, *207*, 109809.
- [7] Ledford C, et al; International Journal of Refractory Metals and Hard Materials, **2023**, *132*, 106148.
- [8] Alur A P, Chollacoop N, Kumar K S; Acta Materialia, **2004**, *52(19)*, 5571-5587.

SCP 2.4:

Application of Thermo-Calc's Additive Manufacturing Module for LPBF of Intermetallics-based Materials

Andre Schneider, Andreas Markström, Amer Malik, Carl-Magnus Lancelot, Minh-Do Quang, Johan Jeppsson, Anders Engström Thermo-Calc Software AB, Sweden

Today's state-of-the-art Finite Element (FE) tools tend to use relatively simplified materials descriptions using handbook values that might have little dependence on chemistry or even temperature. Thermo-Calc has spent the last few years developing new models to predict thermophysical material properties to incorporate with CALPHAD-based materials descriptions. The properties have been widely used to extract CALPHAD-based materials data for use in dedicated FEM codes, and the addition has laid the foundation for our development of a completely integrated tool to simulate Additive Manufacturing (AM) processes. The AM Calculator is recently updated and it gives a unique possibility to address the problem of solidification during AM, where we obtain a unified treatment of both process parameters and chemistry-dependent thermophysical properties when solving the multi-physics problem of a moving heat source that melts and solidifies metal powder. The updated Scheil calculator allows for pre-generating a solidification profile, now also including evaporation properties, that can be saved into your own materials library, or used directly as input to the AM Calculator.

Examples of the AM module applied to laser powder bed fusion processing of Intermetallics-based materials are shown: Titanium Aluminides and Iron Aluminium Alloys. Recent and ongoing developments, such as key-holing prediction and process maps, are demonstrated, along with simulations of precipitation reactions during heat-treatment of as-built structures using TC-Prisma and DICTRA.

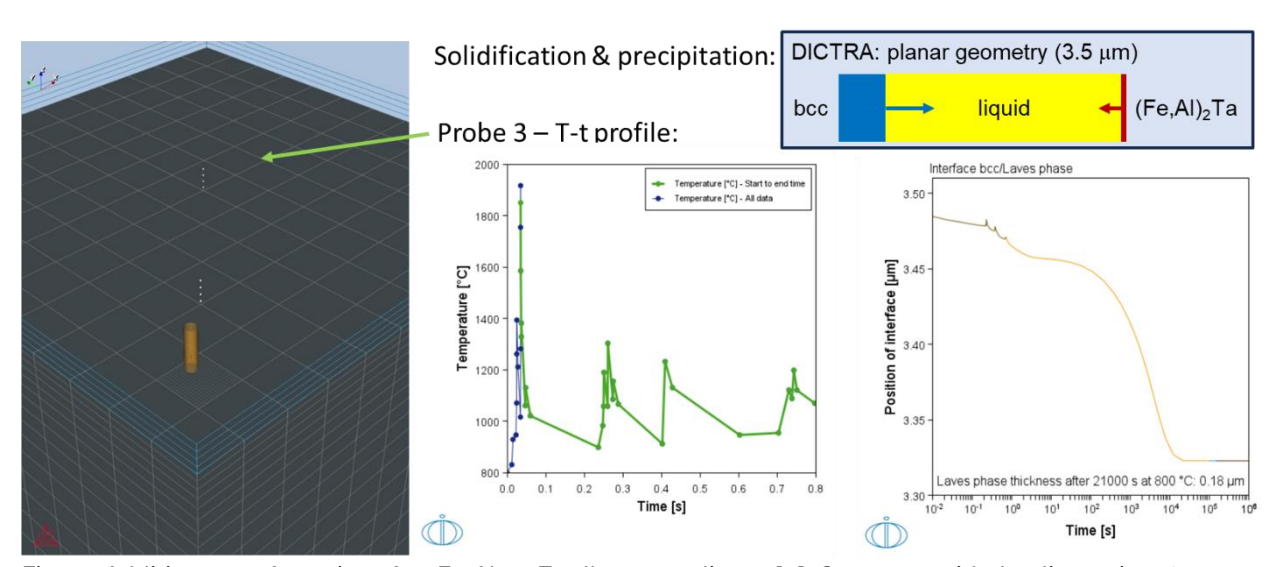


Figure: Additive manufacturing of an Fe₃Al-1.5Ta alloy according to [1]. Geometry with the dimension: 8 mm x 4 mm x 4 mmm. Simulation of production of 4 layers with layer thicknesses of 50 mm each. The applied power is 300 W, the scanning speed 500 mm/s and the plate temperature is 800 °C. This allows for further $(Fe,Al)_2$ Ta Laves Phase growth after the additive manufacturing process.

Reference:

[1] A. Emdadi, S. Bolz, J. Buhl, S. Weiß, M. Bambach: Laser Powder Bed Fusion Additive Manufacturing of Fe₃Al-1.5Ta Iron Aluminide with Strengthening Laves Phase. Metals **12** (**2022**) 997.

SCP 3.1:

Data to Aid Materials Design and Process Optimization of Molybdenumand Niobium-based Refractory Alloys

Anders Engström¹, Bharat Mehta¹, Liangyan Hao² and Weiwei Zhang² and Qing Chen¹

Thermo-Calc Software AB, 169 67 Solna, Sweden, anders@thermocalc.com

Thermo-Calc Software Inc, McMurray, PA 15317, USA

Introduction

Alloys are inherently complex systems, where microstructure and properties are strongly governed by both chemical composition and processing conditions. These dependencies are rarely reflected in conventional handbooks or materials databases, which often provide limited coverage in terms of compositional range, processing parameters (e.g., temperature), or lack representation of time-dependent behavior. As a result, engineering simulations that rely on such data sources are constrained in accuracy and applicability, particularly when applied to novel materials or non-standard processing routes. This often necessitates additional experimental measurements or forces engineers to work with a high degree of uncertainty.

Materials and Methods

The CALPHAD (CALculation of PHAse Diagrams) approach [1] offers a robust framework to model the composition, temperature, and time dependence of properties in industrial multicomponent alloys. It enables the generation of reliable data where experimental measurements are unavailable and allows for the prediction and optimization of location-specific properties within components, liberating manufacturers from relying solely on conservative design minimums.

In this presentation, we introduce the CALPHAD methodology and demonstrate its application in the design and optimization of intermetallic-based materials. We focus on the modelling of intermetallic phases and present case studies involving molybdenum-and niobium-based refractory alloys. We do this using recently developed thermodynamic and kinetic databases [2-3].

Results and Discussion

Calculation results of phase equilibria and predictions of thermophysical properties as functions of both composition and temperature will be presented. One example is seen in Fig. 1 where it is demonstrated that at 1600 °C the addition of Ti to the base composition Mo-12.5Si-8.5B (at.%) stabilizes BCC and T1 phases at the expense of Mo $_3$ Si phase. When Ti content exceeds 30 at.%, the Ti $_5$ Si $_3$ phase starts to form at the expense of the T1 phase. The calculated phase compositions for the Mo-12.5Si-8.5B-27.5Ti (at.%) alloy are consistent with experimental measurements in Ref. [4].

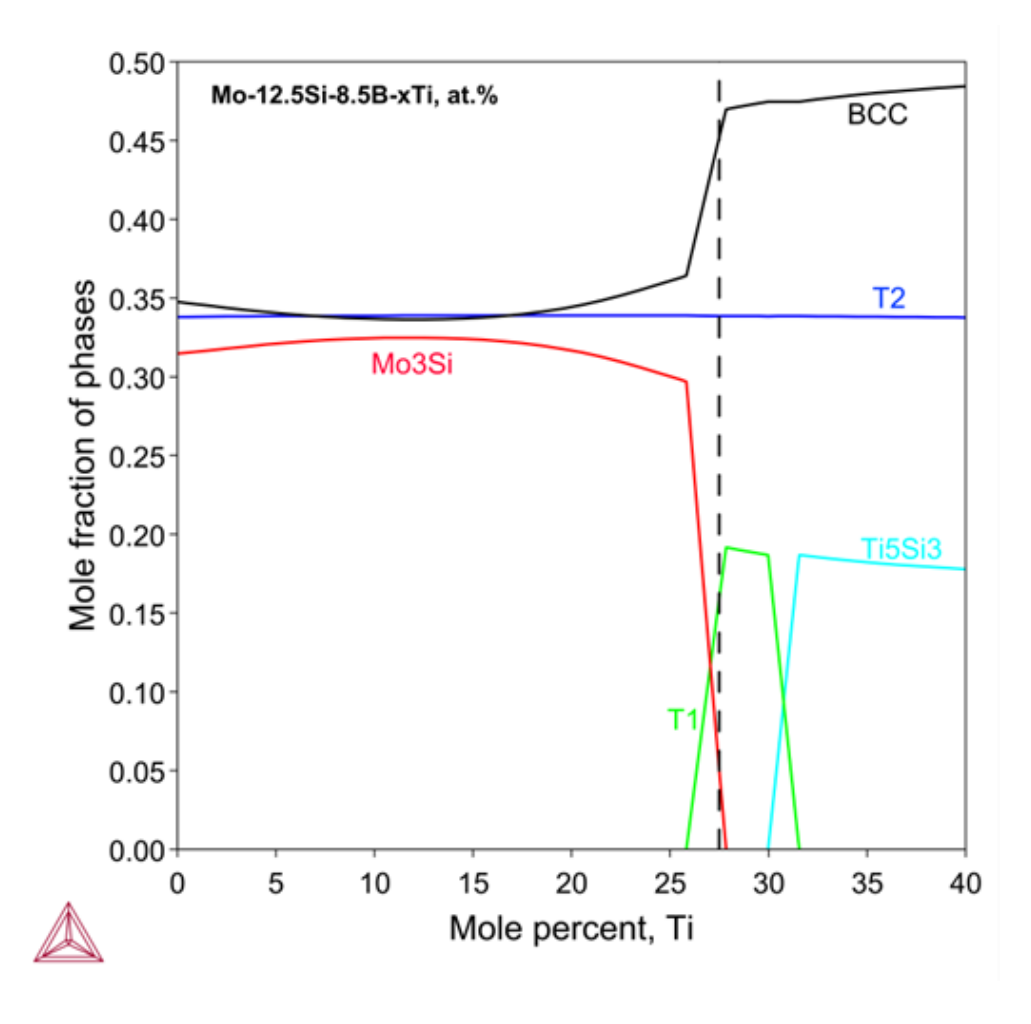


Fig. 1: Calculated phase fractions as a function of Ti concentration in the Mo-12.5Si-8.5B-xTi (at.%) alloys at 1600 $^{\circ}$ C. The dashed line marks the experimentally investigated composition in [4] where x = 27.5.

Furthermore, we demonstrate how complex manufacturing processes, such as the laser powder bed fusion (LPBF) process of molybdenum- and niobium-based refractory alloys, can be successfully simulated. This is achieved by incorporating relevant physical models, as implemented in the Additive Manufacturing Module of Thermo-Calc [5], and by utilizing high-fidelity thermodynamic and thermophysical input data that vary with both composition and temperature [2-3]. Fig. 2 shows simulation result for a Nb-Si-Ti alloy (Nb-18Si-24Ti-2Cr-2Al-2Hf in at%). From the simulation the size and shape of the resulting melt pool can be determined under different process conditions.

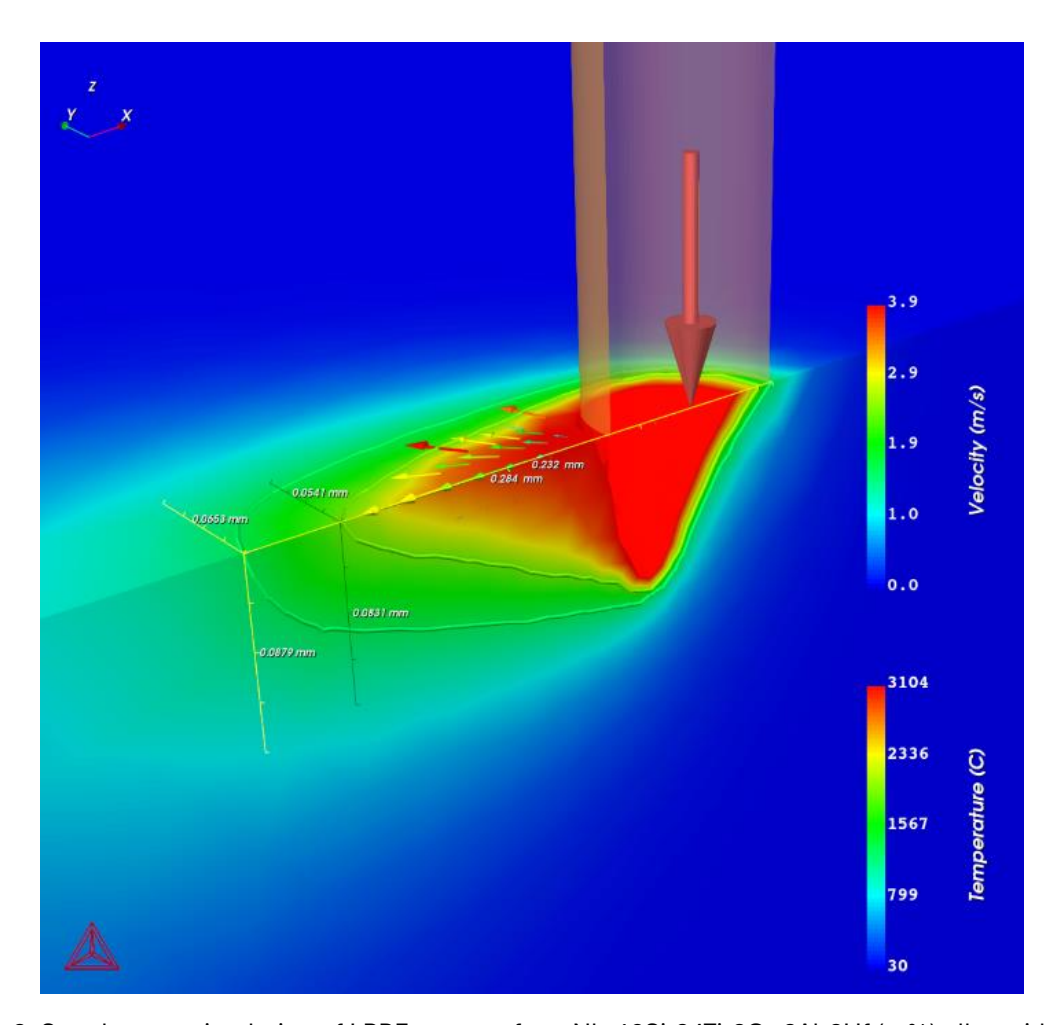


Fig. 2: Steady state simulation of LPBF process for a Nb-18Si-24Ti-2Cr-2Al-2Hf (at%) alloy with a laser power equal to 440W and a scan speed of 1600 mm/s. All necessary material input data required for the simulation was calculated using the database in Ref. [3].

- [1] H. L. Lucas, S. G. Fries, B. Sundman, Computational Thermodynamics "The CALPHAD Method". Cambridge University Press, 40 W. 20 St. New York, NY, United States, **2007**.
- [2] Thermo-Calc Software TCMO1 and MOBMO1 Molybdenum-based Alloys Databases, https://thermocalc.com/products/databases/molybdenum-based-alloys/ (accessed 8 April 2025).
- [3] Thermo-Calc Software TCNB1 and MOBNB1 Niobium-based Alloys Databases, https://thermocalc.com/products/databases/niobium-based-alloys/ (accessed 8 April 2025).
- [4] Y. Yang, et al. Acta Materialia, **2010**, 58, 541-548.
- [5] The Additive Manufacturing Module of Thermo-Calc 2025a, https://thermocalc.com/products/add-on-modules/additive-manufacturing-module/ (accessed 8 April 2025).

SCP 3.2:

Prediction of G-phase precipitation under irradiation by thermodynamic calculation

Toshiaki Horiuchi¹, Satoshi Minamoto², Takamichi Miyazaki³, Hiroshi Abe⁴

¹ Hokkaido University of Science, Sapporo, Hokkaido, 006-8585, Japan, horiuchi@hus.ac.jp

² National Institute for Materials Science (NIMS), Tsukuba, Ibaraki, 304-0044, Japan,

MINAMOTO.Satoshi@nims.go.jp

³ Tohoku University, Sendai, Miyagi, 980-8579, Japan, takamichi.miyazaki.a5@tohoku.ac.jp ⁴ Tohoku University, Sendai, Miyagi, 980-8579, Japan, hiroshi.abe.c3@tohoku.ac.jp

Introduction

Duplex stainless steels consisting of ferrite (a) and austenite (g) phases are used for welding components in nuclear power plants. Although a has better stress corrosion cracking resistance than g, it has been pointed out that prolonged thermal aging under neutron irradiation may cause spinodal decomposition and precipitation of G-phase (an intermetallic compound consisting mainly of Ni, Si, Mn, and Mo [1]) in a, which may lead to embrittlement. Since experimental confirmation of precipitation of G-phase requires long-term experiments under severe conditions, thermodynamic calculation is expected to predict the precipitation of G-phase instead. However, although several thermodynamic models have been reported for G-phase in steel [2], the distribution of elements in the sublattice remains controversial due to a lack of experimental data. In the present study, the generalization performance of the thermodynamic database (TDB) originally developed in our previous study [3] is verified by thermodynamic equilibrium calculations. Furthermore, in order to predict the precipitation behavior of G-phase in duplex stainless steels, taking into account the effect of neutron irradiation, the diffusion parameters necessary for the simulation of precipitation of G-phase are adjusted, and the time-temperature-precipitation (TTP) diagrams for G-phase under neutron irradiation and non-irradiation conditions are calculated.

Materials and Methods

Thermodynamic equilibrium calculations were performed by Thermo-Calc on the alloy compositions in the literature with detailed reports on the composition of G-phase in duplex stainless steels [4], using the developed TDB [3]. The calculation results were compared with the literature values. TC-PRISMA, an add-on module of Thermo-Calc, was used to predict the precipitation behavior of G-phase. The latest version of Thermo-Calc's TCS Alloy Mobility Database (MOB2 Ver. 2.5) [5] was used as the kinetic database, and the interfacial energy was set to 0.2 J/m². Since the values in the kinetics database are for the high temperature range where volume diffusion dominates, it is necessary to determine the Mobility enhancement prefactor (MEP). MEP corrects for this in the low temperature range where short-circuit diffusion dominates. MEP was adjusted as a function of temperature to reproduce the values reported in the various literature on the relationship between isothermal aging time and G-phase grain size.

Since G-phase is an intermetallic compound, it is considered that there are not many atomic vacancies in G-phase even under irradiation. The thermodynamic calculations were performed assuming that the enthalpy of formation in G-phase is the same as that in the non-irradiated phase. In the present study, the effect of excess vacancies by neutron irradiation was modeled as an increased diffusion rate, corresponding to an increase in MEP. In our previous study, D316L stainless steel weld metal (Fe-19.6Cr-

12.5Ni-0.6Si-2.3Mo-1.5Mn-0.02C (wt%)) was isothermally aged at 275 °C for 8000 h under neutron irradiation conditions of 2 × 10^{22} n/m² and 5 × 10^{24} n/m², which resulted in clustering of G phase at 1.2 nm and 1.3 nm, respectively. Therefore, in the present study, the effect of neutron irradiation on the increase in diffusion rate was formulated by dividing the MEP in the irradiated condition by that in the non-irradiated condition. Finally, TTP diagrams for G-phase under neutron irradiation and non-irradiation conditions are predicted.

Results and Discussion

Figure 1 shows the experimental chemical compositions of G-phase precipitated in the Fe-20.4Cr-10.5Ni-1.0Si-2.4Mo-0.8Mn-0.03C alloy after prolonged isothermal aging at 350°C [4] and the equilibrium calculation result in the present study. The experimental and the calculated results seem to be different, however, in the experimental results, the Fe and Cr contents in G-phase decrease with increasing time, while the Ni, Si, and Mo contents increase and approach the calculated results. It might be caused by the incorporation of matrix elements during composition analysis in the early aging stage, when the particle size of G-phase is quite small. After a more extended period of isothermal aging, the experimental results are expected to approach the equilibrium calculation results in the present study. Since similar trends were obtained for other alloy compositions and temperatures, the high generalization performance of the TDB developed in our previous study is confirmed.

After adjustment to reproduce the literature values, MEP is finally expressed as follows,

$$MEP = \exp\left(\frac{17119}{T} - 16.411\right) . {1}$$

The temperature at which the MEP becomes 1 in Eq. (1), i.e., the temperature at which volume diffusion becomes dominant, is estimated to be 768 °C. This value is considered reasonable for steels.

As a result of fitting MEP under neutron irradiation, MEP was estimated to be 11.7 or 17.8 times higher under neutron irradiation conditions of 2×10^{22} n/m² or 5×10^{24} n/m², respectively. By obtaining MEP for an arbitrary temperature using Eq. (1) and adopting MEP multiplied by 11.7 or 17.8, the G-phase precipitation behavior can be predicted under 2×10^{22} n/m² or 5×10^{24} n/m² neutron irradiation conditions. In our previous experiments, isothermal aging for D308L stainless steel weld metal (Fe-19.9Cr-9.8Ni-0.4Si-1.8Mn-0.03C (wt%)) at 275 °C for 8000 h under neutron irradiation of 5×10^{24} n/m² resulted in clustering of G-phase at 1.6 nm. The predicted G-phase grain size of D308L under the above conditions, calculated in the present study, was 1.54 nm, which is in excellent agreement with the experimental results.

Figure 2 shows the resultant TTP diagram for D316L and D308L stainless steel weld metals under neutron irradiation and non-irradiation conditions. Under neutron irradiation conditions, the times for G-phase precipitation shift to the shorter side by a factor of about 10 for both alloys, while the difference in the times for G-phase precipitation due to the different irradiation conditions of $2 \times 10^{22} \, \text{n/m}^2$ and $5 \times 10^{24} \, \text{n/m}^2$ is expected to be not so large. The difference in the times for G-phase precipitation between D316L and D308L is more pronounced at lower temperatures under neutron irradiation conditions. It is thus concluded that the thermodynamic calculations using the TDB developed in our previous study can predict the precipitation behavior of G-

phase for stainless steels with a wide range of temperatures and compositions over a long period of isothermal aging, taking into account the effect of neutron irradiation.

Acknowledgements

A part of this work was supported by JSPS KAKENHI Grant Numbers JP19H02472 and MEXT Innovative Nuclear Research and Development Program Grant Number JPMXD0222682225.

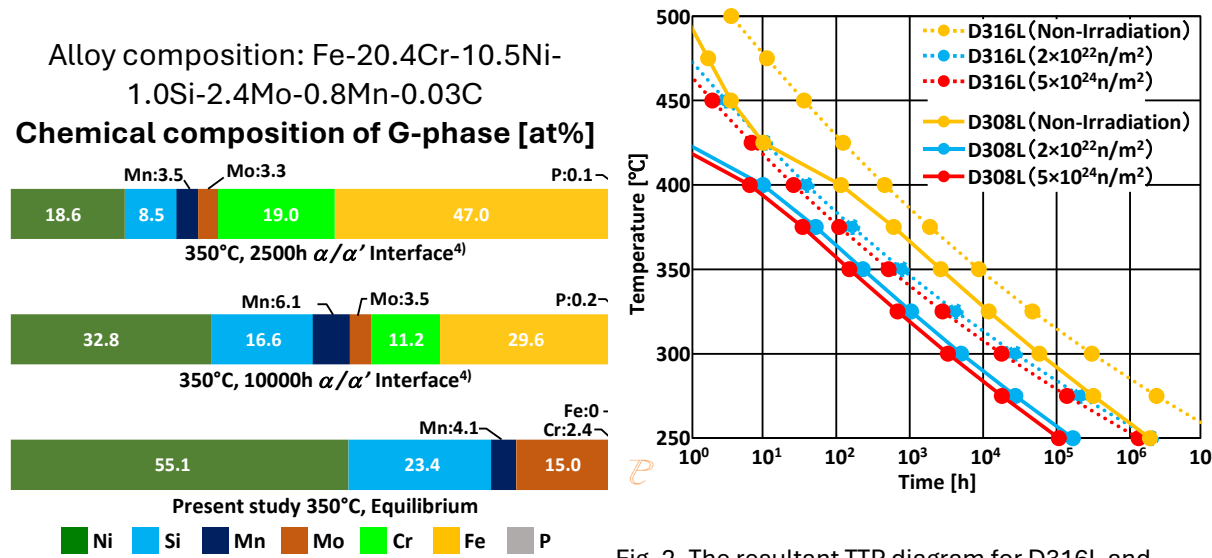


Fig. 1. The experimental chemical compositions of G-phase in the Fe-20.4Cr-10.5Ni-1.0Si-2.4Mo-0.8Mn-0.03C alloy after prolonged isothermal aging at 350°C [4] compared with the equilibrium calculation result in the present study.

Fig. 2. The resultant TTP diagram for D316L and D308L stainless steel weld metals under neutron irradiation and non-irradiation conditions.

- [1] T. Hamaoka, A. Nomoto, K. Nishida, K. Dohi, N. Soneda, Philosophical Magazine, 92, 22, **2012**, 2716–2732.
- [2] A. Jacob, C. Domain, G. Adjanor, P. Todeschini, E. P.-Karadeniz, Journal of Nuclear Materials, 533, **2020**, 152091.
- [3] S. Minamoto, T. Horiuchi, T. Miyazaki, H. Abe, Proc. Intermetallics 2023, Bad Staffelstein, Germany, **2023**, 55-56.
- [4] R. Badyka, S. Saillet, J. Emo, C. Domain, C. Pareige, Journal of Nuclear Materials, 555, **2021**, 153123.
- [5] H. Larsson, L. Höglund, CALPHAD, 33, 2009, 495-501.

SCP 3.3:

Influence of partial occupancy on the elastic tensor of the FeCr σ phase.

Mariano Forti¹, Guillaume Laplanche¹ and Thomas Hammerschmidt¹
¹Ruhr Universität Bochum, Germany.

Introduction

The Fe-Cr system is an important alloy system with applications in high-temperature environments. At Cr concentrations between 45 and 50 at.% and temperatures ranging from 550 to 800°C [1], the Fe-Cr σ -phase forms and may significantly influence the mechanical properties and corrosion resistance of Fe-Cr alloys. The unit cell of this σ -phase (**Fig. 1a**) is tetragonal (space group P4₂/mnm) with five Wyckoff positions. Atomistic calculations of phase stability and mechanical properties of the σ -phase, e.g., by Density Functional Theory (DFT), are usually carried out under the assumption of full sublattice occupancy, i.e., one chemical species per Wyckoff position. Many experiments, however, indicate partial occupancies of the Wyckoff positions, i.e., more than one chemical species on the sublattice sites of the same Wyckoff position. The possibilities of distributing atoms of different chemical species on all sites of each such sublattice lead to a combinatorial explosion that rules a complete sampling intractable for DFT calculations. Interpolations of calculations with full sublattice occupations using ideal mixing [2] or mean-field approaches [3] lead to approximate results but neglect the effects of local atomic configurations.

In this work, we investigate how explicit consideration of partial occupancy influences the elastic properties of the σ -phase in DFT calculations. We focus on a Fe₁₆Cr₁₄ unit cell, which can be modeled with nominal and on-site compositions in agreement with experimental observations.

Methods

We employ DFT calculations to determine the elastic constants of the Fe-Cr σ -phase at a nominal composition of Fe₁₆Cr₁₄ (48 at.% Cr). To capture the impact of atomic disorder, we explicitly explore all possible atomic arrangements within the σ -phase unit cell, incorporating experimentally reported partial occupancies of Wyckoff sites by Yakel [4], see **Fig. 1b**. A subset of representative configurations is selected for detailed elastic constant calculations. These calculations are conducted using the Vienna Ab initio Simulation Package (VASP) [5], utilizing the Perdew-Burke-Ernzerhof (PBE) [6] exchange-correlation functional and the Projector Augmented Wave (PAW) method [7]. The elastic tensor is derived from stress-strain relationships obtained via energy-strain calculations [8].

Results and Discussion

In a full sublattice model, the Fe-Cr σ phase has a tetragonal unit cell in the space group P4₂/mnm in the entire composition range. Positive formation enthalpies with a minimum at around 40 at.% Fe are observed, implying that the σ phase might be stabilized by entropy or vibrational contributions, which are not considered here. Introducing partial occupancies in Fe₁₆Cr₁₄ stabilizes the compound. However, the symmetry of the unit cell is reduced, and the unit cell acquires a space group P. As a result, 22 independent components of the elastic tensor in the triclinic unit cell have to be considered. Their determination is computationally significantly more demanding since at least a hundred single-point calculations are required for each sampled configuration. **Fig. 1c** shows a

comparison of the calculated elastic tensor components accounting for partial occupancy with the expected values if the cell maintained the symmetry with full occupancy. We see deviations ranging from 1 to 20%.

Conclusion

In this work, we are presenting an extensive DFT study of the effects of partial occupancy on the mechanical properties of the Fe-Cr σ -phase. For the first time, the properties of this phase are calculated beyond a full sublattice model. We observe a reduction in symmetry from a tetragonal to a triclinic unit cell, and a change in mechanical properties of about 10% due to partial occupancies. Our results offer a more precise description of the mechanical behavior of the FeCr σ -phase and provide general insights for refining theoretical models for intermetallic phases with complex crystal structures.

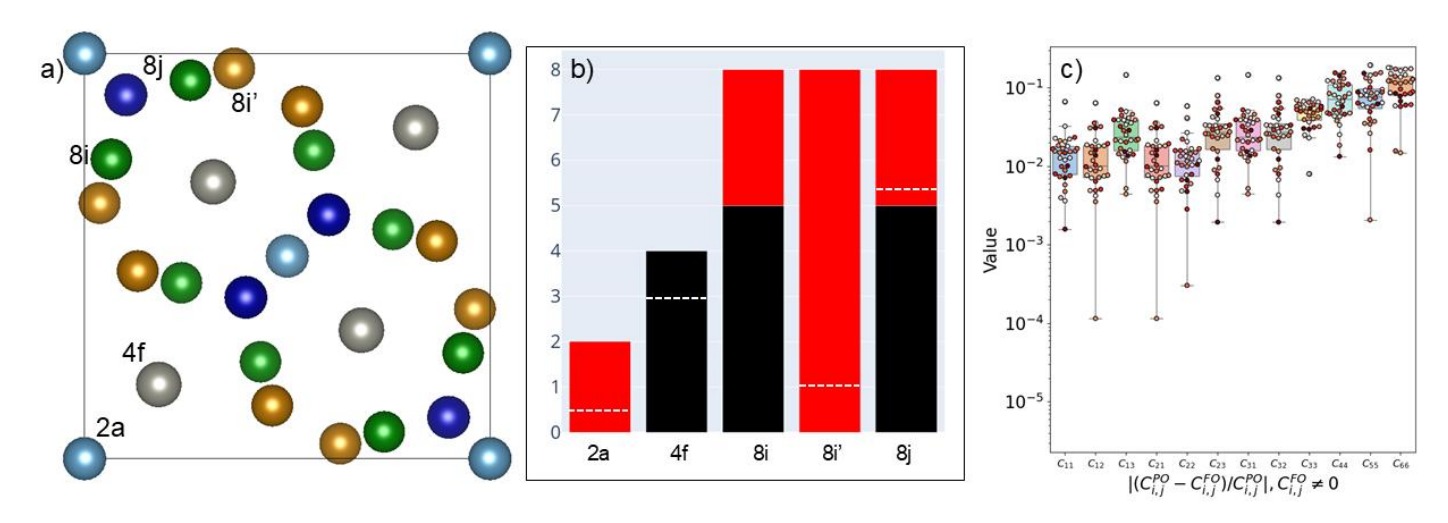


Fig. 1: Graphical Abstract. a) Unit cell of the σ phase with the five sublattices (2a, 4f, 8i, 8i', 8j) encoded in colors. b) Modeled partial occupancy of the five sublattices with Cr (black) and Fe (red) atoms. The experimentally observed occupancy is indicated by the white lines. c) Relative change of the elastic tensor for different configurations of partial sublattice occupancy (PO) as compared to full sublattice occupancy (FO).

- [1] G. Laplanche, S. Berglund, C. Reinhart, A. Kostka, F. Fox, E.P. George: Acta Materialia **2018**, 161, 338-351.
- [2] A. Vesti, P. Hiremath, S. Melin, P. A. T. Olsson: Journal of Nuclear Materials **2023**, 577, 154261.
- [3] E. Kabliman, A. V. Ruban, P. Blaha, O. Peil, K. Schwarz: Applied Sciences **2012**, 2,654-668.
- [4] H. L. Yakel, Acta Crystallographica Section B: Structural Sciences 1983, B39, 20-28.
- [5] J. Hafner: Journal of Computational Chemistry 2008, 29, 2044–2078.
- [6] J. Perdew., K. Burke, M. Ernzerhof: Physical Review Letters **1996**, 77, 3865–386.
- [7] G. Kresse, D. Joubert: Physical Review B **1999**, 59, 1758-1775.
- [8] R. Golesorkhtabar, P. Pavone, J. Spitaler, P. Puschnig, C. Draxl: Computer Physics Communication **2013**, 184, 1861-1873.

SCP 3.4:

Challenges in predicting trends of structural and mechanical properties of refractory CCAs

David Holec¹, Klemens Lechner¹, Jiyao Zhang¹, Anna S. Jelinek¹, Helmut Clemens¹, Wolfram Knabl² Petra Spörk-Erdely³ and Peter Wagatha²

¹Department of Materials Science, Montanuniversität Leoben, Franz-Josef-Strasse 18, 8700 Leoben, Austria, david.holec@unileoben.ac.at

²Plansee SE, Metallwerk-Plansee-Strasse 71, 6600 Reutte, Austria

³Institute of Materials Science, Joining and Forming, Graz University of Technology, Kopernikusgasse 24/I, 8010 Graz, Austria

Refractory high entropy alloys (R-HEAs), or more generally refractory compositionally complex alloys (R-CCAs), offer exceptional mechanical and thermal properties, such as excellent high-temperature strength and corrosion resistance. The compositional space is vast and, therefore, reliable predictions of structural properties, thermal stability, mechanical and functional properties from theory are desirable.

Density Functional Theory (DFT), a tool of choice for unbiased, quantum-mechanically accurate calculations, faces severe challenges: simulation boxes with a handful of atoms do not represent the desired chemical freedom well, while large cells are computationally unfeasible. While the latter can be overcome using molecular dynamics (MD) and Monte Carlo (MC) methods, suitable interatomic potentials are missing and their development is computationally expensive.

In this work we will present results using fast developing so-called universal potentials. These are machine-learned interatomic potentials trained on huge amounts of DFT data spanning large fractions of the periodic table, thereby bridging the gap between DFT (with chemical freedom) and MD/MC (allowing for large structures). Thus, we will compare the obtained predictions against DFT and, whenever possible, experiment, to assess their out-of-the-box applicability to R-HEAs/R-CCAs.

One case study focuses on exploring thermal stability of Mo-Nb-Ta-W-X alloy systems (Fig. 1). In this study we present a theoretical workflow for systematic theoretical investigations of the phase stability of R-HEAs based on both universal potentials (e.g. CHGNet) and DFT. To this end, we combine our calculations with DFT data from Materials Project, a curated online repository. This example will apply simple thermodynamic considerations. In a second case study, we assess the thermal stability of the disordered state with respect to ordered and/or phase-separated states, employing on-lattice MC simulations using a selected universal potential applied to a Mo-Cr-Ti-Al model system (Fig. 2). As a final result, we will discuss compositional impact on the mechanical (primarily elastic) properties, and compare those to available experimental data.

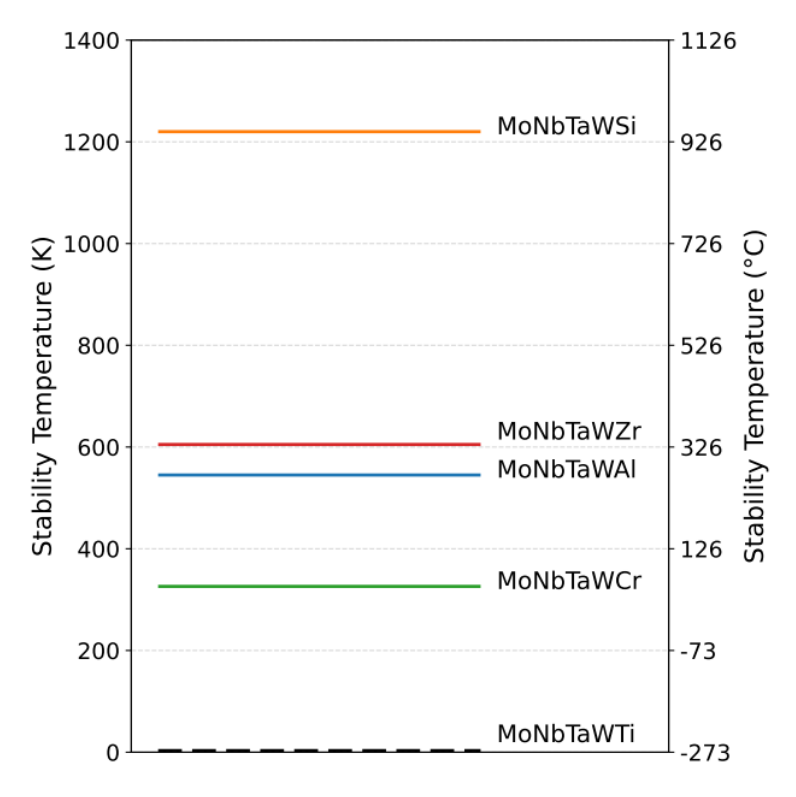


Fig. 1: Predicted thermal stability of several Mo-Nb-Ta-W-X quinary systems based on exploring decomposition routes to various combinarions of intermetallic phases.

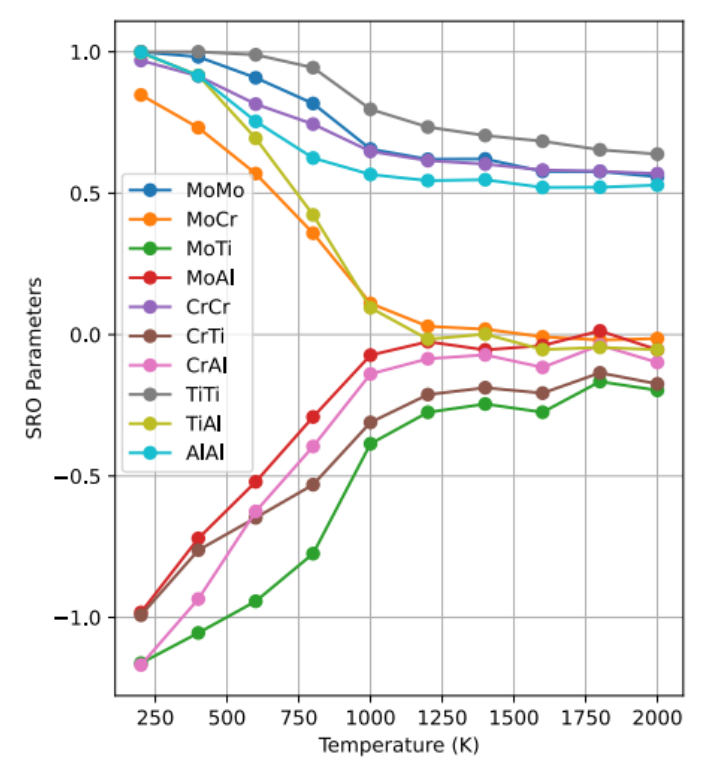


Fig. 2: Example of temperature-dependent short range order parameters of a quaternaty Mo-Cr-Ti-Al. The system prefers fully disordered configuration above 1000 K.

SCP 4.1:

Point defect concentration and atomic diffusion in Laves phases: highthroughput atomistic simulations with universal machine-learning interatomic model

Sergei Starikov¹, Zhuocheng Xie², Sang-Hyeok Lee³, Daria Smirnova⁴, Anton Bochkarev⁵, Yury Lysogorskiy⁶, Ralf Drautz⁷

¹Ruhr-Universität Bochum, ICAMS, 44780, Germany, email: sergei.starikov@icams.rub.de
 ²RWTH Aachen University, 52056 Aachen, Germany, e-mail: xie@imm.rwth-aachen.de
 ³RWTH Aachen University, 52056 Aachen, Germany, e-mail: lee@imm.rwth-aachen.de
 ⁴Ruhr-Universität Bochum, ICAMS, 44780, Germany, email: daria.smirnova@icams.ruhr-uni-bochum.de
 ⁵Ruhr-Universität Bochum, ICAMS, 44780, Germany, email: yury.lysogorskiy@rub.de
 ¬Ruhr-Universität Bochum, ICAMS, 44780, Germany, email: ralf.drautz@rub.de

Introduction

The equilibrium concentration of point defects is a key knowledge for the estimation of diffusion coefficients and phase stability of intermetallic compounds. The lack of description of defects concentration/mobility at different temperatures and compositions can lead to difficulties in developing a reliable thermodynamic model of a compound. One of the most common types of intermetallic structures are Laves phases, and only for a small number of them data on point defects exist. This work is devoted to the universal thermodynamic description of the concentration and mobility of point defects in Laves phases. The high-throughput study was performed using a new universal machine-learning interatomic model GRACE-2L-OMAT developed in ICAMS. By combining the results of atomistic modeling with chemical thermodynamics we created a database of concentrations and atomic diffusion for several hundred compounds. The prediction of the diffusion coefficient is in good agreement with the available experimental data. Generalization of the results revealed a non-trivial relationship between defect concentrations and other properties of Laves phases.

Materials and Methods

Machine-learning (ML) interatomic potentials have revolutionized the field of atomistic modeling by bridging the gap between accuracy and computational efficiency. Recently, a new generation of ML potentials based on the Atomic Cluster Expansion (ACE) has been proposed [1]. Unlike traditional empirical potentials, which rely on predefined functional forms, ACE leverages high-dimensional regression techniques using a formally complete set of descriptors to learn the potential energy surface directly from quantum mechanical data. This allows for a more accurate description of complex atomic interactions. Further generalization of this interatomic model led to the creation of a universal machine-learning interatomic model GRACE (Graph Atomic Cluster Expansion). This model allows modeling of virtually any intermetallic compound thousands of times faster than ab initio methods, without loss of accuracy. Formation/migration energies of various point defects calculated with GRACE are used in the equations of chemical thermodynamics [2], which provide a consistent model of defect concentrations and atomic diffusion.

Results and Discussion

The proposed database has allowed to establish the hierarchy of point defects in Laves phases. While in many cases the composition of compound is controlled by antisite defects, the vacancy concentrations remain relatively low compared to pure metals. This hierarchy is the main reason for the very low atomic mobility in Laves phases observed in many experimental studies. Also, for some compounds, the concentration of interstitial defects becomes comparable to the concentration of vacancies, which is a rather unusual phenomenon for this type of structure. Overall, the created database opens the way to a comprehensive understanding of the behavior of point defects in intermetallic compounds.

- [1] R. Drautz, Phys. Rev. B. 2019, 99, 014104.
- [2] S. Starikov, M. Korneva, Journal of Nuclear Materials. 2018, 510, 373-381.

SCP 4.2:

Highly deformable Laves phase in a high entropy alloy

Pankaj Kumar Ojha^{1*}, S. Yoshida², U. Sunkari¹, B. Tripathy¹, N. Tsuji², and P.P. Bhattacharjee¹

¹Department of Materials Science and Metallurgical Engineering, IIT Hyderabad, Kandi, Sangareddy, Telangana 502284, India

Email: ms21resch11001@iith.ac.in

²Department of Materials Science and Engineering, Kyoto University, Yoshida Honmachi, Sakyo-ku, Kyoto 606-8501, Japan

Email: yoshida.shuhei.5s@kyoto-u.ac.jp

Introduction

Laves phases are one of the most common intermetallic compound phases that may be formed through different elemental combinations. As a result, several Laves phases with different polytypes, such as C14 (hexagonal), C15 (cubic), and C36 (hexagonal), have been reported in different alloys such as steels, titanium alloys, and high entropy alloys. However, almost every binary and ternary stoichiometric Laves phase studied so far is hard and brittle in nature and, therefore, the presence of Laves phase is widely considered detrimental to the mechanical properties of the alloys containing such Laves phases. Thus, improving the plasticity of Laves phases remains a challenge. The present work shows an exciting possibility of designing a highly deformable compositionally complex cubic C15 Laves phase in a novel CoCrFeNi_{2.1} (HfNbTa)_{0.2} high entropy alloy (HEA).

Materials and Methods

The novel (FCC+Laves) dual-phase HEA, CoCrFeNi $_{2.1}$ (HfNbTa) $_{0.2}$ (atomic ratio), was designed by replacing Nb in CoCrFeNi $_{2.1}$ (Nb) $_{0.2}$ (that we designed in our previous work [1]) with HfNbTa. The HEA was prepared by arc melting and then homogenized at 1200 °C for 24 hours followed by water quenching. The homogenized HEA was subjected to heavy cold-rolling up to a 90% reduction in thickness. Microstructural characterization of the homogenized and cold-rolled materials was carried out by scanning electron microscopy (SEM) and transmission electron microscope (TEM) equipped with energy dispersive X-ray spectroscopy (EDS) detector. Nanoindentation tests were carried out to know the nano-hardness of the individual phases.

Results and Discussion

SEM observation of the 90% cold-rolled material revealed Laves phase elongated along the rolling direction that showed the Laves phase was highly deformable in present the HEA. Nano-hardness values for the FCC matrix and the Laves phase were ~4.5 GPa and ~7.3 GPa, respectively, which shows that the present Laves phase was inherently soft in nature and is having lowest hardness among other binary and high entropy Laves phases (HELPs). TEM observations of the homogenized material and the cold-rolled material revealed underlying reason behind the remarkable deformability of the Laves phase in the CoCrFeNi_{2.1} (HfNbTa)_{0.2} HEA. The TEM analysis of the homogenized HEA showed the presence of Hf and Ni enriched cubic C15 Laves phase, different from the hexagonal C14 Laves phase in the CoCrFeNi_{2.1} (Nb)_{0.2} HEA and several other high entropy Laves phases (HELPs). The formation and stability of the cubic C15 Laves phase in the present HEA have been explained by the site occupancy preferences of the constituent elements and the formation energy of possible binary Laves phases. The unusual deformability of the

present Laves phase was attributed to the spectacular propensity for nano-twin formation observed, possibly due to the highly off-stoichiometric composition of the Laves phase. Consequently, the present research showed exciting possibilities of designing deformable Laves phases in HEAs.

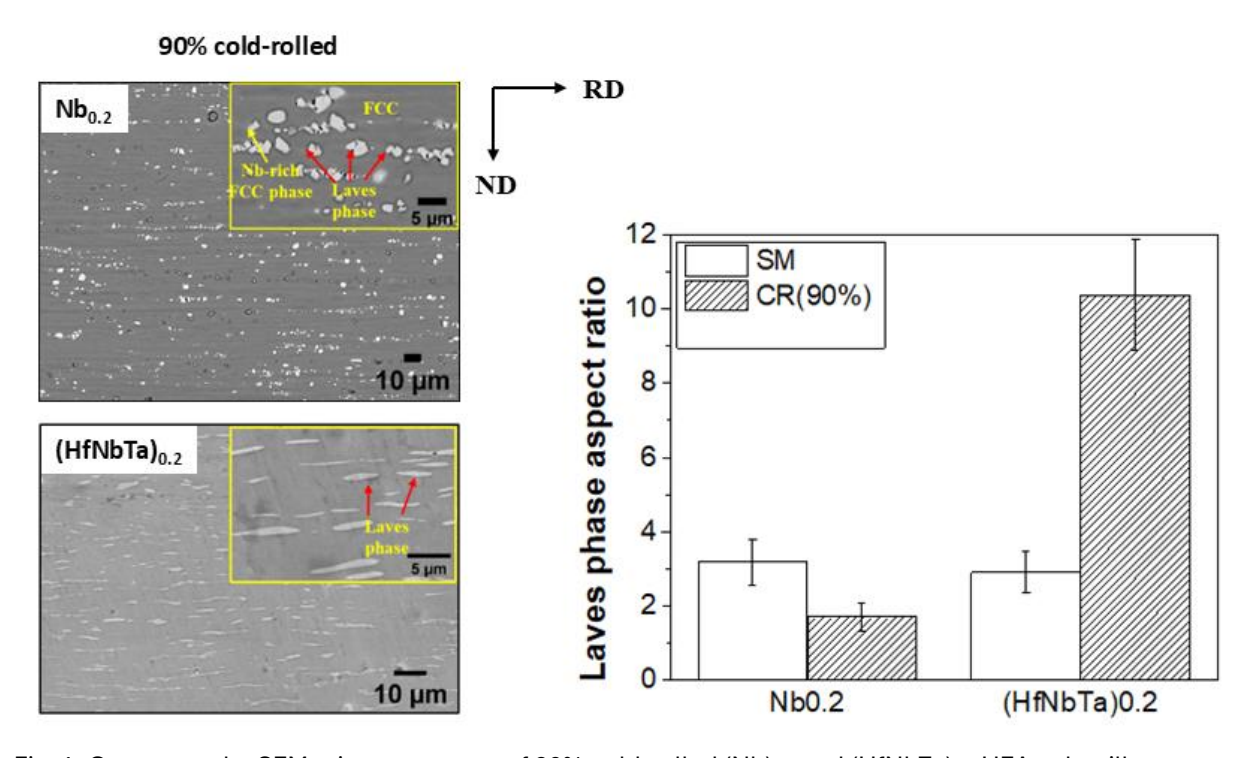


Fig. 1: Compares the SEM microstructures of 90% cold-rolled (Nb) $_{0.2}$ and (HfNbTa) $_{0.2}$ HEAs, that illustrates the deformable Laves phase in (HfNbTa) $_{0.2}$. The bar chart in the figure compares the Laves phase aspect ratio of both the HEAs for starting material (SM) condition and 90% cold-rolled (CR) condition.

- [1] U. Sunkari, S. R. Reddy, B. D. S. Rathod, D. Kumar, R. Saha, S. Chatterjee, and P. P. Bhattacharjee, Materials Science and Engineering: A. **2020**, *769*, 138489.
- [2] P. K. Ojha, S. Yoshida, U. Sunkari, B. Tripathy, N. Tsuji, and P. P. Bhattacharjee, Scripta Materialia. **2024**, *240*, 115828.

SCP 4.3:

A New Family of Ternary Intermetallic Compounds with Two Structural Variants – The ZIP Phases

Konstantina Lambrinou¹, Matheus A. Tunes², Cláudio G. Schön³, Stuart A. Maloy⁴, Tarik A. Saleh⁵, Sylvain Dubois⁶, Amit Keren⁷, Asaf Pesach⁸, Ganesh K. Nayak⁹, Stavros-Richard G. Christopoulos¹⁰, Marco Molinari¹¹, Marcus Hans⁹, Nick Goossens¹², Shuigen Huang¹³, Jochen M. Schneider⁹,

Per. O.Å. Persson¹⁴, Jozef Vleugels¹³

¹Department of Engineering, School of Computing and Engineering, University of Huddersfield, Queensgate, Huddersfield HD1 3DH, UK, email: <u>k.lambrinou@hud.ac.uk</u>

²Department of Metallurgy, Chair of Nonferrous Metallurgy, Montanuniversität Leoben, Franz-Josef-Strasse 18, 87100 Leoben, Austria, email: <u>matheus.tunes@unileoben.ac.au</u>

³Department of Metallurgical and Materials Engineering, Universidade de São Paulo, Av. Prof. Mello Moraes 2463, CEP 05508-030, São Paulo, SP, Brazil, email: schoen@usp.br

⁴Pacific Northwest National Laboratory (PNNL), 902 Battelle Blvd, Richland, WA 99352, USA, email: stuart.malov@pnnl.gov

⁵Los Alamos National Laboratory (LANL), Bikini Atoll Rd, Los Alamos, NM 87544, USA, email: tsaleh@lanl.gov

⁶Institut PPRIME, Département de Physique et Mécanique des Matériaux, CNRS, Université de Poitiers, ENSMA UPR 3346, SP2MI, Téléport 2, Boulevard Marie et Pierre Curie, BP30179 86962 Futuroscope, Chasseneuil Cedex, France, email: sylvain.dubois@univ-poitiers.fr

⁷Faculty of Physics, Technion – Isreal Institute of Technology, Haifa 32000, Israel, email: <u>phkeren@technion.ac.il</u>

⁸Department of Physics, Nuclear Research Centre, Negev, P.O. Box 9001, Beer Sheva 84190, Israel asafp@nrcn.gov.il

⁹Materials Chemistry, RWTH Aachen University, Kopernikusstr. 10, D-52074 Aachen, Germany, emails: hans@mch.rwth-aachen.de; nayak@mch.rwth-aachen.de; schneider@mch.rwth-aachen.de

¹⁰Department of Computer Science, School of Computing and Engineering, University of Huddersfield, Queensgate, Huddersfield HD1 3DH, UK, email: <u>S.R.Christopoulos@hud.ac.uk</u>

¹¹Department of Physical and Life Sciences, School of Applied Sciences, University of Huddersfield, Queensgate, Huddersfield HD1 3DH, UK, email: M.Molinari@hud.ac.uk

¹²Laboratory of High-Performance Ceramics, Swiss Federal Laboratories for Materials Science and Technology (EMPA), Überlandstrasse 129, CH-8600 Dübendorf, Switzerland, email:

Nick.Goossens@empa.ch

¹³Department of Materials Engineering, KU Leuven, Kasteelpark Arenberg 44, 3001 Leuven, Belgium, emails: shuigen.huang@kuleuven.be; jozef.vleugels@kuleuven.be

¹⁴Thin Film Physics, Department of Physics, Chemistry and Biology, Linköping University, SE-581 83 Linköping, Sweden, email: <u>per.persson@liu.se</u>

Introduction

The design and fabrication of advanced materials with exceptional properties demands manipulation of matter on the nanoscale, typically entailing the development of tailored structural 'modules' (dimensions: 1-100 nm), such as ordered atomic clusters, nanoprecipitates, grain boundaries, complex molecules, and atomically thin layers [1-3]. In 1992, Gleiter proposed the term "nanostructured materials", predicting a great potential impact of two novel classes of nanostructured materials, i.e., ceramics and intermetallic phases [2]. Gleiter's prediction came partly true in 1996 when Barsoum et al. [4,5] introduced a new class of nanolaminated ceramics with the $M_{n+1}AX_n$ general stoichiometry, where M is an early transition metal, A is an element mainly from groups 13-15 in the periodic table, X is C or N, and n = 1, 2, or 3; these ceramics are known as "the MAX phases". The 1996 breakthrough by Barsoum and El-Raghy [4] consisted in the synthesis of quasi-phase-pure Ti_3SiC_2 via reactive hot pressing (RHP); notably, the existence of the Ti_3SiC_2 compound, which is regarded as the H-phase of the Ti_3SiC_2

ternary system [6], had first been reported in 1967 by Jeitschko and Nowotny [7]. To date, about 155 ternary carbides and nitrides of early transition metals and numerous chemically complex solid solutions with the $M_{n+1}AX_n$ stoichiometry and precisely tailored properties have been synthesized [8,9]. The exceptional properties of the MAX phases are attributed to their nanolaminated hexagonal crystal structure, where n M₆X ceramic-like octahedra are interleaved with one A metallic-like atomic layer, whilst the M-atoms form a trigonal prismatic unit with the A-element in its center [9]. This work introduces a new family of ternary intermetallic compounds (IMCs), aptly named the "zigzag intermetallic compounds", or simply "the ZIP phases", due to their distinctive 'zigzag' atomic arrangements. Each member of the ZIP phase family has two structural variants, i.e., one with the fcc diamond cubic structure (space group, SG, $Fd\bar{3}m$) and one with the hexagonal structure (SG P6₃/mmc) [10]. For example, the two ZIP phases in the Nb-Si-Ni system are the fcc Nb₃SiNi₂ IMC, also regarded as the H-phase of the ternary Nb-Si-Ni system, and the hexagonal Ni₃SiNb₂ IMC [11–14]. The hexagonal ZIP phase variants exhibit striking similarities with the MAX phases, including crystal structure (SG P63/mmc) and crystal structure nanolamination, as well as the 312 MAX phase stoichiometry. This work reports on the RHP synthesis and characterization of quasi-phase-pure Nb₃SiNi₂ and Ni₃SiNb₂ ZIP phase-based materials. The introduction of the new family of ternary IMCs, herein named "the ZIP phases", validates Gleiter's 1992 prediction vis-à-vis the emergence and potential impact of 'nanostructured intermetallics' [1,2].

Materials and Methods

RHP was employed to produce high-purity Nb_3SiNi_2 ZIP phase materials in the Nb-Si-Ni ternary system. For this purpose, hydride and elemental starting powders (NbH_{0.89}, Ni, and Si) were mixed in the 3Nb:1Si:2Ni ratio. The powder feedstock was cold-pressed into 'green' pellets (\varnothing 30 mm) under a load of 30 MPa in a graphite die. Exploratory RHP runs were conducted in a hot press; the powder compacts were heated in vacuum at 10 K/min to different sintering temperatures (1523, 1623 and 1723 K), where densification was achieved under a uniaxial pressure of 30 MPa for 60 min.

Results and Discussion

RHP was successful in reproducibly synthesizing quasi-phase-pure Nb₃SiNi₂ and Ni₃SiNb₂ ZIP phase-based materials, thus demonstrating synthesis feasibility, and also paving the way for the further development and exploitation of the ZIP phases. The experimentally synthesized Nb₃SiNi₂ and Ni₃SiNb₂ ZIP phase materials were characterized in terms of microstructure by electron probe microanalysis, EPMA, and wavelength-dispersive X-ray spectroscopy, WDS (Fig. 1A); crystal structure by atomically resolved scanning transmission electron microscopy, STEM (Fig. 1B); spatially-resolved chemical composition by atom probe tomography, APT; and selected thermal, electrical, magnetic, mechanical, and physical properties. Density functional theory (DFT) and the temperature-dependent effective potential (TDEP) method were employed in this work to assess the stability of the two ZIP phases in the Nb-Si-Ni ternary system and candidate derivative binary compounds, at different temperatures, and to explore the possible exfoliation of the ZIP phase variants along specific planes to produce 2D derivatives similar to the 2D derivatives of the MAX phases known as MXenes.

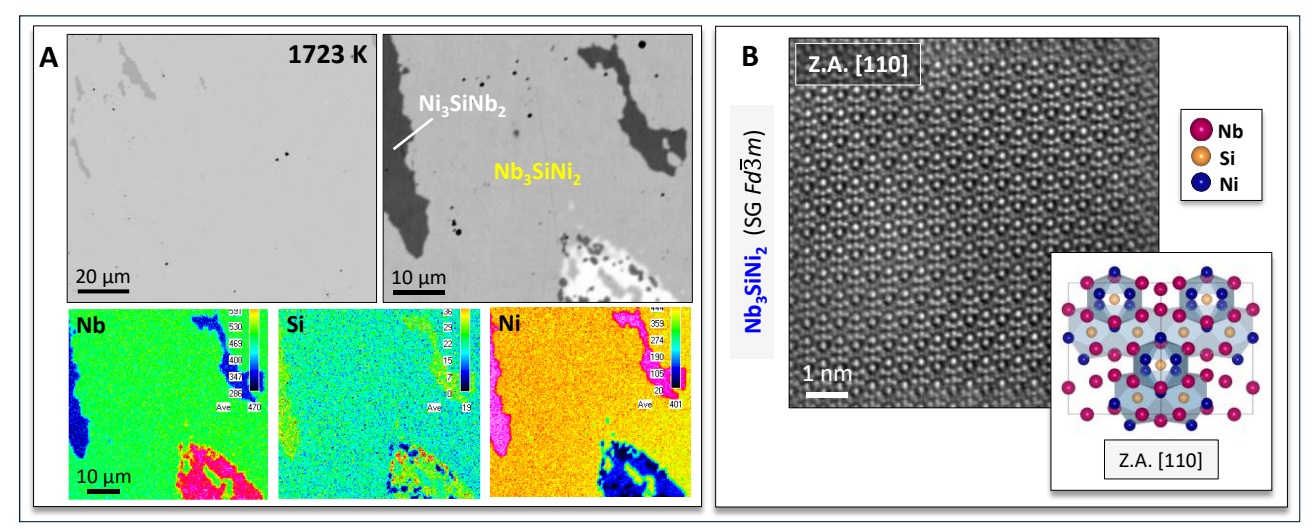


Fig. 1. (A) EPMA/WDS of an RHP Nb-Si-Ni alloy sample sintered at 1723 K shows only the formation of the fcc Nb₃SiNi₂ and the hexagonal Ni₃SiNb₂ ZIP phases. (B) Atomically resolved HAADF (high-angle annular dark-field) STEM image of the [110] zone axis, Z.A., of fcc Nb₃SiNi₂ (SG $Fd\overline{3}m$). The inset schematic, made with the VESTA software, depicts the [110] Z.A. of the fcc Nb₃SiNi₂ ZIP phase, for direct comparison with the corresponding HAADF STEM image.

- [1]. R.W. Cahn, Nature. **1990**, *348*, 389-390;
- [2]. H. Gleiter, Advanced Materials. **1992**, *4*, 474-481;
- [3]. P. Moriarty, Reports on Progress in Physics. **2001**, *64*, 297-381;
- [4]. M.W. Barsoum, T. El-Raghy, Journal of the American Ceramic Society. **1996**, *79*, 1953-1956;
- [5]. M.W. Barsoum, T. El-Raghy, American Scientist. 2001, 89, 334-343;
- [6]. W. Jeitschko, H. Nowotny, F. Benesovsky, Monatshefte fur Chemie und verwandte Teile anderer Wissenschaften. **1963**, *94*, 672-676;
- [7]. W. Jeitschko, H. Nowotny, Monatshefte fur Chemie-Chemical Monthly. **1967**, 98, 329-337;
- [8]. M. Sokol, V. Natu, S. Kota, M.W. Barsoum, Trends in Chemistry. **2019**, *1*, 210-223;
- [9]. N. Goossens, B. Tunca, T. Lapauw, K. Lambrinou, J. Vleugels, in: M. Pomeroy (Ed.), Encyclopedia of Materials: Technical Ceramics and Glasses, Elsevier, Oxford, **2021**, 182-199;
- [10]. M.A. Tunes, K. Lambrinou et al., submitted to Advanced Materials. 2025;
- [11]. E. Gladyshevskii, Y. B. Kuz'ma, P. Kripyakevich, Journal of Structural Chemistry. **1964**, *4*, 343-349;
- [12]. V.O. dos Santos, H.M. Petrilli, C.G. Schön, L.T. Eleno, Calphad. **2015**, *51*, 57-66;
- [13]. V.O. dos Santos, M.A. Tunes, L.T. Eleno, C.G. Schön, K.W. Richter, Scripta Materialia. **2019**, *164*, 96-100;
- [14]. V.O. dos Santos, L.T. Eleno, C.G. Schön, K.W. Richter, Journal of Alloys and Compounds. **2020**, *842*, 155373.

SCP 4.4:

Crystal structure and peritectoid reaction temperature of Ta₂Co₇ in the Co-Ta binary system

Konatsu Yamada¹, Toshiaki Horiuchi², Shota Miyazaki³ and Frank Stein⁴

- ¹ Hokkaido University of Science, Sapporo, Hokkaido, 006-8585, Japan, 9222003@hus.ac.jp
- ² Hokkaido University of Science, Sapporo, Hokkaido, 006-8585, Japan, horiuchi@hus.ac.jp
- ³ Hokkaido University of Science, Sapporo, Hokkaido 006-8585, Japan, 9251102@hus.ac.jp
- ⁴ Max-Planck Institute for Sustainable Materials, 40237 Düsseldorf, Germany, f.stein@mpie.de

Introduction

The Co-Ta binary system is a fascinating and complex binary system as it not only includes three different types of Laves phases but also several more interesting intermetallic phases [1]. Among them, we are particularly interested in Ta_2Co_7 because it has been clarified that Nb_2Co_7 in the Co-Nb binary system, which has a similar phase diagram to the Co-Ta system, exhibits unique mechanical properties by a kink formation as a novel crystalline "mille-feuille" structured material [2]. However, the crystal structure of Ta_2Co_7 is still unknown, and the researchers have proposed various structures [3,4]. In addition, although it has been reported that the peritectoid reaction forms Ta_2Co_7 , the invariant reaction temperature differs significantly from 950°C to 1033°C among the researchers [1,5,6]. These uncertainties might be because Ta is a highly oxidizable element with a high melting point (3020°C), making it challenging to attain an equilibrium state. In the present study, in order to elucidate the crystal structure and peritectoid reaction temperature of Ta_2Co_7 , $Ta_2Co_$

Materials and Methods

The Co-22at%Ta alloy was vacuum induction melted and cast into a $\varphi20\times$ about 200 mm³ cylindrical ingot, then cut into $\varphi3\times3$ mm³ or $\varphi20\times3$ mm³ pieces. The alloy composition was investigated by multipoint analysis using electron probe micro analyzer (EPMA). The samples were encapsulated in quartz tubes with an Ar atmosphere, and isothermally heat-treated at 850-1000°C for up to 10000 h, and subsequently water-quenched. The crystal structure of the heat-treated samples was analyzed by XRD. The XRD measurements were performed using a Cu X-ray source at a tube voltage of 40 kV with the reduced X-ray fluorescence mode. Microstructure was observed by scanning electron microscope (SEM). Detailed DTA analyses were also performed to determine the peritectoid reaction temperature of Ta₂Co₇.

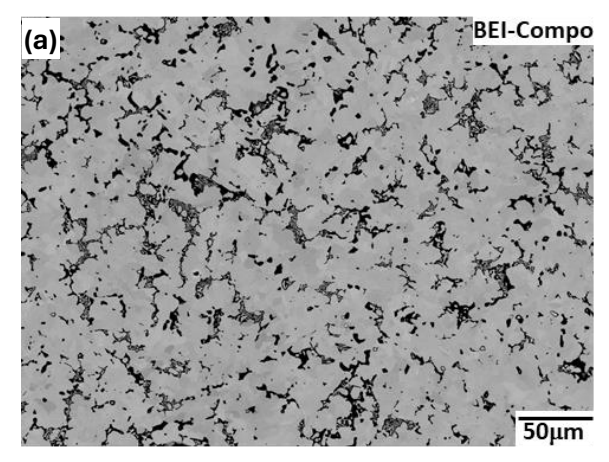
Results and Discussion

As a result of EPMA analysis, the alloy composition is analyzed as Co-21.8at%Ta. SEM observation for the samples before and after isothermal heat treatment indicates that the sample heat-treated at 900°C for 1000 h still shows microstructural heterogeneity and has not reached equilibrium. On the other hand, the samples heat-treated at 850°C for 10000 h, 900°C for 10000 h, and 1000°C for 1000 h are all considered to have reached the equilibrium state. However, none of them has a single-phase microstructure, but multiple phases are present. The samples heat-treated at 850°C for 10000 h and 900°C for 10000 h show similar microstructures. As shown in Fig. 1 (a), the EPMA analysis clarifies that the average composition of the gray part for the sample heat-treated at

900°C for 10000 h is 23.4at%Ta, while that of the black part is 0.7at%Ta. It should be noted that the average composition of the gray part exceeds the stoichiometric composition of Ta_2Co_7 (22.2at%Ta). The sample heat-treated at 1000°C for 1000 h shows a different microstructure compared to the samples heat-treated below 900°C, and the average composition of the gray part is 24.0at%Ta, whereas that of the black part is 2.5at%Ta.

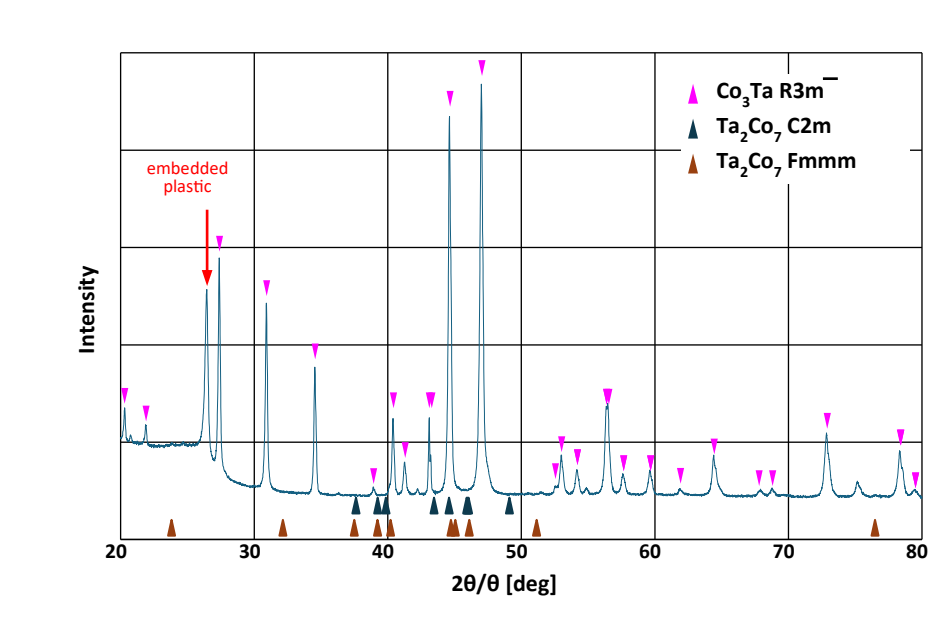
XRD analysis reveals that C36 Laves and fcc-Co phases are identified in the as-cast sample, and Ta_2Co_7 does not exist. On the other hand, no Ta_2Co_7 but β -Co₃Ta (spacegroup: 166, R-3m) is identified in the sample heat-treated at 900°C for 10000 h, as shown in Fig. 1 (b). However, C36 Laves and fcc-Co phases are confirmed in the sample heat-treated at 1000°C for 1000 h. These results suggest that the phase previously reported as Ta_2Co_7 is β -Co₃Ta, and its peritectoid reaction temperature is below 1000°C. Finally, the microstructure shown in Fig. 1 (a) is considered a two-phase region containing Co solid solution and β -Co₃Ta.

Figure 2 shows the DTA heating curves for the samples after isothermal heat treatment at 850°C - 1000°C . The endothermic peaks in Fig.2 correspond to the decomposition of β - Co_3Ta . The endothermic peak is observed after isothermal heat treatment below 994°C, whereas no endothermic peak is observed above 996°C. This result indicates that β - Co_3Ta is already decomposed during isothermal heat treatment at temperatures above 996°C. Finally, it is concluded that the peritectoid reaction temperature of β - Co_3Ta should be 995°C.



(b)

Fig. 1 The resultant SEM microstructure (a) and the result of XRD analysis (b) for the Co-21.8at.%Ta sample



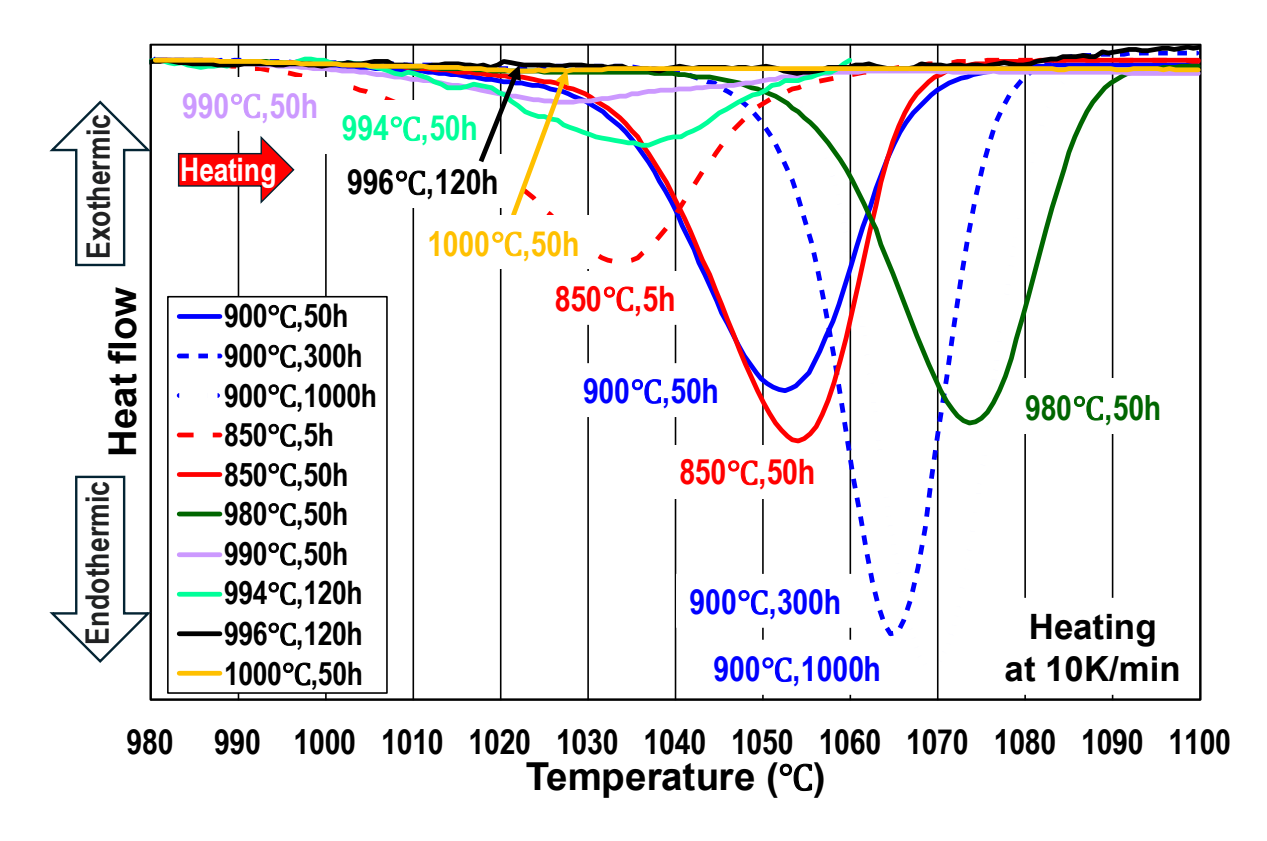


Fig. 2 The result of DTA analyses for the Co-21.8at.%Ta samples after heat treatment at 850°C -1000°C.

- [1] K. Shinagawa, H. Chinen, T. Omori, K. Oikawa, I. Ohnuma, K. Ishida, R. Kainuma, Intermetallics, 49, **2014**, 87-97.
- [2] T. Horiuchi, K. Yamada, S. Saito, K. Ikeda, S. Miura, F. Stein, Materials Transactions, 64, 7, **2023**, 1622-1630.
- [3] C. Zhou, C. Guo, C. Li, Z. Du, Intermetallics, 108, **2019**, 1-18.
- [4] W.-W. Xu, Q. Yu, F. Xia, G. Yin, Y. Huang, L. Chen, Journal of Alloys and Compounds, 797, **2019**, 1198-1204.
- [5] H. Okamoto, Journal of Phase Equilibria and Diffusion, 25, 6, 2004, 571-572.
- [6] Z.-K. Liu, Y. A. Chang, Calphad, 23, 3-4, **1999**, 339-356.

SCP 4.5:

An overview of intermediate phases in metal-zinc systems

Shubhangini Yadav^{1,#}, Varun A. Baheti^{1,*}

¹Department of Metallurgical and Materials Engineering,
Indian Institute of Technology, Roorkee, Haridwar, Uttarakhand 247667, India.

#Email of presenting author: shubhangini_y@mt.iitr.ac.in,

*Corresponding Author Email: varun@mt.iitr.ac.in; varun.iitkgp2018@gmail.com

Introduction

It is well known that the phase diagram of a binary system acts as an essential foundation for developing the understanding of relevant higher-order systems. Phase diagrams are crucial for assessing material properties and developing manufacturing processes. Zinc and its alloys have been extensively used in industries to protect steel against corrosion. However, ambiguity exists about the number of phases reported in the binary Metal–Zinc phase diagrams at a particular temperature in a few M–Zn (M = V, Mn, Nb) based systems. To the authors' knowledge, very limited solid–state interdiffusion studies are available in such M–Zn based systems.

Materials and Methods

Solid–state diffusion bonding of M/Zn couples has been carried out at 400°C to study the evolution of diffusion zone and the growth behaviour of various phases [1-3]. The interdiffusion zone is being analysed using a field emission gun equipped with a scanning electron microscope (FE–SEM) for imaging, and the composition measurements are being done in Electron Dispersive Spectroscopy (FE–EDS) to confirm the presence of various product phases grown across the interdiffusion zone.

Results and Discussion

The V–Zn phase diagram became available after 1990. The existence of the VZn_{16} phase has been questioned mainly. A solid–state diffusion experiment is conducted to reinvestigate the stability of phases. The interdiffusion zone is examined using scanning electron microscopy and energy dispersive spectroscopy. Our analysis confirms that VZn_{16} is one of the stable phases. Additionally, the growth of the VZn_{9} product phase is observed in the V/Zn diffusion couple, indicating that this newly discovered phase is also stable. Furthermore, the formation of the Kirkendall voids is observed in the VZn_{3} phase, which can affect the physico–mechanical reliability of any component during load-bearing application. Moreover, this study's findings could also be beneficial for the ongoing efforts of designing promising Zn–based biomaterials.

The Mn–Zn system, technologically crucial for galvanized Mn–containing steels and potential ZnMn–based biomaterials, has been studied using the conventional diffusion couple technique. The first experimental evidence has been presented to indicate the presence of 3 separate phases, as ε , ε_1 and ε_2 , together in the interdiffusion zone. By taking advantage of local equilibrium present at interphase interfaces in a diffusion couple, the controversial ε -phase region has been resolved after almost more than 6 decades. Incorporating new experimental results of 3 separate phases could be beneficial in refining the present thermodynamic optimization of the Mn–Zn system. Furthermore, MnZn₉ and MnZn₁₃ have also grown in the Mn/Zn diffusion couple, such that there are 5 distinct phase layers, including ε , ε_1 and ε_2 . Diffusion parameters such as integrated diffusion coefficients and the ratio of tracer diffusivities, which are currently

unavailable, are also determined considering ideal molar volumes. It helps to understand the atomic mechanism of diffusion and the probable defects present in phase(s).

The Nb–Zn system, which is technologically crucial for galvanized Nb–containing interstitial–free steels, is studied using diffusion–bonding. It also involves solid–state joining of dissimilar metals, viz. Nb/Zn, with high difference in melting points. In Nb/Zn diffusion couple, NbZn $_3$ and NbZn $_{16}$ grow at 400 °C. NbZn $_7$, present between NbZn $_3$ and NbZn $_{16}$ in phase diagram, could not be detected. This phenomenon is discussed using the physico–chemical approach and existing nucleation theories. Algebraic expressions, unavailable earlier, are developed to calculate the driving force for diffusion in line compounds. They signify a correlation of the driving forces with a difference in slopes of common tangents. Diffusion parameters such as integrated and tracer diffusivities, which are currently unavailable, are also estimated. The estimated tracer diffusivities indicate that Zn diffuses faster than Nb via NbZn $_{16}$. This can be understood from the crystal structure of NbZn $_{16}$ and possible defects in this phase.

This study indicates a need to revisit these systems' phase diagrams.

- [1] S. Yadav, V.A. Baheti, Phase evolutions and the growth of Kirkendall voids in the V–Zn system, Scripta Materialia. **2025**, *255*, 116391.
- [2] S. Yadav, V.A. Baheti, A new experimental result indicating 3 separate phase fields of ε , ε_1 , ε_2 and the estimation of diffusion coefficients in the Mn–Zn system, Journal of Alloys and Metallurgical Systems. **2025**, 100183, <u>doi</u>
- [3] S. Yadav, V.A. Baheti, Growth Behaviour of Phases in the Solid–State Nb–Zn Diffusion Couple, Available at SSRN 5057153: https://ssrn.com/abstract=5057153 or http://dx.doi.org/10.2139/ssrn.5057153, **2024**.

SCP 5.1:

Microstructure-Based Modeling of Temperature-Dependent Yield Strength in Polycrystalline Ni-Based Superalloys

Uwe Glatzel^{1*}, Enrique Galindo-Nava², Howard J. Stone², Moritz Müller¹

¹Metals and Alloys, University of Bayreuth, Germany

²Materials Science and Metallurgy, University of Cambridge, Cambridge, UK

A model for temperature-dependent yield strength of polycrystalline Ni-base superalloys at high strain rates (10-3 to 10-4 s-1) is developed [1], featuring multimodal precipitate microstructures. It extends existing mean field models to higher temperatures, based on the summation of particle strengthening and other strengthening contributions, originally created to describe room temperature behavior. Temperature dependence is introduced for each contribution using existing models or datasets from literature, while maintaining physical validity and avoiding unnecessary fitting parameters. Further, the expected change in precipitate distribution at high temperatures is achieved using CALPHAD. By considering such microstructural changes, the model can predict the yield strength from room temperature up to the precipitate solvus temperature. Due to the strategy for combining different strengthening contributions, the model can also predict the active deformation modes at any temperature and can be extended easily to incorporate additional deformation mechanisms. The model's sensitivity to microstructural parameters and its strengths and weaknesses are discussed. The application of the model to three commercial alloys shows good agreement over the whole temperature range.

References:

[1] Müller, M., Stone, H.J., Galindo-Nava, E., Schleifer, F., Fleck, M., Glatzel, U. (**2024**) in Superalloys 2024. https://doi.org/10.1007/978-3-031-63937-1_39.

SCP 5.2:

Deformation-induced transformation of intermetallic phases and their impact on strength

Steffen Neumeier¹, Andreas Bezold², Nicolas Karpstein³, Julian Völkl¹, Ashton J. Egan¹, Erdmann Spiecker³, Michael J. Mills², and Mathias Göken¹

¹Friedrich-Alexander-Universität Erlangen-Nürnberg, Department of Materials Science & Engineering, Institute MSE I, Martensstraße 5, Erlangen, Germany, steffen.neumeier@fau.de, julian.voelkl@fau.de, ashton.egan@fau.de, mathias.goeken@fau.de

²Center for Electron Microscopy and Analysis, The Ohio State University, Columbus, OH, USA, Bezold.8@osu.edu, Mills.108@osu.edu

³Friedrich-Alexander-Universität Erlangen-Nürnberg, Department of Materials Science & Engineering, Institute of Micro- and Nanostructure Research, and Center for Nanoanalysis and Electron Microscopy (CENEM), Erlangen, Germany, nicolas.karpstein@fau.de; erdmann.spiecker@fau.de

Introduction

Superalloys are strengthened by a high fraction of L1₂-structured intermetallic precipitates. Shearing of L1₂-structured γ' phases by partial dislocations during deformation can lead to the formation of superlattice stacking faults. Depending on defect composition and structure, segregation causes local transformations along defects. In cases of softening, defect composition resembles that of unordered A1-structured γ matrix phase, making them less ordered and allowing stacking fault ribbons and extensive microtwin formation. Conversely, defects can align with the composition of ordered hexagonal phases, known as localized phase transformation (LPT) strengthening. Superlattice intrinsic stacking faults (SISFs) represent four-layered D0₁₉-ordered χ phases and may become enriched with χ formers, maintaining order and impeding stacking fault ribbons. Similarly, superlattice extrinsic stacking faults (SESFs) are locally D0₂₄-ordered η phases, which restrict microtwin formation when enriched in η formers. Additionally, the structure of microtwin boundaries can be either ordered or unordered, affecting microtwin thickening.

The purpose of this work is to analyze (i) the role of specific elements regarding the local phase transformation weakening or strengthening effect in intermetallic phases, (ii) the role of changing deformation mechanisms and (ii) the effect of local phase transformation on the resulting creep properties.

Materials and Methods

Polycrystalline samples of different CoNi-base superalloys were investigated, which were vacuum arc melted, cast, homogenized (1250 °C/3 h), cold-rolled and subsequently aged (900 °C / 4 h + 750 °C / 16 h). Cylindrical samples (\varnothing 5 mm, height 7.5 mm) were crept using a pneumatic creep machine at 750 °C and compressive stresses of 620 and 800 MPa. Creep tests were interrupted at different creep strains. After testing, foils were cut, mechanically ground and electrolytically polished using a 16.7 % nitric acid – 83.3 % methanol solution at 45 V and -20 °C in a Tenupol twin-jet polishing device. Transmission electron microscopy (TEM) was performed on a Philips CM200 operated at 200 kV. High-resolution scanning TEM (HRSTEM) investigations were conducted on a double-corrected Thermo Fisher Scientific Themis-Z equipped with a Super-X EDS detector operated at 200 kV. High-resolution EDS mappings were processed using the Velox software.

Results and Discussion

After production and processing, no other phases besides the fcc γ solid solution phase, the L1₂-structured intermetallic γ' phase and some carbides/borides were observed in the investigated alloys. In the W- and Al-rich CoWAlloy2, the γ' precipitates have a more globular shape indicating a lower lattice misfit compared to the Ta- and Ti-rich CoWAlloy1 and the Ti-rich CoWAlloy5 [1]. Otherwise, the γ' volume fractions and sizes were quite similar for the alloys (approximately 58 - 63 % ± 2 %, 35-50 nm). CoWAlloy1 and CoWAlloy5 exhibit significantly lower creep rates than CoWAlloy2, particularly after 0.2 plastic strain is passed. TEM investigations of the defect structures after creep deformation revealed that plastic deformation in CoWAlloy2 is initially concentrated in the γ matrix channels and with increasing strain, anti-phase boundary (APB)-coupled dislocation pairs and isolated stacking faults are observed. In contrast, in CoWAlloy1 and CoWAlloys5 APB-coupled dislocation pairs are rarely observed, the vast majority of the observed defects are extended stacking faults and microtwins. HRSTEM investigations revealed that most of the planar faults in CoWAlloy1 are intrinsic and extrinsic stacking faults and microtwins. To explore the differences in these underlying defect structures, HRSTEM-EDS investigations were conducted across all types of planar defects within the L12-ordered intermetallic phase. Fig. 1a shows a typical high-angle annular dark-field (HAADF) STEM image of an SESF in CoWAlloy1, with atomic-scale EDS maps. While in CoWAlloy1, SESFs as well as SISFs exhibit an enhanced Z-contrast and a local ordered structure, indicating local phase transformation from the L1₂-structure to the D0₂₄ordered η phase along the SESFs and to the D0 $_{19}$ -ordered χ phase along the SISFs, such phenomena do not occur to similar extent in CoWAlloy2. The EDS maps and the integrated line profiles reveal depletion of Ni and Al, and enrichment of Co, Cr, W. However, in CoWAlloy1, Ta is enriched, which is associated with a significant increase of the energy penalty for subsequent Shockley partials to shear along the planar fault, which indicates a strengthening effect. W exhibits an also enhanced segregation and ordering tendency, however W as a more slowly diffusing element than Ta, cannot achieve something similar. Although the Ti-rich alloy CoWAlloy5 shows also an excellent creep strength, Ti does not show such a strong segregation to the stacking fault and a local phase transformation. These results indicate that the transitions from APB-based shearing to stacking fault shearing mechanisms is the decisive mechanism and prerequisite for enhanced creep strength [2]. However, if this transition in deformation mechanisms occur, the strength can be increased even further by transforming the intermetallic L1₂ phase locally to an intermetallic D0₂₄- or D0₁₉-ordered η - or χ -phase at the deformation-induced planar defect.

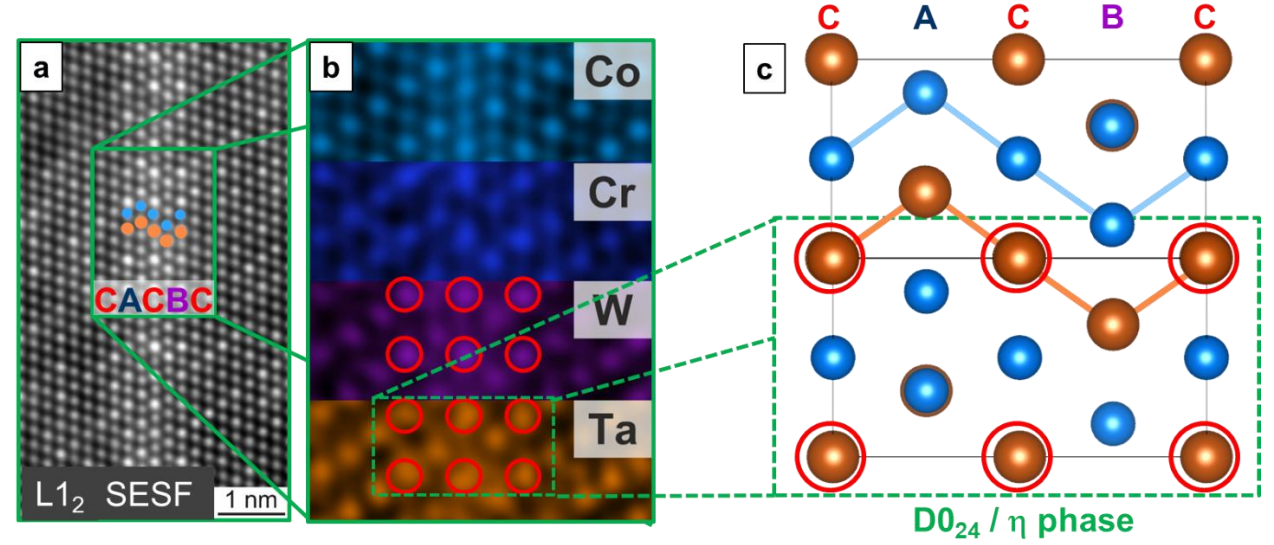


Fig. 1: Exemplary deformation-induced defect in CoNi-base superalloy CoWAlloy1: (a) HAADF STEM image of the investigated superlattice stacking fault, here a SESFs, in the L1 $_2$ structured phase. (b) Corresponding atomic-scale EDS mappings presented as net count images, which were manually integrated along the shown repetitive unit to improve the signal-to-noise ratio. (c) Crystal structure of the η -phase with D0 $_{24}$ crystal structure.

- [1] S. Neumeier, L.P. Freund, A. Bezold, M. Köbrich, J. Vollhüter, D. Hausmann, C. Solis, A. Stark, N. Schell, F. Pyczak, P. Felfer, R. Gilles, M. Göken, Metall Mater Trans A. **2024**, *55*, 1319–1337.
- [2] A. Bezold, S. Neumeier, Scripta Materialia. 2023, 226, 115250.

SCP 5.3:

Grain size effects on interdiffusion in complex concentrated alloys

M. Vaidya¹, Bhawna Yadav¹, T. N. Prasanthi², K. Guruvidyathri³, Sadhasivam M.⁴, C. Sudha², Pradeep K.G.⁴

^aDepartment of Materials Science and Metallurgical Engineering, Indian Institute of Technology Hyderabad, Kandi, Sangareddy 502285, Telangana, India

^bPhysical Metallurgy Division, Metallurgy and Materials Group, Indira Gandhi Centre for Atomic Research, Kalpakkam, Tamil Nadu 603102, India

^dSchool of Engineering Sciences and Technology, University of Hyderabad, Gachibowli, Hyderabad 500046, India

^eCorrelative Microscopy Lab, Department of Metallurgical and Materials Engineering, Indian Institute of Technology Madras, Chennai, 600036, India

Introduction

Complex concentrated alloys (CCAs) have garnered significant interest due to their unique multi-principal element design, exceptional mechanical properties, and promising thermal stability[1]. Diffusion plays a fundamental role in determining these properties by influencing key phenomena such as creep, grain growth, and precipitation[2]. While previous studies have focused primarily on bulk diffusion[3–6], grain boundary diffusion remains relatively unexplored, particularly in interdiffusion experiments involving CCAs[7].

Grain size effect during interdiffusion in the CoFeNi/Sn system is explored by investigating diffusion couples of coarse-grained (CG >200 μ m) and ultrafine-grained (UFG ~800 nm) CoFeNi alloys with Sn in the temperature range 175 – 215 °C.

Materials and Methods

The CG CoFeNi and UFG CoFeNi samples were prepared through vacuum arc melting (VAM) and spark plasma sintering (SPS) of mechanically alloyed CoFeNi powders, respectively. The CoFeNi/Sn diffusion couples were prepared using hot compaction and annealed at 175 °C -215 °C for various durations in an Ar atmosphere. Post-annealing analysis, microstructural and compositional analyses were performed using SEM, EDS, EPMA, Micro-XRD, TEM, STEM, and TKD. Phase formation in the IDZ was evaluated using CALPHAD-based Thermo-Calc simulations.

Results and Discussion

At 175 °C, formation of (CoNi)Sn₃ and FeSn₂ intermetallic phases is observed at both the interfaces. At 200 °C, (CoNi)Sn₃ and FeSn₂ persisted across annealing durations of 120, 180, and 240 h, with a gradual increase in their thickness. However, at 300 h, a phase mixture of (CoNi)Sn₃ and FeSn₂ emerged between the two single phase layers. At 215 °C, the presence of FeSn₂, (CoNi)Sn₃, and their phase mixture was observed consistently, with progressive thickening over time. While utilizing the time-dependent studies at various temperatures, the pronounced phase growth in UFG CoFeNi/Sn compared to CG CoFeNi/Sn could be realized. The accelerated diffusion kinetics at the UFG interface are likely associated with the higher fraction of grain boundaries (GBs), which leads to enhanced GB contribution to the diffusion flux. The comparison of CoFeNi/Sn diffusion couples with reported studies of Ni/Sn and CoNi/Sn reveal that the effect of enhanced GB fraction on kinetics is partially nullified by the compositional complexity of end members and the interdiffusion zone. The experimental data across the 175–215 °C range

provide valuable insights that can aid in refining the phase diagram and expanding the available database for this alloy system.

Literature References

- [1] D.B. Miracle, O.N. Senkov, Acta Mater 122 (**2017**) 448–511.
- [2] Kaur Inderjeet, Wolfgang Gust., Fundamentals of Grain and Interphase Boundary Diffusion., **1995**.
- [3] M. Vaidya, K.G. Pradeep, B.S. Murty, G. Wilde, S. V. Divinski, Acta Mater 146 (**2018**) 211–224.
- [4] M. Vaidya, S. Trubel, B.S. Murty, G. Wilde, S. V. Divinski, J Alloys Compd 688 (**2016**) 994–1001.
- [5] J. Zhang, G.M. Muralikrishna, A. Asabre, Y. Kalchev, J. Müller, B. Butz, S. Hilke, H. Rösner, G. Laplanche, S. V. Divinski, G. Wilde, Acta Mater 203 (**2021**).
- [6] M.M. G., M. Vaidya, B.S. Murty, S.V. Divinski, G. Wilde, Scr Mater 178 (**2020**) 227–231.
- [7] Z. Zhang, S. Fellner, S. Ketov, M.J. Cordill, H. Sheng, C. Mitterer, K. Song, C. Gammer, J. Eckert, Intermetallics 153 (**2023**).

SCP 5.4:

Diffusion-induced phase growth kinetics in CoNi/Al and CoCrNi/Al diffusion couples

Tamanna H. Panigrahi^{1,2}, Bhawna Yadav¹, Ramya S. Lakshmi¹, Mayur Vaidya¹
¹ Department of Materials Science and Metallurgical Engineering, Indian Institute of Technology
Hyderabad, Kandi, Sangareddy 502284, India.

²Institute for Frontier Materials, Deakin University, Geelong, Victoria 3216, Australia.

Introduction

The performance and reliability of modern materials rely on their ability to maintain structural integrity under extreme conditions. At high temperatures, materials in applications like jet engines, nuclear reactors, and power plants, often undergo interdiffusion-a process where atoms diffuse/migrate when placed in contact with each other. This interaction creates new phases at their interface, which can profoundly influence their strength, durability, and overall performance.

Complex Concentrated Alloys (CCAs) are an emerging class of materials, known for their multicomponent compositions and high configurational entropy, offering exceptional properties such as high strength, thermal stability, and corrosion resistance [1]. These alloys also present a unique opportunity to study diffusion behaviour, as they retain simple crystal structures despite compositional diversity.

This study aims to explore how compositional complexity affects phase evolution and growth kinetics in materials, providing insights into the role of atomic interactions in shaping material properties. To achieve this, the phase growth behaviour of CoNi/Al and CoCrNi/Al diffusion couples is compared, which differ in alloying elements but share similar crystal structures. By conducting systematic annealing at controlled temperatures and durations, the development of multicomponent intermetallic phases at the interdiffusion zone (IDZ) is investigated. This understanding can be applied to tackle the growth of unwanted phases and optimise phase stability, leading to improved material performance in applications like diffusion bonding, bond coatings, flip-chip technology, and brazing [2,3].

Materials and Methods:

CoNi and CoCrNi alloys were synthesized through arc melting, followed by homogenization to ensure chemical uniformity. Phase identification and microstructural characterization were performed using X-ray diffraction (XRD) and scanning electron microscopy (SEM), respectively. Discs with a diameter of 10 mm and a thickness of approximately 1.2 mm were prepared via Electrical Discharge Machining (EDM) cutting. Diffusion couples were assembled by pairing CoNi or CoCrNi with aluminum (Al), separated by Mo foil to prevent any interaction with the stainless steel fixture. The assembled diffusion couples were annealed at 630°C for durations ranging from 48 to 192 hours. Post-annealing, the IDZ were analyzed using SEM, Electron Probe Microanalysis EPMA, micro-XRD, and Transmission Electron Microscopy (TEM) to investigate phase evolution and growth kinetics.

Results and Discussion

Diffusion couple experiments conducted at 630 °C for varying durations (48–192 h) revealed the formation and growth of distinct intermetallic phases within the IDZ of both CoNi/Al and CoCrNi/Al systems. With increasing annealing time, the IDZ widened significantly, reaching a maximum width of ~106 µm in CoNi/Al and ~326 µm in CoCrNi/Al at 192 h.Backscattered electron (BSE) micrographs revealed the presence of up to four distinct phases in the CoNi/Al system (Fig. 1) and five in the CoCrNi/Al system (Fig. 2). In the CoCrNi/Al couple, a transition zone containing segregated phases became increasingly prominent at longer annealing durations. Compositional analysis using SEM-EDS and EPMA, combined with comparisons to binary Al-Co, Al-Cr, and Al-Ni phase diagrams, indicated the formation of predominantly Al_xCo_V-type intermetallics such as Al₉Co₂ and Al₅Co₂. In the CoCrNi/Al diffusion couple, the cobalt sublattice also incorporates chromium and nickel, forming complex multicomponent intermetallics like Al₉(Co,Cr,Ni)₂. This equiatomic incorporation of Cr and Ni into the sublattice is notably absent in the CoNi/Al system, where Co and Ni do not distribute equally. These phase identifications were confirmed by micro-XRD and further supported by EBSD phase mapping. The presence of Cr in the CoCrNi/Al system appears to enhance the solubility of other elements within the intermetallic structures, contributing to the broader range and complexity of phases formed, which is not observed in the simpler CoNi/Al system. To examine the growth rate of the formed phases, the overall phase thickness was measured at different annealing times. The Δx vs $t^{0.5}$ plot showed a linear relationship, indicating parabolic growth behaviour given by the equation:

$$\Delta x^2 = K_p t \tag{1}$$

where Δx is the phase thickness, K_p is the parabolic rate constant and t denotes the annealing time. The estimated growth rate constants are on the order of 10^{-7} m/s^{0.5}, aligning well with values reported for similar diffusion studies [4].

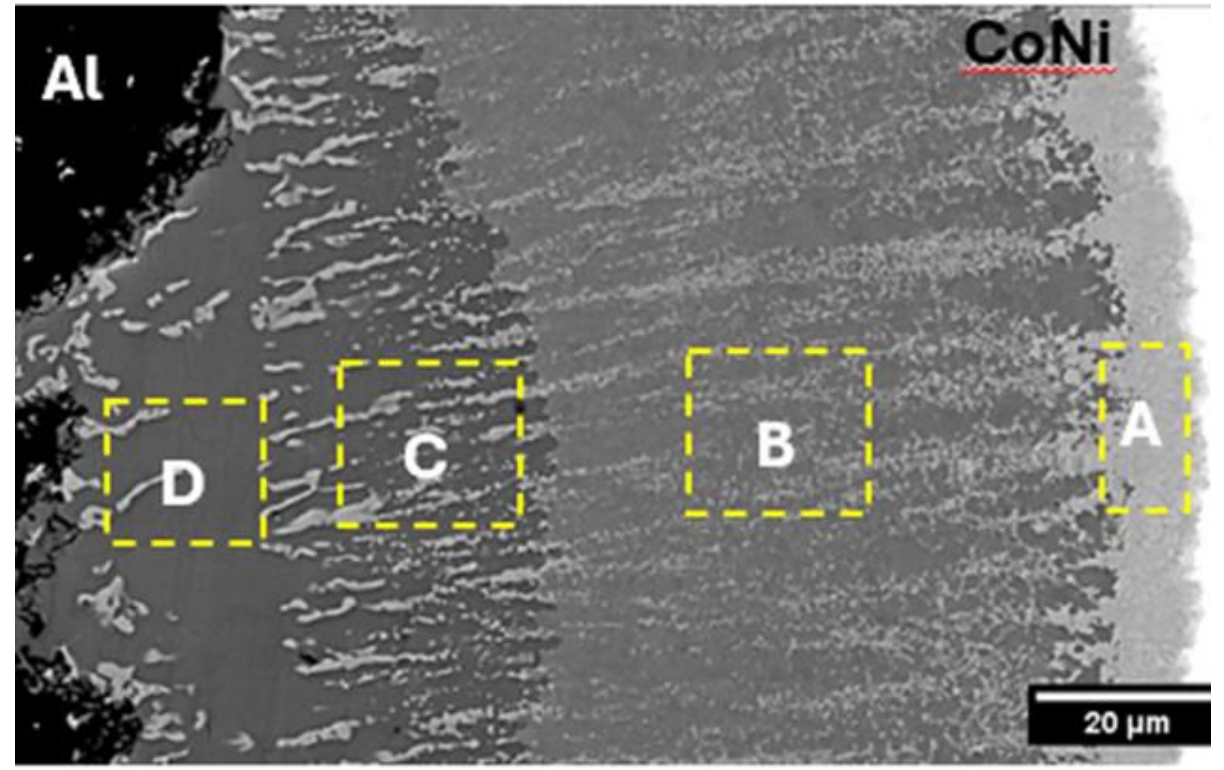


Fig. 1: BSE micrograph of the CoNi/Al diffusion couple annealed at 630 °C for 192 h, showing the formation of four distinct intermetallic phases within the IDZ.

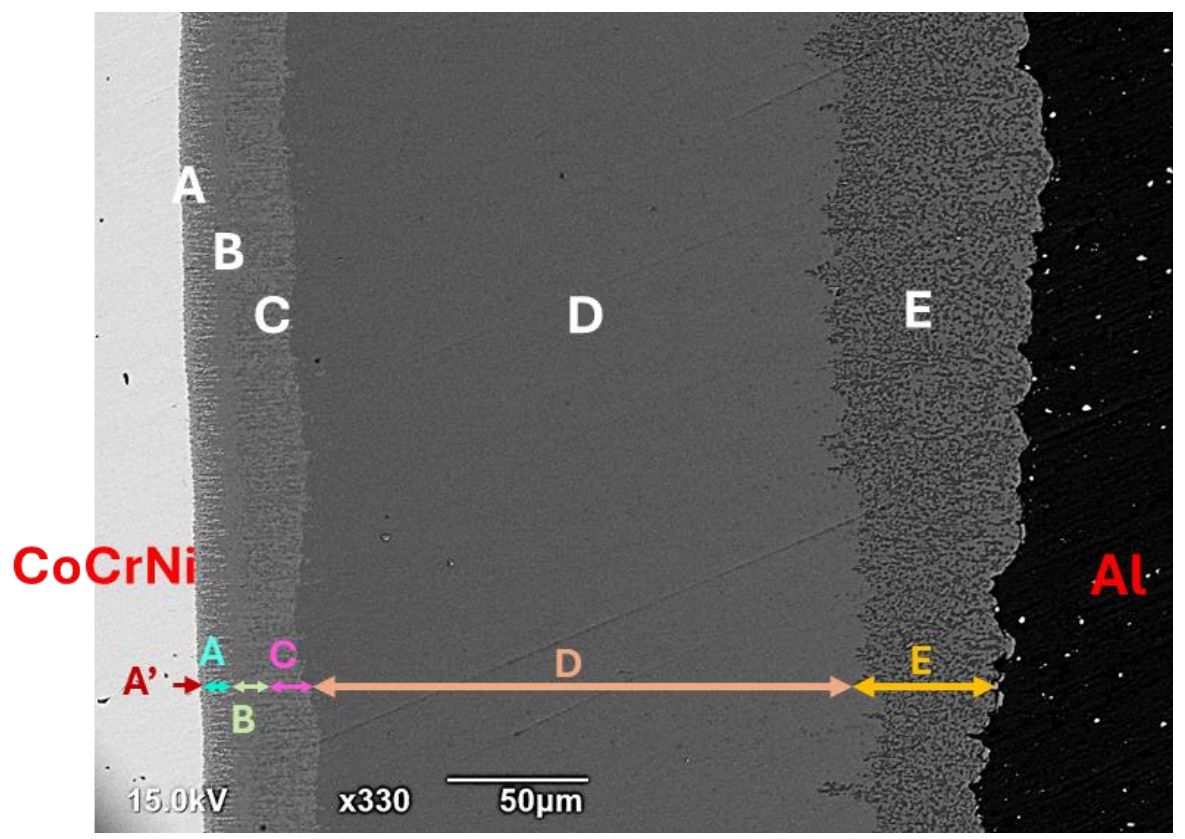


Fig. 2: BSE micrograph of the CoCrNi/Al diffusion couple annealed at 630 °C for 144 h, showing the formation of five distinct intermetallic phases within the IDZ, along with a transition zone (A') near CoCrNi interface.

- 1. J.W. Yeh, Recent progress in high-entropy alloys, Ann. Chim. Sci. Des Mater. 31 (2006) 633–648. https://doi.org/10.3166/acsm.31.633-648.
- S. Kumar, Comprehensive review on high entropy alloy-based coating, Surf. Coatings Technol. 477 (2024) 130327. https://doi.org/10.1016/j.surfcoat.2023.130327.
- 3. H. Gao, G. He, Q. Li, Y. Li, W. Hu, S. Zhou, F. Liu, J. Yi, Y. Zhang, Z. Cai, S. Ogata, L. Qiao, L. Gao, Diffusion bonding of high entropy alloy and stainless steel at a relative lower temperature via surface nano-crystallization treatment, J. Mater. Res. Technol. 24 (2023) 475–487. https://doi.org/10.1016/j.jmrt.2023.03.026.
- 4. Ren, X., Chen, G., Zhou, W. *et al.* Formation and growth kinetics of intermediate phases in Ni-Al diffusion couples. *J. Wuhan Univ. Technol.-Mat. Sci. Edit.* 24, 787–790 (2009). https://doi.org/10.1007/s11595-009-5787-9

SCP 6.1:

Additive manufacturing of β-containing TiAl alloys

Hiroyuki Y. Yasuda¹, Ken Cho², Masao Takeyama³, Takayoshi Nakano⁴
¹Division of Materials and Manufacturing Science, Graduate School of Engineering, The University of Osaka.

- 2-1, Yamada-oka, Suita Osaka 565-0871, Japan, hyyasuda@mat.eng.osaka-u.ac.jp ²Division of Materials and Manufacturing Science, Graduate School of Engineering, The University of Osaka,
- 2-1, Yamada-oka, Suita Osaka 565-0871, Japan, k_cho@mat.eng.osaka-u.ac.jp

 3 Department of Materials and Engineering, School of Materials and Chemical Technology, Institute of Science Tokyo, 2-12-1 Ookayama, Meguro-ku, Tokyo 152-8550, Japan, takeyama@mtl.titech.ac.jp

 4Division of Materials and Manufacturing Science, Graduate School of Engineering, The University of Osaka.
 - 2-1, Yamada-oka, Suita Osaka 565-0871, Japan, nakano@mat.eng.osaka-u.ac.jp

Introduction

TiAl alloys have attracted much attention due to their excellent strength to weight ratio and good oxidation resistance at high temperatures. In particular, the β -containing alloys show high strength at high temperatures, compared with Ti-48Al-2Cr-2Nb alloys which are used for low pressure turbine blades of aircraft jet engines. However, during casting process, contamination from crucibles and oxidation are of great concern. Additive manufacturing (AM) technique, especially electron beam-powder bed fusion (EB-PBF), is favorable for fabricating TiAl alloys. It is also noted that AM technique can control not only shape but also microstructure of the products. Microstructure of TiAl, fabricated by EB-PBF, generally depends on process parameters such as beam current and scanning speed [1]. Moreover, Signori et al. [2] suggest that the formation of the β/γ cellular structure along the grain boundaries by post annealing is effective in an improvement of ductility in TiAl alloys. In this paper, we report the effect of the process parameters and post heat treatment on the microstructure of β -containing TiAl alloys fabricated by EB-PBF. The relationship between the microstructure and mechanical properties of the alloys was also discussed.

Materials and Methods

Ti-44Al-4Cr (at.%) raw powder was provided by Osaka Yakin Kogyo Ltd. Rectangular specimens of the alloys were fabricated by EB-PBF (Arcam Q10) at different process parameters. After the fabrication, these specimens were solutionized at 1300°C, followed by annealing at 1000°C to obtain the α/γ lamellar grains surrounded by the β/γ cells. The microstructure of the alloys was observed using an optical microscope (OM) and a scanning electron microscope (SEM). Tensile tests were performed at room temperature and 750°C at an initial strain rate of 1.7x10⁻⁴ /s. The hardness of the local area was measured by nanoindentation tests with a maximum load of 59 mN at room temperature.

Results and Discussion

Microstructure of as-built samples depends strongly on the energy density (E) given by,

$$E = \frac{VI}{VPd} \,. \tag{1}$$

where V is the beam voltage, I is the beam current, v is the scanning speed, p is the scanning pitch and d is the powder layer thickness. At high E, fine mixed structure composed of the α , β and γ phases is observed (Fig. 1). Since the cooling rate during EB-

PBF process is slow at high E, the α phase is formed from the β phase, followed by the precipitation of the γ phase in the α and β phases, resulting in the formation of the fine mixed structure. On the other hand, at low E, the α/γ lamellar grains can be seen and the grains are surrounded by the cell structure composed of the β and γ phases (Fig. 1). It is also noted that the lamellar spacing at low E is less than 20 nm. At low E, the cooling rate is so high that the β to α massive transformation takes place during fabrication, followed by the precipitation of the plate-like γ phase in the α phase, resulting in the ultrafine lamellar structure. Yamabe et al. [3] also reported the β to α massive transformation at high cooling rate. In addition, to decrease the supersaturation of Cr, the β/y cellular structure is formed along the boundaries of the lamellar colonies by discontinuous precipitation. The mechanical properties of β -containing TiAl alloys are dependent on E. For instance, the ultimate tensile strength (UTS) at room temperature decreases with increasing E up to 33 J/mm³. Further increase in E results in an increase in UTS. At low E, the α/γ lamellar structure contributes to high strength, since the lamellar spacing is so small. A decrease in UTS is associated with a decrease in the volume fraction (V_f) of the α/γ lamellar structure. In contrast, at E > 33 J/mm³, the UTS increases again due to an increase in V_f of the β phase. It is also noted that the UTS at 750°C also increases with an increase in V_f of the β phase. These results suggest that both the ultrafine α/γ grains and the β grains play an important role in strengthening of TiAl alloys. It is also noted that the strength of Ti-44Al-4Cr alloys fabricated by EB-PBF is much higher than that of Ti-48Al-2Cr-2Nb alloys. The effect of post annealing on the microstructure and mechanical properties of Ti-44Al-4Cr alloys fabricated by EB-PBF was also examined. Annealing at 1000°C after solutionization at 1300°C leads to the formation of the α/γ lamellar grains surrounded by the β/γ cells, which is similar to the as-built samples fabricated at low E. In addition, V_f of the β/γ cells increases with increasing annealing time at 1000°C. The UTS of the annealed specimens at 750°C increases with increasing V_f of the α/γ lamellar structure. From nanoindentation tests, the α/γ grains exhibit higher hardness than the β/γ cells. Thus, the lamellar grains can increase the UTS through the Hall-Petch law. In contrast, the elongation at 750°C rises as V_f of the β/γ cells rises. Fine γ phase in the β/γ cells seems to enhance the ductility.

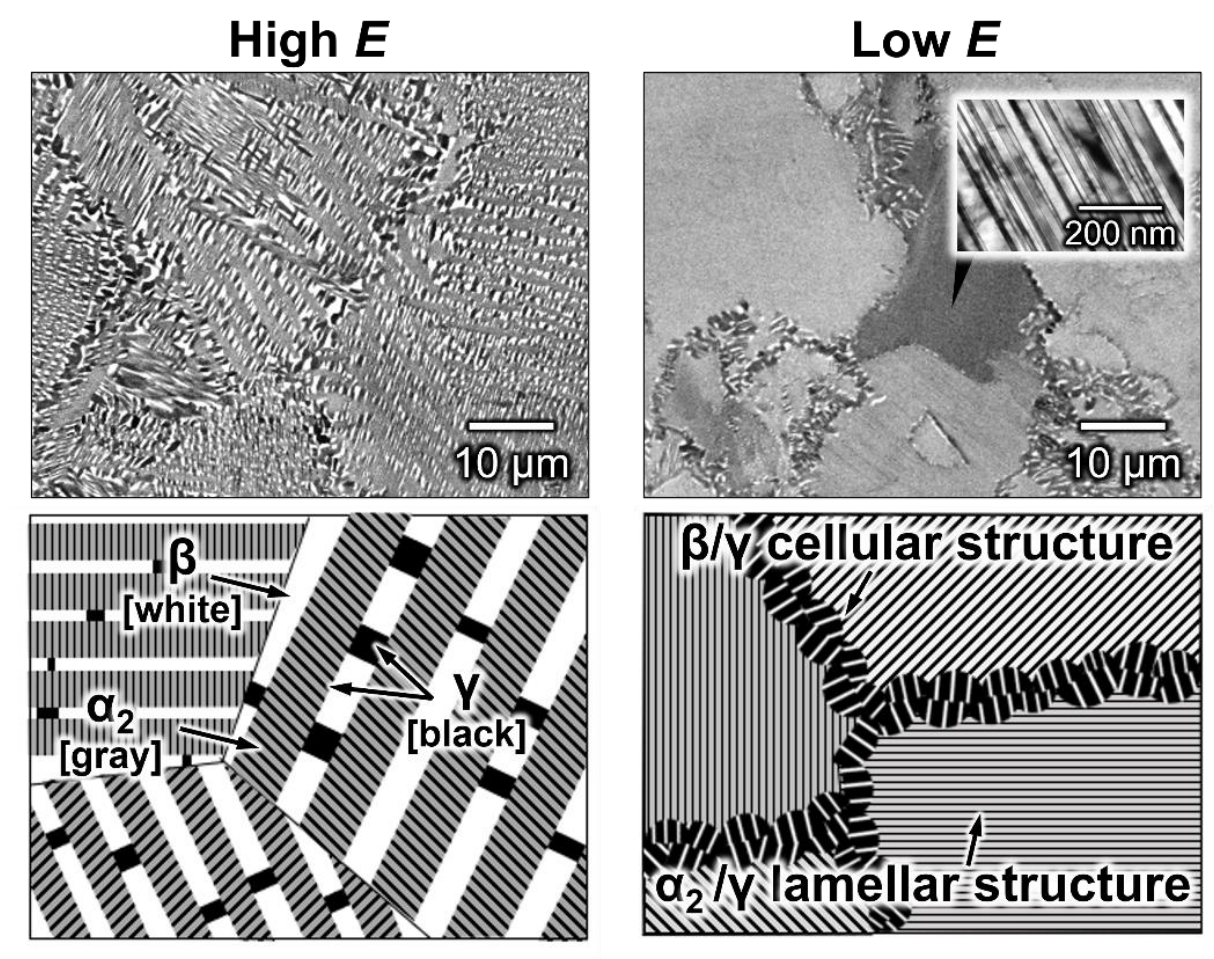


Fig. 1: Microstructure of Ti-44Al-4Cr alloys fabricated by EB-PBF at high and low *E*; as built samples.

- [1] M. Todai, T. Nakano, T. Liu, H. Y. Yasuda, K. Hagihara, K. Cho, M. Ueda, M. Takeyama, Additive Manufacturing, **2017**, 13, 61–70.
- [2] L. J. Signori, T. Nakamura, Y. Okada, R. Yamagata, H. Nakashima, M. Takeyama, Intermetallics, **2018**, 100, 77–87.
- [3] Y. Yamabe, M. Takeyama, M. Kikuchi, Gamma Titanium Aluminides, Eds. by Y.-W. Kim, R. Wagner and M. Yamaguchi, TMS, **1995**, 111-129.

SCP 6.2:

Deformation mechanisms at high temperatures in TiAl alloys - Role of addition elements

Alain Couret¹, Michael Musi², Guy Molénat¹, Petra Spoerk-Erdely³, Helmut Clemens², Jean-Philippe Monchoux¹

Introduction

Following the successful implementation of TiAl blades in aero-engines produced by GENERAL ELECTRIC and SAFRAN, the aim is now to increase the operating temperature of TiAl alloys up to 800°C, if possible. This requires optimization of the microstructures and chemical compositions of this family of alloys. In this context, the aim of the present work is to provide an in-depth understanding of deformation mechanisms of TiAl alloys in the temperature range above 700°C and of the role of addition elements on these deformation mechanisms.

Materials and Methods

The work was performed on two alloys densified by spark plasma sintering [1]: an IRIS alloy (Ti-Al48-W2-B0.1) [2] and an IRIS⁺ alloy in which 0.3 at % of C were incorporated. Their microstructures are formed by small lamellar grains surrounded by borders made of single-phase γ grains that contain B2 precipitates. Creep tests under constant tensile loading were carried out in air at 800°C and 200 MPa. Transmission electron microscopy (TEM) observations and atom probe tomography (APT) analyses were performed on thin foils extracted from the sample crept at 800°C, until a plastic strain of 3 % was reached.

Results and Discussion

Creep curves for IRIS and IRIS⁺ alloys at 800°C and 200 MPa are shown in Figure 1. Compared to the IRIS alloy, the IRIS⁺ alloy is more resistant to creep. For instance, for the former, it takes 88 h to attain 5% deformation, while for the latter, it takes 112 h to do so. In addition, the IRIS⁺ alloy has a minimum creep rate that is lower than IRIS: 1.1 10⁻⁷ s⁻¹ with respect to 1.4 10⁻⁷ s⁻¹. Previous research investigated the deformation microstructure in the crept IRIS alloy [3].

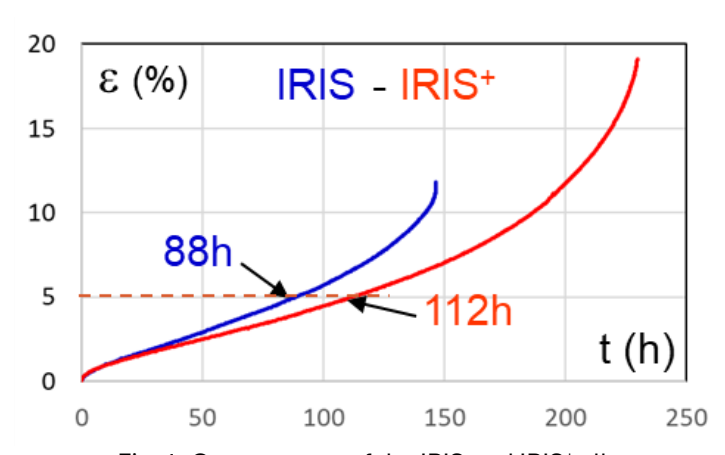


Fig. 1. Creep curves of the IRIS and IRIS⁺ alloys at 800°C and 200 MPa.

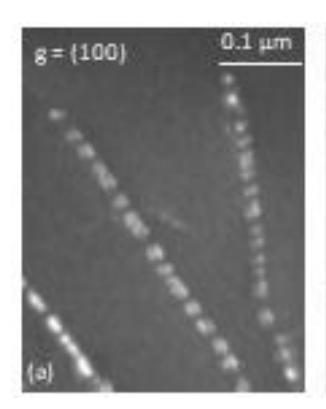
We found that dislocations move by a mixed climb mechanism, with a tendency to spread out in close-packed planes situated perpendicularly to the tensile axis. With two distinct diffraction conditions and tilt inclinations, ordinary dislocations in the crept IRIS⁺ alloy are shown in Figure 2.

¹ CEMES, Université de Toulouse, CNRS, 29 rue Jeanne Marvig, BP 94347, 31055 Toulouse, France

² Department of Materials Science, Montanuniversität Leoben, Franz Josef-Straße 18, 8700 Leoben, Austria

³ Institute of Materials Science, Joining and Forming, Graz University of Technology, Kopernikusgasse 24/I, 8010 Graz, Austria

These studies have demonstrated the formation of rows of dislocation loops (a) and the dislocations hanging on them (b). We verified that dislocations in the crept IRIS⁺ alloy move by mixed climb, much like in the IRIS alloy, using tilting experiments. Coprecipitation of W and C at the dislocation moving by climb has been demonstrated by APT studies (Fig. 2, c) [4].





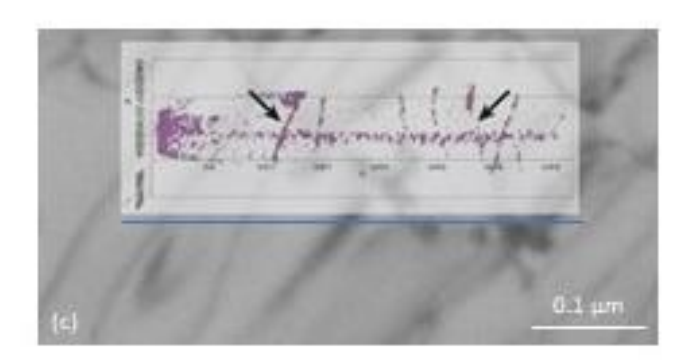


Fig. 2. Studies of the IRIS⁺ alloy crept at 800°C and 200 MPa. (a) and (b) TEM observations of loops and dislocations under different diffracting conditions.

(c) Superposition of an APT W + C isosurface on a TEM view of the same area, illustrating the precipitation on the dislocations.

Conclusion

Based on these results, we will propose that the co-segregation of C and W at dislocations moving by mixed climb is the cause of the IRIS+ alloy's superior creep behavior [4].

- [1] T. Voisin, L. Durand, N. Karnatak, S. Le Gallet, M. Thomas, Y. Le Berre, J.F. Castagne and A. Couret A, **2013**, Journal of Materials Processing Technology, 213, 269.
- [2] A. Couret, T. Voisin, J. P. Monchoux, M. Thomas, 2017, JOM 69, 2576.
- [3] A Couret, J. P. Monchoux, 2019, Acta Material 181, 331-341.
- [4] J.P. Monchoux et al., 2025, in preparation.

SCP 6.3:

Three-dimensional Characterization of the β -Ti Phase in γ -TiAl Base Alloy

Yotaro Okada¹, Ryosuke Yamagata^{1,2}, and Masao Takeyama¹
¹ School of Materials and Chemical Technology, Institute of Science Tokyo (formerly Tokyo Institute of Technology),

2-12-1 Ookayama, Meguro-ku, Tokyo 152-8552 Japan, okada.y.am@m.titech.ac.jp,
takeyama@mtl.titech.ac.jp

² Department of Mechanical Engineering, Chiba University,
1-33 Yayoi-cho, Inage-ku, Chiba-shi, Chiba 263-8522 Japan, yamagata@chiba-u.jp

Introduction

γ-TiAl base alloy was first in the world introduced into service in commercial aircraft engines by GE in 2011 as low-pressure turbine blades [1], and is still being actively studied. The microstructures of conventional alloys including the GE alloy typically consist of two phases of α_2 -Ti $_3$ Al and γ-TiAl, whereas the alloys developed later, called third-generation, contain the β -Ti (or β_0) phase. Takeyama et al. have demonstrated that the introduction of the β phase is effective in improving the strength and toughness [2, 3]. The β phase on lamellar grain boundaries plays a role in preventing crack propagation across the lamellar grain boundaries. Not only on the grain boundaries, the β phase can also forms on lamellar interfaces in the grains depending on alloy composition and heat treatment, and this β phase on lamellar interfaces can be expected to improve the mechanical properties as well. Characterizing the microstructural features of the β phase on lamellar interfaces can be effective to understand its effect on the mechanical properties.

It is difficult to evaluate the three-dimensional (3D) features of precipitations only from the observation by scanning electron microscopy (SEM). There are various methods for observing microstructures in 3D. Serial sectioning using focused ion beam (FIB) is one method that allows 3D observation at the microscopic scale. In the present study, the microstructure formation in a model TiAl alloy was investigated, focusing on the β phase, and the obtained microstructure was characterized in 3D using the FIB-SEM serial sectioning method.

Materials and Methods

A model alloy with a nominal composition of Ti-45Al-6Cr-0.75O (at.%) was investigated in this study. This alloy was prepared by cold crucible induction melting and gravity casting, followed by forging by one stroke at 1573 K. Pieces cut from the hot-forged pancake were heat-treated in two steps. For the first step, the alloy was maintained at 1573 K for 24 h and cooled to 1523 K slowly at a rate of 0.5 K/min, followed by air cooling. In this step, a nearly α -Ti single phase microstructure with small amount of the β phase form at the high temperatures, and the α grains turn into α_2/γ lamellar grains by the precipitation of γ phase and the ordering of α phase during cooling. Secondly, the alloy was aged at 1273 K for 3 to 100 h to precipitate the β phase. The microstructures of the as-forged and heat-treated alloys were observed in 2D and 3D by a field emission SEM. The 3D observation was conducted by the serial sectioning method using FIB. By repeating the FIB milling and SEM imaging, the microstructure was observed in 3D. The milling thickness was set to 20 nm per slice, and 568 slices were observed in total. After the 3D observation, a crystallographic orientation analysis was performed on the observed cross section by the electron backscatter diffraction method.

Results and Discussion

Fig. 1 shows the backscattered electron (BSE) images of the alloy after first-step heat treatment (a, b) and 3 h aging treatment (c, d). After the first-step treatment, the microstructure consists of the α_2/γ lamellar grains with β + γ two-phase microstructure on the grain boundaries (Fig. 1 (a, b)). The grain size is approximately 50 µm. The β phase is the dominant phase in the grain boundary β + γ region in this microstructure. It can be deduced that this β -dominant microstructure was the β phase at high temperatures of 1573–1523 K before cooling, and the γ phase was precipitated during the cooling. There is no β phase observed in grain interior. On the other hand, after the 3 h aging, the β phase particles were precipitated on lamellar interfaces in the grains, and the β + γ two-phase microstructure in cellular morphology was formed near the grain boundaries (Fig. 1 (c, d)). The γ phase is predominant in this cellular microstructure, hereafter called β/γ cell. The β/γ cells were formed in a discontinuous precipitation mode, and the β phase particles on lamellar interfaces were formed in a continuous precipitation mode.

The 3 h-aged sample was observed in 3D to deeply understand the morphology of the β phase particles in lamellar grains. Fig. 2 shows the reconstructed 3D BSE image (a) and one of the extracted lamellar interfaces from the reconstructed image (b). The β precipitates exhibit an elongated plate-like shape, and they show a Widmanstätten pattern. On each of the lamellar interfaces, up to six variants of the β phase were observed. As a result of crystallographic orientation analysis, it was found that the longitudinal directions of the precipitates are offset by approximately $\pm 12.5^{\circ}$ from the three <110> directions of the γ phase. It has been reported that there is Kurdjumov-Sachs (K-S) orientation relationship, where close-packed planes and directions of two phases are parallel, between the γ lamella and the continuous precipitated β phase on the lamellar interface [4]. The three <110> directions of a (111) plane in the γ phase are parallel to the two <111> directions of a (110) plane in the β phase, and consequently, the six variants were produced.

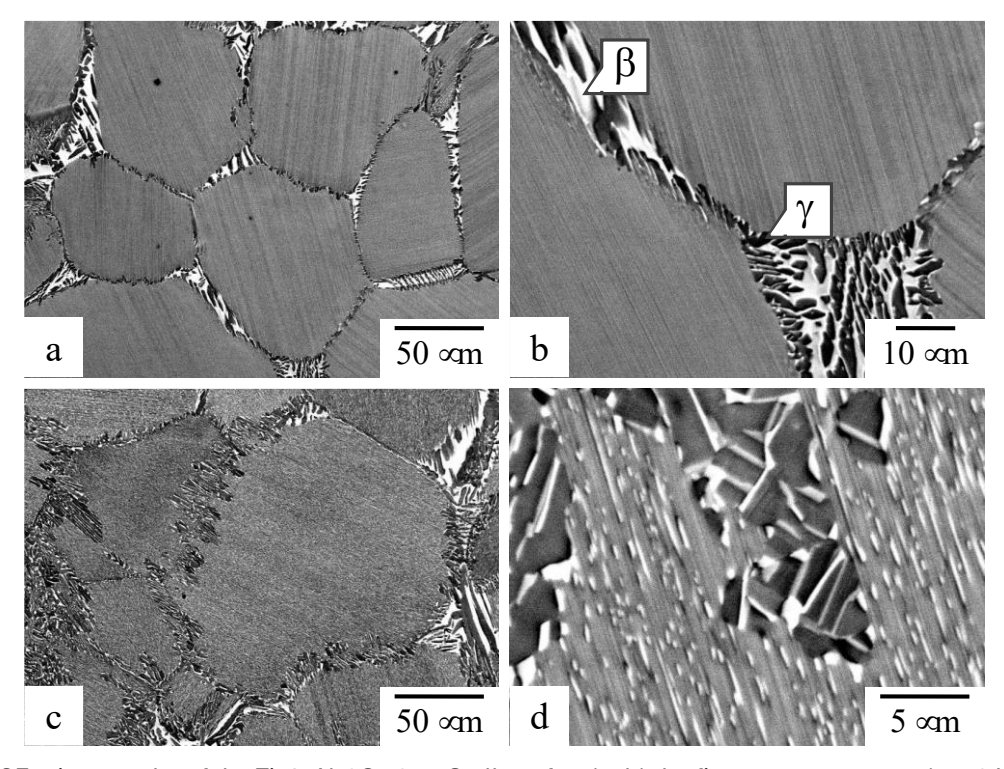


Fig. 1: BSE micrographs of the Ti-45Al-6Cr-0.75O alloy after (a, b) the first-step treatment (1573 K for 24 h and controlled cooling) and (c, d) aged at 1273 K for 3 h.

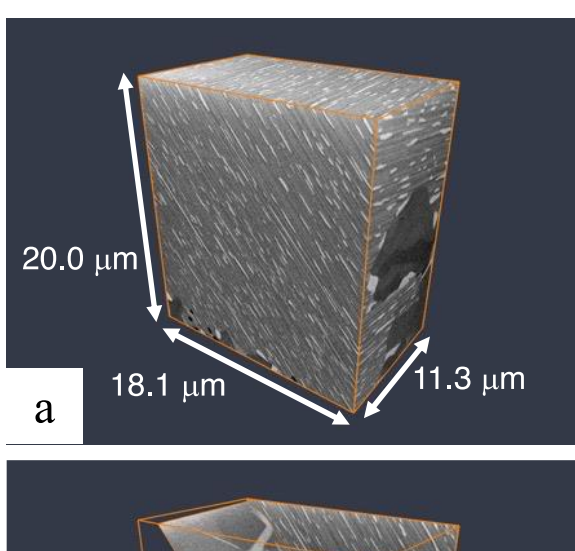
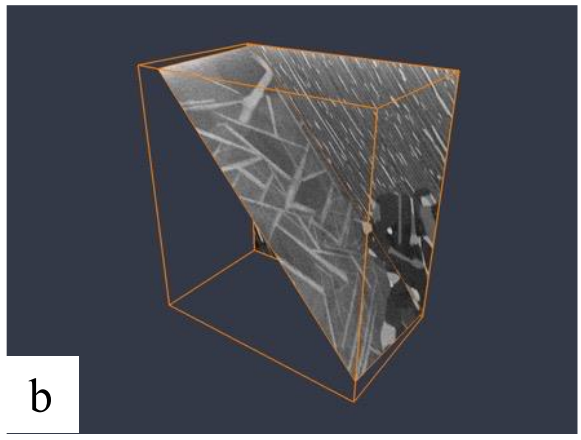


Fig. 2: (a) Reconstructed 3D image of the 3 h aged sample and (b) an extracted lamellar interface.



- [1] B.P. Bewlay, S. Nag, A. Suzuki, M.J. Weimer, Materials at High Temperatures. **2016**, 33, 549-559.
- [2] L.J. Signori, T. Nakamura, Y. Okada, R. Yamagata, H. Nakashima, M. Takeyama, Intermetallics. **2018**, *100*, 77–87.
- [3] R. Yamagata, H. Nakashima, M. Takeyama, MRS Advances. 2021, 6, 198–202.
- [4] H. Fukushima, S. Kobayashi, T. Matsuo, M. Takeyama, Report on the 123rd Committee on Heat-Resisting Materials and Alloys, Japan Society for Promotion of Science. **2004**, *45*, 327–335

SCP 6.4:

Principle of Novel Alloy Development for Thermal Power Generation toward Carbon Neutrality

Masao Takeyama

School of Materials and Chemical Technology, Institute of Science Tokyo (formerly Tokyo Institute of Technology),

2-12-1 Ookayama, Meguro-ku, Tokyo 152-8552 Japan, takeyama@mtl.titech.ac.jp

It is undoubtedly unrealistic that all power can be generated only by variable renewable energy (VRE). It should be noted that as the fraction of VRE is increased, thermal power generation becomes more important since it is the only power generation system that can prevent power failure from a shortage of power caused by weather dependent VRE power. Thus, from a scientific viewpoint, it is impossible to supply all the power by VRE, although such articles are seen sometimes. For future carbon neutral society, thus, a novel thermal power generation system with no CO_2 emission is needed, that is, oxygen/hydrogen combustion gas turbine combined with steam turbine with the steam temperature of 700°C, as shown in Fig. 1.

The key to realize the novel thermal power plant is in the developments of new wrought alloys applicable to both gas turbine and steam turbine components under higher temperature operation conditions. In the national project of JST (Japan Science and Technology Agency)-Mirai program, we have constructed an innovative *Integrated Materials Design System* (Fig. 2) consisting of a series of mechanical property prediction modules (MPM) and microstructure design modules (MDM).

Based on the design system, novel austenitic steels strengthened by Laves phase, so called ALS (Austenitic Laves Steels), was developed for the stream turbine components. The ALS has an allowable stress higher than 100 MPa for 105 h at 700°C, even stronger than the conventional Ni-based alloys (Fig. 3). In addition, for gas turbine components, novel solid-solution type Ni-Cr-W superalloys were designed and found to exhibit superior creep life longer than 105 h under 10 MPa at 1000°C, nearly three times stronger than the conventional solid-solution type alloy Hastelloy X (Fig. 4). The superior long-term creep strengths of these alloys are attributed to the "*Grain-boundary Precipitation Strengthening* (GBPS)" effect due to C14 Fe₂Nb Laves phase and bcc A2-W phase precipitated at the grain boundaries, respectively. It should be noted that the developed Ni-Cr-W alloy can also be a promising candidate alloy applied to the intermediate heat exchanger materials for high-temperature gas cooled reactor (HTGR) for hydrogen production. This project is also going on in Japan.

In presentation, the details of *Integrated Materials Design System* as well as the mechanism of the GBPS will be presented. This work was supported by JST-Mirai Program Grant Number JPMJMI21E7, Japan.

References

[1] Realization of a low carbon society through game changing technologies, Japan Science and Technology Agency (JST) Mirai Programs: https://www.jst.go.jp/mirai/en/program/lowcarbon/theme01.html

[2] M. Takeyama, "Materials Technology for Thermal Power Generation toward Carbon Neutrality", R&D Project under JST-Mirai Program (2021), https://www.jst.go.jp/mirai/en/uploads/saitaku2021/JPMJIM2050nenl21E7_summary_en.pdf

[3] M. Takeyama, Advances in Materials, Manufacturing, and Repair for Power Plants: Proceedings from the Tenth International Conference, October 15–18, **2024**, Bonita Springs Florida, USA https://doi.org/10.31399/asm.cp.am-epri-2024p1033

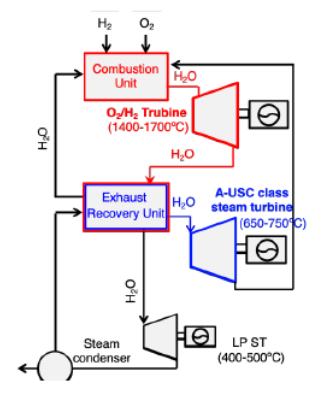


Fig. 1 A Schematic diagram of oxygen/hydrogen combustion GTCC power generation system.

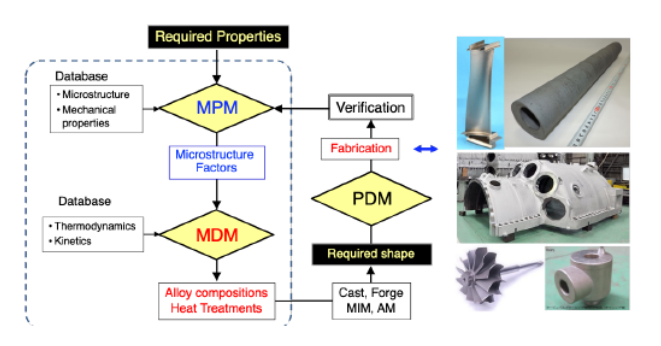


Fig. 2 Integrated Materials Design System consisting of three modules of MPM (Mechanical Property Prediction module), MDM (Microstructure Design module) and PDM (Process Design module) for development of novel alloys.

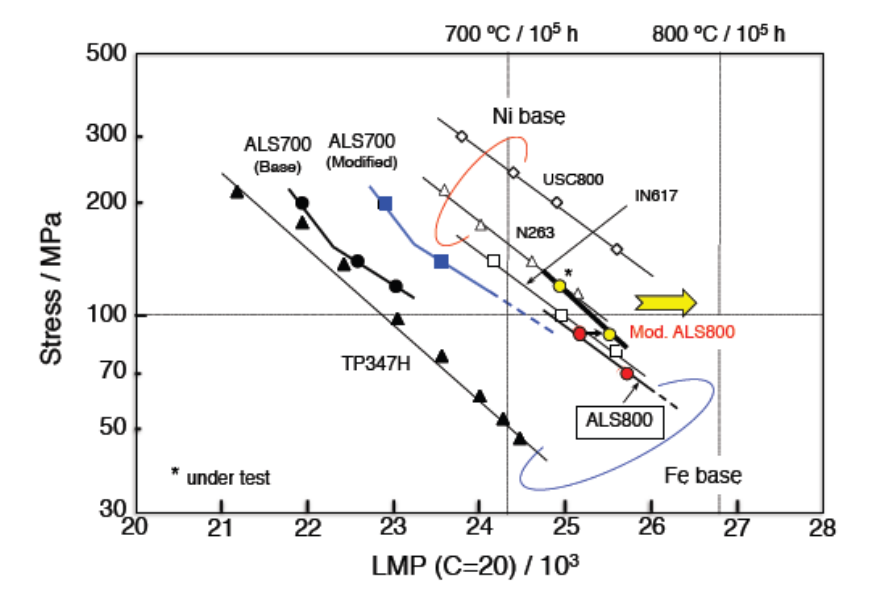


Fig. 3 The stress/Larson-Miller parameter curves of the newly developed austenitic steels strengthened by intermetallic phases (ALS), together with other Fe-based and Ni-based alloys.

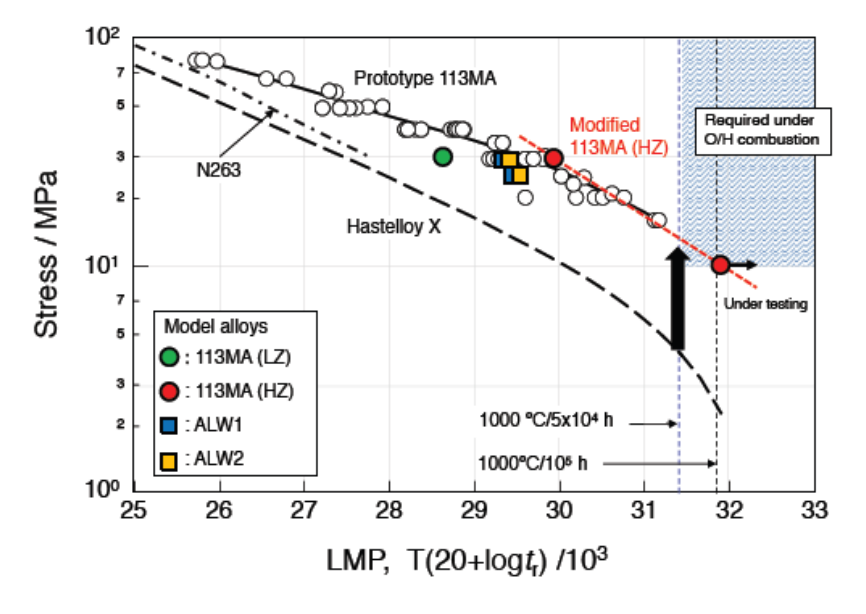


Fig. 4 The stress/Larson-Miller parameter curves of the newly developed solid solution strengthening type Ni-based alloys (113MA and ALW series), together with conventional Ni-based alloys of Hastelloy X and N263.

SCP 7.1:

A journey through TiAl development in IHI Corporation- from alloy design to advanced manufacturing

Rachel Jennings1, Yoshihiko Nagata2, Koji Nezaki2, Sadao Nishikiori3

1 IHI Europe Ltd., London, UK
2 IHI Corporation, Yokohama, Japan
3 Osaka University, Osaka, Japan

Abstract

To fully realise the potential of TiAl alloys in aerospace, advanced alloy design and microstructural control strategies must be continuously progressed to achieve superior high- temperature strength, creep, and oxidation resistance compared to conventional Ni-based superalloys Inconel 718 and Inconel 713C.

Since IHIs efforts in TiAl development began over thirty years ago, an interdisciplinary approach to alloy development has been responsible for their successful implementation in aerospace and automotive components. From the early stages of prototyping, experts in design, manufacturing, quality assurance and materials engineering collaborate closely to ensure robust market-ready solutions.

To expand the application of TiAl alloys, in recent years IHI are embracing advanced manufacturing technologies including Electron Beam Powder Bed Fusion (EPBF). Such technologies are enabling the reintroduction of alloying elements whose addition was restricted by conventional production methods due to segregation problems. While EPBF provides promise for furthering the performance of TiAls, challenges still remain for the widespread implementation of these alloys in aerospace applications.

SCP 7.2:

Systematic evaluation of load partitioning and deformation mechanisms in a multi-phase intermetallic γ-TiAl based alloy: A synchrotron-based approach

Benjamin Seligmann¹, Michael Musi², Sabine Bodner¹, Helmut Clemens¹, Emad Maawad³, Thomas Antretter⁴, Petra Spoerk-Erdely⁵

¹Department of Materials Science, Montanuniversität Leoben, Franz-Josef-Straße 18, 8700 Leoben, Austria;

benjamin.seligmann@unileoben.ac.at, helmut.clemens@unileoben.ac.at, sabine.bodner@unileoben.ac.at;

² Department of Materials Science and Engineering, KTH Royal Institute of Technology, SE-100 44 Stockholm, Sweden; micm@kth.se;

³ Institute of Materials Physics, Helmholtz-Zentrum Hereon, Max-Planck Straße 1, 21502 Geesthacht, Germany; emad.maawad@hereon.de;

⁴ Chair of Mechanics, Montanuniversität Leoben, Franz-Josef-Straße 18, 8700 Leoben, Austria; thomas.antretter@unileoben.ac.at;

Introduction

The material class of intermetallic γ-titanium aluminide (TiAl) based alloys is suitable for high-temperature applications up to 750°C, due to its outstanding performance in terms of mechanical properties, oxidation and creep resistance [1,2]. Its combination of lightweight nature with the high specific strength and stiffness makes them ideal materials for the aerospace industry. One of the most important properties in this context is the tensile behavior at different temperatures, i.e., from room temperature up to 800 °C. In particular, possible applications are turbine blades in aircraft engines, where tensile loads are applied during usage [3]. The hierarchical, multi-phase composition of γ-TiAl based alloys leads to a so-called load partitioning behavior, where the material does not deform plastically in unity on the microscale. One phase, in this case y-TiAl (L1₀ structure), starts to deform, while other phases such as α_2 -Ti₃Al (D0₁₉ structure) and in β -stabilized variants also β_{\circ} -TiAl (B2 structure) reinforce the microstructure elastically [4]. Load partitioning cannot be investigated using conventional tensile tests. Instead, it requires the use of synchrotron facilities. There the specimen loaded in tension (or compression) is probed in situ using high-energy X-ray diffraction (HEXRD) in transmission, resulting in a characteristic pattern on a 2D-detector. Each reflection within the pattern can be attributed to a subset of grains of a certain phase and orientation. The behavior of these reflections during the macroscopic deformation is then investigated regarding peak position, peak broadening as well as the integrated intensity. Due to the crystallographic nature of the complex material, a large variety of peaks is available to be evaluated, regarding elastic and plastic properties. This study introduces a systematic approach to enhance the understanding of the deformation mechanisms in TNM-based alloys, taking into account the Schmid factor (m), the critical resolved shear stress (CRSS) and specific textures in TNM bulk metals, combined with the theory of Xray diffraction and reciprocal space.

Material and Methods

A TNM alloy with a nominal chemical composition of $\underline{T}i$ -43.5Al-4 $\underline{N}b$ -1 $\underline{M}o$ -0.1B in at.% was investigated. This alloy consists of a variety of phases and is – depending on

⁵ Institute of Materials Science, Joining and Forming, Graz University of Technology, Kopernikusgasse 24/I, 8010 Graz; Austria; petra.spoerk-erdely@tugraz.at;

microstructure and temperature – capable of plasticity to some degree. Using established heat treatments, various microstructures can be adjusted, which aim to enhance mechanical properties such as room temperature ductility or creep resistance [4]. In the present work, the applied heat treatment was selected to create an industrially relevant microstructure, which shows the majority γ -phase (70 wt.% according to Rietveld analysis) in combination with the α_2 -phase showing the Blackburn orientation relationship in lamellar colonies [6]. The β_0 -phase is situated at the boundaries of these lamellar colonies.

The *in situ* tensile experiments were performed at the high-energy materials science beamline P07B at Deutsches Elektronen-Synchrotron in Hamburg, Germany, using a tensile rig capable of 20 kN which was combined with an inductive heating setup, providing test temperatures of up to 900°C in air. The average photon energy was set to 87.1 keV (0.14235 Å), and the sample-to-detector-distance, calibrated with a LaB $_6$ standard, was chosen to cover a sufficient number of reflections, as necessary for a holistic interpretation in a next step.

During evaluation, the 2D patterns are split into 10° azimuthal cake segments. Afterwards, the cake segment in tensile direction as well as the one rotated 90° to it are evaluated, showing the opposing reactions of the material to the applied load.

Results and Discussion

The evaluation and interpretation of the experiment require integrating various aspects of the theories of crystal plasticity, mechanics and X-ray diffraction. In crystal plasticity, the use of Schmid´s law is well established for calculating the resolved shear stress acting on a specific slip system during deformation. According to Eq. (1), the Schmid factor links the orientation of slip plane and slip direction to the tensile direction and yields values between 0 and 0.5:

$$m = \cos\lambda \cos\Phi,$$
 (1)

where λ is the angle between tensile direction and slip plane normal and Φ is the angle between tensile direction and slip direction. Similar considerations as in Eq. (1) are valid for twinning. Usually, the Schmid factor is only used for single crystals. However, it is often also considered in HEXRD and micromechanical experiments [5], as a specific reflection in a certain tensile direction represents the average behavior of a similarly oriented subset of grains.

Following crystal plasticity, the Schmid factor of a certain deformation mechanism has to be weighted with its critical resolved shear stress (CRSS), which can be calculated according to Eq. (2)

$$CRSS \le m \sigma$$
 (2)

where σ is the macroscopic stress in tensile direction. It represents the threshold above which plastic deformation is possible, if Eq. (2) is fulfilled.

For the sake of clarity, all possible deformation mechanisms are combined and displayed within one inverse pole figure (IPF) as shown in Fig. 1. The displayed directions represent the tensile direction of the rotational symmetric tensile sample. To better visualize the expected deformation behavior, the mechanisms are weighted using the previously introduced *CRSS* values via their ratios, which are related to the softest mechanism. Darker shades indicate soft deformation modes and directions, whereas lighter shades correspond to harder modes and directions. It is possible to subdivide the IPF into regions where specific deformation mechanisms are expected to dominate. The *CRSS* ratios used in this analysis are based on the work by Marketz [7].

Finally, experimental details are considered, as the map cannot be evaluated as a whole during the HEXRD experiment but needs to be analyzed afterwards. Figure 1 shows the positions of measurable reflections for the γ -phase up to 2Θ = 7.5°. This visualization helps to estimate whether the set of reflections is sufficient to clarify specific research questions, e.g., the dominating deformation mechanisms. Post experiment, it also helps to put the observed data into context, as observed plasticity might be linked to darker regions in the IPF. As an example, selected peaks of the γ -TiAl phase can be observed in Figure 2.

The proposed tool also features the ability to plot tensile directions of horizontally observed peaks, facilitating the process of imagining 90° rotations in crystal orientation. It is also possible to consider texture measurements.

In conclusion, this study provides a systematic approach to evaluate the load partitioning behavior in the γ -phase in γ -TiAl based alloys by performing *in situ* tensile experiments at synchrotron facilities. The approach may be applied to all other present phases. Furthermore, the combination of the behavior of all phases (by using suitable CRSS ratios) can also be observed within one IPF. By considering aspects of crystal plasticity, *CRSS* and a material's texture, the approach helps to improve experimental planning before the experiment as well as to deepen the understanding of load partitioning behavior during tensile loading of multi-phase alloys.

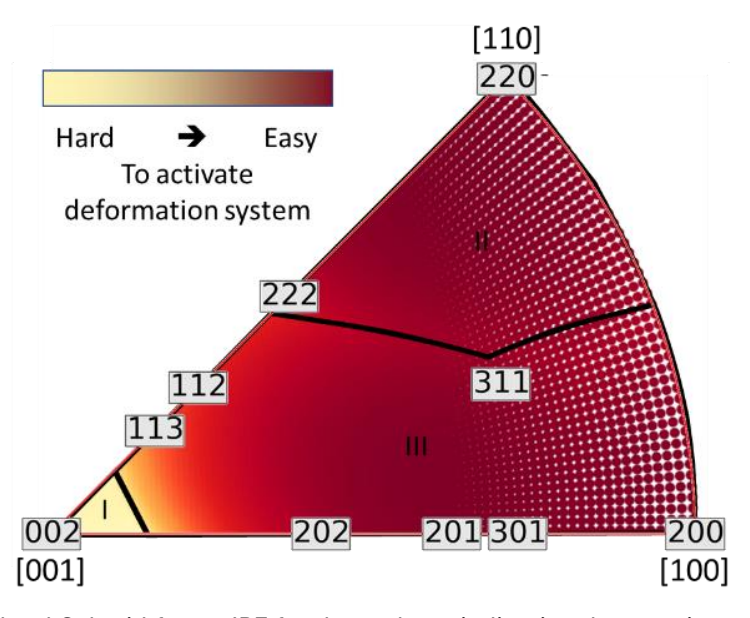


Fig. 1: A *CRSS* weighted Schmid factor IPF for the γ -phase indicating three main areas associated with different deformation mechanisms: superdislocation motion in region (I), twinning in (II) and ordinary dislocation motion in region (III). Peaks observable in HEXRD experiments are indicated, while peaks that cannot be evaluated due to overlap with signals from other phases are not shown.

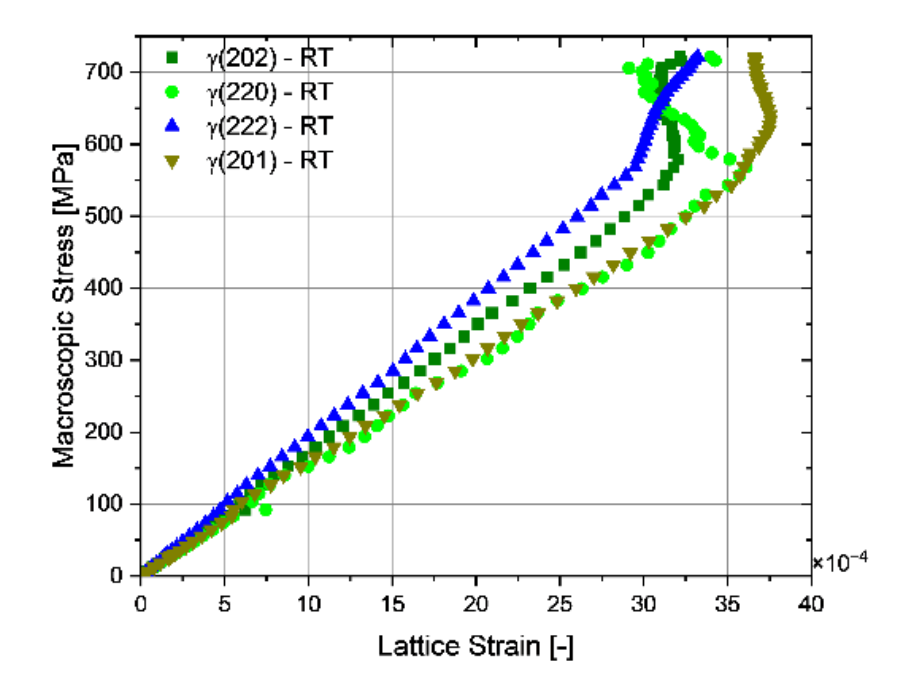


Fig. 2: Selection of peaks belonging to the plastically deforming γ -TiAl phase. The plastic onset can be identified by the upwards trajectory at the end of the elastic region at approximately 550 MPa macroscopic stress. Note that the horizontal axis shows the lattice strain, not the macroscopic strain.

Acknowledgments

The authors thank V. Güther and M. Allen, GfE Metalle und Materialien GmbH, for providing the cast TNM sample material. We acknowledge DESY (Hamburg, Germany), a member of the Helmholtz Association HGF, for the provision of experimental facilities. Parts of this research were carried out at the Hereon-run beamline P07B at PETRA III and we would like to thank N. Schell, P. Staron, E. Maawad and B. Schwebke for assistance in using the tensile testing setup.

- [1] F. Appel et al., 2011, Gamma Titanium Aluminides, Weinheim, Germany, Wiley-VCH
- [2] H. Clemens, S. Mayer, Advanced Engineering Materials, 2013, 15, 4, 191-215
- [3] E. Schwaighofer et al., Intermetallics, **2014**, 44, 128-140
- [4] P. Erdely et al., Acta Materialia, 2018, 158, 193-205
- [5] M. Kastenhuber et al., Intermetallics, **2018**, 97, 27-33
- [6] M. J. Blackburn, (Eds. R. I. Jaffee, N. E. Promisel), **1970**, *The Science, Technology and Application of Titanium*, Pergamon Press, Oxford, p. 633
- [7] W. T. Marketz, 2003, International Journal of Plasticity, 19, 281-321

SCP 7.3:

Reversible stress-induced orthorhombic O phase in TiAl alloys

Xu Liu^{1,2}, Lin Song¹, Florian Pyczak², Andreas Stark², Li Wang³, Xiang Guo¹, Tiebang Zhang¹

¹State Key Laboratory of Solidification Processing, Northwestern Polytechnical University, Xi'an 710072, China, liuxu@mail.nwpu.edu.cn, songlin@nwpu.edu.cn

²Institute of Materials Research, Helmholtz-Zentrum Hereon, Geesthacht 21502, Germany, xu.liu@hereon.de, florian.pyczak@hereon.de, andreas.stark@hereon.de

³State Key Laboratory of Powder Metallurgy, Central South University, Changsha 410083, China, li.wang@csu.edu.cn

Introduction

The O phase has attracted much attention in α_2 -based TiAl alloys for decades due to its good ductility [1]. More recently, this orthorhombic O phase in the form of nanoscale domains has also been found in high Nb containing γ-based TiAl alloys [2-5]. The emergence of the O phase presents a potential route to improve the ductility and mechanical performance of γ-based TiAl alloys. For O phase precipitation during heat treatment, alloying with elements such as Nb or V is pivotal. Specifically, a Nb content higher than 5-7.5 % and an Al content below 46-47 % is essential after annealing at 550 °C for 20 h [6]. Furthermore, the presence of volume and coherency stresses within the $(\alpha_2+\gamma)$ lamellar structures is a prerequisite [2, 7]. It is interesting to note that the highest temperatures before the dissolution of the O phase are near the service temperature of high Nb-TiAl alloys (higher than 800 °C) [8]. Comparing alloys Ti-(43-47)Al-8.5Nb and Ti-45Al-(4-10)Nb, the increase in Nb content and decrease in Al extend the maximum temperature where O phase still exists to higher values but still below 750 °C in general [9]. As described, internal stresses within the $(\alpha_2+\gamma)$ lamellar structures seem to be important for the O phase stability. In the present study, the O phase precipitation within the α₂ phase stimulated by applied external stresses at 800 °C was investigated. The reversal of the O phase formation, the preferential precipitation of the O phase and the O phase formation mechanism were clarified.

Materials and Methods

Button ingots with a nominal composition of Ti-38Al-10Nb were produced using a non-consumable arc melting furnace and were annealed at 800 °C for 25 h and then air cooled to fully eliminate the O phase in the microstructure. Cylinders with 4 mm in diameter and 8 mm in height were machined from the annealed ingots for in-situ compression tests. The samples were compressed at a strain rate of 0.01 s⁻¹ up to an engineering strain of 0.1. The temperature was maintained at 800 °C during removal of the applied loads. The deformed sample was held at 800 °C for 5 min after unloading. The in-situ experiments were performed on a DIL805A/D dilatometer, which was mounted in the P07 synchrotron radiation beamline operated by Helmholtz-Zentrum Hereon at the PETRA $\rm III$ storage ring in Deutsches Elektronen-Synchrotron in Hamburg. TEM observation was executed on a Spectra 300S double aberration-corrected TEM operated at 300 kV. To better observe the O phase precipitation from the α_2 phase, the images were mainly viewed along the $[0001]_{\alpha 2}$ direction.

Results and discussion

In-situ synchrotron HEXRD reveals that the O phase precipitates at 550 °C while it dissolves into the α_2 phase at 750 °C during heat treatments. However, under external

stress the O phase unexpectedly precipitates from the α₂ phase at 800 °C and even 900 °C. Interestingly, this phase transformation shows reversibility in parallel with internal stress evolution in the α_2 phase. Specifically, the O phase formation is insignificant in the beginning but largely proceeds within the stress range of rapid internal stress accumulation in the α_2 phase. The reverse $O \rightarrow \alpha_2$ transformation occurs during removal of the applied loads and continued during isothermal holding in parallel with the relaxation of internal stresses in the α_2 phase (Fig. 1a). Additionally, it has been revealed that the O phase preferentially precipitates from the α_2 grains with one of their <11 $\bar{2}$ 0> directions in the largest tension and their <0001> directions almost unstrained (Fig. 1b), which facilitates the $\alpha_2 \rightarrow 0$ crystal transition since this transition is accomplished primarily via the atomic shuffle on the $(0001)_{\alpha 2}$ plane. TEM study shows that merely small atomic shifts contribute to the stress-induced $\alpha_2 \rightarrow 0$ transformation. The compositional transition dominated by Nb diffusion is largely retarded (Fig. 1c). Assuming this structural transition is decomposed @nto the lattice distortion and rigid body rotation, the distortion of the a_2 lattice with ~2.9 % elongation along the $[11\overline{2}0]_{a2}$ direction (corresponding to $[100]_0$) and ~3.0 % contraction along the $[1\bar{1}00]_{\alpha 2}$ direction (corresponding to $[010]_0$) transforms it into the O lattice. An additional rotation of about \sim 1° around [0001]₀₂ completes this transition.

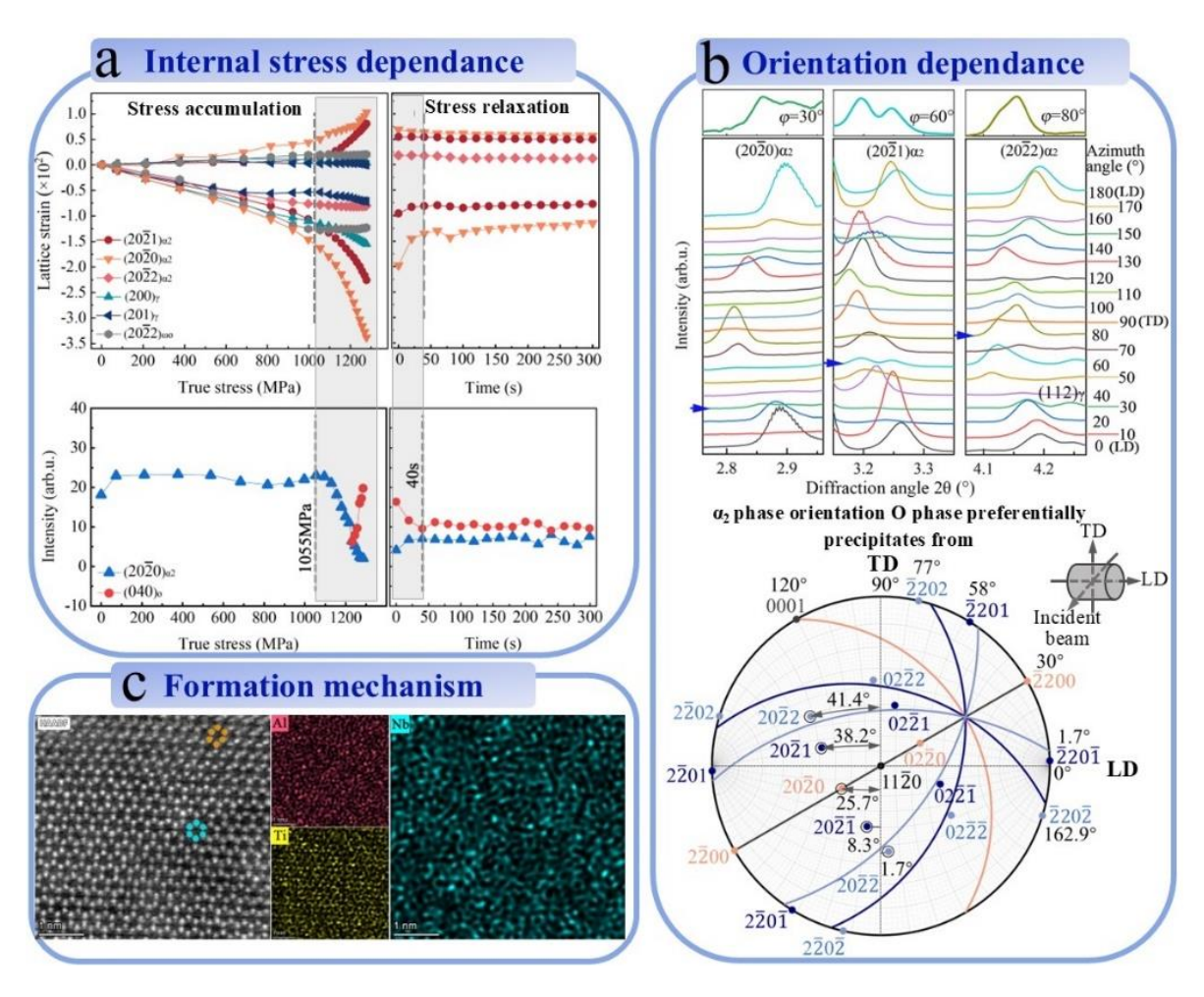


Fig. 1 (a) Lattice strain evolution of the α_2 phase and intensity evolution of the O phase during loading and subsequent holding. (b) 1D HEXRD profiles of the $(20\bar{2}0)_{\alpha_2}$, $(20\bar{2}1)_{\alpha_2}$ and $(20\bar{2}2)_{\alpha_2}$ reflections integrated along φ from 0° to 180° over a range of ±5° at a stress of ~1200 Mpa (on the top). Schematic of spatial preferential orientation of the O phase forming out of the α_2 phase (on the bottom). (c) HRSTEM-HAADF image and EDS mappings taken along [0001] $_{\alpha_2}$ direction containing regions with α_2 and O lattices.

- [1] D. Banerjee, Prog. Mater. Sci. 1997, 42, 135-158.
- [2] H. Gabrisch, U. Lorenz, F. Pyczak, M. Rackel, A. Stark, Acta Mater. **2017**, 135, 304-313.
- [3] H. Gabrisch, M. Janovská, M.W. Rackel, F. Pyczak, A. Stark, J. Alloys Compd. **2023**, 932, 167578.
- [4] G.D. Ren, J. Sun, Acta Mater. **2018**, 144, 516-523.
- [5] G.D. Ren, C.R. Dai, W. Mei, J. Sun, S. Lu, L. Vitos, Acta Mater. **2019**, 165, 215-227.
- [6] M.W. Rackel, A. Stark, H. Gabrisch, F. Pyczak, Intermetallics 2021, 131, 107086.
- [7] M.W. Rackel, A. Stark, H. Gabrisch, N. Schell, A. Schreyer, F. Pyczak, Acta Mater. **2016**, 121, 343-351.
- [8] W.J. Zhang, S.C. Deevi, G.L. Chen, Intermetallics **2002**, 10, 403-406.
- [9] C.R. Dai, Z.B. Yang, J. Sun, S. Lu, L. Vitos, Acta Mater. **2021**, 221, 117419.

SCP 7.4:

Effect of Initial Lamellar Microstructure on Formation Kinetics of Grain Boundary Cellular Microstructure in y-TiAl Alloys

Ryosuke Yamagata¹, Taro Kanda¹, Ken Cho², Hiroyuki H Yasuda², Takayoshi Nakano², Masao Takeyama³, Takaomi Itoi¹

¹Department of Mechanical Engineering, Chiba University, 1-33 Yayoi-cho, Inage-ku, Chiba-shi, Chiba, Japan,

email: yamagata@chiba-u.jp

²Division of Materials and Manufacturing Science, Graduate School of Engineering, Osaka University, 2-1 Yamadaoka, Suita-shi, Osaka, Japan

³ Department of Materials Science & Engineering, School of Materials and Chemical Technology, Institute of Science Tokyo, 2-12-1-S8-8, Meguro-ku, Tokyo, Japan

Introduction

γ-TiAl alloys have received significant attention as jet engine materials, especially for applications to the low-pressure turbine (LPT) blades, because of their high specific strength at elevated temperatures [1]. Recently, we have established an integrated computational inverse problem approach to accelerate the development of TiAl LPT blades in jet engines and reduce the extensive experimental efforts. This system includes two modules, one of which is the "mechanical properties prediction module (MPM)" and the other is the "microstructure design module (MDM)". The input into the former is specific values of the properties required by industries, such as tensile strength (UTS) and fracture toughness ($K_{\rm IC}$). Then the output is a concrete value, such as the volume fraction of the microstructural constituent to meet the requirement. The input into the latter is the output value of MPM. Then the output is the chemical compositions and heat treatment conditions to obtain the required microstructure based on the phase diagrams and the kinetics database. The second input value in the MPM is the "cooling rate" after heat treatment. From this value and the relationship between lamellar spacing and cooling rate (e.g., Ref [2]), the lamellar spacing after heat treatment is predicted. Furthermore, from this calculated lamellar spacing and the relationship between the lamellar spacing and UTS or KIC (e.g., Ref [3, 4]), the mechanical properties of the initial α_2 -Ti₃Al/ γ lamellae are calculated. We also revealed that the introduction of the β-Ti phase on grain boundaries improves the strength and toughness simultaneously [5]. In this case, the \(\beta \) phase formed as β/γ cellular microstructure by eutectoid reaction. Thus, the main microstructure constituent governing the mechanical properties is the β/γ cellular microstructure. Then, the output of MPM becomes the volume fraction of the β/γ cell. The driving force of cellular microstructure formation is assumed to be in two essentials. One of which is the supersaturation of the matrix (α_2/γ lamella), and the other is the internal energy of the matrix. In TiAl alloys having a lamellar microstructure, the latter would be governed by the total interfacial energy of α₂/γ lamellae, which means lamellar spacing would be related to that. To accurately predict the heat treatment condition in MDM, accurate information on the dependence of the formation kinetics of cellular microstructure on lamellar spacing is required. Because the second input value of MPM is the cooling rate, this knowledge is important for the connection between MPM and MDM. Therefore, this study investigated the formation kinetics of the cellular microstructure in TiAl alloys with different initial lamellar spacing.

Materials and Methods

The Ti-Al-Nb-Cr quaternary alloy was used in this study. The alloy was elaborated on using the electron beam melting method. Two-step heat treatments were conducted to control the microstructure. The first step was carried out at 1573 K for 10 minutes to obtain a fully α_2/γ lamellar microstructure. After holding to change the lamellar spacing, the samples were cooled at different rates (R) of 3, 30, and 100 K/min down to 1273 K and then aircooled. The second step heat treatments (aging) were carried out at 1373-1473 K at a specific time (1-1000 h) to generate cellular microstructure. The initial lamellar spacing was measured by transmission electron microscopy with the lamella edge-on condition (beam incidence axis is <110> $_{\gamma}$ and <11 $\bar{2}$ 0] $_{\alpha2}$) and linear intercept method. The volume fraction of cellular microstructure (V_c) was measured by using a scanning electron microscope and image analysis.

Results and Discussion

After the first step heat treatment, the initial lamellar spacing λ became 63 nm (R=3 K/min), 151 nm (R=30 K/min) and 361 nm (R=100 K/min). The lamellar spacing was roughly proportional to the -0.5 power of the cooling rate. This result came into the previous study [2]. The α_2/γ lamellar colony size was the same ($d \cong 200 \mu m$) under all cooling rates. Fig. 1 shows the changes in the V_c as a function of aging time aged at 1373 K. Regardless of the initial lamellar spacing, the cellular microstructure was formed in accordance with the Johnson-Mehl-Avrami-Kolomogorov (JMAK) equation, V_c =1-exp(kn¹). However, the formation kinetics were strongly dependent on the initial lamellar spacing. The JMAK constant k were not dependent on the initial lamellar spacing, kshowed 0.035, 0.049 and 0.057 when λ =63, 151 and 361 nm, respectively. However, JMAK exponent n were strongly dependent on the λ , n showed 0.83, 0.59 and 0.38 when λ =63, 151 and 361 nm, respectively. In addition, this λ dependence on n became stronger at higher temperatures. From these results, we can predict the formation kinetics of cellular microstructure (quantitatively JMAK equation) only using the cooling rate after homogenized heat treatment and aging temperature. Therefore, the aging temperature and aging time can be easily estimated for the required volume fraction of cellular microstructure to meet the required mechanical properties.

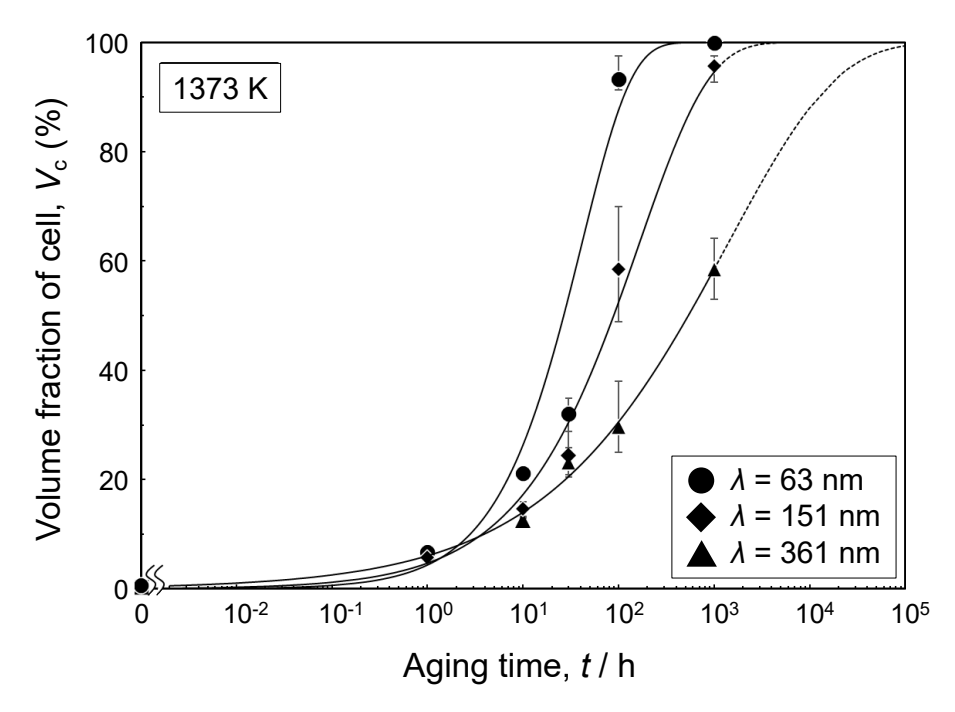


Fig. 1: Changes in the volume fraction of cellular microstructure as a function of aging time.

- [1] B.P. Bewlay, S. Nag, A. Suzuki, M.J. Weimer, Materials at High Temperatures. **2016**, 33, 549-559.
- [2] M. Takeyama, T. Kumagai, M. Nakamura, M. Kikuchi, in R. Darolia, J. J. Lewandowski, C. T. Liu, P. L. Martin, D. B. Miracle, M. V. Nathal (Eds.): Structural Intermetallics, The Minerals, Metals and Materials Society, Warrendale, PA, USA, **1993**, 167-177.
- [3] C. T. Lium J. K. Schneibel, P. J. Maziasz, J. L. Wright, D. S. Eastom, Intermetallics, **1996**, *4*, 429-440.
- [4] R. T. Zheng, G. A. Cheng, X. J. Li, G. X. Cao, L. F. Fu, Y. G. Zhang, C. Q. Chen, Journal of Materials Science, **2007**, *42*, 1251-1260.
- [5] R. Yamagata, H. Nakashima, M. Takeyama, MRS Advances. 2021, 6, 198–202.

SCP 8.1:

Microstructure and Mechanical Behavior at High Temperatures of Multi-Phase Iron-Aluminides

S. Nizamoglu¹, A. Gedsun^{2,3}, C. Schulz¹, C. Breuner¹, S. Seils¹, D. Schliephake¹, S. Laube¹, M. Ghosh⁴, H. Michels⁴, T. Groten⁵, M. Palm², M. Heilmaier¹, A. Kauffmann^{1,6}

¹Institute for Applied Materials (IAM-WK), Karlsruhe Institute of Technology (KIT), Engelbert-Arnold-Str. 4, 76131 Karlsruhe, Germany, camelia.schulz@kit.edu, daniel.schliephake@kit.edu, martin.heilmaier@kit.edu

²Max Planck Institute for Sustainable Materials, Max-Planck-Str. 1, 40237 Düsseldorf, Germany
 ³now at IMTEK, University of Freiburg, Georges-Köhler-Allee 103, 79108 Freiburg, Germany
 ⁴Access e.V., Intzestraße 5, D-52072 Aachen, Germany

⁵Leistritz Turbinentechnik GmbH, Lempstraße 24, D-42859 Remscheid, Germany ⁶Chair Materials Science and Engineering (LWW), Institute for Materials (IM), Ruhr University Bochum (RUB), Universitätsstr. 150, 44801 Bochum, alexander.kauffmann@rub.de

Introduction

To achieve the targeted efficiency improvements in energy conversion, new developments in power plant technology are required. Conventional power plants play a crucial role in balancing fluctuations in the supply of renewable energy. These plants must be able to start quickly and operate efficiently. At the same time, there is significant cost pressure on existing and new conventional power plants. Key contributions to reducing costs include increasing efficiency by raising operating temperatures and reducing the weight of moving parts, as well as savings in manufacturing and operation through the use of affordable, wear- and corrosion-resistant materials. In this sense, innovative iron aluminide alloys are promising candidates to replace high alloyed steels or even Ni-based alloys in some application scenarios due to their low density, good corrosion and wear resistance, and low cost [1-3]. Synthesis and processing of iron aluminides were frequently showcased via standard techniques like casting, rolling, and forging. However, their mechanical properties, such as creep resistance, yield strength above 500 °C, and room temperature ductility, need improvement. Current applications are therefore still niche [3]. Various alloying strategies have been explored to enhance these properties, including the addition of intermetallic precipitates, carbides, borides, and solid solution strengthening [1,2]. Strengthening by incoherent Laves phase precipitates in D0₃-ordered Fe-Al-(Ti, Zr, Nb or Ta) showed particular promise [2]. In Fe-Al-Ta and Fe-Al-Nb [4], the formation of C14 Laves phase is preceded by the precipitation of a metastable Heusler phase Fe₂AlTa or Fe₂AlNb with considerable offstoichiometry, respectively. For Ta-containing Fe-Al [5], the Heusler phase is obtained even after prolonged thermal exposure at 700 °C up to 1000 h. However, from 10 h depending on the Al content the Heusler phase dissolves and stable C14 is formed. In Fe-Al-Nb, which might be preferred in terms of costs, the same transformation sequence evolves faster. In general, the homogeneous precipitation of the coherent Heusler phase substantially contributes to strength and creep resistance of the alloys. However, accompanied with a substantial drop when the transformation to the incoherent Laves phase occurs. The strengthening potential of the stable Laves phase is limited if no counter measures are applied to control its size and distribution. In the present study, we investigated the potential of Fe-Al-Nb alloys by near-industrial manufacturing of steam turbine blades intended to be used at temperatures up to 700 °C conditions [6]. The focus was on a combined casting and forging route with cast preforms and single-step forging into the intended final shape. The yield strength and creep behavior are correlated to the formed Heusler and Laves phases as well as to microstructural changes occurring during synthesis, processing and testing. The results are compared to those of reference alloys produced on laboratory scale and to results from established Fe-Al-Ta alloys which serves as a benchmark.

Materials and Methods

The Fe-25Al-2Nb alloy was cast into preforms using gravity casting that were subsequently forged into the final geometry. Casting yielded the anticipated chemical composition within tolerable error margins. Forging was done using a uniaxial press after soaking at 900°C or 1050°C. The true strains were 0.5 to maximal 2.0 depending on the location in the parts. Quasistatic compression tests and compression creep tests were performed at an initial engineering strain rate of about 10⁻⁴ s⁻¹ and temperatures between RT and 1050 °C. Specimens of 3 mm in diameter and 5 mm in height were tested. Sample preparation for microstructural analysis by scanning electron microscopy (SEM) was carried out by a standard metallographic procedure. Focus was on backscattered electron contrast (SEM-BSE) imaging with orientation and atomic number Z contrast. SEM-BSE micrographs were evaluated by means of threshold binarizing. Furthermore, grain boundary characters were analyzed using electron backscatter diffraction (SEM-EBSD).

Results and Discussion

The as-cast microstructure of Fe-25Al-2Nb in Fig. 1a from the blade part of the preform consists of a polycrystalline, D0 $_3$ Fe-Al matrix and C14 Laves phase precipitates. Grain sizes of the Fe-Al matrix range from 280 to 550 µm, with smaller grains in sections with higher cooling rates. C14 forms inter- and intragranular, with volume fractions of 2.6 to 4.6 vol.%. During forging, the Fe-Al matrix recrystallizes with subgrains (< 15° misorientation angle by SEM-EBSD) of about 4 µm in size, see Fig. 1b. The C14 content substantially increases to about 7.8 vol.% during this processing step, close to the maximum possible volume fraction for the selected alloy composition. A fine distribution of C14 is achieved and the continuous decoration of Fe-Al grain boundaries with C14 is partially removed. At RT and 300 °C, forged samples exhibit higher strength than cast samples with up to 1100 Mpa (at 1% offset plastic strain), attributed mainly to Hall-Petch strengthening due to smaller grain sizes and dislocation strengthening. At 700 °C, the coarser grained cast samples showed higher strength, indicating diffusion-controlled deformation processes to be operative.

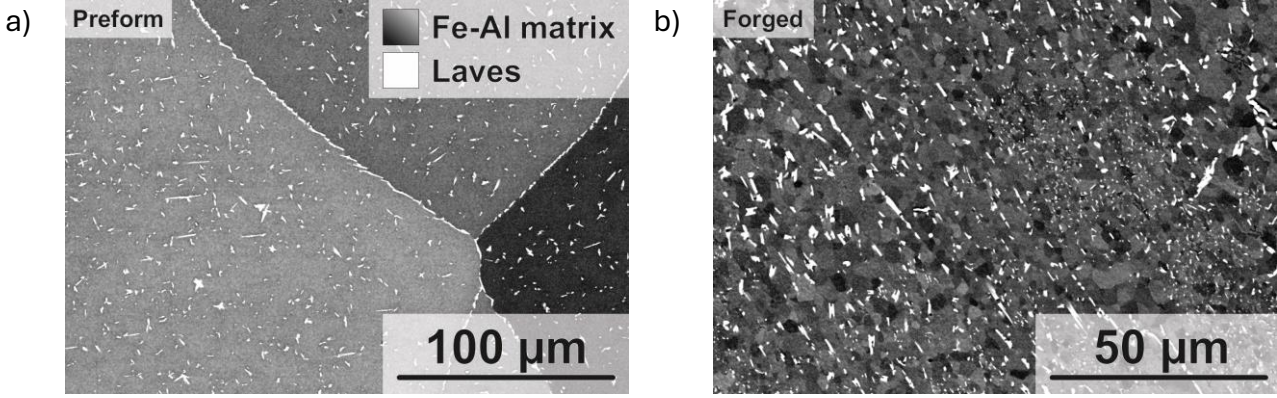


Fig. 1: SEM micrographs of the microstructures in the: b) as-cast and forged (900 °C) condition.

For the non-equilibrium as-cast condition, the creep behavior is complex as the transient Heusler phase leads to a significant strengthening in the early stages of creep, see Fig. 2a. Its dissolution and the formation of Laves phase as well as the occurrence of recrystallization, lead to the acceleration of creep in the later stages of creep. Long-term annealing treatments and forging result in steady-state creep behavior at higher creep rates as compared to Ta-containing Fe-Al and the as-cast condition at minimum creep rate, see Fig. 2b. The presentation will discuss the accompanied microstructural changes occurring during thermal exposure, quasistatic and creep testing at high temperatures as well as the comparison to Fe-Al-Ta alternatives. Furthermore, processing routes are envisaged to reduce the initial grain size of the Fe-Al matrix with fine distribution of the Laves phase.

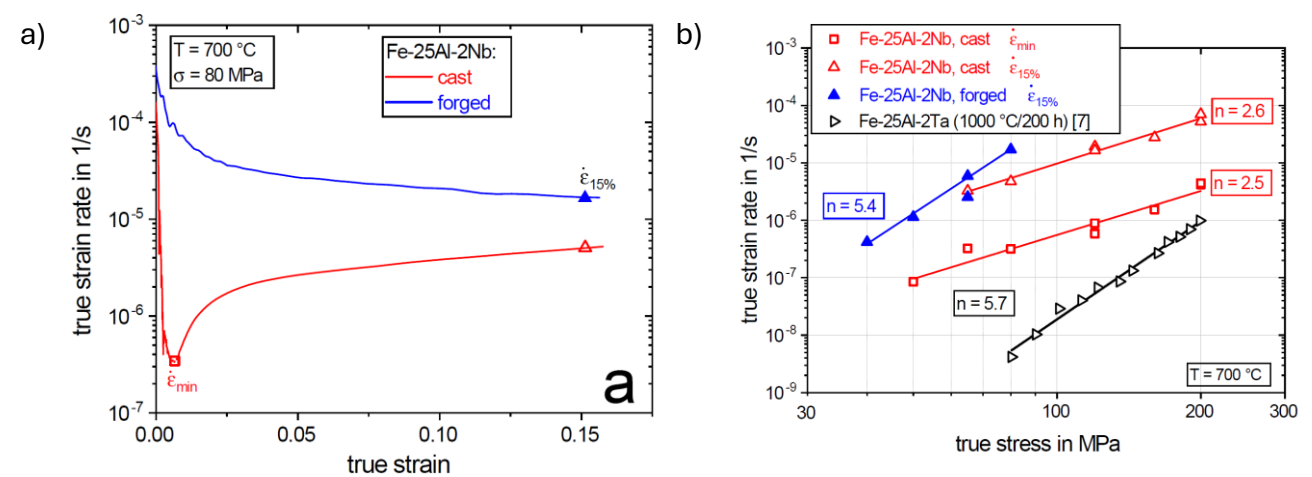


Fig. 2: Creep behavior of as-cast and forged samples; true strain rates as function of (a) true strain and (b) true stress.

Acknowledgement

The Pro-FeAl project was financially supported by the BMWK, grant no. 0324317E.

- [1] M. Palm, F. Stein, G. Dehm, Annual Review of Materials Research, **2019**, *49*, 297–326.
- [2] M. Palm, International Journal of Materials Research. 2009, 100, 277–287.
- [3] D.G. Morris, M.A. Muñoz-Morris, Advanced Engineering Materials. **2011**, *13*, 43–47.
- [4] A. Gedsun, S. Antonov, T.S. Prithiv, M. Palm, Scripta Materialia. 2023, 226, 115220.
- [5] P. Prokopčáková, M. Švec, M. Palm, International Journal of Materials Research. **2016**, *107*, 396–405.
- [6] S. Nizamoglu, A. Gedsun, Kauffmann, A., M. Ghosh, H. Michels, T. Groten, C. Schulz, C. Breuner, S. Seils, D. Schliephake, S. Laube, M. Palm, M. Heilmaier, Advanced Engineering Materials. **2024**, *26*, 2300148.

SCP 8.2:

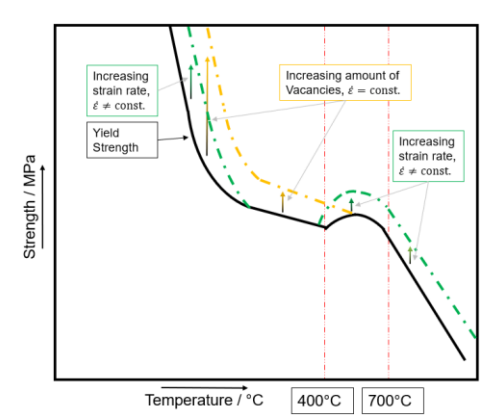
Re-Assessing the Mechanical Properties of Iron Aluminides: Deformation Behavior and Brittle-to-Ductile Transition

Jan Lars Riedel¹, Alexander Kauffmann^{1,2}, Stefan Guth¹, Marcel Münch¹, Sandipan Sen¹, Jung Soo Lee³, Anwesha Kanjilal³, James P. Best³, Frank Stein³, Martin Heilmaier¹

¹Institute for Applied Materials (IAM-WK), Karlsruhe Institute of Technology (KIT), Engelbert-Arnold-Straße 4, 76131 Karlsruhe, Germany, email: lars.riedel@kit.edu, alexander.kauffmann@kit.edu, stefan.guth@kit.edu, marcel.muench@kit.edu, sandipan.sen@kit.edu

Introduction

Iron aluminides (FeAI) provide outstanding corrosion and sulfidation resistance [1,2,3] as well as a high specific Young's modulus with low density compared to Ni-based superalloys. These make them attractive for the potential use in energy conversion systems, as coatings or aerospace connectors [1,2,3]. However, iron aluminides exhibit low strength and inherent brittleness at room temperature and below, but become ductile at temperatures beyond the brittle-to-ductile transition temperature (BDTT) [4]. Furthermore, their strength is strongly influenced by point defects, like impurity solute atoms or vacancies [5]. In addition, vacancies also influence the strength of iron aluminides at temperatures up to 500 °C, as depicted in Figure 1. As the temperature increases, thermally generated vacancies can lead to an increase in yield strength between 400 °C and 700 °C, typically referred to as yield strength anomaly. Besides that, the BDTT was found to strongly depend on the Al content with a steep increase between 42 and 45 at.% Al [4], see Figure 1b.



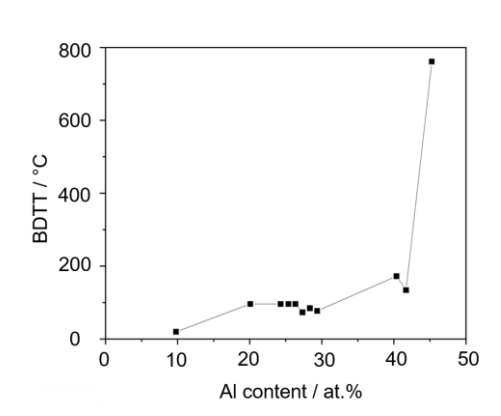


Fig. 1a: Yield Strength of iron aluminides, data Fig. 1b: BDTT vs. Al-content according to Ref. [4] adapted from Ref. [6,7]

Currently, literature does not provide appropriate datasets on yield strength, hardness and BDTT over the entire Al concentration range of B2-ordered iron aluminides. The present work aims at generating such dataset. The mockup of the dataset is focused on (i) keeping consistent impurity concentrations between the different alloys and (ii) establishing comparable heat treatment conditions. By utilizing compression tests in conjunction with three-point bending experiments in the temperature range from room temperature up to 700°C in vacuum, Vickers hardness testing and nanoindentation at room temperature, we aim at clarifying the following research questions:

² Chair Materials Science and Engineering (LWW), Institute for Materials (IM), Ruhr University Bochum (RUB), Universitätsstr. 150, 44780 Bochum, Germany

³ Max-Planck Institute for Sustainable Materials, Max-Planck-Straße 1, 40237 Düsseldorf, Germany, f.stein@mpie.de, js.lee@mpie.de

- 1. How does the testing temperature affect yield strength and strain hardening behavior of B2-ordered FeAl alloys and how is this related to the BDTT?
- 2. How are Vickers hardness and nanohardness affected by a) different compositions and b) different grain orientations in the investigated B2-ordered FeAl alloys? How do macroscopic yield and offset strength correlate to hardness measurements?

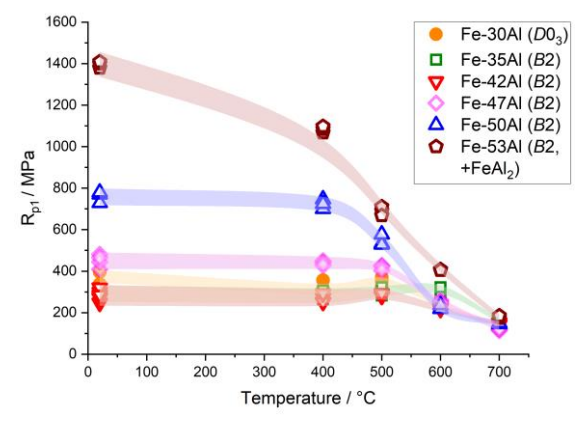
Materials and Methods

The alloys used in this study were cast to ingots in a vacuum induction from the same batches of raw material of Fe and Al to keep the impurity contents similar among the alloys. The ingots were cut to specimens with the nominal size of $(3 \times 3 \times 5)$ mm³ and (2×1) $2.5 \times 25) \text{ mm}^3$ for compression testing and three-point bending tests, respectively. The specimens were wire electric discharge machined (BA24 by Mitsubishi Electric, Tokio, Japan) and the surfaces were ground to remove the surface layer. For the two-stage heat treatment process, the samples were wrapped in Mo-foil and encapsulated into fused silica ampoules, which were five times evacuated and back-filled with Ar of 99.996% purity. The heat treatment consisted of homogenization at 1000°C for 48 h (except for Fe-53Al were the duration was extended to 168 h) followed by a low temperature heat treatment at 400°C for 120 h to remove excess vacancies, according to Refs. [8,9,10]. Each heat treatment was terminated by water quenching. Quasi-static compression and three-point bending tests were performed on an electro-mechanical Z100 universal testing machine supplied by ZwickRoell GmbH & Co. KG (Ulm, Germany) equipped with a three-zone vacuum furnace and temperature controller by Maytec GmbH (Singen, Germany). The initial engineering strain rate $\dot{\varepsilon}$ was set to $10^{-4}~{\rm s}^{-1}$. Hexagonal BN was used as a lubricant to reduce friction forces between samples' faces and the punches. The temperature of the sample was measured during testing with a type S thermocouple. The pressure inside the furnace was maintained below 10^{-5} mbar. The microhardness of the alloys was evaluated by using a Q10A+ semi-automatic Vickers hardness indenter from ATM Qness GmbH (Mammelzen, Germany) with a load of 1kg (HV1). A minimum number of 10 indents within a random selection of grains were evaluated according to DIN EIN ISO 6507. The minimum distance between two indents was at least three times the mean diagonal of the indents. Nanoindentation was performed on different grains of the specimens using a G200 nanoindenter by KLA Corporation (CA, USA). A diamond Berkovich indenter was used, reaching a maximum depth of 1 µm at a constant strain rate of $0.02 \, s^{-1}$ to minimize the indentation size effect. The lateral spacing between the indents of 25 µm was maintained to avoid the influence of adjacent indents. The analysis developed by Oliver and Pharr [11,12] was used on the unloading part of the loaddisplacement curves to determine the hardness and Young's modulus assuming 0.25 as the Poisson's ratio of the alloys.

Results and Discussion

Contrary to data reported in literature, we found the temperature dependent strengths of the alloys as depicted in Figure 2: (i) When varying the Al-content, the room temperature strength changes in a non-linear manner, displaying a minimum among the investigated alloys at 42 at.% Al and a maximum at 53 at.% Al. (ii) Only for 30 and 35 at.% Al, the yield strength anomaly was found, the other alloys do not show an increase in yield strength at intermediate temperatures. The strain hardening behavior for all alloys is different at room temperature as depicted in Figure 3. For up to 42 at.%, the alloys show pronounced

strain hardening during deformation at room temperature. If there are no other crack-initiating mechanisms active, these alloys could homogeneously deform without necking in tensile tests up to a minimum strain of 15%. In contrast, for an Al-content > 47 at.%, the alloys suffer from low strain hardening and hence, the potential for homogeneous plastic deformation is restricted. Further elaboration on this and the importance of the temperature dependent strength for the BDTT will be provided in the talk by analyzing the results from compression tests more thoroughly. The results are discussed based on the microstructural changes obtained by electron microscopy investigations.



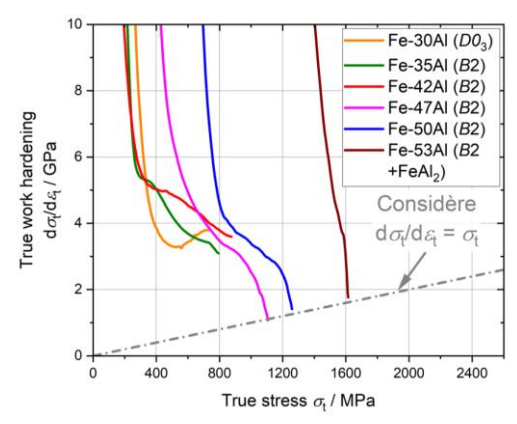


Fig. 2: The yield strength as a function of temperature of the investigated alloys from room temperature up to 700°C.

Fig. 3: The strain hardening of all alloys during compression testing at room temperature.

- [1] D. G. Morris and M. A. Muñoz-Morris, Adv. Eng. Mat. **2011**, 13, 43-47.
- [2] M. Palm, Int. J. Mat. Res. 2009, 100, 277-287.
- [3] S. C. Deevi, Prog. Mat. Sci. 2021, 118, 100769.
- [4] D. Risanti et al., Intermetallics. **2005**, 13, 1337-1342.
- [5] I. Baker and P. R. Munroe, Int. Mat. Rev. 1997, 42, 181-205.
- [6] M. Palm, F. Stein, and G. Dehm, Annu. Rev. Mater. Res. 2019, 49, 297-326.
- [7] I. Baker and Y. Yang, MSE A. 1997, 239-240, 181-205.
- [8] M. A. Morris, O. George, and D. G. Morris, MSE A. **1998**, 258, 99-107.
- [9] I. Baker et al., Acta Metall. Mater. **1995**, 43, 1723-1730.
- [10] M. Zhao et al., Acta Materialia. 2014, 64, 382-390.
- [11] W.C. Oliver and G.M. Pharr, J. Mat. Res. 1992, 7, 1564-1583.
- [12] W.C. Oliver and G.M. Pharr, J. Mat. Res. 2004, 19, 3-20.

SCP 8.3:

The effect of vacancy concentration on the micromechanical behaviour of B2 FeAl diffusion couples covering a wide range of compositions

Jung Soo Lee¹, Jan Lars Riedel², Alexander Kauffmann², Stefan Guth², Martin Heilmaier²,
Anwesha Kanjilal¹, Gerhard Dehm¹, James P. Best¹, Frank Stein¹

¹Max Planck Institute for Sustainable Materials, Max-Planck-Str. 1, 40237 Düsseldorf, Germany,
js.lee@mpie.de; a.kanjilal@mpie.de; dehm@mpie.de; j.best@mpie.de; f.stein@mpie.de

²Institute for Applied Materials (IAM-WK), Karlsruhe Institute of Technology (KIT), Engelbert Arnold Str.4,
76131 Karlsruhe, Germany, lars.riedel@kit.edu; alexander.kauffmann@kit.edu; Stefan.guth@kit.edu;
martin.heilmaier@kit.edu

Introduction

B2-ordered FeAl is a possible replacement of steels used in harsh environments owing to its excellent corrosion resistance, high wear resistance, and lower density [1]. This intermetallic phase possesses an unusually wide homogeneity range that extends from 23.5 to 53 at.% Al [1]. The strong off-stoichiometry is compensated by varying concentrations of defects such as vacancies and anti-site atoms [2,3]. It is well known that these defects, predominantly the vacancies whose concentration increases with increasing Al content, strongly affect the mechanical properties such as the yield stress and hardness [4,5]. Interestingly, literature data of single-phase B2 FeAl alloys with different Al contents indicate that the mechanical properties as a function of composition behave in an unexpected way showing an abrupt change near 40 at.% Al [6,7], which is not well understood. Since the vacancy concentration (and thus the mechanical properties) in a B2 FeAl alloy strongly depends on its thermal history, care must be taken when comparing the mechanical properties of different FeAl alloys. To mitigate this problem, diffusion couples were employed in this work to study the concentration dependence of the mechanical properties within a single specimen by small-scale mechanical testing along the concentration gradient that covers the entire B2 composition range. This ensures identical conditions (impurity level, surface condition, thermal history, and so on) for all compositions. Different levels of vacancy concentrations were set by a series of different heat treatments. With these differently heat-treated diffusion couples, nanoindentation and micropillar compression tests were then carried out to comprehensively investigate the mechanical response of B2 FeAl as a function of composition with different levels of vacancy concentration.

Materials and Methods

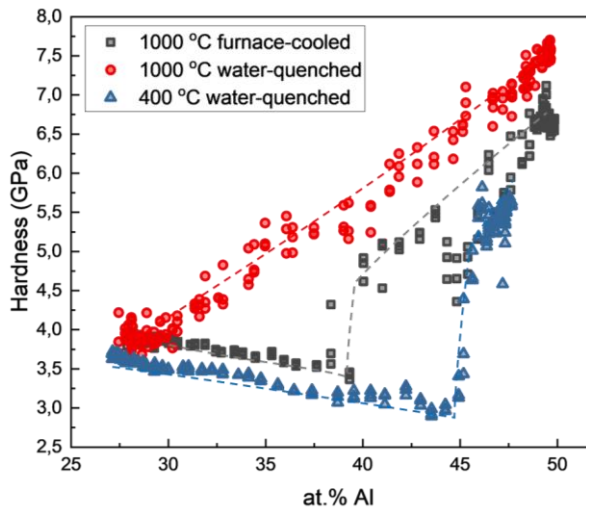
A series of binary FeAl alloys with nominal compositions of 30, 35, 42, 47, 50 and 53 at.% Al were produced using vacuum induction melting. Specimens with dimensions $10 \times 5 \times 5$ mm³ were cut from the as-cast alloys via electrical discharge machining. The surfaces of the specimens to be used as diffusion couple interface were ground and polished. Two specimens from different alloys (i.e. with different Al content) were then contacted and held by Mo clamps that were tightened using stainless steel screws and nuts. Mineral wool was placed between the specimens and the molybdenum discs to avoid interdiffusion. The setup was encapsulated in a silica glass ampoule under Ar atmosphere together with a Ti getter. After heat treatment at 1000 °C for 240 h, the ampoule was cooled to room temperature by switching off the furnace. The diffusion couples were then cut into thin slices with thickness of about 2 mm using a diamond wire saw. Some of the diffusion couple slices, wrapped in Ta foil, were again encapsulated in silica glass ampoules under Ar atmosphere and with Ti getter and were heat-treated at

400 and 1000 °C for 168 and 24 h, respectively, followed by water-quenching. The specimens for mechanical testing were prepared by polishing finally using 1 µm diamond suspension and then electropolishing using Struers A2 electrolyte. Nanoindentation was performed using a G200 device from KLA Corporation (formerly Agilent). Indentation was performed up to a maximum depth of 1 µm to minimize the indentation size effect, at a constant strain rate of 0.02 s⁻¹ using a diamond Berkovich indenter. The minimum lateral spacing between the indents was kept at 30 µm (that is more than 25 times the maximum indentation depth) to minimize the influence from adjacent indents. The Oliver-Pharr method [8] was used to determine the hardness and Young's modulus from the unloading curve, assuming a Poisson's ratio of 0.25 for FeAl. For micropillar compression, cylindrical micropillars with a top diameter of 2 µm and a diameter-to-height aspect ratio of approximately 1:2.5 were fabricated using a Ga⁺ ion Zeiss Auriga dual-beam focused ion beam-scanning electron microscope (FIB-SEM). Currents of 2 nA, and 120 pA at 30kV were used for coarse and fine milling of the pillars, respectively. The in situ micropillar compression tests were performed using a Bruker Hysitron PI 88 instrument inside a Zeiss Gemini 500 SEM. A conductive flat punch diamond indenter tip with 5 µm diameter was used for testing in a pseudo-displacement-controlled mode applying a nominal strain rate of 1.2×10^{-3} s⁻¹. The orientations of the grains were characterized by electron backscatter diffraction in a Zeiss Auriga dual-beam FIB-SEM equipped with an EDAX TSL-OIM system. The post-deformed micropillars were imaged and a Mathematica code was used for slip trace analysis. The compositions along the composition gradient were measured using a JEOL JXA-iSP100 electron probe microanalyzer. The positions of the measuring points were in close proximity to the nanoindents and micropillars to achieve a correct assignment between composition and mechanical values. The microhardness of individual alloys was measured using a Q10A+ semi-automatic Vickers hardness indenter from ATM Qness GmbH. A load of 1 kg (HV1) was used.

Results and Discussion

Fig. 1 shows the nanoindentation results as a function of composition measured at room temperature after different heat treatments. A continuous, approximately linear increase of the hardness is observed for the diffusion couple that was water-quenched from 1000 °C. A completely different behavior is obtained after slow cooling ("furnace cooling") from 1000 °C. In this case, the hardness first slightly decreases with increasing Al content before there is a sudden increase in the hardness at about 39 at.% Al. Finally, in the case of the diffusion couple that was heat-treated at 400 °C and then water-quenched, the sudden increase in the hardness is shifted to about 45 at.% Al. From the literature it is known that there is a direct relation between vacancy concentration and hardness [4]. Therefore, it is very likely that the observed changes in hardness are due to the presence of different concentrations of vacancies that vary with composition for different heat treatments and cooling. Previous studies have shown that a high number of thermal vacancies can be retained in B2 FeAl by quenching from 1000 °C, while a heat treatment at 400 °C for 120 h can annihilate a substantial amount of thermal vacancies [9]. The situation becomes even more complicated by the fact that, in addition to single vacancies, there are also divacancies and triple defects. Conclusions from these diffusion couple experiments and from comparisons with results from nano- and microhardness tests on individual B2 FeAl alloys will be presented in the talk. The slip trace analysis of post-deformed micropillars of furnace-cooled diffusion couple showed that families of $\{110\}\langle \bar{1}11\rangle$ slip systems activate at room temperature despite the higher

Schmid factor of $\{11\overline{2}\}\langle111\rangle$ and $\{12\overline{3}\}\langle111\rangle$ slip systems, see Fig. 2. This topic will also be discussed in the talk.



1 μm

Fig. 1: Hardness as function of composition in single-phase B2 FeAl as obtained from nanoindentation of diffusion couples with three different heat treatment conditions: (i) 1000 °C/240 h/furnace-cooled, (ii) 1000 °C/24 h/water-quenched, and (iii) 400 °C/168 h/water-quenched. Dotted lines are drawn for guidance.

Fig. 2: SEM image of a post-deformed B2 FeAl micropillar on the 1000 °C/240 h/furnace-cooled diffusion couple, showing the active $\{110\}\langle\bar{1}11\rangle$ slip systems marked by yellow lines.

- [1] M. Palm, F. Stein, G. Dehm, Annual Review of Materials Research. 2019, 49, 297-326.
- [2] T. Haraguchi, F. Hori, R. Oshima, M. Kogachi, Intermetallics. 2001, 9, 763-770.
- [3] R. Wang, Y. Zhao, Z. Li, H. Chen, X. Tao, Y. Ouyang, Materials Research Express. **2018**, 5, 026512.
- [4] Y.A. Chang, L.M. Pike, C.T. Liu, A.R. Bilbrey, D.S. Stone, Intermetallics. **1993**, 1, 107-115.
- [5] E.P. George, I. Baker, Philosophical Magazine A. 1998, 77, 3, 737-750.
- [6] P. Nagpal, I. Baker, Metallurgical Transactions A. 1990, 21, 2281-2282.
- [7] D. Risanti, J. Deges, L. Falat, S. Kobayashi, J. Konrad, M. Palm, B. Pöter, A. Schneider, C. Stallybrass, F. Stein, Intermetallics. **2005**, 13, 12, 1337-1342.
- [8] W.C. Oliver, G.M. Pharr, Journal of Materials Research. 1992, 7, 6, 1564-1583.
- [9] J.L. Jordon, S.C. Deevi, Intermetallics. **2006**, 11, 6, 507-528.

SCP 8.4:

The structure and properties of Fe-28Al powdered iron aluminide strengthened by the MeB boride phase produced by DPF technology under dynamic recrystallization conditions

Oleksandr Tolochyn, Oleksandra Tolochyna, Yurii Podrezov, Gennadii Bagliuk Frantsevich Institute for Problems of Materials Science National Academy of Science of Ukraine, Kyiv 03142, Ukraine, o.tolochyn@ipms.kyiv.ua, o.tolochyna@ipms.kyiv.ua, y.podrezov@ipms.kyiv.ua, g.bagliuk@ipms.kyiv.ua

Introduction

Fe₃Al-based intermetallic alloys have long attracted attention due to their low cost and promising mechanical and physical properties. Evolving performance demands have shifted focus toward refining their structure through innovative processing methods. Given the thermal instability of the ordered D0₃ phase, the more stable A2 phase is increasingly favoured at elevated temperatures. Mechanical properties are enhanced via thermomechanical processing, microalloying, and dispersion strengthening. Modern powder metallurgy techniques—especially direct powder forging (DPF)—enable nearnet-shape production and improved structural dispersion. Current research aims to significantly boost heat resistance by integrating microstructural refinement, alloying and in situ formation of ultrafine particles at service temperatures around 700°C.

Materials and Methods

Iron aluminide Fe-28 at.% Al reinforced with boride particles was produced using a two-stage technological scheme. In the first stage, the initial charge consisting of iron powder (particle size 150 μm), aluminum powder (particle size 70 μm), and one of the borides—Ni $_3$ B, CrB $_2$, or B $_4$ C—at the appropriate concentration was mixed. The resulting powder mixture was pressed in air at room temperature and sintered in vacuum at 1050°C, forming an A2 phase reinforced with boride particles. In the second stage, the synthesized samples were crushed mechanically into powder and further dispersed by milling in a planetary mill. The milled powders of the synthesized Fe-28Al-MeB iron aluminide were consolidated using a novel DPF scheme at 1150°C, as described in [1]. This multi-pass deformation processing scheme was proposed to achieve complete pore closure and to activate the mechanism of dynamic recrystallization (DRX) in the dispersed iron aluminide powders[2]. The synthesized heat-resistant A2 phase prevents oxidation during heating and thermomechanical processing stages.

Results and Discussion

The application of severe plastic deformation methods during the powder milling stage and thermomechanical treatment under dynamic recrystallization conditions enabled the development of iron aluminide with a fine-grained intermetallic matrix structure reinforced by dispersed particles. After triple forging at 1150°C, nearly all investigated boride-reinforced iron aluminide samples exhibited a fine-grained structure with a grain size of 3–5 µm (Fig. 1). No continuous films were observed along interparticle boundaries; instead, the boundaries were decorated with nanoscale oxide and boride particles. Severe deformation processing during powder milling and triple forging led to a certain degree of structural anisotropy, which significantly decreased with an increase in the reinforcing phase content. The chemical composition of the matrix is close to Fe₃Al, although the solid solution contains a small amount (~1%) of Cr/Ni. This potential

solubility should be considered, as alloying the matrix with chromium or nickel can alter the deformation mechanisms, influencing ductility and high-temperature strength.

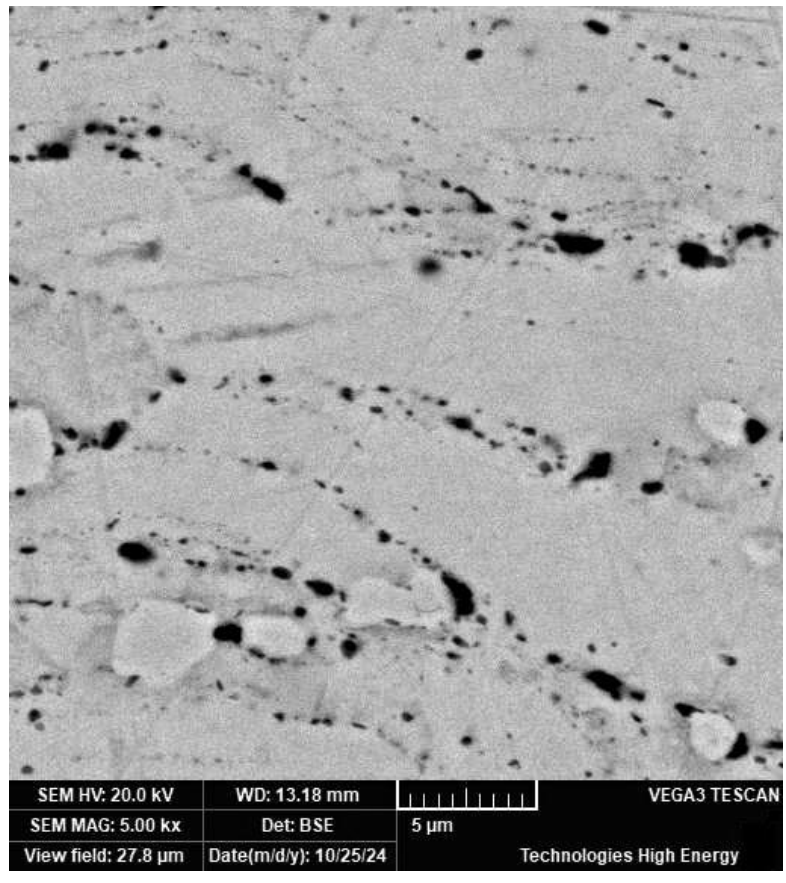


Fig. 1: Microstructure of boride-phase-reinforced iron aluminide produced using the DPF triple forging scheme at 1150°C (Fe-28Al-0.3CrB₂).

The results of room-temperature bend tests for the studied alloys (Table 1) show that structure refinement nearly doubles the mechanical properties compared to other thermomechanical processing methods for materials of this class. While strength values are comparable across all types of introduced particles, samples reinforced with boron carbide show significantly lower ductility and crack resistance compared to those with nickel and chromium borides. Excessive boride content negatively affects the mechanical properties at room temperature.

Table 1: Mechanical properties of boride-phase-reinforced iron aluminide Fe-28 at.% Al

Type of reinforcing	Content of reinforcing phase		σ _{0,2} , MPa	σ _{bend,} MPa	$\epsilon_{ ext{plast}}, \%$	K₁₀, MPa∙m ^{0,5}		
phase	vol.%	ат.%	Triple forging at 1150°C					
Ni₃B	0.82	0.26	1167	1646	0.64	39.7		
Ni₃B	2.46	0.78	1206	1481	1.13	42.8		
CrB ₂	0.59	0.3	1441	2029	2.81	48.6		
CrB ₂	2.93	1.5	1213	1676	1.47	35.6		
B ₄ C	0.82	0.25	1490	1508	0.22	34.5		
$\sigma_{0,2}$ –yield strength; σ_{bend} – strength ; ϵ_{plast} – strain, K_{1c} – fracture toughness								

Table 2: Effect of temperature on yield strength in compression test of	of Fe-28Al-MeB alloy
---	----------------------

Type of reinforci	Content of	Yield strength σ _{0,2} MPa Test temperature T _{test} , °C					
ng phase	reinforcing phase (at.%)	20	400	500	600	700	
Ni₃B	0.78	1136	808	754	672	482	
CrB ₂	0.3	1176	808		647	454	
CrB ₂	1.5	995	826	783	656	453	
B ₄ C	0.25	888	932	714	789	378	

Table 2 presents the results of compression tests of the studied alloys at elevated temperatures. At all test temperatures, the alloys demonstrate exceptionally high yield strength. For instance, at 700°C, the yield strength $\sigma_{0\cdot2}$ reaches approximately 450 MPa. TEM studies (Fig. 2) allowed the assessment of structural element sizes that contribute to strengthening at both low and elevated temperatures. The yield strength values $\sigma_{0\cdot2}$, calculated based on structural features using the Hall–Petch and Orowan mechanisms, show good agreement with experimental results.

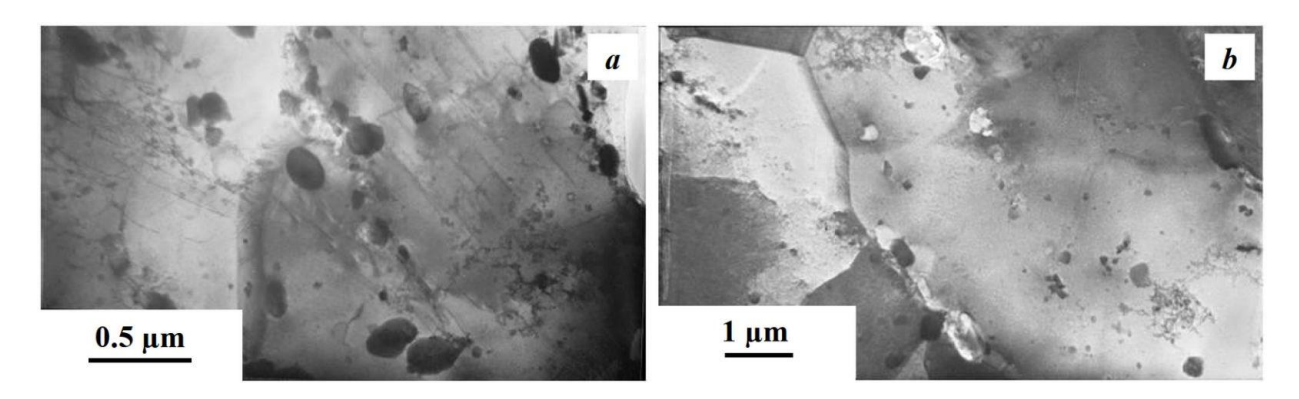


Fig. 2: TEM images of the Fe-28Al-0.78 CrB_2 alloy: a – interparticle boundaries decorated with boride particles; b – cluster-free boundaries formed through dynamic recrystallization.

The developed triple forging processing scheme, in combination with the optimized amount of strengthening boride phase, enables the production of iron aluminides with mechanical properties that exceed those of similar materials in this class over a wide temperature range.

Acknowledgment

The present work was financially supported by the National Research Foundation of Ukraine (Grant No. 2021.01/0278)

- [1] O. Tolochyn, O. Tolochyna, G. Bagliuk, Y. Yevych, V. Danylenko, Y. Podrezov. Intermetallics. **2024**, 175, 108537.
- [2] O.I. Tolochyn, O.V. Tolochyna, Yu.M. Podrezov, V.I. Danylenko, G.A. Bagliuk. JOM. **2025**, 77, 1940–1953

SCP 9.2:

Effects of Aluminium and Tantalum addition on the mechanical behaviour of multicomponent alloys

Gajendra Patel, Rajesh Korla, Mayur Vaidya

Department of Materials Science and Metallurgical Engineering, Indian Institute of Technology Hyderabad

Introduction

Despite the monumental progress made in expanding the high-temperature operating capability of superalloys, the quest for materials with better structural properties for high temperature applications (such as jet propulsion, aircraft engines and industrial gas turbines) has given space for high-temperature materials development. One of the important phase combinations in high-temperature structural alloys is γ/γ' microstructure, which consists of Ni-rich solid solution (γ) with face-centred cubic (FCC) crystal structure and is strengthened by an L1₂-ordered intermetallic phase(γ '). Conventional Ni-based superalloys have ~8 to 12 alloying elements and a γ/γ' microstructure, which contributes to the synergistic combination of strength and degradation resistance at temperatures around ~1100 °C [1]. In the past two decades, multi-principal element alloys (MPEAs) consisting of three to five principal elements have gained increasing interest as they offer multi-dimensional composition proportions of alloy bases for exploration. The most investigated FCC single-phase MPEAs are the CoCrNi-based alloys (such as CoCrNi and CoCrNi Al/Mo/Ta/W/Nb), which are regarded as model MPEAs and promising engineering materials due to their excellent mechanical properties, fatigue and fracture toughness [2]. However, it doesn't show promising ductility and fracture strength at elevated temperatures, which limits this alloy's ability to be applied for high-temperature structural applications [3]. Equiatomic CoCrNi-based MPEAs limit the solid solubility limit of alloying elements and excessive alloying results in the formation of brittle phases like B2 phase, μ phase and σ phase, causing the deterioration of the plasticity during the application. Hence, a non-equiatomic strategy was proposed by X. Huang et al., based on the element composition ratio, thereby increasing the solid solubility of the matrix and significantly enhancing the volume fraction of the precipitate [4]. Alloying with refractory solid solution and precipitationstrengthening elements (such as Ta, Nb, Mo, W, etc.) generally enhances the hightemperature strength and ductility of the alloys. Chen et.al. reported that adding Ta can improve the high-temperature structural stability of the L1₂ precipitate [5]. However, the co-addition of Al and Ta to non-equiatomic CoCrNi-based alloy has not been reported yet.

Materials and Methods

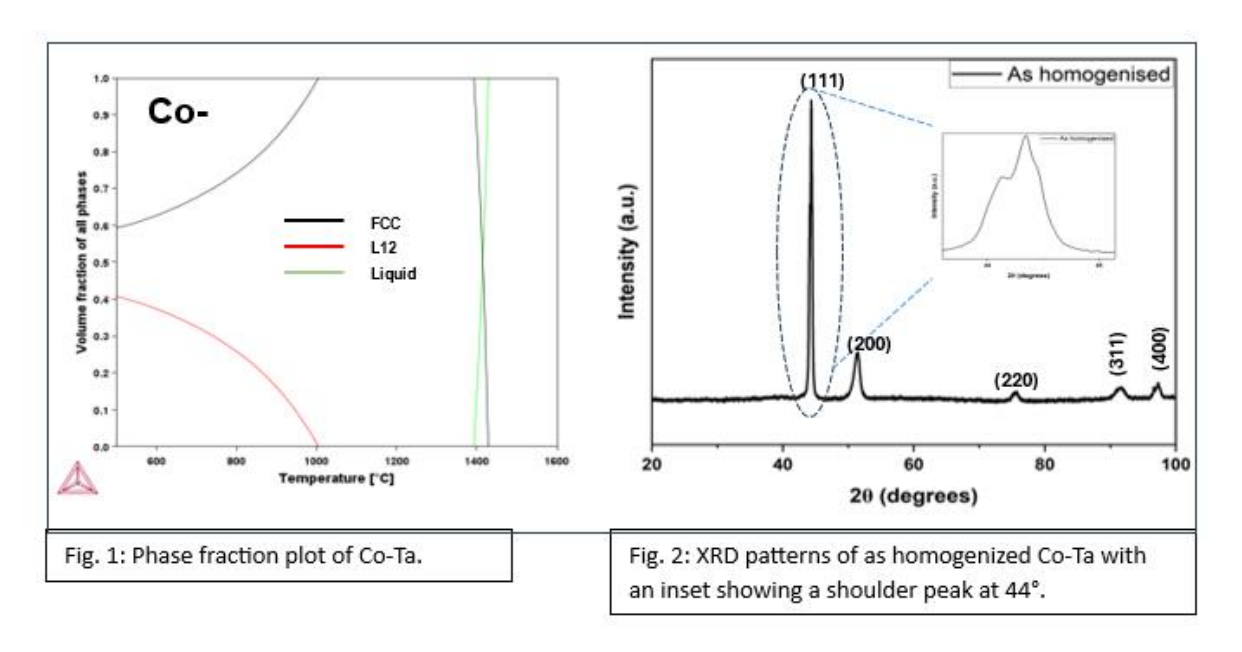
With the help of thermodynamic calculations, we developed non-equiatomic CoCrNi-based alloys [(Co-Cr-Ni)_{100-(x+y)} Al_xTa_y (Co-Ta in short) using phase separation, aiming to create an alloy matrix with significant fraction improvement of ordered L1₂ nanoprecipitates. The alloys were prepared by using a vacuum arc melting furnace and repeatedly melted at least five times under a Ti-gettered high-purity Ar atmosphere. To chemically homogenise the as-cast alloy, the ingots were homogenised at 1200 °C for 24 h and followed by water quenching. The homogenised alloys were then heat-treated at 800°C, 900°C and 1000°C for 24 h each, followed by water quenching to obtain the desired precipitates. The preliminary characterization was done to detect nominal composition and the secondary phases/ordered precipitates by employing X-ray diffraction (XRD), Scanning Electron Microscope (SEM) using Secondary electron (SE),

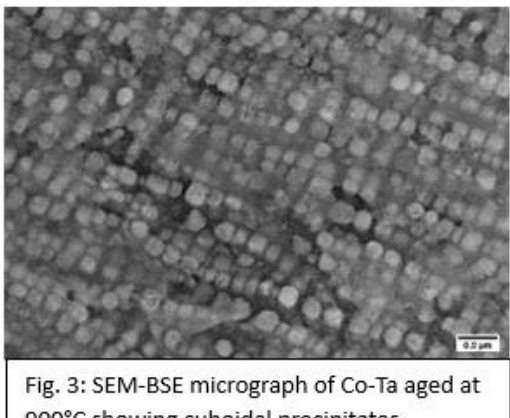
Backscattered electron (BSE), Electron Backscatter diffraction (EBSD) modes as well as Energy Dispersive spectroscopy (EDS) and Transmission Electron Microscope (TEM) using Scanning-transmission electron microscope (STEM-EDS) and High-resolution transmission electron microscope (HRTEM) modes. Phase stability experiments and thermomechanical processing will be analysed by performing heat treatment in the temperature window for the solution heat treatment and ageing temperatures. The mechanical properties were evaluated using microhardness and tensile tests.

Results and Discussion

In this work, the phase fraction plot was calculated using Thermo-Calc software 2023a in combination with the TCHEA6 database. A non-equiatomic Co-Cr-Ni base was used for alloy optimisation. To introduce the L1₂ phase (γ') , γ' -forming elements such as Al and Ta were added to the base alloy. γ' V_f exceeding 50 pct at all ageing temperatures (800°C to 1000°C). The thermodynamic calculations of equilibrium phases in Co-Ta are shown in Figure 1. The presence of superlattice peaks confirms L1₂ phase (inset of Figure 2).

The SEM microstructure revealed the γ' particles are uniformly distributed in the FCC matrix (γ) . The γ' particles are both spherical and cuboidal in shape, depending upon the ageing temperature, having an average size of 78 ± 11 nm in the sample aged at 900°C (Figure 3).





900°C showing cuboidal precipitates.

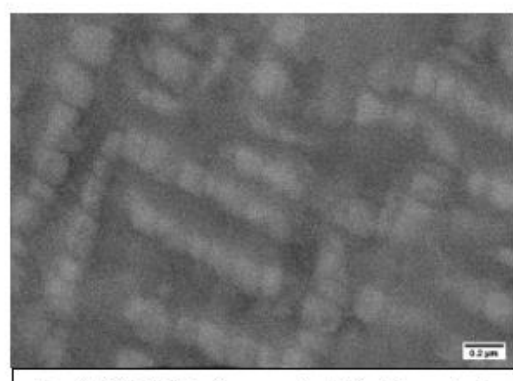


Fig. 4: SEM-BSE micrograph of Co-Ta aged at 1000°C showing cuboidal precipitates.

- [1] K. Kawagishi, H. Harada, A. Sato, A. Sato, T. Kobayashi, The Journal of The Minerals, Metals & Materials Society. **2006**, Volume 58, 43-46.
- [2] K. Lu, A. Chauhan, D. Litvinov, M. Schneider, G. Laplanche, J. Aktaa, Journal of The Mechanics and Physics of Solids. **2023**, Volume 180, 105419.
- [3] M. Zhang, E.P. George, J.C. Gibeling, Acta Materialia. 2021, Volume 218, 117181.
- [4] X. Huang, L. Huang, H. Peng, Y. Liu, B. Liu, S. Li, Scripta Materialia. **2021**, Volume 200, 113898.
- [2] Z. Chen, K. Kishida, H. Inui, M. Heilmaier, U. Glatzel, G. Eggeler, Acta Materialia. **2022**, Volume 238, 118224.

SCP 9.3:

Precipitation in Ti-Fe-Mo-Al alloys

Annie M. L. Andersson¹, Rosie F. L. Mellor¹, James M. Hogg¹, Hannah C. Cole¹, Giulio I. Lampronti¹, Nicole Church¹, Owain S. Houghton¹, Nicholas G. Jones¹, and Howard J. Stone¹

¹Department of Materials Science & Metallurgy, 27 Charles Babbage Road, University of Cambridge, Cambridge, UK

Introduction

Ti-rich alloys from the Ti-Fe binary system offer the prospect of ductile A2 matrices with intragranular dispersions of intermetallic B2 precipitates. Binary alloys of this type have shown impressive strengths both in the as-cast state [1] and after solution treatment and ageing [2], but the matrix A2 phase is often unstable and breaks down into embrittling A3 and ω phases [3]. Mo additions stabilise the A2 phase and prevent the microstructural break-down [4], and Al additions can allow for lattice misfit adjustment between precipitates and matrix [5]. While the Ti-Fe-Mo and Ti-Fe-Al ternaries have been studied, few studies have been performed on alloys compositions within the quaternary Ti-Fe-Mo-Al system.

In this work, the microstructures of Ti-Fe-Mo-Al alloys with 70 at.% Ti were studied following thermal exposure at 600°C, 800°C, and 1000°C to determine equilibrium phases. The alloy with the greatest stability range of the A2+B2 microstructure was studied further to ascertain the effect of different cooling rates on the competition between discontinuous and continuous precipitation.

Materials and Methods

Alloys of compositions Ti-20Fe-5Mo-5Al, Ti-15Fe-10Mo-5Al, Ti-15Fe-5Mo-5Al, Ti-10Fe-15Mo-5Al, Ti-10Fe-10Mo-10Al, and Ti-10Fe-5Mo-15Al at.% were predicted to have A2+B2 phase equilibria at 800°C using Thermo-Calc 2022b [6]. Ingots of each of these alloys were arc-melted, solution treated at 1115°C under Ar for 50h, then aged at 600°C, 800°C, and 1000°C, respectively, for 1000h under Ar. Samples of solution heat treated Ti-20Fe-5Mo-5Al were also raised back to 1115°C in a DIL805 dilatometer and quenched to room temperature at 40°C s⁻¹, 10°C s⁻¹, 1°C s⁻¹, 0.1°C s⁻¹, and 0.01°C s⁻¹. Samples were examined using Cu-Kα X-ray diffraction (XRD) and back-scattered electron (BSE) imaging. Synchrotron X-ray diffraction (s-XRD) data from the Ti-20Fe-5Mo-5Al samples cooled at controlled rates were acquired using the ID22 beamline at the European Synchrotron Radiation Facility. Additional phase characterization was also performed on the sample cooled at 0.1°C s⁻¹ by transmission electron microscopy (TEM).

Results and Discussion

The equilibrium phases predicted at 600°C, 800°C, and 1000°C by Thermo-Calc [6] for the 70 at.% Ti pseudo-ternary phase diagrams are shown in Fig. 1. All alloy compositions investigated were predicted to lie in the A2+B2 two-phase field at 800°C. However, the XRD data indicated only two alloys (Ti-20Fe-5Mo-5Al and Ti-15Fe-10Mo-5Al) were A2+B2, with the low Fe, low Al alloys being single-phase A2 and the high Al alloys having an additional deleterious D0₁₉ phase. This is indicated by the symbols used in Fig. 1. At 1000°C, only Ti-20Fe-5Mo-5Al had detectable B2, with the other compositions being single-phase A2, and at 600°C, either or both of the A3 and D0₁₉ phases were present in all compositions. These phase identifications were consistent with the BSE imaging, which showed bright B2 precipitates of varying morphology, depending on composition and temperature, and dark precipitates indicative of an Al-rich hexagonal phase. As examples, the aged Ti-20Fe-5Mo-5Al images are in the top of Fig. 2. This shows A2+B2

microstructures are less stable than thermodynamic modelling suggests, and that the A3, D0₁₉, and single-phase A2 regions extend further than predicted.In Ti-20Fe-5Mo-5Al after the 800°C age, the B2 precipitate size distribution was bimodal, with fine and coarse precipitates, the latter having a precipitate-free zone, see Fig. 2. It is suggested that the coarse precipitates formed during the long-term age, giving rise to a solute-depleted zone, and the fine precipitates formed in the remaining matrix during the quench as the solubility of Fe in A2 decreased. This indicates that cooling rates strongly impact the microstructure of Ti-20Fe-5Mo-5Al, hence it was chosen for controlled cooling tests to examine precipitation behaviour. The temperature profiles experienced are in the middle of Fig. 2, and the resulting BSE micrographs at the bottom. A high cooling rate (40°C s⁻¹) led to single-phase A2, confirmed by s-XRD. Cooling at 10°C s⁻¹ and 1°C s⁻¹ led to discontinuous B2 formation, seen in Fig. 2 and confirmed by A2 peak splitting in s-XRD as the matrix composition varied discontinuously. Cooling at 0.01°C s⁻¹ led to a microstructure most like long-term ages, with precipitates consistent with continuous nucleation and growth. Notably, cooling at 0.1°C s⁻¹ led to two types of precipitates, continuous and discontinuous, seen in Fig. 2. Both were structurally identified as B2 using TEM. This suggests a transition between mechanisms, where partial continuous precipitation occurs at high temperature, but subsequent cooling hinders bulk diffusion, changing the mechanism to discontinuous precipitation [7]. As a result, discontinuous precipitation, which relies on grain-boundary diffusion, occurred in the remaining supersaturated matrix, but the reduced supersaturation in the continuously precipitated regions hindered overgrowth and resulted in the dual morphology microstructure [8].

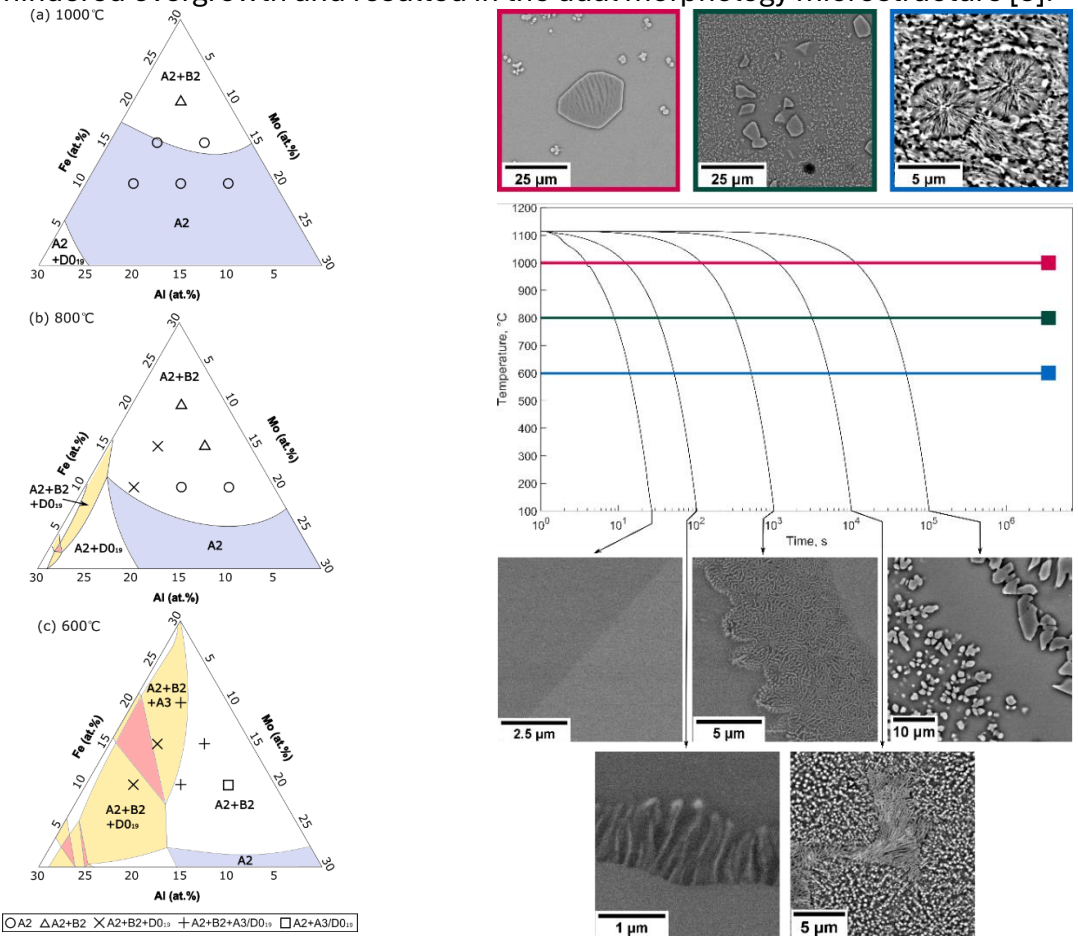


Fig. 1: Pseudoternary phase diagram predicted using Thermo-Calc [6], tested compositions, and phases seen.

Fig. 2: Microstructures of Ti-20Fe-5Mo-5Al after ageing (above) and controlled cooling at varying rates (below).

In addition to temperature, the concentration of the slow-diffusing Mo could be a key factor in the competition between these precipitation mechanisms. After the long-term age at 800°C, Ti-15Fe-10Mo-5Al was the only alloy with lamellar and spherical B2. This sample had the highest Mo concentration of the B2 forming alloys at 800°C, and as B2 has low Mo solubility, it would require more bulk Mo diffusion to form continuous B2. If, at 800°C, the rate of Mo bulk diffusion is low, this additional need for Mo transport may stop continuous precipitation, but the grain-boundary Mo diffusion may still be sufficient to mediate discontinuous B2 precipitation. A 10% Mo concentration may lie on the borderline between the two regimes at 800°C, hence leading to both of the morphologies. This would also explain the morphology variation seen in Ti-Fe-Mo with Mo content seen by Knowles et al. [5].

In conclusion, this work has investigated the phases present in Ti-rich quaternary Ti-Fe-Mo-Al alloys. The A2+B2 two-phase region was found to be smaller than thermodynamic modelling suggested but remained sufficient to allow future alloy design. The precipitation mechanisms in Ti-20Fe-5Mo-5Al upon varying the cooling rate were also investigated, which identified discontinuous precipitation at intermediate cooling rates. This putatively explains the origin of lamellar microstructures reported in similar alloys. The Mo concentration in the alloys has been identified as a possible factor contributing to the transition from continuous to discontinuous precipitation.

- [1] D.V. Louzguine-Luzgin, Materials Transactions. 2018, 59, 1537-1544.
- [2] R.D. Jones, A.J. Knowles, W.J. Clegg, Scripta Materialia. **2021**, *200*, 113905.
- [3] A.J. Knowles, T.S. Jun, A. Bhowmik, N.G. Jones, T.B. Britton, F. Giuliani, H.J. Stone, D. Dye, Scripta Materialia. **2017**, *140*, 71-75.
- [4] R.F.L. Mellor, P. Vacek, N.G. Jones, P.A. Midgley, H.J. Stone, Scripta Materialia. **2023**, 232, 115476.
- [5] A.J. Knowles, N.G. Jones, C.N. Jones, H.J. Stone, in: Proceedings of the 13th World Conference on Titanium. **2016**, 1229–1236.
- [6] J.O. Andersson, T. Helander, L. Höglund, P. Shi, B. Sundman, Calphad. **2002**, *26*, 273-312.
- [7] D. Duly, J.P. Simon, Y. Brechet, Acta Metallurgica et Materialia. 1995, 43, 101-106.
- [8] J.D. Robson, Acta Materialia. **2013**, *61*, 7781-7790.

SCP 9.4:

Mechanical Properties and Deformation Mechanism of Additively Manufactured NiAl-CrMo in-situ Composites

Jan Vollhüter¹, Andreas Bezold², Katharina Titz³, Benjamin Wahlmann³, Carolin Körner³, Michael J. Mills², Steffen Neumeier¹, Mathias Göken¹

¹Friedrich-Alexander-Universität Erlangen, Materials and Engineering Institute I, Erlangen, Germany, jan.vollhueter@fau.de, steffen.neumeier@fau.de, mathias.goeken@fau.de

²Ohio State University, Center for Electron Microscopy and Analysis, Columbus, USA, Bezold.8@osu.edu,

Mills.108@osu.edu ³Friedrich-Alexander-Universität Erlangen, Materials Science and Engineering for Metals, Erlangen, Germany,

katharina.titz@fau.de, benjamin.wahlmann@fau.de, carolin.koerner@fau.de

Introduction

NiAl-CrMo in-situ composites have demonstrated an excellent combination of mechanical properties at both room temperature and elevated temperatures, significantly outperforming their single-phase counterparts. Optimal mechanical properties have been achieved through directional solidification, where the well-aligned lamellar or rod-like reinforcement phase significantly enhances both room-temperature fracture toughness and high-temperature strength. This well aligned morphology of the CrMo reinforcement phase leads to significant anisotropic mechanical properties in fracture toughness as well as the expected creep strength [1]

Using electron beam powder bed fusion (PBF-EB), a nanostructured microstructure with a high interface density is formed, resulting in improved yield strength across a wide temperature range compared to conventionally cast NiAl-CrMo composites [2]. By optimizing the process parameters to promote an equiaxed microstructure, additively manufactured specimens exhibit near-isotropic mechanical properties under creep conditions [2]. To achieve a perfect eutectic microstructure, a new alloy composition (Ni30.6Al36Cr31.4Mo2) has been developed, featuring a significantly reduced solidification interval, which is more suitable for additive manufacturing [3]. However, during the in-situ heat treatment during the PBF-EB process, discontinuous coarsening occurs, transforming the "as-built" interconnected microstructure in a rod-like morphology of the CrMo reinforcement phase. This microstructural evolution in the as-built samples is expected to enhance the room temperature ductility and fracture toughness due to the increased interphase spacing.

Materials and Methods

For the additive manufacturing of NiAl–CrMo in-situ composites, gas-atomized powder supplied by Praxair Surface Technologies GmbH is utilized. The powder is processed via electron beam powder bed fusion (PBF-EB) using an Arcam A2 system (GE Additive; formerly Arcam AB, Mölndal, Sweden). Two distinct parameter sets are employed to fabricate cuboidal specimens with dimensions of 15 × 15 × 20 mm³. Additionally, samples with the composition of the B2 matrix and the A2 precipitates, respectively, are produced by arc melting from pure elements under argon atmosphere. The composition of both phases was determined by atom probe tomography measurements conducted on a LEAP 4000X HR (Cameca) operated in Laser mode with a pulse rate of 200 kHz and a Laser energy of 50 pA at a temperature of 44 K and a detection rate of 1 %. To evaluate the mechanical properties and a subsequent analysis of the defect structure, cylindrical samples with a height of 4.5 mm and a diameter of 3 mm are machined from bulk

specimens using electric discharge machining (EDM). Room temperature compression tests are performed using an Instron 4505 testing machine at a constant strain rate of $10^{-4} \, \mathrm{s^{-1}}$. Both tests to fracture and interrupted tests at 2%, 5%, 10%, and 15% plastic strain are conducted to study the evolution of defect structures during deformation. Electron backscatter diffraction (EBSD) measurements are carried out using a Zeiss Crossbeam 540 dual-beam system equipped with a Nordlys detector (Oxford Instruments). Site-specific FIB foils are extracted from regions of interest and prepared for transmission electron microscopy (TEM) using standard lift-out and milling procedures within the same SEM-FIB. TEM investigations are conducted on a Philips CM200 operated under two-beam conditions at an acceleration voltage of 200 kV. High-resolution scanning transmission electron microscopy (HRSTEM) analyses are performed on a Thermo Scientific Themis Z, also operated at 200 kV.

Results and Discussion

The room temperature strength of the PBF-EB manufactured is significantly higher than the arc-melted specimens and the directional solidified ones. Due to the significant refinement of the microstructure, an increase in yield strength of 200 MPa in comparison to conventionally cast specimens can be reported (see Fig. 1(a)). The work hardening of the additively manufactured specimens (see Fig. 1 (b)) is comparable with the cast ones. The defect structure of the PBF-EB manufactured specimens consists after a plastic deformation of 2 % of shear bands in the interconnected as built microstructure as well as the discontinuously coarsened regions. Even though slip transfer between the intermetallic NiAl matrix and the bcc based CrMo precipitation phase has been observed, most dislocations in the matrix seem only to be connected to the interfacial dislocation network, while not shearing the bcc precipitates. The character of the dislocations in the matrix and the precipitates will be discussed, as well as the influence of the interfacial dislocation network. The analysis of bulk single phase samples with the respective composition of the matrix and the bcc-based precipitates will give more insight into the deformation behavior of the respective phases at room temperature. After a plastic deformation of 10 %, a significant dislocation density has been formed. While the dislocation density in the CrMo precipitates increased slightly, the NiAl matrix shows a significant increasement, featuring pronounced slip bands with an extremely high dislocation density (see Fig 1(c)). On the macroscopic scale, no cracking is observed after the plastic deformation of 10 %, while a stress close to 2 GPa is reached.

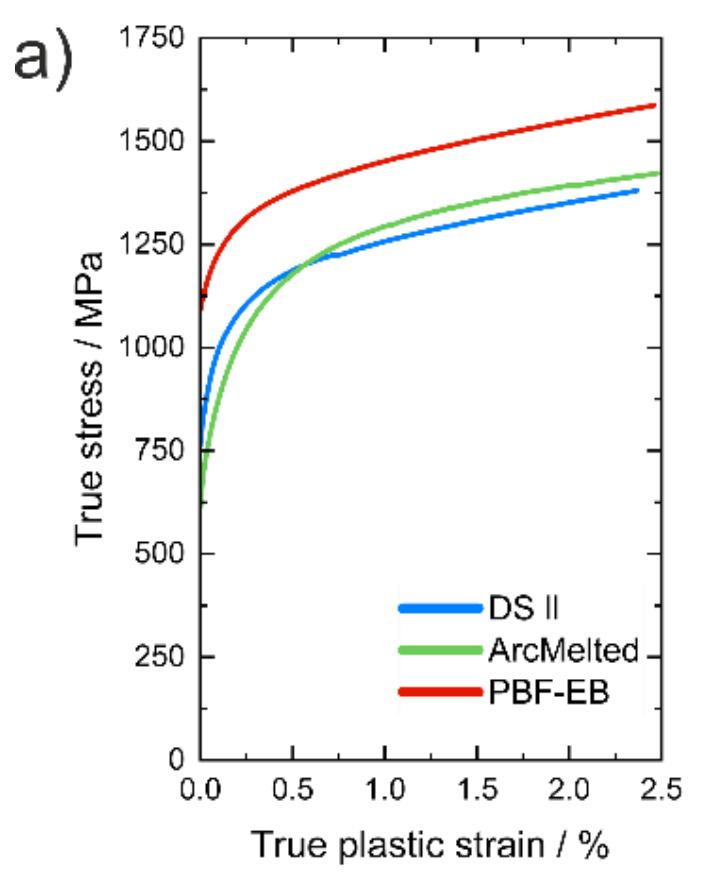
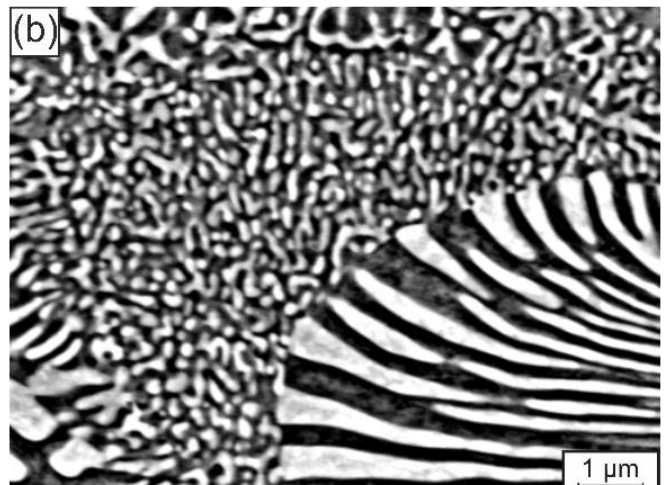
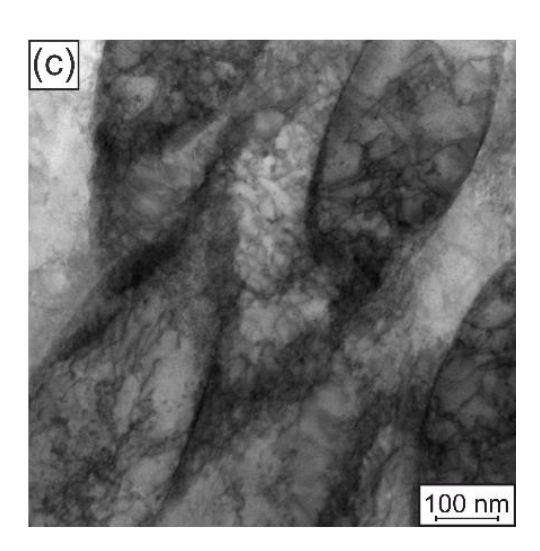


Fig. 1: (a) Stress strain curve of the additively manufactured, melted, and arc directionally solidified NiAl-CrMo composites at room temperature. (b) As built microstructure of the additively manufactured specimens, showing the interconnected "as-built" microstructure and the discontinuously coarsened areas. (c) BF-STEM image of the additively manufactured specimens after a plastic deformation of 10 %.





- [1] D. Wicht, A. Kauffmann, M. Schneider, M. Heilmaier, Thomas Böhlke, Acta Mater. **2022**, 226, 117626.
- [2] A. Förner, J. Vollhüter, A. Krapf, A. Jamjoom, D. Hausmann, B. Wahlmann, Z. Fu, C. Körner, S. Neumeier, M. Göken, Adv Eng Mater. **2023**, 25, 2300407.
- [3] K. Titz, J. Vollhüter, P. Randelzhofer, S. Neumeier, M. Göken, B. Wahlmann, C. Körner, Adv Eng Mater. **2024**, 26, 2302079.

SCP 10.1:

Strategies to improve oxidation resistance of Mo-Si-B based intermetallic alloys

Rahul Mitra

Department of Metallurgical and Materials Engineering Indian Institute of Technology Kharagpur Kharagpur, West Bengal 721302, INDIA Email: rahul@metal.iitkgp.ac.in

Introduction

The oxidation resistance of Mo-Si-B based alloys is ensured by the formation of a continuous oxide scale of B_2O_3 -SiO $_2$ (borosilicate glass) having a self-healing character contributed by its ability to undergo plastic flow. However, the evolution of a continuous layer of B_2O_3 -SiO $_2$ scale has to compete with the rapid formation of MoO $_3$, which vaporizes subsequently causing mass-loss. Typically, the mass loss by vaporization of MoO $_3$ precedes the formation of a continuous and protective scale of B_2O_3 -SiO $_2$. As expected, the formation kinetics of both MoO $_3$ and B_2O_3 -SiO $_2$ depends on temperature. Alloying is one of the strategies which have shown success in improving the oxidation resistance of the Mo-Si-B alloys. In the author's research group, the influence of selective alloying and the accompanying microstructural modification on oxidation kinetics and oxide scale evolution have been systematically examined. Alloying has been carried out selectively using elements (Al, Ce, Zr, and Ti), whose oxides have lower free energy of formation and are therefore more stable compared to Mo-oxides (MoO $_2$ and MoO $_3$) as well as B_2O_3 and SiO $_2$.

Materials and Methods

Alloys having the composition of Mo₇₆Si₁₄B₁₀ (base alloy) have been fabricated by reactive hot pressing of uniformly mixed powders of Mo, Si and B having >99% purity at 1600 °C in vacuum. Alloys having similar compositions have been fabricated by spark-plasma sintering (SPS) at 1300 °C in argon atmosphere, or by arc-melting, using the aforementioned elemental powders as raw materials. To examine the role of alloying elements on microstructural evolution and oxidation resistance, alloys with 7.3% Al, 7.3% Al +0.16% Ce, 2% Zr, or 20-40% Ti (at%) added at the expense of Mo, have been processed by arc-melting or SPS. Isothermal oxidation tests have been carried out in dry air at temperatures from 500 °C to 1300 °C for a duration of 24 h, with the mass being measured at intervals of 1 h. Additionally, short duration isothermal oxidation tests have been carried out at on selected alloys to examine the early stages of oxide scale evolution. Additionally, isothermal oxidation tests have been carried out in moist air (85% relative humidity) in the temperature range of 1000-1300 °C to examine the effect of Zr addition on mass change and oxide scale evolution. The oxide scales have been characterized by Xray diffraction as well as scanning electron microscopy accompanied by energy dispersive spectroscopy.

Results and discussion

The mass loss in the $Mo_{76}Si_{14}B_{10}$ alloy has been found to be unabated causing pest-type disintegration at 700 °C, because of sluggish rate of protective scale formation compared to that of MoO_3 formation and vaporization [1]. On the other hand, mass loss is found to be the least at 1150 °C, as a continuous B_2O_3 -SiO₂ scale has formed in 8 minutes [2].

Moreover, the formation of a protective scale through prior exposure at 1150 °C has enhanced the oxidation resistance at 700 °C [1,3]. The strategy to improve the oxidation resistance therefore should involve enhancing the kinetics of B₂O₃-SiO₂ formation, along with reduction in the rate at which MoO₃ forms and vaporizes. Processing of the Mo-Si-B alloys with finer grain size has been found to improve the oxidation resistance by enhancing the kinetics of protective oxide scale formation, which is facilitated by faster diffusion of B and Si through the grain boundaries [4]. Furthermore, the alloys having minor amounts of Zr and Al added at the expense of Mo has been found to consume the volatile MoO₃ to form respectively, Zr(MoO₄)₂ [4] and Al₂(MoO₄)₃ [5], resulting in noticeable reduction of mass loss along with strengthening of the glass network in B₂O₃-SiO₂. Additionally, alloying with Zr has been found to reduce the mass loss in moist air by forming ZrSiO₄ through the consumption of SiO₂, which otherwise would have vaporized in hydrated form [6]. Furthermore, minor addition of 0.16 at% Ce to Al containing alloy has been found to stabilize the glass network in the oxide scale and increase the vaporization temperature of B₂O₃, causing shortening of the transient stage as well as reduction of mass loss during exposure at 900 °C and 1300 °C [7]. On adding 20 to 40 at% Ti at the expense of Mo, not only the alloy becomes lighter and the net mass change is considerably reduced, but also a transition is observed from mass loss to gain. The oxide scales formed on 20 and 30 at% Ti added alloy contain TiO₂ and B₂O₃-SiO₂ as outer and inner layers, respectively, while that formed on the 40 at% Ti-added alloy contains an additional innermost layer of MoO2. The oxidation resistance of the Ti-added alloys could be further improved through minor additions of Zr, which is considered to be due to the mechanisms discussed above. The alteration in the nature and magnitude of mass change along with oxide scale evolution is considered to have been caused by various alloying additions along with the accompanying modifications of their microstructures. The mechanisms through which various alloying additions have resulted in improved oxidation resistance will be discussed in the presentation.

- [1] Sharma Paswan, R. Mitra, S.K. Roy, Intermetallics. **2007**, *15*, 1217-1227.
- [2] Barna Roy, J. Das, R. Mitra, Corrosion Science. 2013, 68, 231-237.
- [3] Sharma Paswan, R. Mitra, S.K. Roy, Metallurgical and Materials Transactions A. **2009**, *40*, 2644-2658.
- [4] N.K. Kumar, J. Das, R. Mitra, Metallurgical and Materials Transactions A. **2019**, *50*, 2041-2060.
- [5] J. Das, R. Mitra, S.K. Roy, Intermetallics. **2011**, *19(1)*, 1-8.
- [6] N.K. Kumar, J. Das, R. Mitra, Oxidation of Metals. **2020**, 93, 483-513.
- [7] J. Das, B. Roy, N.K. Kumar, R. Mitra, Intermetallics. **2017**, *84*, 101-109.

SCP 10.2:

Development of Mo-Si-B Alloys for Additive Manufacturing

J.H. Perepezko, L. Liu, L.F. Wood, B. Rankouhi, D.J. Thoma University of Wisconsin-Madison, Department of Materials Science and Engineering, 1509 University Ave., Madison, WI 53706, USA

Introduction

Refractory metal alloys offer an attractive option to extend operational capability beyond what is currently available with Ni-base superalloys to provide enhanced efficiency and power generation in gas turbines [1]. In order to achieve enhanced performance an alloy must be designed to satisfy several challenging requirements involving mechanical properties and a number of thermophysical properties as well as environmental resistance at 1300°C [2] However, the processing of the refractory metal alloys (RMAs) to manufacture dimensionally controlled shapes - such as a turbine airfoil in a commercially cost-effective way is challenging. For refractory metal alloys, the directional solidification approach that has been very successful for Ni-base superalloys has difficulties. To address these challenges an effective design has been established based upon additive manufacturing (AM) utilizing a reactive synthesis of component powders of Mo, Si₃N₄, BN, and Ti where a high throughput synthesis and characterization are employed together with guidance from computational thermodynamics to identify promising alloy compositions [3]. The selected Mo-3.3Si-4.5B-10Ti alloy includes Ti for both density reduction and to limit the Si solubility in Mo and the associated embrittlement effect of Si. The alloy design exhibits a high compressive strength of about 1.6 GPa and ductility above 20% at room temperature. An effective oxidation resistance is provided by a pack cementation borosilica coating. With AM and optimized processing parameters turbine blades have been produced at full scale.

Materials and Methods

The Mo-Si-B-Ti alloy was manufactured using the laser powder bed fusion (LPBF) technique. The component Mo, Si₃N₄, BN, Ti powders were blended before being loaded into the 3D printer—an EOS M290 unit equipped with a Ytterbium fiber laser operating at a wavelength of 1060 nm, with a maximum power of 400 W and a focused spot diameter of 100 µm. For the printing process, the Ti build plate was preheated to 80°C, and an inert argon environment was maintained within the print chamber. The blended powder had a nominal alloy composition of Mo-3.3Si-4.5B-10Ti (atomic percent), as depicted in the calculated phase diagram shown in Figure 1. The red dashed lines in Figure 1 represent density contours and the target composition aimed for a density of around 9 g/cm3, comparable to existing Ni-based superalloys. The compositional adjustments towards reduced Si solubility in the Mo matrix were intended to enhance the alloy ductility. Hardness testing was carried out by Vickers hardness tester (Wilson VH1150), and a test force was 1000gf. Compression tests were performed in an Instron® universal testing machine attached with a 100 kN load cell. The microstructures of all samples were observed by scanning electron microscopy (Zeiss Gemini-450 FESEM) with backscattered electron images. A FEI Tecnai F30 with a field emission gun TEM and highresolution TEM were used to examine the microstructure and detailed dislocation morphology. The oxidation testing and environmental resistant coasting method has been published [4].

Results and Discussion

With optimized LPBF processing parameters and reactive synthesis samples with high density (99%) and uniform composition were fabricated including a full-scale turbine blade with internal cooling channels and a dimensional tolerance of 30µm. In the asprinted condition significant residual stress was detected by XRD and was associated with a high dislocation density as confirmed by TEM. In a Vickers hardness test with a 10kgf no cracking was detected around the indent indicating good ductility. This is supported by a room temperature compression test where the sample had a strength of 1.6 GPa and plastic strain of over 25%. Microstructural examination revealed transgranular failure in the Mo solid solution and intergranular fracture in the Mo and Mo₅SiB₂ (T₂) eutectic. There were well-developed deformation bands with the T₂ phase acting as a precipitate strengthening source that also partially blocks the deformation flow. A high dislocation density in the Mo-T₂ eutectic region indicated that most of the deformation occurred in this region. As with most refractory metal alloys the oxidation performance at 1300°C indicated a large mass loss, but the coated samples exhibited low mass changes (below 1 mg/cm²) during both isothermal and thermal cycling exposure (350 1 hour cycles). In effect, AM circumvents the main problems with the traditional casting method for production and represents a new manufacturing paradigm.

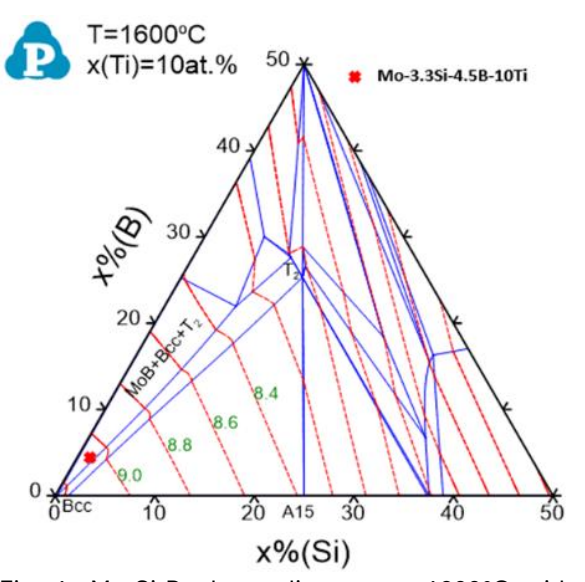


Fig. 1: Mo-Si-B phase diagram at 1600°C with 10at% Ti, red lines ae density contours.

Fig. 2: Full scale turbine blade with internal cooling channels.

- [1] J.H. Perepezko, Science, **2009**, 326, 1068.
- [2] R. Su, L. Liu, J. H. Perepezko, Int. Jnl of Refractory Metals and Hard Mater., **2023**, 113, 106199.
- [3] Z. Islam, M. Amalra, L. Liu, L. D. Marks, J. H. Perepezko, D. J. Thoma, **2023**, JOM 75, 5037–5045
- [2] J.H. Perepezko, R. Sakidja, JOM. 2010, 62, 13-19.

SCP 10.3:

Microstructure Coarsening of Additively Manufactured Mo-9Si-8B at Elevated Temperatures

Christopher Schmidt¹, Georg Hasemann¹, Manja Krüger¹, Benjamin Wahlmann², Yong Chen² and Carolin Körner²

¹Otto-von-Guericke-University, Institute for Materials, Technologies and Mechanics, Universitätsplatz 2, Magdeburg, Germany, christopher1.schmidt@ovgu.de, georg1.hasemann@ovgu.de, manja.krueger@ovgu.de

²Friedrich-Alexander-Universität Erlangen-Nürnberg, Department of Materials Science and Engineering, Martensstraße 5, Erlangen, Germany, <u>benjamin.wahlmann@fau.de</u>, <u>yong.chen@fau.de</u>, <u>carolin.koerner@fau.de</u>

Introduction

Molybdenum-silicon-boron (Mo-Si-B) alloys are promising candidates for high-temperature applications due to their excellent oxidation resistance and mechanical stability. Among these, Mo-9Si-8B exhibits a favorable combination of properties for structural components operating under extreme conditions. However, the stability of its microstructure at elevated temperatures remains a crucial factor influencing its long-term performance.

This work investigates the microstructural evolution of Mo-Si-B alloys produced via Laser Powder Bed Fusion (L-PBF) and Electron Beam Melting (EBM), as well as their modification during heat treatment. The objective is to analyze grain growth kinetics and to provide a fundamental understanding of how thermal exposure affects the microstructure. Particular focus is placed on the influence of grain and phase size, as both have a critical impact on the creep properties of the material. The obtained insights will serve as a basis for further research on mechanical behavior and the optimization of heat treatment strategies.

Materials and Methods

Mo-Si-B specimens were fabricated using the Laser Powder Bed Fusion (L-PBF) in an Aconity3D machine with an inductive preheating system to achieve temperatures of up to 1200 °C in the substrate as well as the Electron Beam Melting (EBM) system (Freemelt® ONE, Freemelt AB, Gothenburg, Sweden). The additively manufactured material was analyzed in the as-built state to determine the microstructural constituents and parameters. The additively manufactured materials were then sectioned into 5×5×5 mm³ cubes using Wire Electrical Discharge Machining (Wire EDM) to ensure precise and damage-minimized sample preparation. To investigate the effect of high-temperature exposure on microstructure evolution, a design of experiments (DOE) was conducted, varying heat treatment temperatures from 1200°C to 1600°C and dwell times up to 50 hours. This approach allowed the observation of both short-term and long-term coarsening effects. Following thermal exposure, the specimens were metallographically prepared using sequential grinding and polishing steps to obtain high-quality surfaces for microstructural analysis. Each sample was examined in two cross-sectional orientations - one perpendicular (Z-plane) and the other parallel to the build plane (XY-plane). Microstructural characterization was carried out using Scanning Electron Microscopy (SEM) in Backscattered Electron (BSE) mode to assess grain morphology and phase distribution. Electron Backscatter Diffraction (EBSD) was employed to measure grain sizes, phase fractions, and crystallographic orientations. Additionally, X-ray Diffraction (XRD) analysis was conducted to identify and quantify the present phases.

Results and Discussion

The microstructural analysis indicates a temperature-dependent coarsening behavior. Fine-microstructures in as-built L-PBF and EBM samples coarsen progressively with increasing heat treatment temperature and holding time, which is in good agreement with the literature [1]. Existing studies indicate that larger grain sizes reduce the contribution of grain boundary sliding to deformation [2], [3]. In conventionally processed Mo-Si-B alloys, increasing grain size by a factor of 5 to 10 has been shown to reduce creep rates by an order of magnitude [4]. *Figure* shows the microstructural difference between as-built and heat-treated condition of a L-PBF processed near-eutectic Mo-Si-B alloy. The microstructure of as-built L-PBF samples consists of fine molybdenum solid solution (Mo_{ss}) dendrites surrounded by a silicide matrix (*Figure*). According to EBSD analysis, the phase composition of as-built L-PBF samples consists of 29.7% Mo_{ss} phase, 22.2% Mo_s-SiB₂-phase, and 48.1% Mo₃-Si phase. After heat treatment at 1600 °C for 10 hours, the microstructure coarsens slightly while maintaining a similar phase composition [1].

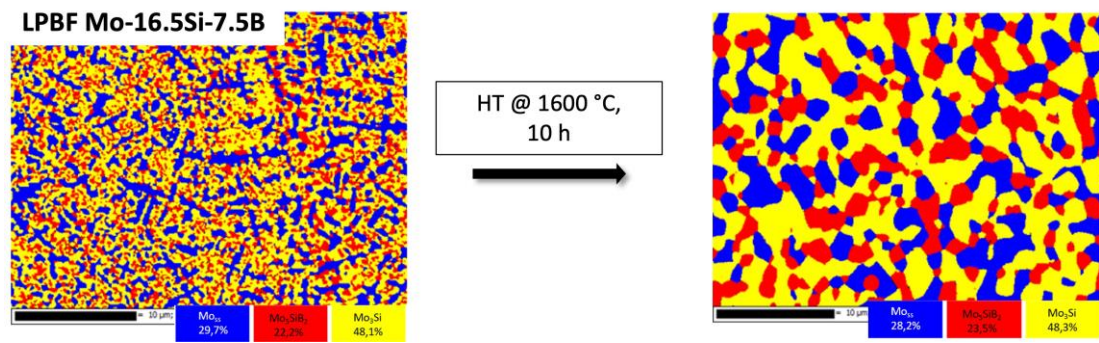


Figure 1 Microstructure of a Mo-Si-B sample manufactured with L-PBF; left: EBSD image of the "as-built" sample with Mo_{ss} (blue), Mo_3Si (yellow) and Mo_5SiB_2 (red) and right: EBSD image of a sample heat treated at 1600 °C for 10h – more details are given in [1]

Due to similar process characteristics (rapid cooling rates, layer wise process, etc.) between EBM and L-PBF, a comparable microstructural evolution is expected for EBM-processed samples. The observed microstructural changes provide essential groundwork for future studies on the relationship between grain size and high-temperature performance.

Fightner et al. [1] evaluated creep properties of L-PBF Mo-Si-B alloys and compared them to those processed by other manufacturing routes. Figure illustrates the creep behavior of different Mo-Si-B alloys and a nickel-based superalloy demonstrating that additively manufactured (AM) samples exhibit superior creep resistance. This improved performance can be attributed to the distinct microstructure of L-PBF materials, particularly the higher fraction of intermetallic phases, which form a silicide matrix during solidification. The increased silicon and boron content in L-PBF samples promotes the formation of silicides, resulting in enhanced creep resistance compared to powder metallurgically (PM) processed alloys, which primarily contain a Moss matrix. The annealing procedure will affect the creep response of AM samples significantly, as depicted by the arrows in Figure 2. Directional solidification (DS) processed Mo-17.5Si-8B alloys display even better creep performance than AM samples. This behavior is due to processing effects, which lead to the formation of elongated grains with specific orientations, as well as a coarser microstructure compared to the ultrafine-grained L-PBF material. Consequently, enhanced creep resistance can be attributed to both the specific phase composition and the morphological characteristics of grains and phases.

By leveraging the favorable phase constitution inherent to additively manufactured materials and applying targeted heat treatments to modify grain size and morphology, a further improvement in creep properties may be anticipated.

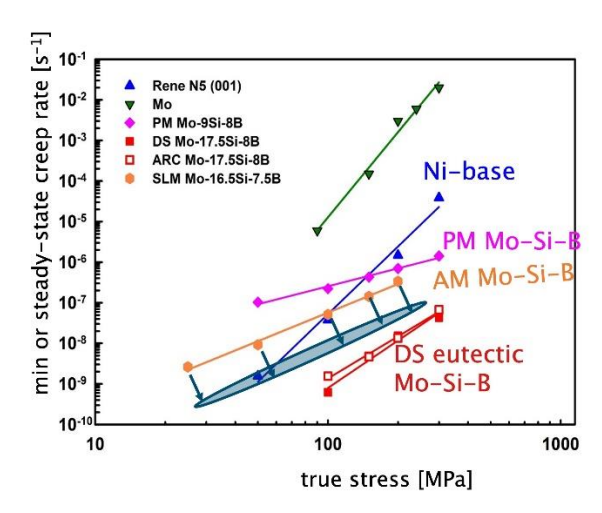


Figure 2 Creep properties of Mo–Si–B alloys manufactured by additive manufacturing (AM), powder metallurgy (PM) [5] and by directional solidification/zone melting technique (DS) [3] at 1093 °C.

In summary, the performed investigations demonstrate that the microstructure of additively manufactured Mo-Si-B alloys undergoes significant coarsening during heat treatment, with the extent of growth being strongly temperature-dependent. This study provides a foundation for further investigations into the relationship between grain size and mechanical properties, particularly creep resistance. These findings highlight the potential of microstructural engineering through optimized heat treatments to enhance the high-temperature performance of Mo-Si-B alloys, particularly in terms of creep resistance and phase stability.

- [1] D. Fichtner, J. Schmelzer, W. Yang, C. Heinze, and M. Krüger, "Additive manufacturing of a near-eutectic Mo–Si–B alloy: Processing and resulting properties," Intermetallics, vol. 128, p. 107025, **2021**, doi: 10.1016/j.intermet.2020.107025.
- [2] J. L. Yu et al., "Deformation Behavior of a Multiphase Fine-Grained Mo-Si-B Alloy," AMR, vol. 284-286, pp. 544–549, **2011**, doi: 10.4028/www.scientific.net/AMR.284-286.544.
- [3] G. Hasemann, "Microstructure and properties of near-eutectic Mo-Si-B alloys for high temperature applications," Dissertation, Fakultät für Maschinenbau, Ottovon-Guericke-Universität Magdeburg.
- [4] M. Heilmaier, M. Krüger, and H. Saage, "Recent Advances in the Development of Mechanically Alloyed Mo Silicide Alloys," MSF, vol. 633-634, pp. 549–558, 2009, doi: 10.4028/www.scientific.net/MSF.633-634.549.
- [5] M. Krüger, P. Jain, K. S. Kumar, and M. Heilmaier, "Correlation between microstructure and properties of fine grained Mo–Mo3Si–Mo5SiB2 alloys," Intermetallics, vol. 48, pp. 10–18, **2014**, doi: 10.1016/j.intermet.2013.10.025.
- [6] M. Heilmaier, M. Krüger, H. Saage, J. Rösler, D. Mukherji, U. Glatzel, R. Völkl, R. Hüttner, G. Eggeler, Ch. Somsen, T. Depka, H.-J. Christ, B. Gorr, and S. Burk, "Metallic Materials for Structural Applications Beyond Nickel-based Superalloys," JOM, Vol. 61 No. 7.

SCP 10.4:

Development of Nb-Si Based Ultrahigh Temperature Alloys and their Integral Directional Solidification Technique

Xiping Guo¹, Rui Ma¹, Haisheng Guo¹, Song Zhang¹, Yanqiang Qiao¹ and Ping Guan²
¹State Key Laboratory of Solidification Processing, Northwestern Polytechnical University, Xi'an 710072, China, xpguo@nwpu.edu.cn

²School of Chemistry and Chemical Engineering, Northwestern Polytechnical University, Xi'an 710129, China, guanping1113@nwpu.edu.cn

Introduction

Nb-Si based ultrahigh temperature alloys are potential alternatives for Ni based superalloys to operate at higher temperature (1200~1400 °C) due to their lower densities and excellent high temperature strength [1]. However, their insufficient room temperature fracture toughness and poor high temperature oxidation resistance are the bottlenecks for the practical applications of Nb-Si based ultrahigh temperature alloys. Alloying is an effective way to improve the comprehensive properties of the alloys [2]. Nb-Si based ultrahigh temperature alloys have now been developed to multi-elemental systems with six or more elements, so the composite alloying effects become complex and is worthy of exploring. It is essential to systematically investigate the effects, especially the composite effects of Mo, V and Zr on the comprehensive properties of multi-elemental Nb-Si based ultrahigh temperature alloys [3].

Directional solidification process can significantly modify the microstructures and improve their room and high temperature mechanical properties of Nb-Si based ultrahigh temperature alloys [4,5]. Up to now, the directional solidification of Nb-Si based ultrahigh temperature alloys was conducted only by either cold crucible Czochralski method or floating zone melting techniques such as electron beam floating zone melting, optical floating zone melting and induction floating zone melting by other research workers. However, low thermal gradients and relatively severe perturbation motion in the melt ahead of the solid/liquid (S/L) interface of these methods have led to the directionally solidified microstructure relatively coarser and aligned divergently. Different with these methods, integrally directional solidification process with the use of crucibles (IDSPC) employs either a cold trap or a liquid-metal-cooling crystallizer, so the axial thermal gradient ahead of the S/L interface could be improved evidently, thus alleviating both "Kelvin effect" and convection ahead of the S/L interfaces and resulting in a better directionally solidified microstructure. In addition, components such as an engine turbine blade with a complex shape and varying sections could be prepared by IDSPC. In the present talk, the microstructural evolution of Nb-Si based ultrahigh temperature alloys with different compositions was revealed. The integrally directional solidification of the alloy was conducted in a self-made high vacuum and ultrahigh temperature directional solidification furnace with the use of ceramic crucibles. Microstructural evolution and variation of S/L interfaces with the withdrawing rates have been illustrated, and room temperature mechanical properties and high temperature stress-rupture properties of the alloys were investigated.

Materials and Methods

The ingots of Nb-Si based ultrahigh temperature alloy, with the nominal composition of Nb-15Si-22Ti-5Cr-3Hf-3Al-xMo-yZr-zV (at.%), were prepared by vacuum non-consumable arc-melting and then vacuum high frequency induction melting. The

experimental samples with dimensions of 6.8 mm in diameter and 75 mm in length were cut by electro-discharged machining (EDM). Integrally directional solidification was conducted at the melt temperature of 2050 °C and withdrawn rates of 100, 200, 300, 500 and 1000 μ m/s, respectively. When solidification was in steady-state, the sample was quenched by rapidly pulling them into the Ga-In-Sn liquid alloy pool. The directionally solidified samples were cut along the longitudinal and transverse direction by EDM for metallographic analysis.

Results and Discussion

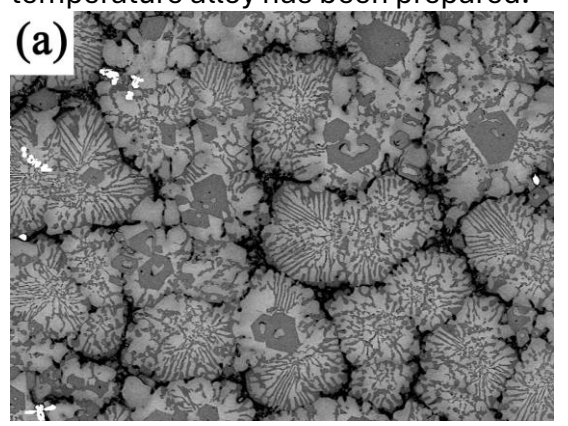
The phase constituents of the multi-elemental Nb-Si based ultrahigh temperature alloys are Nbss (Niobium solid solution), $\alpha/\gamma(Nb,X)_5Si_3$ and Laves Cr_2Nb phases. Alloying with V or Zr promotes the formation of hypereutectic structure, and cooperatively alloying with V and Zr further increases the content of primary silicides. While in the presence of V or Zr, further adding Mo decreases the content of primary silicides. The additions of Mo, V and Zr can suppress the formation of $\alpha(Nb,X)_5Si_3$, whilst promote the formation of $\gamma(Nb,X)_5Si_3$. During heat treatment at 1450 °C for 50 h, some $\gamma(Nb,X)_5Si_3$ phases in 0Mo-0V-0Zr and 0Mo-3V-0Zr alloys have transformed to $\alpha(Nb,X)_5Si_3$ phases, but this phase transformation is not observed in Mo- or Zr-containing alloys. In addition, the heat treatment at 1450 °C for 50 h eliminates segregation microstructures and promotes the formation of $(Nb,X)_3Si$ phase in the alloys.

Adding V causes serious element segregation in the solidified microstructure, and thus increases the content of $Cr_2Nb/Nbss$ eutectic, $Cr_2Nb/Nbss/(Nb,X)_5Si_3$ three phase eutectic, Nbss dendrites and H-shaped primary silicides. Adding Mo promotes to form lamellar Nbss/ $\gamma(Nb,X)_5Si_3$ eutectic structure. Adding Zr decreases the content of silicides during eutectic solidification, and thus promotes the formation of fine Nbss/ $\gamma(Nb,X)_5Si_3$ eutectic structure. Additionally, V and Mo elements primarily dissolve in Nbss, while Zr almost wholly dissolves in silicides.

The oxidation performances of fifteen arc-melted multi-elemental Nb-Si based ultrahigh temperature alloys were evaluated at 1250 °C for 1 and 20 h, respectively. The effects of Mo, V and Zr additions on the oxidation resistance of multi-elemental Nb-Si based ultrahigh temperature alloys have been investigated. The results show that all scales have double layered structure, namely outer layer and inner layer. Both of them consist of Nb₂O₅, (Ti,X)O₂ and TiNb₂O₇ oxides. Besides, some V₂O₅, CrVNbO₆ and Nb₉VO₂₅ oxides form in the scales of V-containing alloys. Solely adding Mo or V ameliorates the adhesion of the scales and thus improves the oxidation resistance of the alloys. Solely adding Zr does not affect the adhesion of the scales, but can improve the oxidation resistance of the alloys by increasing the oxidation resistance of silicide phases. Cooperative additions of Mo and Zr further improves the high temperature oxidation resistance, and the mass gain per unit area of 5Mo-0V-4Zr-AC alloy oxidized at 1250 °C for 20 h is only 30.3 mg/cm². The cooperative additions of V with Mo/Zr do not improve, but degrade the oxidation resistance of alloys, since more liquid V_2O_5 flow out of the scales. In the presence of V and Zr, the limited addition of Mo (2 at.%) marginally improves the oxidation resistance of the alloys, while further increasing the Mo content decreases the oxidation resistance of the alloys owing to the increase in the amounts of micro holes in their scales.

As shown in Figs. 1 (a) and (b), the directionally solidified microstructure grew regularly along the longitudinal direction, and the eutectic cells in the cross-sections had nearly round shape. The quenched S/L interfaces were composed of a series of protruded

parallel eutectic cells that aligned erectly along the growth direction. With increase in withdrawing rates, the S/L interfaces changed from the planar to the coarse cellular and then to fine cellular; the number of eutectic cells in the directionally solidified microstructure increases; the average diameter of eutectic cells and the interlamellar spacing in the eutectic cells decrease, and the eutectic coupling growth degree enhance. The integrally directional solidification significantly improves the room-temperature fracture toughness, high-temperature tensile strength and stress-rupture life of the Nb-Si based ultrahigh temperature alloy. After integral directional solidification, the maximum $K_{\rm Q}$ average value reaches 26.8 MPa·m¹¹², the creep elongation at 1250 °C/75 MPa for 216 h is only 0.79%, the tensile strength at 1400 °C reaches 183.5 MPa, and the tensile strength at 1500 °C reaches 113.8 MPa. Special ceramic molds for the investment casting of Nb-Si based ultrahigh temperature alloy turbine blade have been successfully developed. Under the conditions of a melt temperature of 2000 °C and a withdrawing rate of 20 μ m/s, a directionally solidified model turbine blade of Nb-Si based ultrahigh temperature alloy has been prepared.



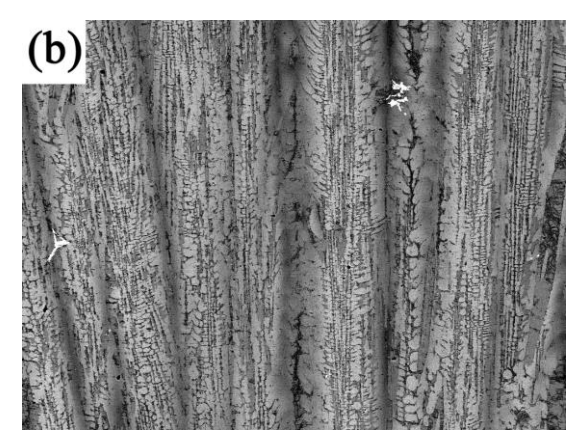


Fig. 1 SEM images of the microstructures of the Nb-Si based ultrahigh temperature alloy specimens integrally directionally solidified at a withdrawing rates of 20 μ m/s. The melt temperature is 2050 °C. (a) cross-sectional and (b) longitudinal microstructures.

Conclusions

Multi-component Nb-Si based ultrahigh temperature alloys with excellent mechanical properties and oxidation resistant performance have been developed. The synergetic alloying effects of Mo, V, Zr have been revealed.

Integral directional solidification technique including the used ceramic crucibles has been developed for Nb-Si based ultrahigh temperature alloys. The evolution of directionally solidified microstructure as well as the change of S/L interface morphology with the increase in withdrawing rates have been elucidated.

Integral directional solidification significantly improves the room-temperature and very high-temperature mechanical properties.

- [1] P. Tsakiropoulos, Progress in Materials Science, 2022, 123, 100714.
- [2] J.H. Perepezko, Science, 2009, 326, 1068-1069.
- [3] R. Ma, X.P. Guo, Journal of Materials Science & Technology, 2023, 132, 27-41.
- [4] H.S. Guo, X.P. Guo, Scripta Materialia, **2011**, 64, 637-640.
- [5] B.P. Bewlay, M.R. Jackson, J.C. Zhao, P.R. Subramanian, M.G. Mendiratta, J.J. Lewandowski, MRS Bulletin, **2003**, 28 (9), 646-653.

SCP 11.1:

Phase Equilibria in the V-Rich Region of the V-Si-B System at 1400 °C

Georg Hasemann¹, Weiguang Yang², Mustafa Carrion Saldaña³, Bronislava Gorr⁴, Ruth Schwaiger^{2,5}, Manja Krüger¹

Otto-von-Guericke University Magdeburg, Institute of Materials, Technologies and Mechanics, Universitätsplatz 2, 39106, Magdeburg, Germany georg1.hasemann@ovgu.de, manja.krueger@ovgu.de
 Forschungszentrum Jülich GmbH, Institute of Energy Materials and Devices, Structure and Function of Materials (IMD-1), Leo-Brandt-Str.1, 52425, Jülich, Germany w.yang@fz-juelich.de, r.schwaiger@fz-juelich.de

Introduction

Most high-temperature properties, e.g. high-temperature strength and creep resistance, are correlating with the high melting temperature. Thus, similar to molybdenum-based alloys, vanadium-based alloys are promising candidates for high-temperature structural applications due to the high melting temperature of vanadium and a comparably low density. V–Si–B alloys are one of the most promising vanadium-based alloys because the addition of Si and B can improve the oxidation resistance by facilitating the formation of a protective silica layer primarily through the intermetallic phases such as V_3Si , V_5Si_3 and V_5SiB_2 .

For alloy design and development, the phase diagram is one of the most important tools. The isothermal section of the V–Si–B system was first investigated at 1450 °C by Kudielka et al. [1] using XRD measurement in 1957. According to the XRD results of the three alloys, Kudielka et al. found two three-phase phase fields, namely $\sim V_{0.7}B_{0.3}-VB-V_5SiB_2$ and $V_5SiB_2-V_3Si-D8_8$.

The latest systematic experimental investigation of the isothermal section of the V–Si–B system was carried out by Nunes et al. [2] at 1600 °C in 2009. They produced the samples via arc-melting under argon followed by a heat treatment at 1600 °C for 24/72 h under a high vacuum). The samples were furnace cooled to room temperature after heat treatment. Based on wavelength-dispersive spectroscopy measurements, they proposed the isothermal section of the V–Si–B system at 1600 °C in the V_{ss} –VB–VSi $_2$ region of the V–Si–B system. Nunes et al. [2] found that the B solubility in V_{ss} , V_3 Si and V_5 Si $_3$ was negligible, as was the Si solubility in V_3 B $_2$ and VB and confirmed the stabilities of the two ternary phases at 1600 °C, V_5 Si $_3$ B and V_5 SiB $_2$, and observed a solubility range of the V_5 SiB $_2$ phase.

Most recently, we have observed a new ternary phase, V_8SiB_4 [3], in the alloy V–5Si–9B annealed at 1400 °C. The new ternary phase has nearly the same composition as the V_5SiB_2 phase in the V_{ss} – V_3B_2 – V_5SiB_2 phase field at 1600 °C but a different crystal structure [3]. The presence of the new ternary phase at 1400 °C indicates the major difference between the isothermal sections of the V-rich V–Si–B system at 1400 °C and 1600 °C. Thus, this work aims to experimentally investigate the isothermal section of the V-rich V–Si–B system, especially at 1400 °C.

³ University Siegen, Institute of Materials Technology, Paul-Bonatz-Strasse 9-11, 57076, Siegen, Germany Mustafa.CarrionSaldana@uni-siegen.de

⁴ Karlsruhe Institute of Technology, Institute for Applied Materials–Applied Materials Physics (IAM–AWP), Hermann–von–Helmholtz–Platz 1, 76344, Eggenstein-Leopoldshafen, Germany <u>bronislava.gorr@kit.edu</u> ⁵ Chair of Energy Engineering Materials, Faculty 5, RWTH Aachen University, Templergraben 55, 52056, Aachen, Germany

Materials and Methods

For producing samples, the raw materials were carefully weighed in the form of highpurity elemental turnings of V (99.7 wt.%) and granules of Si (99.99 wt.%) and B (99.0 wt.%). For each of the investigated V–Si–B alloy compositions having B concentration lower than 30 at.%, a 15 g button was produced by remelting five times in a conventional arc-melter under flowing argon gas, while for each of the investigated compositions having B concentration higher than 30 at.%, a 10 g button was produced by remelting three times in a conventional arc-melter, followed by re-melting two times in a levitation melter under argon gas. A negligible weight loss (< 1 wt.%) indicates that the compositions after melting are very close to the nominal compositions. For confirmation, the inductively coupled plasma optical emission spectroscopy (ICP-OES, iCAP 7600, Thermo Fisher Scientific, USA) was performed. As-cast buttons were cut in half using the electrical discharge machining (EDM). One half was used to investigate the as-cast microstructure, while the other half was heat-treated at 1400 °C for at least 100 h under a high vacuum (1.5x10⁻⁵ mbar) and furnace cooled within 3 h below 200 °C.

For metallographic preparation, the samples were embedded in a cold mounting resin (Epoxy 2000, Cloeren Technology, Wegberg, Germany), and subsequently ground down to 2000 grit using SiC paper, followed by polishing down to 1 µm diamond suspension and finished using colloidal silica. A Zeiss Merlin (Zeiss Microscopy, Oberkochen, Germany) scanning electron microscope (SEM) was used to observe the microstructures using the backscattered electron (BSE) mode. EDS spot measurements were performed to quantitatively measure the chemical compositions of phases with the electron high tension (EHT) of 10 kV.

X-ray diffraction (XRD) measurements were performed on the polished bulk samples at room temperature by using a diffractometer EMPYREAN (Malvern Panalytical, UK) or a diffractometer D8 ADVANCE (Bruker, USA) to identify the crystal structures of phases. The lattice parameters of the phases were determined using the software GSAS-II and the Pawley refinement.

Results

The isothermal section at 1400 °C was experimentally assessed, based on experimental alloys and is shown in Fig.1 [4]. It should be noted that the phase field of VB–V₈SiB₄ is assumed as a coexisting line. Compared to the isothermal section of V₈s–VB–V₅Si₃ proposed by Nunes et al. [2] at 1600 °C, the presence of the recently found V₈SiB₄ phase [3] is responsible for main changes at 1400 °C. The V₅SiB₂ phase field at 1600 °C is partially replaced by the phase field of V₈SiB₄–V₅SiB₂ at 1400 °C. Accordingly, it divides the V₅SiB₂–V₃Si phase field at 1600 °C into three phase fields at 1400 °C, i.e. the V₃Si–V₈SiB₄, V₃Si–V₈SiB₄–V₅SiB₂ and V₃Si–V₅SiB₂ phase fields. Similarly, the VB–V₅SiB₂ phase field at 1600 °C is divided into VB–V₈SiB₄–V₅SiB₂ and VB–V₅SiB₂ phase fields. Furthermore, the V₅SiB₂ phase of the V₈s–V₃SiB₂–V₅SiB₂, V₈s–V₃Si–V₅SiB₂ and VB–V₅SiB₂ phase fields at 1600 °C is replaced by the V₈SiB₄ phase. Like the binary coexisting line of V₈s–V₅SiB₂ at 1600 °C, the phase field of V₈s–V₈SiB₄ is still represented by a coexisting line at 1400 °C.

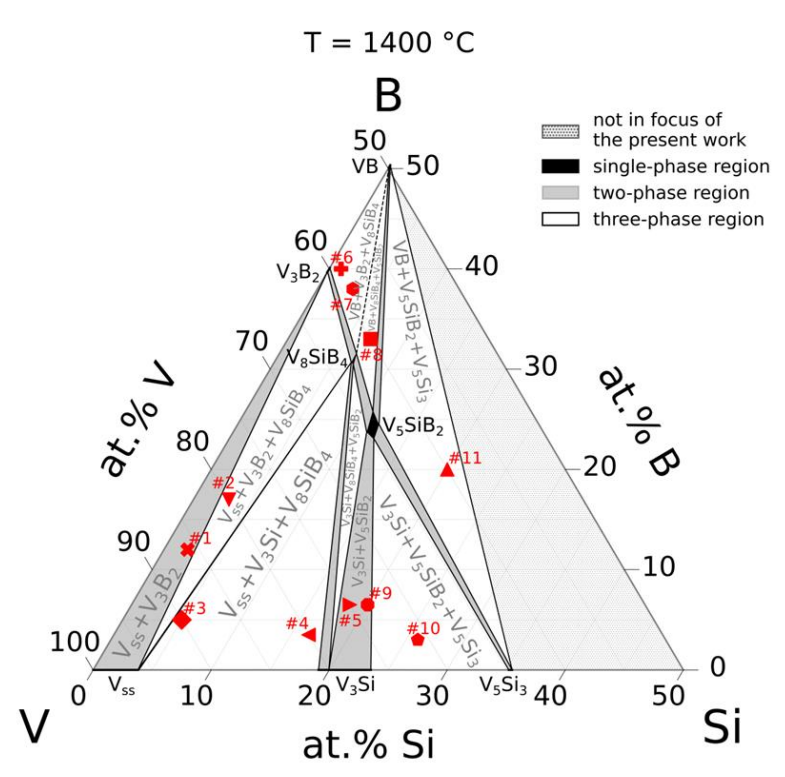


Fig.1 The isothermal section of the V-rich corner of the V-Si-B system at 1400 °C based on the marked alloys, where the phase field of VB-V₈SiB₄ is assumed as a coexisting line [4].

- [1] H. Kudielka, H. Nowotny, G. Findeisen, Untersuchungen in den Systemen: V-B, Nb-B, V-Si-B und Ta-B-Si, Mh. Chem. 88 (1957) 1048–1055.
- [2] C.A. Nunes, B.B. De Lima, G.C. Coelho, P.A. Suzuki, Isothermal Section of the V-Si-B System at 1600°C in the V-VSi2-VB Region, J. Phase Equilibria Diffus. 30 (2009) 345–350. https://doi.org/10.1007/s11669-009-9533-y.
- [3] W.G. Yang, R.S. Touzani, G. Hasemann, M. Yazlak, M. Ziegner, B. Gorr, R. Schwaiger, M. Krüger, V8SiB4 A new ternary phase in the V–Si–B system, Intermetallics. 151 (2022) 107691. https://doi.org/10.1016/j.intermet.2022.107691.
- [4] W. Yang, G. Hasemann, M. Carrion Saldaña, B. Gorr, R. Schwaiger, M. Krüger, Phase Equilibria in the V-Rich Region of the V-Si-B System at 1400 °C, J. Phase Equilibria Diffus. (2025). https://doi.org/10.1007/s11669-025-01177-4.

SCP 11.2:

Solid solution strengthening in V-9Si-6.5B-xCr alloys: Role of Cr and Si in the BCC phase

Weiguang Yang¹, Georg Hasemann², Shuntaro Ida³, Kyosuke Yoshimi³, Manja Krüger², Ruth Schwaiger^{1,4}

¹ Forschungszentrum Jülich GmbH, Institute of Energy Materials and Devices, Structure and Function of Materials (IMD-1), Wilhelm-Johnen-Straße, Jülich, 52428, Germany, w.yang@fz-juelich.de, r.schwaiger@fz-juelich.de

²Otto-von-Guericke University Magdeburg, Institute of Materials, Technologies and Mechanics, Universitätsplatz 2, Magdeburg, 39106, Germany, georg1.hasemann@ovgu.de, manja.krueger@ovgu.de

³Tohoku University, Department of Materials Science, Graduate School of Engineering, 6-6-02 Aramaki Aza Aoba, Sendai, Miyagi, 980-8579, Japan, shuntaro.ida.e1@tohoku.ac.jp,

yoshimi@material.tohoku.ac.jp

⁴RWTH Aachen University, Faculty 5, Chair of Energy Engineering Materials, Templergraben 55, 52056, Aachen, Germany

Introduction

Vanadium-silicide-based alloys are promising candidates for high-temperature applications, such as turbine components. In previous work, we modified the V-9Si-6.5B ternary eutectic alloy — where V_3Si and V_5SiB_2 intermetallic phases are uniformly distributed within the V-based body-centered cubic (BCC) phase — by substituting up to 30 at.% of V with Cr. This Cr addition significantly improved the high-temperature compressive strength without altering the ternary eutectic microstructure [1]. This improvement is primarily attributed to solid solution strengthening of the BCC phase. Given the limited solubility of B in V, this study focuses on the solid solution strengthening effects of Si and Cr in the BCC phase.

Materials and Methods

Alloys with compositions V-9Si-6.5B-xCr (x=0, 5, 10, 20 and 30 at.%) were arc-melted from pure elements and annealed at 1400 °C for 100 h. Both as-cast and annealed samples were investigated. The composition of the BCC phase was measured using energy-dispersive X-ray spectroscopy (EDS), and nanoindentation was used to assess hardness. To evaluate the strengthening effect, we applied the screw dislocation-based Maresca-Curtin model [2]. Model parameters were fitted to experimental yield stress data of V-xSi [1,3] and V-xCr [1] alloys, assuming additive effects of Si and Cr on solute-dislocation interaction energy.

Results and Discussion

The measured variation in hardness was strongly correlated with BCC phase composition (Fig. 1). Silicon consistently increased hardness regardless of Cr content. Similarly, Cr additions above ~7 at.% significantly increased hardness, with a plateau near 30 at.% Cr and a slight continued increase to at least 40 at.% Cr. The Maresca-Curtin model accurately captured these trends (Fig. 1), suggesting superimposable effects of Si and Cr on strengthening. This model also enabled quantification of the roles of kink glide and cross-kink mechanisms in the strengthening behavior, depending on the solute concentration and associated enthalpy barriers.

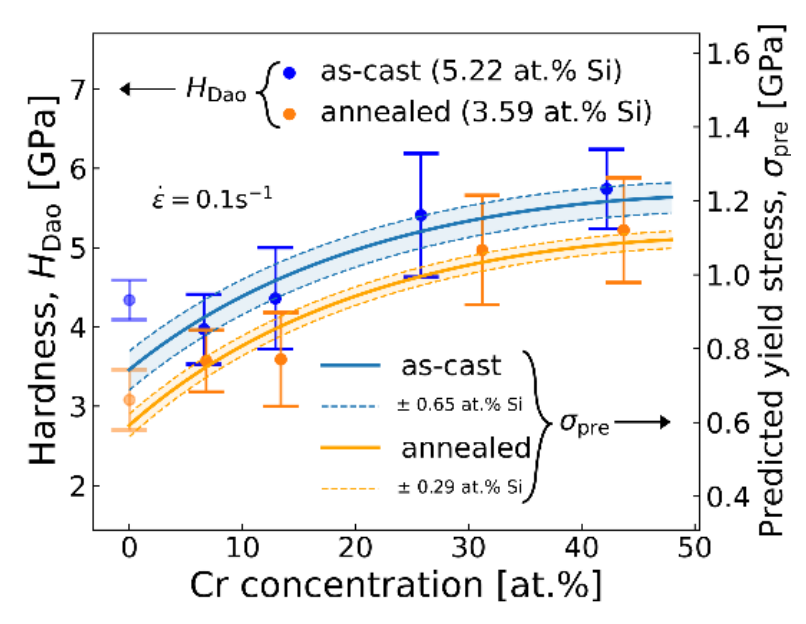


Fig. 1: Comparison of measured hardness and predicted yield stress of the V-based BCC phase in as-cast and annealed V-9Si-6.5B-xCr alloys, showing good agreement between experimental trends and Maresca-Curtin model predictions.

- [1] G. Hasemann, L. Thielemann, W. Yang, S. Ida, R. Schwaiger, K. Yoshimi, M. Krüger, Journal of Alloys and Compounds. **2024**, *1005*, 176041.
- [2] F. Maresca, W.A. Curtin, Acta Materialia. 2020, 182, 144-162.
- [3] G. Hasemann, C. Müller, D. Grüner, E. Wessel, M. Krüger, Acta Materialia. **2019**, *175*, 140-147.

SCP 11.3:

Grain refinement and interfacial IMCs suppression via Zn addition to enhance the mechanical properties of Cu/Sn-58Bi/Cu microbump

Pin-Ling Lin¹ and Jenq-Gong Duh¹

¹Department of Materials Science and Engineering, National Tsing Hua University, 101, Section 2, Kuang-Fu Road, Hsinchu, Taiwan 30013, 2001ginalin@gmail.com, jgd@mx.nthu.edu.tw

Introduction

In three-dimensional integrated circuits (3D-IC), using low temperature bonding helps to reduce warpage and improve the joint reliability [1]. Recently, eutectic Sn-58Bi solder has emerged as a viable lead-free solder option due to its relatively low melting point of 138°C [2]. Researchers have been drawn to its benefits, including strong joint strength, superior creep resistance, low thermal expansion coefficient and excellent wettability [3]. However, Bismuth is inherently brittle and tends to segregate at the interface between Cu substrates and Sn-58Bi solders [4]. Besides, as micro-bump dimensions shrink to 10µm or smaller, the influence of solder and intermetallic compounds (IMCs) becomes more pronounced, directly impacting the mechanical properties and reliability of solder joints. It was reported that the formation of thick IMCs could shift the fracture path from the bulk solder to the solder/IMC interface, which negatively impacts the shear strength of solder joints [5]. Liu et al. revealed that low Zn concentration would affect the overall IMC growth rate, which can be utilized to control the IMC thickness in microbumps [6]. Additionally, doping Zn to Cu substrate can eliminate Bi segregation that causes interfacial embrittlement in Sn-58Bi/Cu bump [7]. Also, the addition of Zn to substrates contributes to greater stability in melting behavior [8]. Therefore, this study aims to enhance the mechanical properties of Cu/Sn-58Bi/Cu joints with sub-bump heights by doping Zn into substrates, elucidating the mechanisms of the improvement in mechanical properties.

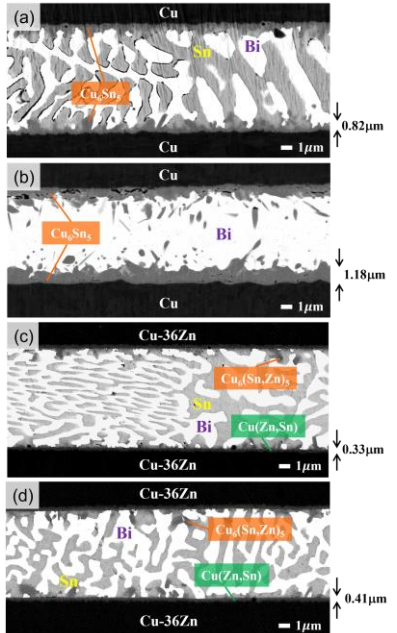
Materials and Methods

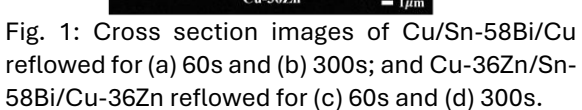
In this study, Cu and Cu-36Zn (wt%) were employed as double-sided substrates. Sn-58Bi solder balls with a diameter of 300µm were positioned between these substrates to form sandwich-structured samples, named as Cu/Sn-58Bi/Cu and Cu-36Zn/Sn-58Bi/Cu-36Zn. The dimensions of upper substrates were 3 mm x 3 mm x 0.4 mm, while the bottom substrates were 10 mm x 3 mm x 1 mm. All substrates were properly ground and cleaned by immersion in 2M HCl. In addition, water-soluble flux was applied to the surfaces to eliminate oxides and contaminants, ensuring that the components were free of impurities. The bonding process applied a constant pressure of 0.7 MPa, and the peak temperature of reflowing was 165°C for 60 and 300 seconds. Subsequently, the samples were air-cooled to room temperature. To acquire clear interfaces for microstructural observation, epoxy resin was used to mount samples after reflow process, and further polishing was carried out. Cross-sectional images and the element analysis of the samples were conducted using field emission scanning electron microscopy (FE-SEM/EDX; JSM-7600F, JEOL). Shear strength was assessed by a bonding tester (Condor Sigma, Xyztec), with a shear speed of 100µm/s and a shear height of 30µm above the bottom substrate.

Results and Discussion

Figs. 1 (a) to (d) are the cross-sectional back-scattered electron images of Cu/Sn-58Bi/Cu and Cu-36Zn/Sn-58Bi/Cu-36Zn samples reflowed at 165°C for 60 and 300 seconds,

respectively. The bump height of samples was controlled at $9.5 \pm 1 \mu m$. As shown in Figs. 1 (a) and (b), needle-like Cu₆Sn₅ IMC was revealed in Sn-58Bi/Cu interfaces after 60s reflow. When the reflow time extended to 300 seconds, Sn was completely consumed, leaving continuous Bi blocks, which suggests a deterioration in mechanical performance. Meanwhile, the morphology of Cu₆Sn₅ tended to transition from needle-like to scalloplike. In Cu-36Zn/Sn-58Bi/Cu-36Zn system, two types of IMCs, Cu₆(Sn,Zn)₅ and CuZn, were observed. The layer-type CuZn phase formed between Cu₆(Sn,Zn)₅ and Cu substrates, as illustrated in Figs. 1 (c) and (d). The microstructure following 60s reflow, as shown in Figs. 1(a) and (c), revealed that the average distance between Bismuth grains was 1.12µm for Cu/Sn-58Bi/Cu and 0.43 µm for Cu-36Zn/Sn-58Bi/Cu-36Zn. The substantially larger Bi grain size in Cu/Sn-58Bi/Cu samples could be attributed to two factors. Firstly, a thicker Cu-Sn IMC layer was formed in Cu/Sn-58Bi/Cu. The IMC thicknesses were measured to be 0.82µm and 0.33µm for Cu/Sn-58Bi/Cu and Cu-36Zn/Sn-58Bi/Cu-36Zn, respectively. Since Bi does not react with Sn or Cu, a significant amount of Sn was consumed during the process, resulting in the presence of larger Bi phase. In Cu-36Zn/Sn-58Bi/Cu-36Zn, the inhibition of Cu-Sn IMC growth can be attributed to the stronger Cu-Zn atomic interaction [9] and the formation of a stable Zn-rich phase at the Cu-36Zn/solder interfaces that impedes Cu dissolution into the solder [10]. Secondly, Zn atoms may diffuse into the solder during reflow process, acting as heterogeneous nucleation sites and thereby significantly refining the grain size of the eutectic Sn-58Bi alloy [11]. The finer eutectic Sn-58Bi in Cu-36Zn/Sn-58Bi/Cu-36Zn is expected to exhibit superior mechanical properties compared to that in Cu/Sn-58Bi/Cu. Although the grain size was not further reduced after 300s reflow in Cu-36Zn/Sn-58Bi/Cu-36Zn, as shown in Figs. 1 (d), no substantial growth of IMCs was observed, with thickness around 0.41µm. This finding indicates that the mechanical performance is unlikely to degrade significantly with prolonged reflow time. Shear test was performed to reveal shear strength. At least fifteen samples were evaluated for each condition, and the results are illustrated in Fig. 2 as a box plot. Under 60s reflow, the average peak force of Cu-36Zn/Sn-58Bi/Cu-36Zn was 55.19MPa, representing a 24.76% increase as compared to Cu/Sn-58Bi/Cu, which had a peak force of only 44.24MPa. Additionally, a 34.48% increase of end energy was observed in Cu-36Zn/Sn-58Bi/Cu-36Zn, suggesting a superior capacity for energy absorption under external stress. The improved mechanical performance can be linked to the reduced grain sizes of Sn-58Bi, which is the primary component of the solder joint. After 300s reflow, there was a slight reduction in both the average peak force and end energy of Cu/Sn-58Bi/Cu and Cu-36Zn/Sn-58Bi/Cu-36Zn. Nevertheless, the average peak force and end energy of Cu-36Zn/Sn-58Bi/Cu-36Zn exhibited increases of 24.09% and 28.57%, respectively, in comparison to Cu/Sn-58Bi/Cu. The observed rise in deviation may be ascribed to a transition in the fracture path from Sn-58Bi solder to the interface between the solder and IMCs due to thicker formation of IMCs [5]. As a result, the addition of Zn into the substrate effectively refined the grain sizes of Sn-58Bi and suppressed the growth of interfacial IMCs, leading to an overall enhancement of the mechanical properties, even following prolonged reflow durations.





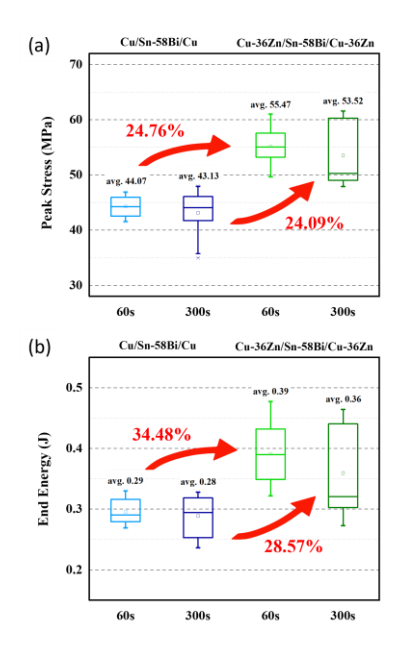


Fig. 2: (a) peak force and (b) end energy of Cu/Sn-58Bi/Cu and Cu-36Zn/Sn-58Bi/Cu-36Zn reflowed at 165°C for 60 and 300 seconds.

- [1] C. T. Ko, K. N. Chen, Low temperature bonding technology for 3D integration, *Microelectron. Reliab.* **52** (2) (2012) 302-311.
- [2] H. Okamoto, Bi-Sn (Bismuth-Tin), J. Phase Equilibria Diffus. 31 (2010) 205-205.
- [3] B. L. Silvaa, M. G.C. Xavierb, A. Garciac, J. E. Spinelli, Cu and Ag additions affecting the solidification microstructure and tensile properties of Sn-Bi lead-free solder alloys, *J. Mater. Sci. Eng. A.* **705** (2017) 325-334.
- [4] H. F. Zou, Q. K. Zhang, Z. F. Zhang, Interfacial microstructure and mechanical properties of SnBi/Cu joints by alloying Cu substrate, *Mater. Sci. Eng.* **532** (2012) 167-177.
- [5] O. Mokhtari, H. Nishikawa, Correlation between microstructure and mechanical properties of Sn-Bi-X solders, *Mater. Sci. Eng. A.* **651** (2016) 831-839.
- [6] Y. Liu, L. Pu, A. Gusak, X. Zhao, C. Tan, K. N. Tu, Ultra-thin intermetallic compound formation in microbump technology by the control of a low Zn concentration in solder, *Mater.* **12** (2020) 100791.
- [7] H. F. Zou, Q. K. Zhang, Z. F. Zhang, Eliminating interfacial segregation and embrittlement of bismuth in SnBi/Cu joint by alloying Cu substrate, *Scr. Mater.* **61** (3) (2009) 308-311.
- [8] R. W. Song, C. J. Fleshman, Y. C. Wang, S. Y. Tsai, J. G. Duh, IMC suppression and phase stabilization of Cu/Sn-Bi/Cu microbump via Zn doping, *Mater. Let.* **282** (2021) 128-73.
- [9] W. Feng, C. Wang, M. Morinaga, Electronic structure mechanism for the wettability of Sn-based solder alloys, *J. Electron. Mater.* **31** (2002) 185-190.
- [10] P. W. Huang, Z. Y. Wu, Y. K. Lee, C. S. Chao, S. Y. Tsai, S. Y. Chang, J. G. Duh, Microstructure and mechanical strength of Cu/Sn/Cu microbump via Ni and Zn doping into Cu substrate, *Mater. Chem. Phys.* **298** (2023) 350-358.
- [11] S. Zhou, Y. A. Shen, T. Uresti, V. C. Shunmugasamy, B. Mansoor, H. Nishikawa, Improved mechanical properties induced by In and In & Zn double additions to eutectic Sn58Bi alloy, *J. Alloys Compd.* **765** (2018) 1243-1252.

SCP 11.4:

Liquidus projection of the Fe-Nb-Si system

Aurélie Jacob^{1,2}, Clemens Schmetterer^{1,3} and Frank Stein⁴
11EK-2, Forschungszentrum Jülich, Jülich, Germany
2Now with: TU Wien, Karlsplatz 4, 1040 Vienna, Austria, aurelie.jacob@tuwien.ac.at
3Now with: University of Vienna, Währinger Str. 42, 1090 Vienna, Austria,
clemens.schmetterer@univie.ac.at
4Max Planck Institute for Sustainable Materials, Düsseldorf, Germany, stein@mpie.de

Introduction

In the context of the development of a high-Cr ferritic steel named Crofer 22H [1], it was found that the formation of Laves phases significantly improved the mechanical properties of the material. However, at the time of the study it was realized that there is a lack of fundamental understanding of this binary and ternary based (Fe,Cr)₂(Nb,Si,W) Laves phase. While the studies of several subsystems out of the five mentioned elements were published to date, e.g. Fe-Nb, [2], Fe-W [3], Cr-Nb [4], Fe-Cr-Nb [5], essential data on the important but complex Fe-Nb-Si system are still missing. Thus, in the present work, we present a comprehensive study of the Fe-Nb-Si system and more specifically its liquidus projection.

Materials and Methods

A series of 40 ternary Fe-Nb-Si alloys was prepared from high-purity metals by induction melting under Ar. The primary crystallization and co-existing phases were evaluated from as-cast microstructures using SEM/EDX and XRD measurements. Examples of typical ascast microstructures are shown in Figs. 1 and 2. The invariant reactions were then studied by DTA measurements carried out on a Netzsch Jupiter instrument up to 1500°C. For measurements at higher temperatures up to 1740°C, we used a Setaram SETSYS-18 DTA with heating and cooling rates of 10°C/min.

Results and Discussion

The Fe-Nb-Si system is characterized by the existence of six ternary intermetallic compounds and the extended phase fields of the two binary compounds Fe₂Nb (Laves phase) and Fe₇Nb₆ (μ phase), which both have a high solubility of Si. Due to the refractory nature of Nb, the ternary system possesses high melting temperatures which adds technical constraints for the determination of the liquidus projection (a two-dimensional representation of the ternary liquidus univariant lines).

Due to the presence of six ternary compounds and since most invariant reactions occur at temperatures above 1350°C, we used a combination of experimental techniques and a theoretical approach that included thermodynamic modeling and the application of the Alkemade theorem [6]. This combination allows us to provide a comprehensive and detailed description of the complex liquidus projection of the Fe-Nb-Si system.

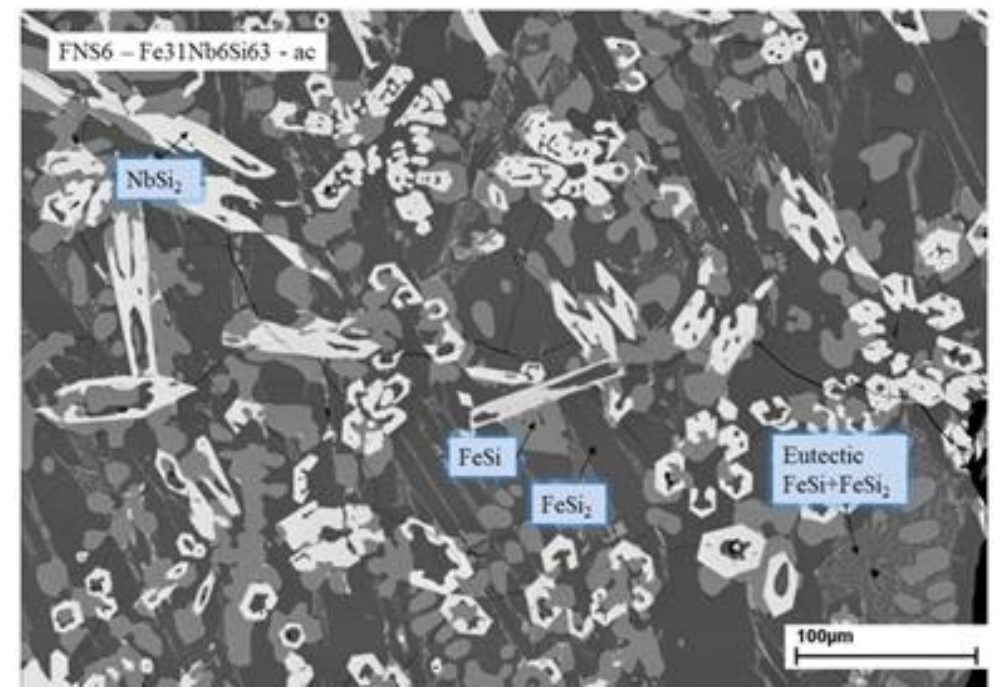


Fig. 1: As cast microstructure of $Fe_{31}Nb_6Si_{63}$ (composition in at. %) showing primary crystallization of FeSi.

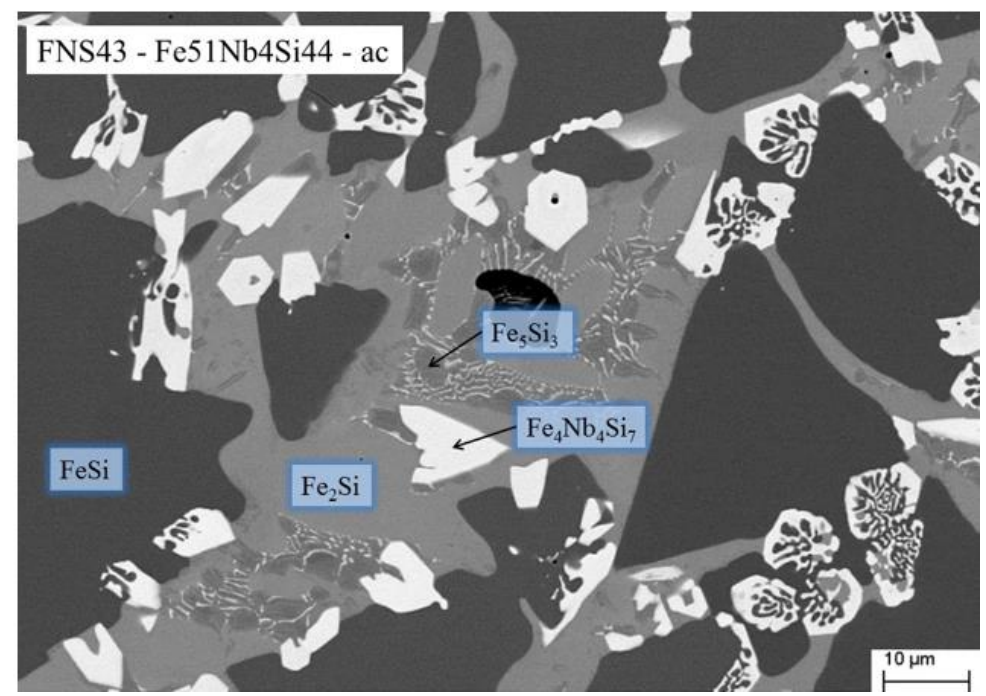


Fig. 2: As cast microstructure of $Fe_{51}Nb_{45}Si_{44}$ with FeSi as primary crystallizing phase.

- [1] J. Quadakkers, L. Niewolak, P. Ennis, Crofer 22H, **2006**, Patent Numbers: PCT/DE2007/000166, WO2007093148–A1
- [2] S. Voß et al., Journal of Phase Equilibria and Diffusion. 2011, 32, 97-104.
- [3] A. Jacob et al., Calphad. **2015**, *50*, 92-104.
- [4] C. Schmetterer et al., Journal of Phase Equilibria and Diffusion. **2014**, *35*, 434-444.
- [5] A. Jacob et al., Journal of Alloys and Compounds. **2015**, 648, 168-177.
- [6] F. Stein et al., Journal of Phase Equilibria and Diffusion. 2024, 45, 489-501.

SCP 11.5:

Implications for the homogeneity range of the α_c-Al-Si-Mn phase with the 3d-transition metal elements V, Cr, Fe, Co, Ni, Cu, Zn

Hanka Becker¹, Andreas Leineweber²

¹Institute of Materials, Technology and Mechanics, OVGU Magdeburg, Universitätsplatz 2, 39106 Magdeburg, Germany, hanka.becker@ovgu.de

²Institute of Materials Science, TU Bergakademie Freiberg, Gustav-Zeuner-Straße 5, 09599 Freiberg, Germany, andreas.leineweber@iww.tu-freiberg.de

Introduction

The α_c-Al-Si-Mn phase, often labeled as Al₉Mn₂Si_{1.8}, frequently occurs in Al-Si alloys containing Fe and further 3d-transition metal elements which enrich in the alloy during recycling. Furthermore, the α_c phase can evolve in intermetallic layers formed during bonding of Al- and Fe-based alloys. The α_c phase has the space group $Im\overline{3}$ (or $Pm\overline{3}$ for high contents of Fe versus Mn) [1]. The crystal structure with ideally 138 atoms per unit cell is regarded as 1/1 approximant to icosahedral quasicrystals. It can be described as bcc-based packing of near icosahedral clusters with some, so-called, glue atoms in between the clusters [1] (Figure 1). The 3d-transition metal elements occupy the outer icosahedron of the clusters comprising 17.3 at%. Al, Si and also Cu occupy the other sites [2]. A specific characteristic of the α_c phase is its broad homogeneity range extending from the ternary Al-Si-Mn system [3] into quaternary and quintenary systems. The ternary α_c -Al–Si–Mn phase provides a narrow homogeneity range for Mn with 17–18 at% Mn and a broad range for Al and Si with variation of Si from 7 to 17at%. It is well known that Fe can replace 97% of Mn [4]. Mn can completely be substituted by Fe+Cr in ratios from $Fe_{0.88}Cr_{0.12}$ [5] to $Fe_{0.51}Cr_{0.49}$ [6]. Additionally, it was recognized that the Si content and the ratio of the 3d-transition metal elements interact [7]. For a narrow range of chemical composition of the α_c phase containing 9 at% Si and varying the Mn vs. Fe content, a Hume-Rothery based approach was concluded as stabilization mechanisms [1], assuming that the phase can exist for a specific very narrow range of electrons per atom. Although it is known that further 3d-transition metal elements solve in significant amounts in the α_c phase, the homogeneity range is not known and underlying principles based on the crystal structure are not understood.

The aim of the present work is to clarify the homogeneity range of the α_c phase and to derive a Hume-Rothery based substitutional rule for the phenomenological description of the homogeneity range of the α_c phase considering a large range of transition metals of the 3d series. This will support the implementation of the α_c phase in phase diagrams beyond the Al–Si–Fe–Mn system and the understanding of the formation of the α_c phase in secondary Al–Si alloys and intermetallic layers.

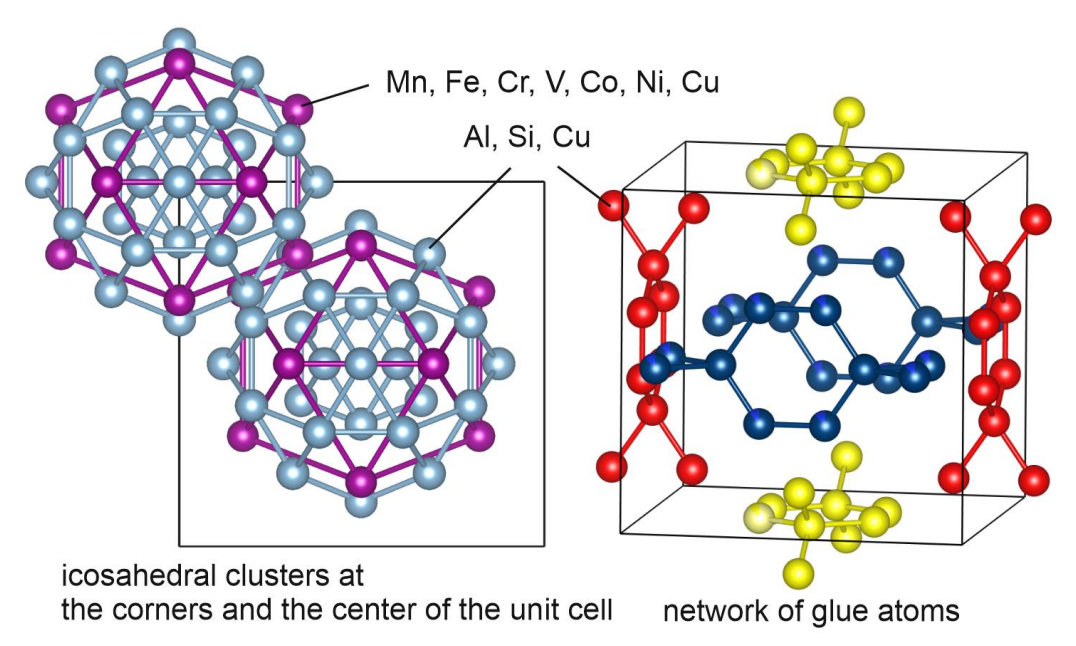


Figure 1: Crystal structure of the α_c phase illustrating exemplarily icosahedral clusters located at the center and one corner of the cubic unit cell and the glue atoms in between of the clusters.

Materials and Methods

In the present study, the intermetallic phase formation in quaternary Al7.1at%Si(1.5at%x)FexM alloys and quintenary Al7.1at%Si0.6at%Fe0.3at%Mn/Cr0.6at%M alloys with M =V, Cr, Mn, Co, Ni, Cu, Zn and x = 0, 0.3, 0.375, 0.6, 0.75 at% were investigated for cooling rates of 0.05. 11.4 K/s. Additionally, quaternary Al7.1at%Si1.5at%Fe4at%Cu was investigated. The alloys were produced by arc melting from the pure elements and then remolten at 850°C or 950°C in Ar atmosphere in Al₂O₃ crucibles prior cooling. The microstructure of all samples was scrutinized using scanning electron microscopy. EDS measurements were employed for measurement of the chemical composition with minimum 5 points per condition. Only particles of sufficient size to cover the excitation volume of the EDS measurement were used. EBSD patterns were analyzed for phase discrimination.

Results and Discussion

The microstructures of all investigated alloys consist of Al dendrites surrounded by an AlSi eutectic region. Additionally, various intermetallic phases occur while the present study focuses on the $\alpha_{\rm c}$ phase only. The $\alpha_{\rm c}$ phase occurs in the quaternary alloys with Fe for all cooling conditions when V, Cr and Mn are present. Additionally, it occurred in the alloy with a Cu content of 4 at%. In the quintenary alloys, the $\alpha_{\rm c}$ phase is observed for all investigated conditions except of the quintenary alloy with Cr and Cu. The characteristic morphology of the $\alpha_{\rm c}$ phase allows to distinguish the stage of formation. Coarse polyhedral or coarse dendritic particles spanning across other microstructural components have formed as primary particles, while finer dendritic structures located within Al dendrites or within the interdendritic space have formed during co-dendritic or co-eutectic solidification. The chemical composition of the $\alpha_{\rm c}$ phase differs with the stage of formation.

In the present investigation, the chemical composition of the α_c phase ranges from 8 to 12 at% Si. The sum of the 3d-transition metal element contents is in all cases between 16 to 17.5 at% while their specific fractions vary considerably. To facilitate an interpretation

of the large number of compositional data, the Hume-Rothery based approach is adapted. The ratio of valence electron per atom e/a is evaluated. While for Al and Si e/a values of 3 and 4 can be clearly adapted, unambiguous values are not directly available for the 3d-transition metal elements and the value might vary depending on the amount and type of the present 3d-metal elements. Pragmatically, an e/a value of 2 is chosen for Mn and kept constant. Hence, it is accepted that the ternary α_c phase is stable in a range of the total number valence electrons per atom Ω which depends on the Al vs. Si content (Figure 2). Thus, the e/a values for V, Cr, Fe, Ni, Co and Cu (from A to F) are determined from the experimental data according to

$$\Omega = (3x_{\rm Al} + 4x_{\rm Si} + 2x_{\rm Mn} + Ax_{\rm Fe} + Bx_{\rm V} + Cx_{\rm Cr} + Dx_{\rm Co} + Ex_{\rm Ni} + Fx_{\rm Cu})/138$$
(1)

with x_M representing the alloy composition in at%. The following a/e values result: A=1.91, B=1.81, C=1.97, D=1.6, E=1.34, F=3.25. The result are graphically represented in Figure 2 along with results from literature. The very good fit to the initial line even for α_c phase without any Mn supports that a Hume-Rothery stabilization mechanism is applicable to the α_c phase. Thereby, Fe, Cr and V contribute with e/a values near to the assumed e/avalue of 2 for Mn which explains their broadly stabilizing effect. The e/a values of Co and Ni are significantly smaller and are consistent with the observation that the α_c phase forms with Co and Ni in the Fe-containing Al-Si alloys in the additional presence of Mn and Cr as α_c phase stabilizer. Cu is known to occupy not only the outer icosahedron but also Al and Si sites which is in agreement with an e/a value larger than 2 which likely reflects two different e/a values. Note that, according to those results, simpler electron counting rules related to the location of the elements in the periodic table do not apply. The robustness of the results will be further discussed based on defect structures of the α_c phase as vacancies. Interpretation related to the stabilization mechanisms of icosahedral quasicrystals and related approximants will be addressed. Conclusions for the prediction of the homogeneity ranges of the α_c phase will be presented.

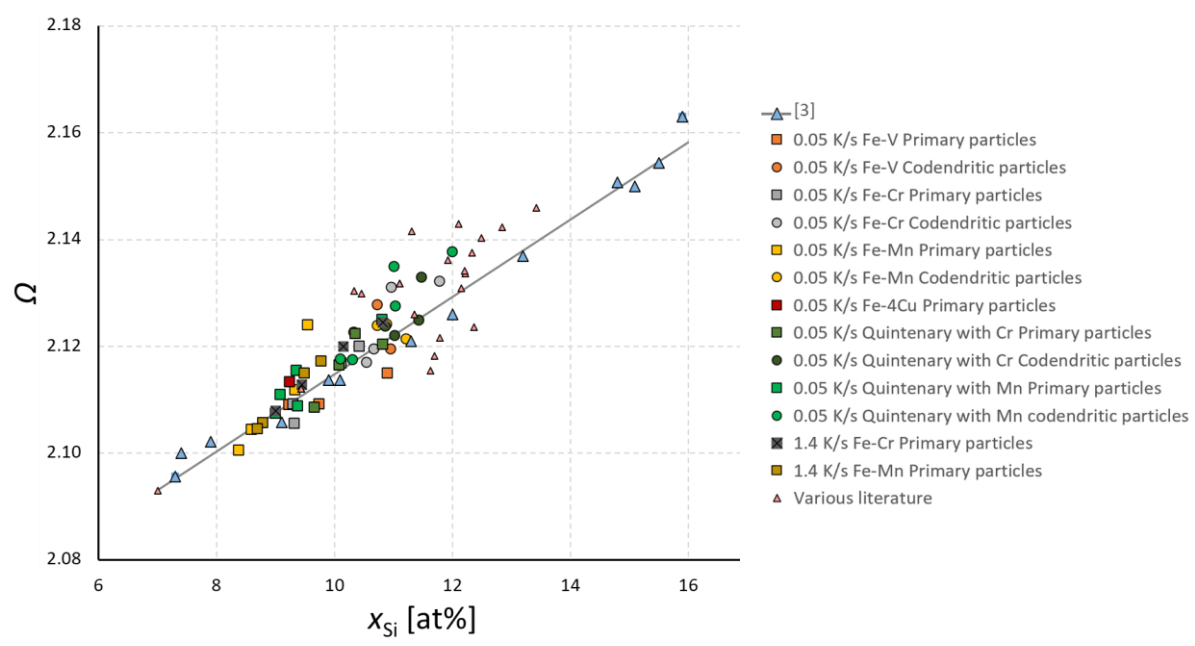


Figure 2: Total number valence electrons per atom Ω vs. Si content x_{Si} according to equation 1 in the α_c phase contained Fe-containing Al-Si alloys with the transition metal elements V, Cr, Mn, Co, Ni, Cu, Zn.

- [1] T. Takeuchi, T. Onogi, E. Banno, U. Mizutani, Mater. Trans. **2001**, *42*, 933–938.
- [2] V. Simonet, F. Hippert, R. A. Brand, Y. Calvayrac, J. Rodriguez-Carvajal, A. Sadoc, Phys. Rev. **2005**, *72*, 024214 1–14.
- [3] N. V. Kazennov, K. B. Kalmykov, S. F. Dunaev, N. L. Zvereva, N. E. Dmitrieva, Mosc. Univ. Chem. Bull. **2010**, *65*, 374–379.
- [4] H. Y. Kim, T. Y. Park, S. W. Lee, H. M. Lee, J. Cryst. Growth. **2006**, *291*, 207–211.
- [5] A. Fabrizi, G. Timelli, IOP conference series: Mater. Sci. Eng. **2016**, *117*, 012017 1–6.
- [6] Z. Zhou, Z. Li, Y. Xie, X. Wang, Y. Liu, Z. Long, F. Yin, Int. J. Mater. Res. **2015**, *106*, 470–480.
- [7] J. E. Tibballs, R. L. Davis, B. A. Parker, J. Mater. Sci. **1989**, *24*, 2177–2182.

SCP 11.6:

Crystallography and mechanical properties of τ_2 -Al₃FeSi

Lukas Richter¹, Andreas Leineweber¹

¹Institute of Materials Science, TU Bergakademie Freiberg, Gustav-Zeuner-Straße 5, 09599 Freiberg, Germany, lukas.richter@iww.tu-freiberg.de

Introduction

Lightweight design often requires combinations of the two most important metallic construction materials, aluminium and steel. One method to achieving joints between these dissimilar materials is hybrid casting the aluminium to a steel substrate, whereby the bonding can be strongly supported by prior deposition of an Al-Si bond coating [1]. As expected, at the contact between the steel and the Al-rich bond coat, intermetallic phases of the Al-Fe-Si ternary alloy system develop.

In order to contribute to understanding of the reliability of the joints prepared by the hybrid casting upon mechanical load and, in particular, the role of the Al-Fe-Si phases, we (re)investigate their fundamental properties. This involves crystal structure, typical microstructural features as well as mechanical properties studied by nanoindentation. In the present contribution we focus on the τ_2 phase of the approximate formula Al₃FeSi. Its rhombohedral crystal structure has been reported in two apparently independent works [2, 3]. The reported crystal structure models seem to agree about an (unusual) Fe site partially occupied by Al and about the preferential location of the Si atoms, in spite of having a very similar scattering power as Al.

Materials and Methods

Samples of various compositions within the extended homogeneity range of τ_2 -Al₃FeSi have been produced from pure elements by arc melting and subsequent heat treatment at 800°C to archive chemical equilibrium. After quenching, the samples have been investigated by X-ray diffraction (XRD) on the powdered alloy for the reassessment of crystal structure models indicating the mixed occupancy of iron sites in the crystal structure by Al and Si [2, 3]. As prerequisite to the planned and to be presented nanoindentation studies, the microstructure of cross-sectioned alloy was analysed by scanning electron microscopy including electron backscatter diffraction (EBSD).

Results and Discussion

XRD analysis of the intermetallic phase τ_2 -Al $_3$ FeSi as outlined in Fig. 1 confirmed the presence of a rhombohedral crystal, consistent with reported literature data of τ_2 -Al $_3$ FeSi. Rietveld refinement indicates a nearly complete occupation of the designated iron Wyckoff sites, suggesting a highly ordered atomic arrangement under the treatment conditions and the composition of the τ_2 attained in the corresponding sample.

EBSD measurements as shown in Fig. 2 were conducted on the same equilibrated alloy which was powdered for diffraction analysis. This allowed evaluating the multiphase grain microstructure and texture of the phases. The EBSD maps revealed a non-textured grain orientation distribution being a good starting point to study the orientation-dependent indentation properties.

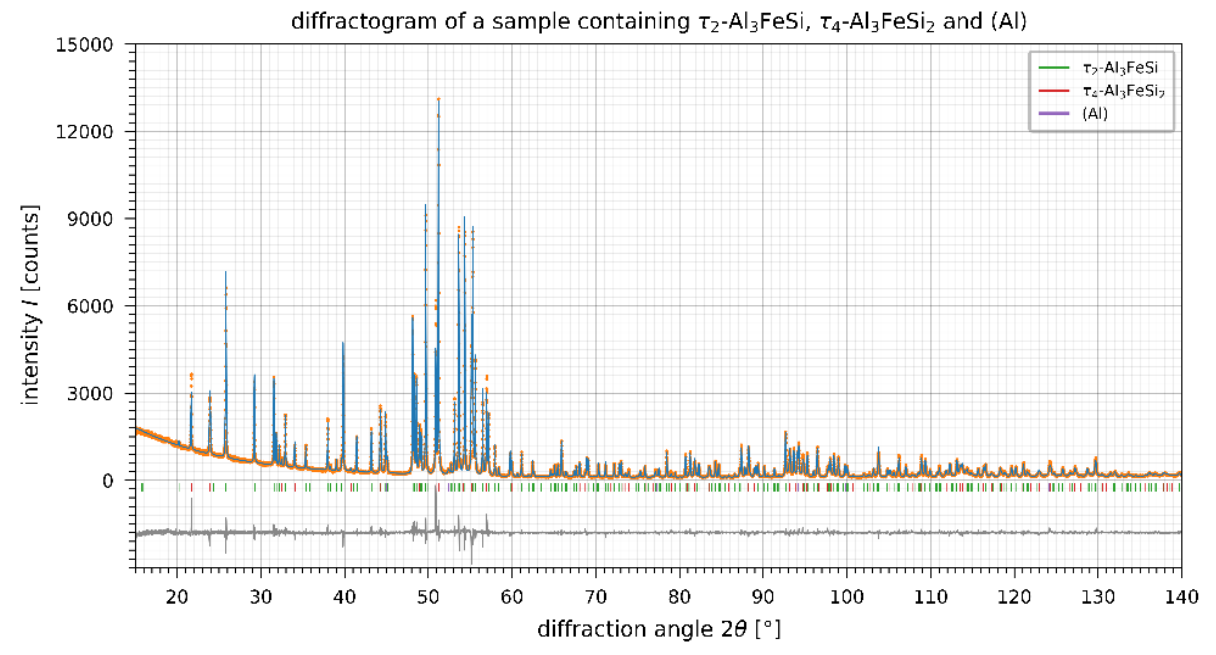


Fig. 1: X-ray diffraction pattern (CoK α_1 radiation) from a powder of an Al-Fe-Si alloy equilibrated at 800 °C and quenched containing τ_2 -Al₃FeSi, lesser amounts of τ_4 -Al₃FeSi₂ and solidified Al solid solution: Red observed data points, blue calculated intensity profile (Rietveld method) and grey difference curve.

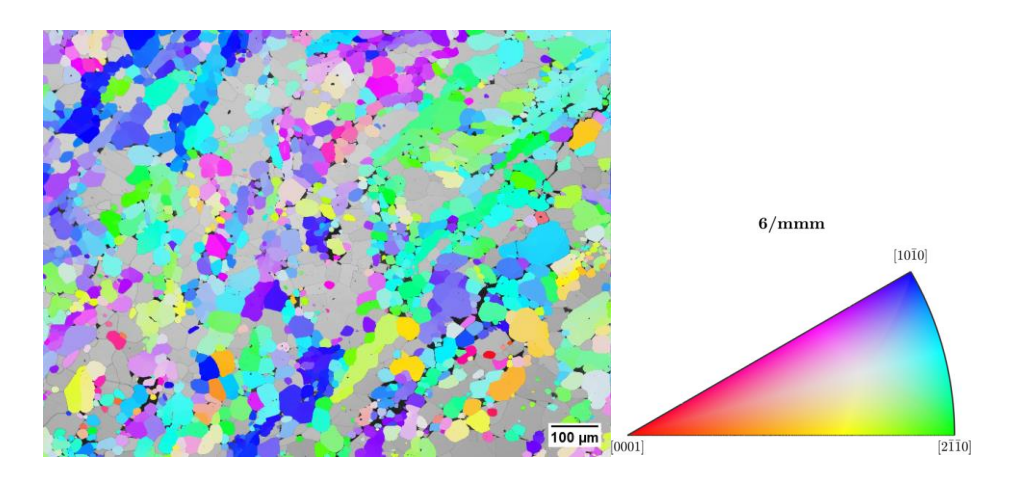


Fig. 2: EBSD inverse-pole figure map of the cross-sectioned alloy also investigated in Fig. 1. Only the orientation of the τ_2 phase is depicted according to the colorkey with respect to the cross section normal; the grey regions depict the indexing confidence of the non- τ_2 regions (mainly τ_4).

- [1] S. Martin, D. Sulik, X. Fang, H. Becker, A. Leineweber, Intermetallics **2022**, *151*, 107712.
- [2] J. Roger, E. Jeanneau, J. Viala, Z. Kristallogr. **2011**, *226*, 805-813.
- [3] K. Sugiyama, N. Kaji, K. Hiraga, J. Alloys Compd. **2004**, 368, 251-255.

Poster Sessions

P 001:

A large family of crystal structures observed for transition groupmain group metal intermetallic phases: structures derived from body-centred cubic with vacancies

Andreas Leineweber¹, Guido Kreiner¹

¹Institute of Materials Science, TU Bergakademie Freiberg, Gustav-Zeuner-Straße 5, 09599 Freiberg, Germany, andreas.leineweber@iww.tu-freiberg.de

Introduction

The crystal structures of intermetallic phases developing by combining transition metals (7) and main group metals (B) are often quite complex and difficult to rationalize. One relatively successful approach is known for the crystal structures of the Hume-Rothery phases, where certain types of characteristic crystal structures develop as a function of the electron/atom ratio e/a (counting s+p electrons) [1]. This principle is quite successful for T = Cu, Ag and Au combined with B = Zn, Cd, Hg (and elements to the right; thus counting Zn-Hg as main-group metals). For example, in the prototypical Cu-Zn system, there is a β-CuZn phase with a bcc (A2) structure at high and ordered CsCl (B2) structure at lower temperatures. This phase has e/a = 1.5. For higher Zn contents (and higher e/a) the γ-Cu₅Zn₈ phase occurs, which can be conceived as an ordered 3 x 3 x 3 cubic superstructure of bcc (A2) with a fraction of y_{Va} = 1/27 vacant sites (2 "vacancies" per cubic supercell). Mott & Jones rationalized the structure transition from β to γ upon increasing e/a by considering a free-electron like Fermi sphere increasing in size and coming into contact with strongly scattering Brillouin (or Jones) zone boundaries [2]. Later Schubert tried to generalize the structure principle by reporting other intermetallic phases with bcc-derived T-B-Va crystal structures [3,4] and tried to elaborate special real-space concepts to rationalize chemical bonding. Although these bonding concepts have rarely been adopted by others (and are likely obsolete), the structure collections made in this context are invaluable.

The presenting author, again and again, has been rediscovering this structure principle in the course of the research he was and is involved in. Thereby, it was possible to assign many previously known and some new crystal structures of intermetallic phases to the corresponding family of crystal structures, in particular, also for low symmetry, e.g., monoclinic and triclinic cases. In the present contribution an overview is presented on the occurrence of such examples.

Materials and Methods

Basic experimental crystal structure information is unit cell, space group symmetry and atomic coordinates, including possible information on disorder concluded from the diffraction data. Furthermore, data from first-principles calculations, either dedicatedly performed by cooperation partners or from corresponding databases (materials project, OQMD, AFLOW) can be used as basis for structure analysis. Until now the relation to the bcc structure is elaborated by visual inspection and by finding superstructure cells formulated as a matrix equation relating line vectors containing the basis vector of the parent-bcc and the derived superstructure (*X*):

$$(\mathbf{a}_X \quad \mathbf{b}_X \quad \mathbf{c}_X) = (\mathbf{a}_{bcc} \quad \mathbf{b}_{bcc} \quad \mathbf{c}_{bcc})\mathbf{P}.$$
 (1)

The determinant of the transformation matrix describes the factor by which the volume of the supercell is larger than that of a bcc parent cell. This is conveniently done for the conventional unit cells, while a version of Eq. (1) pertaining to the primitive unit cells is a unique measure for the loss of translational periodicity [5]. In this case $n = \det(\mathbf{P})$ becomes 2, 3, 4... depending on the size of the primitive supercell size. Methods exist to quantify the displacements of the atoms from the ideal sites and to evaluate the (deviatoric) strain quantifying the deformation of the lattice away from an ideally pseudocubic one [6].

Results and Discussion

The intermetallic phases which can be identified to exhibit bcc-derivative $T_{y_T}B_{y_B}$ Va $_{y_{Va}}$ crystal structures $(y_T+y_B+y_{Va}=1)$ can be characterized according to a multitude of features: the molar fraction of B $x_B=y_B/(y_T+y_B)$, the vacancy fraction y_{Va} , the group number of T and B, the number of atoms + vacancies per primitive superstructure cell n. The classical e/a ratio suffers from the difficulty to assign a unique value of e/a to the T elements (except for Cu, Ag, Au with e/a=1). As common practice (but not fully satisfying), the value of 0 is adopted for such T elements. While the ideal structures can be derived by decorating the supercell, the experimentally observable crystal structure will be characterized by macroscopic deviatoric strains and the type of local displacements of the atoms from their ideal sites. This may further reduce the symmetry away from what is implied by decoration of the supercell, but sometimes also new symmetry elements are generated.

Table 1 lists a series of phases with corresponding crystal structures. There is a wide range of B contents but also a wide range of e/a values well exceeding the ranges classically considered [1,2]. Also, the vacancy contents can be much larger than the values of $y_{Va} = 1/27$ of the classical case of Cu_5Zn_8 (Figure 1a).

Table 1 includes the monoclinic intermetallic phases Fe $_{13}$ Ga $_9$, α -Fe $_6$ Ga $_5$ and Fe $_3$ Ga $_4$ occurring in the Fe-Ga system, which were recently investigated in more detail by the present authors. Identification of these structures as bcc-derivative $T_{y_T}B_{y_B}$ Va $_{y_{Va}}$ ones allows identifying their interrelations. The case of α -Fe $_6$ Ga $_5$ is shown in Figure 1b. As in the case of Cu $_5$ Zn $_8$, B atoms (here Ga) collapse into the vacancies (red). Results from microstructure analysis by means of scanning electron microscopy and electron backscatter diffraction of alloys containing these phases shows characteristic orientation relationships between grains which reflect the symmetry reduction from a real or virtual cubic phase to the ordered monoclinic structure variant.

Table 1 List of bcc-derivative $T_{y_T}B_{y_B}$ Va $_{y_{Va}}$ crystal structures of transition metals T, main group elements B (including Zn, Cd, Hg) and vacant sites Va. n is the number of atoms + vacancies per primitive unit cell, y_{Va} is the vacancy fraction and e/a is the electron/atom ratio.

Example	Space	n	Χ _B	y Va	e/a
	group				
W	Im3̄m	1	-	0	-
NiAl	Pm3̄m	2	0.5	0	1.5
β'-CuZn	$Pm\overline{3}m$	2	0.5	0	1.5
Ni ₂ Al ₃	$P\overline{3}m1$	6	0.6	1/6 = 0.167	1.8
AuAl ₂	Fm3m	4	0.67	1/4 = 0.25	2.33
CuAl ₂	I4/mcm	8	0.67	1/4 = 0.25	2.33
MnGa₄	Im3̄m	8	0.8	3/8 = 0.375	2.4
γ-Cu₅Zn ₈	I43m	27	0.62	1/27 = 0.037	1.62
Cu ₉ Al ₄	P43m	54	0.31	1/27 = 0.037	1.62
ζ-Fe _{6.41} Al _{12.59} [6]	$P\overline{1}$	21	0.66	2/21 = 0.095	1.99
Ni ₃ Sn ₄ [6]	C2/m	10	0.57	3/10 = 0.3	2.3
Fe ₁₃ Ga ₉	C2/m	24	0.41	1/12 = 0.083	1.23
α-Fe ₆ Ga₅	C2/m	24	0.45	1/12 = 0.083	1.36
Fe ₃ Ga ₄	C2/m	24	0.57	1/8 = 0.125	1.71
Cu ₁₀ Sn ₃	P6 ₃ /m	27	0.23	1/27 = 0.037	1.69
Ni ₃ Sn ₂	Pnma	32	0.4	1/6 = 0.167	1.6

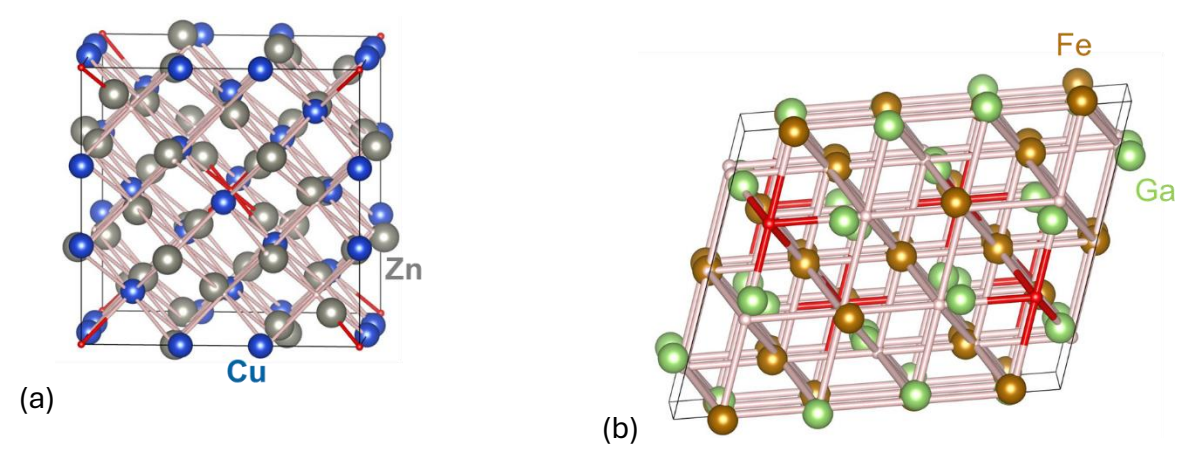


Figure 1: Crystal structures of (a) Cu_5Zn_8 (γ brass) and (b) α -Fe₆Ga₅ superposing the ideal atomic/vacancy sites (pink/red) with nearest-neighbour $\frac{1}{2}\langle111\rangle_{bcc}$ bonds and large actual atomic sites, illustrating the displacements of the atoms from the ideal sites.

- [1] T.B. Massalski, H.W. King, Prog. Mater. Sci. **1961**, *10*, 3–78.
- [2] N. F. Mott, H. Jones, The Theory of the Properties of Metals and Alloys, Clarendon Press, Oxford, 1936.
- [3] K. Schubert, Kristallstrukturen zweikomponentiger Phasen, Springer, Berlin/Heidelberg, 1964.
- [4] K. Schubert, Structure and Bonding **1977**, 33, 139–177.
- [5] G.L.W. Hart, R.W. Forcade, Phys. Rev. B **2008**, *77*, 224115.
- [6] A. Leineweber, Z. Kristallogr. **2023**, *238*, 321-332.

P 002:

Correlation between mechanical flexibility and magnetic properties in metallic microwires

Alexander Chizhik¹, Arcady Zhukov²

¹University of Basque Country, UPV/EHU, 20018 San Sebastian, Spain, oleksandr.chyzhyk@ehu.eus ²IKERBASQUE, Basque Foundation for Science, 48011 Bilbao, Spain, arkadi.joukov@ehu.eus

Introduction

Magnetic microwires occupy the great segment in the industrial sensor application. As one of the recognized leaders in magnetic sensors, they attract much attention of researchers working in related scientific fields. One of the central problems of the sensor application of amorphous microwires is the optimization of the basic parameters. In the frame of this problem, we have performed systematical study of the surface magnetic properties of microwires using magneto-optical Kerr effect (MOKE) technique. The influence of mechanical stresses on giant magneto-impedance (GMI) effect of wires and microwires is studied quite extensively. Taking into account the surface nature of the GMI effect, the MOKE study of the stress induced transformation of surface magnetic structure acquires a special meaning [1]. In this situation, we directed our efforts to the study of influence of the external mechanical stresses (transversal and longitudinal) on the surface anisotropy and in turn on the surface magnetic structure.

The main idea of the present work is the controlling of the transformation of the domain structure induced by the torsion and bending stress of different values and directions and determination of the stress caused changes of the surface magnetization reversal. Knowing the basic difference in the magnetic structures of the Fe- and Co-rich microwires, we expected to found the strong influence of the external stress on the magnetic behavior in microwires of two different types.

Materials and Methods

We studied glass-coated amorphous microwires with nominal compositions $Fe_{71.7}B_{13.4}Si_{11}Nb_3Ni_{0.9}$ (metallic nucleus radius 40 µm, glass coating thickness 20 µm) (Ferich microwire) and $Co_{64,04}Fe_{5,71}B_{15,88}Si_{10,94}Cr_{3.4}Ni_{0,3}$ (metallic nucleus radius 47 µm, glass coating thickness 16 µm) (Co-rich microwire). The microwires were fabricated using a modified Taylor–Ulitovsky (quenching-and drawing) method. The study of the magnetic domains in the surface of microwires has been performed by means of polarizing microscopy working in reflective mode using the longitudinal MOKE configuration [1]. Torsional, bending and spiral mechanical stresses have been applied to amorphous microwire to transform the magnetic structure (Fig. 1). Also, magnetic metallic microwire was subjected to a bending-annealing-unbending procedure.

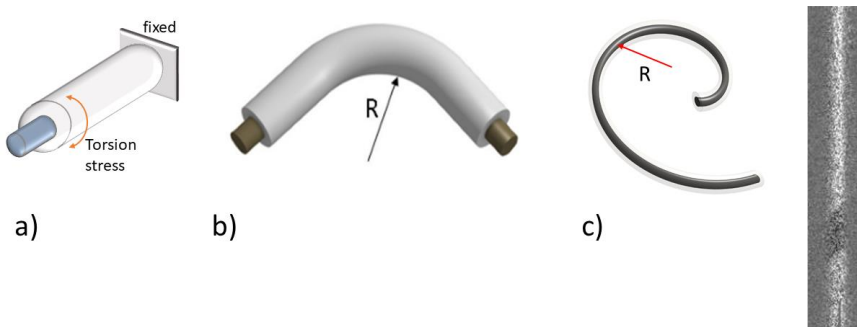


Fig. 1: Torsion (a), bending (b) and spiral (c) mechanical stresses applied to the studied microwires.

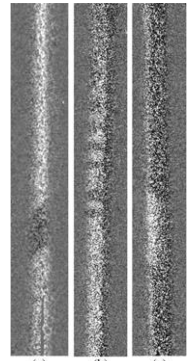


Fig. 2: MOKE images of surface domain structure obtained in Corich microwire in the presence of torsion stress with angle ϕ : (a) -180° (-21π rad·m⁻¹); (b) 45° (5π rad·m⁻¹); (c) $+180^{\circ}$ (21π rad·m⁻¹).

Results and Discussion

The strong influence of torsion stress on domain structure and magnetization reversal has been found in Fe- and Co-rich microwires (Fig. 2). The limits of the stress-induced inclination of magnetization have been determined in two types of microwires. The stress-induced rotation of surface magnetization occurs across the longitudinally magnetized state in Fe-rich and transversally magnetized state in Co-rich microwires. The jump between states with different inclination of magnetization and the formation of the dynamic structure containing different magnetic states are reversible mechanisms of the magnetization reversal in magnetic microwires.

Our concept for explaining this phenomenon revolved around the presence of a transverse stress gradient from tension to compression within the bent specimen. This gradient extends across the axial axis of the microwire. As per existing models of back stresses, annealing under such a stress gradient leads to alterations in the ratio of the inner core to outer shell size. Consequently, this induces changes in the magnetic structure both internally and on the surface of the sample. Variances in the gradient degree across different areas of the microwire contribute to the diverse domain structure observed, particularly on the sample's surface.

Spiral annealing introduces two notable effects. First, the bending induces a gradient of internal stresses across the sample's cross-section, transitioning from tensile stress to compressive stress. Second, the variation in the sample's curvature along its length results in a smooth longitudinal change in this stress gradient. On the microwire's surface, a gradual variation in the anisotropy field along the sample length was observed. This variation exhibited a near-linear correlation between the local anisotropy field and the local geometric curvature of the sample.

References

[1] A. Chizhik, J. Gonzalez, Magnetic Microwires: A Magneto-Optical Study, Singapore: Pan Stanford Publishing Pte. Ltd. **2014.**

P 003:

In Situ Synchrotron HE-XRD Investigation of Phase Stability and Transformation Kinetics in a Ternary Eutectic V-9Si-6.5B Alloy

Zahra Sabeti¹, Roja Rani Korrayi², Georg Hasemann¹, Andreas Stark², Florian Pyczak², Manja Krüger²

¹ Otto-von-Guericke University Magdeburg, Institute of Materials, Technologies and Mechanics, Universität Platz 2, 39106 Magdeburg, Germany, zahra.sabeti@ovgu.de, georg1.hasemann@ovgu.de, manja.krueger@ovgu.de.

² Helmholtz-Zentrum Geesthacht, Institute of Materials Physics, Max-Planck-Str. 1, 21502 Geesthacht, Germany, Roja.Korrayi@hereon.de, <u>andreas.stark@hereon.de</u>, florian.pyczak@hereon.de.

Introduction

Recent advances in refractory metal-silicon-boron (RM-Si-B) systems have revealed complex phase evolution paths [1,2]. Yet, the dynamic mechanisms governing intermetallic stability under extreme thermal conditions remain poorly resolved [2]. This study addresses this gap through a comprehensive in situ analysis of phase transitions in a ternary eutectic V-9Si-6.5B (at.%) alloy, by combining synchrotron high-energy X-ray diffraction (HE-XRD) with dilatometry, to elucidate real-time crystallographic and microstructural evolution during heating up to 1590°C.

Recently, the isothermal section of the V-Si-B phase diagram at 1400°C was assed experimentally [3] highlighting the new ternary phase V_8SiB_4 in the V-Si-B system [1]. The formation of the new V_8SiB_4 phase occurs during a heat treatment at 1400°C for 100h and it might be a transformation product of the V_5SiB_2 phase. The present work aims to investigate the $V_5SiB_2 - V_8SiB_4$ transition.

Materials and Methods

The alloy, synthesised via arc melting [4], was subjected to a rapid heating rate of $\approx \! 120^{\circ} \text{K/min}$ and isothermal holding times up to 90 minutes at 1400°C to investigate phase stability and transformation kinetics of the V-9Si-6.5B (at.%) alloy, specifically the $V_{5} \text{SiB}_{2}$ phase and its potential conversion to the newly identified $V_{8} \text{SiB}_{4}$ phase. HE-XRD data, captured in a transmission geometry (73.3 keV beam energy, 0.16934 Å wavelength), were analysed by Rietveld refinement to determine the lattice parameters, phase fractions, and growth dynamics.

Results and Discussion

The results indicate that the relative stability of the phases V, V_3Si , V_5SiB_2 , and the newly identified V_8SiB_4 phases is influenced by temperature and the holding time. As shown in Fig. 1(a) for the virgin (as-cast) specimen, no V_8SiB_4 was initially found at room temperature (RT). In Fig. 1(b), it is revealed that the fraction of V_8SiB_4 increased to 6% after 8 minutes at 1400°C and exhibited an exponential growth rate, reaching about 22% after 90 minutes of annealing at 1400°C.

In contrast, the fraction of the V_5SiB_2 phase decreased significantly, dropping from 23% (Fig. 1(a)) to 5% (Fig. 1(b)) over the same period of time. This suggests that the formation of V_8SiB_4 results from a transformation of V_5SiB_2 to V_8SiB_4 at 1400°C. Similarly, the fraction of the V_3Si phase decreased from an initial 31% at RT to 16% after holding at 1400°C for 90 minutes, indicating its instability at elevated temperatures.

This work provides unique insights into the RM-Si-B systems, emphasising the critical role of thermal history in governing intermetallic stability. This methodology offers critical

insights into transformation kinetics, enhancing microstructural optimisation for high-temperature applications in V-Si-B alloys.

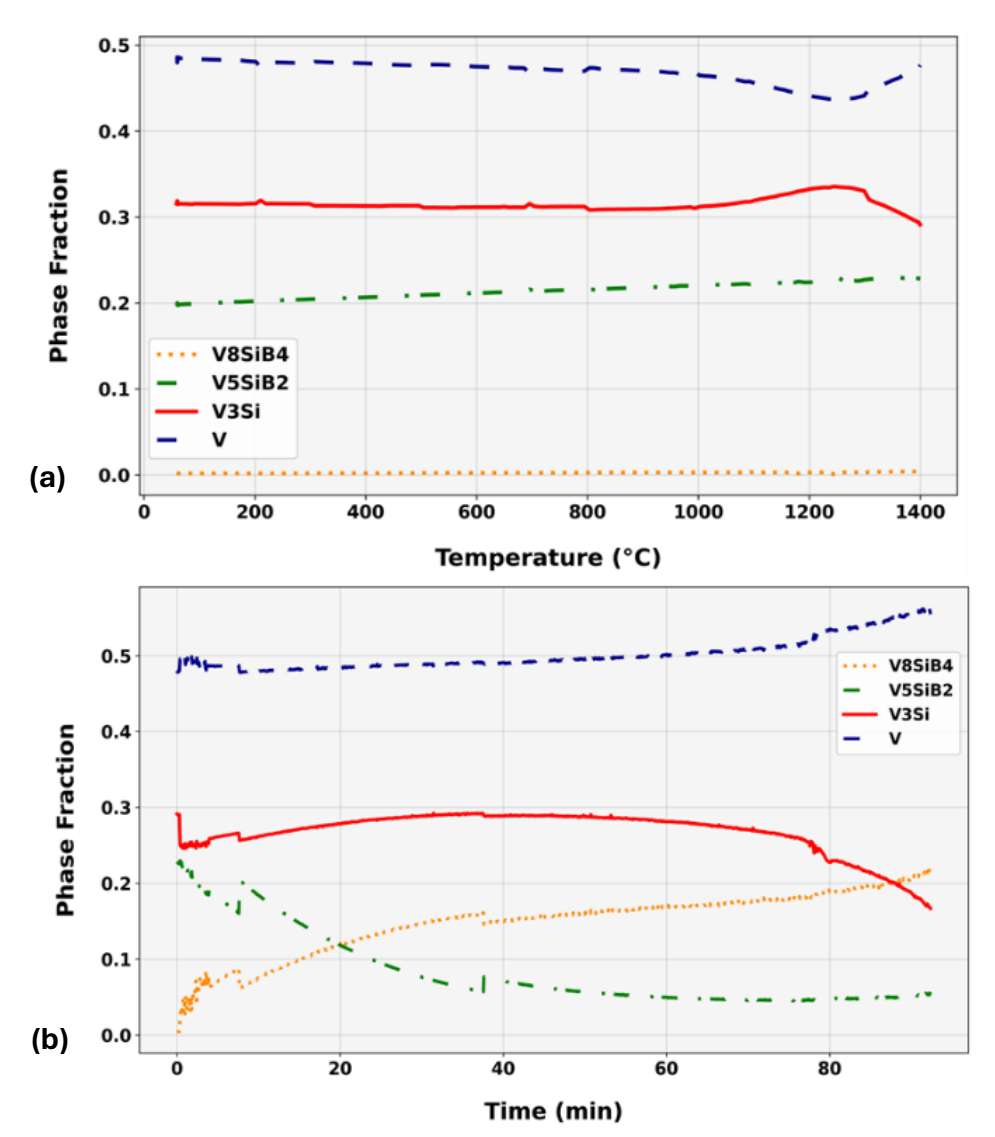


Fig. 1: Evolution of the phase fraction in V-9Si-6.5B alloy: (a) during heating up to the target temperature of 1400 °C; (b) during the holding step.

- [1] Yang, W. G.; Hasemann, G.; Gorr, B.; Schwaiger, R.; Krüger, M. V_8SiB_4 —A New Ternary Phase in the V–Si–B System. Intermetallics **2022**, 151, 107691.
- [2] Hasemann, G. Experimental Study of the Liquidus Surface in the V-Rich Portion of the V-Si-B System. J. Alloys Compd. **2020**, 824, 153843.
- [3] Yang, W. G.; Hasemann, G.; Carrion Saldaña, M.; Gorr, B.; Schwaiger, R.; Krüger, M. Phase Equilibria in the V-Rich Region of the V–Si–B System at 1400 °C. Intermetallics **2025**, 46, 151–169.
- [4] Yang, W. G.; Hasemann, G.; Yazlak, M.; Gorr, B.; Schwaiger, R.; Krüger, M. Ternary V_{ss}-V₃Si-V₅SiB₂ Eutectic Formation in the V-Si-B System. J. Alloys Compd. **2022**, 902, 163722.

P 004:

Oxygen diffusion mechanisms and kinetics in model y-TiAl alloys

Habiyaremye Frederic¹, Daniel Monceau², Thomas Vaubois³, Pierre Sallot³, Aidar Zakirov⁴, Williams Lefebvre⁴, Michal Kuris⁵, Maria Tsoutsouva, ⁵Marc Thomas⁵, Damien Texier⁶, Jean-Philippe Monchoux¹

1CEMES-CNRS UPR 8011, 29 rue J. Marvig, BP 94347, CEDEX 4, 31055 Toulouse, France, frederic.habiyaremye@cemes.fr, monchoux@cemes.fr

2 CIRIMAT Laboratory, University of Toulouse, INPT-ENSIACET, 4 allée Emile Monso, 31030 Toulouse, France, daniel.monceau@toulouse-inp.fr

3Safran Tech, Materials and Processes, Rue des Jeunes Bois, Châteaufort, 78114, Magny-Les-Hameaux, France. pierre.sallot@safrangroup.com, thomas.vaubois@safrangroup.com

4Univ Rouen Normandie, CNRS, INSA Rouen Normandie, Groupe de Physique des Matériaux UMR 6634, F-76000 Rouen, France, aidar.zakirov0@univ-rouen.fr, williams.lefebvre@univ-rouen.fr 5DMAS, ONERA, Université Paris Saclay, 92322, Châtillon, France, marc.thomas@onera.fr, maria.tsoutsouva@onera.fr, michal.kuris@onera.fr

6Institut Clement Ader (ICA) - UMR CNRS 5312, Université de Toulouse, CNRS, INSA, UPS, Mines Albi, ISAE-SUPAERO, Campus Jarlard, 81013 Albi Cedex 09, France, <u>damien.texier@mines-albi.fr</u>

Introduction

Intermetallic γ-TiAl alloys are promising lightweight substitutes for heavy nickel-based superalloys in aircraft engine components operating at temperatures up to 850°C[1]. Their high strength, low density, and excellent resistance to corrosion and oxidation make them attractive for such applications [2]. However, exposure to elevated temperatures in air leads to loss of ductility[3], [4], while the fundamental mechanisms driving the deterioration of mechanical properties remain poorly understood. According to several studies, the loss in mechanical properties following high-temperature exposure originates from microstructural evolution induced by the diffusion of solute atoms, such as oxygen, carbon, and nitrogen [5], [6]. Such assumptions are supported by comparative analyses of ductility loss in specimens subjected to heat treatments under different environmental conditions, revealing that embrittlement is most pronounced in oxygenrich atmospheres [7], [8]. Nevertheless, systematic investigations into oxygen's diffusion mechanisms, penetration depth, and its effect on local mechanical properties remain limited, particularly due to the restricted solubility of oxygen in the y-phase (< ~250 ppm at.% %)[9]. Thus, this study aims to investigate the diffusion mechanisms of oxygen into the y-phase, either by bulk or grain boundary diffusion. For this purpose, the diffusion layer has been characterized by secondary ion mass spectrometry (SIMS), atom probe tomography (APT), and nanoindentation. Moreover, the use of model alloys allowed us to assess the role of the Ti/Al ratio and the presence of the Hf interstitial solute (high oxygen trapping effect according to DFT calculations), both factors that impacted the diffusion rates by orders of magnitude.

Materials and Methods

For this study, model binary alloys (Ti48Al and Ti52Al) and a ternary alloy (Ti51.5Al1Hf), synthesized by arc melting at ONERA, as well as a Ti48Al2Cr2Nb alloy (referred to as the GE alloy, provided by SAFRAN), were selected. Diffusion experiments were carried out on $5 \times 5 \times 2$ mm samples extracted from these materials at 700°C for 1 hour and 100 hours in a controlled Ar-1% ¹⁸O atmosphere. The ¹⁸O isotope of oxygen was employed to distinguish the diffusing ¹⁸O species from the ¹⁶O contaminating the alloys in the asprocessed state.

For studying the oxygen penetration phenomena, and given the limited solubility of oxygen in the γ -phase, SIMS was utilized due to its high detection limit and sensitivity for trace elements [10]. For bulk diffusion studies, depth profiling was performed using a dynamic instrument with a magnetic sector (IMS7f, CAMECA), operating with a 10 keV primary Cs+ ion beam and a primary current of 40 nA. The analysis area, confined by a diaphragm, had a diameter of 33 μ m and was centered on a scanned crater of 150 × 150 μ m². Post-analysis, crater depths were measured using a stylus profiler (Dektak8, BRUKER) to determine the matrix's sputtering rate of approximately 1 nm/s. In addition, cross-sectional chemical mapping is being carried out to detect diffusion along grain boundaries.

Quantification of intergranular oxygen segregation phenomena is being investigated via APT on GE alloys exposed to 700°C for 100 hours in 80% Ar - 20% ¹⁶O. APT was chosen for its capability to perform three-dimensional compositional mapping with sub-nanometer resolution and unique chemical sensitivity in the ppm range [11]. Tips for APT were prepared using lift-out followed by annular milling via ThermoFisher Helios PFIB. Data acquisition was conducted using a LEAP 5000 XS (CAMECA) in laser and voltage modes, with reconstruction performed using IVAS and subsequent data analysis conducted using Gpm_3dSAT software. The concentration of oxygen at the grain boundary will be characterized by plotting concentration profiles across a box oriented perpendicular to it. Additionally, nanoindentation is also being carried out on the GE alloy, which was exposed to 700°C for 100 hours in 80% Ar–20 % ¹⁶O, to assess the change in the local mechanical properties of the diffusion layer.

Results and Discussion

Figure 1 shows SIMS depth profiles of 18 O, expressed as the evolution of the intensity ratio of the 18 O and 16 O signals, for the Ti48Al, Ti52Al, and Ti51.5Al-Hf alloys. The representation of the 18 O/ 16 O ratio has been selected because it converges towards the natural isotopic ratio of oxygen (18 O/ 16 O = 0.002) in the bulk, far from the diffusion region. Therefore, the penetration depth can be evaluated when the 18 O/ 16 O intensity ratio reaches this value. It can thus be seen that the penetration depths of 18 O in the Ti48Al, Ti51.5-Hf, and Ti52Al are about 2 μ m, 6-8 μ m, and above 8 μ m, corresponding to diffusion coefficients of 5.0×10^{-18} - 5.0×10^{-17} m²/s, 2.5-6.0×10⁻¹⁶ m²/s and 1.0-3.0×10⁻¹⁵ m²/s, respectively. Therefore, a strong Ti/Al ratio dependence of the diffusion coefficient is obtained. It is recalled here that the Ti/Al ratio (equals to 1.08 and 0.92 for the Ti48Al and Ti52Al alloys, respectively). Moreover, for the fixed Ti/Al ratio of 0.92 of both Ti52Al and Ti51.5Hf alloys, a strong effect of the Hf solute is observed. This can be attributed to elevated interaction energies between the 18 O interstitial diffusing species with the Ti antisites in the first case, and with the Hf substitutional solutes in the second case.

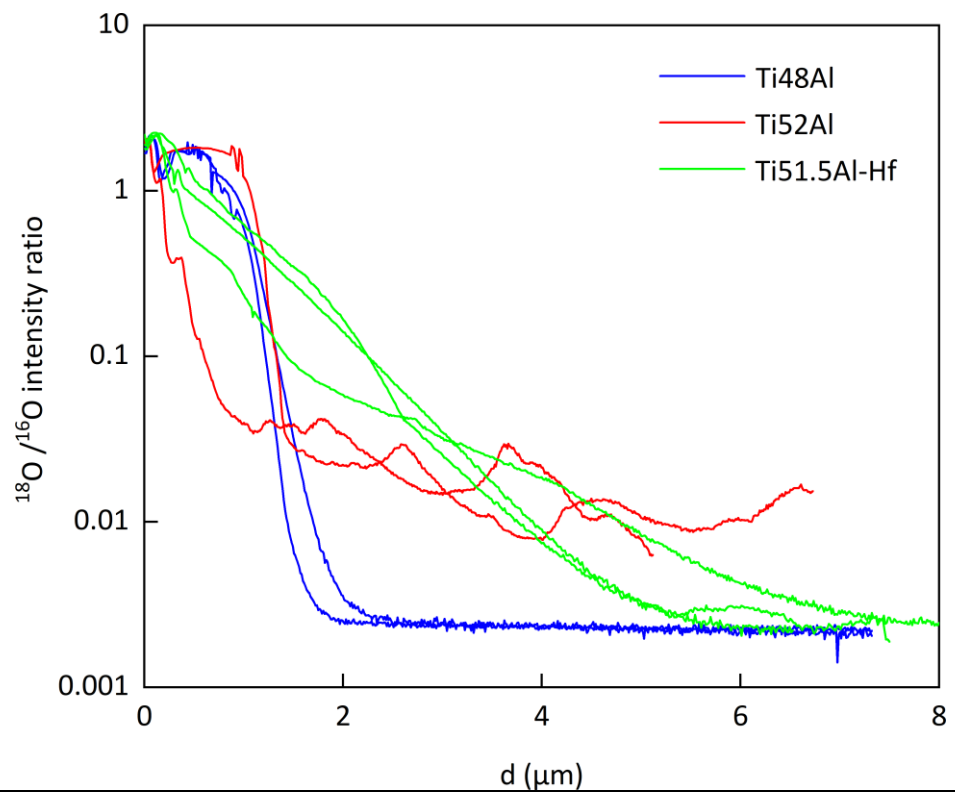


Figure 1. SIMS profiles of 18 O penetration at 700°C for 1 h in the γ phase of Ti48Al, Ti52Al, and Ti51.5Al-Hf alloys (ratio of the 18 O and 16 O intensities as a function of sputtering depth).

APT analysis is also being carried out to identify enhanced oxygen diffusion along grain boundaries and to calibrate the oxygen SIMS concentration profiles. Moreover, nanoindentation tests will be conducted to assess the influence of oxygen penetration, via bulk and grain boundary diffusion, on mechanical properties at the micrometric scale.

Conclusion

This study will thus provide valuable insights into the bulk and grain boundary diffusion of the oxygen interstitial, to help elucidate the oxidation and embrittlement mechanisms of γ -TiAl alloys exposed to oxygen at elevated temperature. In particular, this demonstrates the decisive role of the Ti antisites and substitutional solutes like Hf on the oxygen bulk diffusion kinetics.

- [1] H. Clemens and S. Mayer, "Advanced Intermetallic TiAl Alloys," *Mater. Sci. Forum.* **2016**, 879, 113–118.
- [2] B. P. Bewlay, M. Weimer, T. Kelly, A. Suzuki, and P. R. Subramanian, "The Science, Technology, and Implementation of TiAl Alloys in Commercial Aircraft Engines," *MRS Proc.* **2013**, 1516, 49–58.
- [3] M. Thomas et al., "Effects of exposure at 700°C on RT tensile properties in a PM γ -TiAl alloy," Intermetallics. **2006**, 14 (10–11),1143–1150.
- [4] C. Stangl, E. Kollmannsberger, T. A. Zimogliadova, M. Krüger, and H. Saage, "Influence of a fine-grained surface structure on the tensile behaviour of a beta stabilised intermetallic y-TiAl-based alloy," *Intermetallics*. **2022**, 146, 107566.
- [5] C. Thenot, R. Besson, P. Sallot, J.-P. Monchoux, and D. Connétable, "Interactions of oxygen with intrinsic defects in L1 0 γ -TiAl in presence of substitutional solutes: Influence on diffusion kinetics," *Comput. Mater. Sci.* **2022**, 201, 110933.

- [6] S. L. Draper and D. Isheim, "Environmental embrittlement of a third generation γ TiAl alloy," *Intermetallics*. **2012**, 22, 77–83.
- [7] R. Pather, W. A. Mitten, P. Holdway, H. S. Ubhi, A. Wisbey, and J. W. Brooks, "The effect of high temperature exposure on the tensile properties of γ TiAl alloys," *Intermetallics*, **2003**, 11 (10), 1015–1027.
- [8] S. L. Draper, B. A. Lerch, I. E. Locci, M. Shazly, and V. Prakash, "Effect of exposure on the mechanical properties of Gamma MET PX," *Intermetallics*. **2005**, 13 (9), 1014–1019.
- [9] A. Menand, A. Huguet, and A. Nérac-Partaix, "Interstitial solubility in γ and α 2 phases of TiAl-based alloys," *Acta Mater.* **1996**, 44 (12), 4729–4737.
- [10] D. S. McPhail, "Applications of Secondary Ion Mass Spectrometry (SIMS) in Materials Science," *J. Mater. Sci.*, vol. **2006**, 41(3), 873–903.
- [11] B. Gault et al., "Atom probe tomography," Nat. Rev. Methods Primer. 2021 1 (1) 51.

P 005:

Base-Metal Nanoparticles: Synthesis, Reactivity and Reactions

Christian Ritschel¹, Radian Popescu², Yolita Eggeler², and Claus Feldmann¹

¹Institute for Inorganic Chemistry, Karlsruhe Institute of Technology (KIT), Engesserstrasse 15, D-76131

Karlsruhe, Germany, claus.feldmann@kit.edu

²Laboratory for Electron Microscopy, Karlsruhe Institute of Technology (KIT), Engesserstraße 7, D-76131 Karlsruhe, Germany, yolita.eggeler@kit.edu

Introduction

The knowledge of metal nanoparticles is the lower the more negative the electrochemical potential and the smaller the particle size. As a result, little is known about nanoparticles of the most basic and most reactive metals. During the last five years, the Feldmann group has addressed the synthesis of base-metal nanoparticles (with E_0 (bulk) below -1.5 V) in the liquid phase. For the first time, we now have metal nanoparticles (1-10 nm) of all group-3 to group-5 transition metals and of all lanthanide metals (La to Lu) available (all red-marked metals in Fig. 1a available as THF suspensions or powder, Fig 1b,c). The asprepared base-metal nanoparticles are highly reactive (e.g., reaction with H_2O or O_2 comparable to alkali metals) [1-6].

Materials and Methods

The liquid-phase synthesis of the base-metal nanoparticles was performed by reduction of metal halides as most common and cheap starting materials with lithium or sodium naphthalenide in THF as the liquid phase at room temperature (20 °C) [1-3].

Due to the high reactivity of the as-prepared base-metal nanoparticles, both synthesis and sample handling need to be conducted under inert conditions (dried argon, vacuum) using standard Schlenk techniques or glove boxes. This includes all centrifugation and washing steps. Furthermore, all sample transfers for analytical characterization were performed under strictly controlled inert conditions (e.g., using appropriate transfer modules).

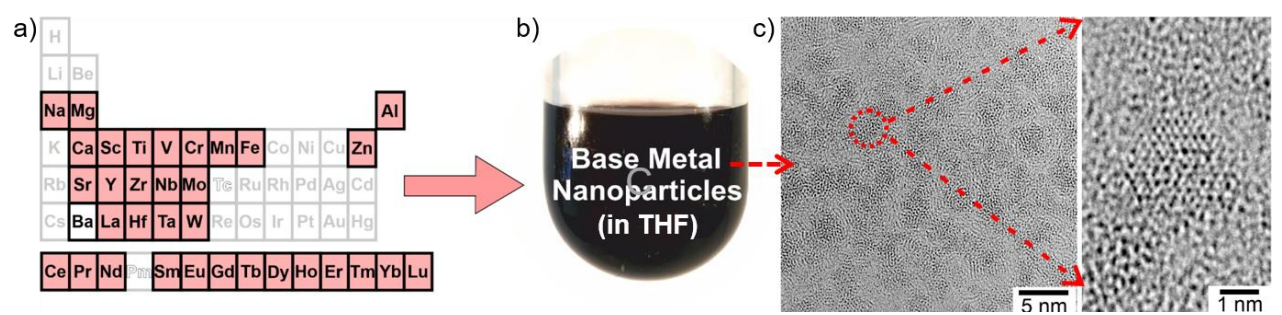


Fig. 1: Base-metal nanoparticles with a) red-marked metals available as nanoparticles, b) exemplary suspension of Sm(0) nanoparticles in THF, c) electron microscopy of base-metal nanoparticles with Sm(0) nanoparticles as example.

Results and Discussion

Particle size and size distribution of the as-prepared base-metal nanoparticles were examined by transmission electron microscopy (TEM). The base-metal nanoparticles exhibit diameters in the 1 to 10 nm range. A statistical evaluation of >100 nanoparticles on TEM images, for instance, results in mean diameters of 2.4 ± 0.2 nm for Sc(0), 4.0 ± 0.9 nm for Zr(0), 10.3 ± 1.7 nm for Mg(0). According to electron diffraction and X-ray powder diffraction, the base-metal nanoparticles are monocrystalline after synthesis [1-3].

Aiming at the reactivity and reactions of the as-prepared base-metal nanoparticles, their surface functionalization is relevant. Here, Fourier-transform infrared (FT-IR) spectroscopy, thermogravimetry (TG), and elemental analysis (EA) indicate the solvent THF to be adsorbed on the particle surface. X-ray absorption spectroscopy confirms the zerovalent oxidation state of the metals even for the particle surface. Violent reactions when in contact with air or water already indicate the high reactivity of the as-prepared base-metal nanoparticles. Here, surface functionalization with low-molecular-weight THF is particularly advantageous, as it can be easily removed by evacuation or by other reactants or ligands – unlike commonly used high-molecular-weight stabilizers (e.g., polyethylene glycol) or strongly binding agents (e.g., oleylamine).

To explore the reactivity in suspension near room temperature at the border of heterogenous and homogeneous conditions, the base-metal nanoparticles were reacted with sterically demanding and/or multidentate alcohols or amines [4-6]. As a result, a range of new coordination compounds could be realized, which were characterized by single-crystal structure analysis. Furthermore, the base-metal nanoparticles can be used to establish metal-metal bonding or to realize metal clusters. Beside first synthesis, the base-metal nanoparticles are highly relevant for catalysis or for hydrogen storage [7]. Finally, a combination of metals is possible and results in bimetallic nanoparticles with different structure and shape.

This presentation will show the chemical synthesis, the characterization of the basemetal nanoparticles as well as selected reactions and properties.

- [1] C. Schöttle, P. Bockstaller, R. Popescu, D. Gerthsen, C. Feldmann, *Angew. Chem. Int. Ed.* **2015**, *54*, 9866-9870.
- [2] D. Bartenbach, O. Wenzel, R. Popescu, L.-P. Faden, A. Reiß, A. Zimina, J.-D. Grunwaldt, D. Gerthsen, C. Feldmann, *Angew. Chem. Int. Ed.* **2021**, 60, 17373-17377.
- [3] A. Egeberg, T. Block, O. Janka, O. Wenzel, D. Gerthsen, R. Pöttgen, C. Feldmann, *Small* **2019**, *15*, 1902321.
- [4] L.-P. Faden, A. Reiß, R. Popescu, C. Donsbach, J. Göttlicher, T. Vitova, D. Gerthsen, C. Feldmann, Inorg. Chem. **2024**, 63, 1020-1034.
- [5] C. Ritschel, C. Donsbach, C. Feldmann, Chem. Eur. J. 2024, 30, e202400418.
- [6] A. Reiß, A. Appenzeller, J. Baur, J. Wenzel, R. Popescu, K. Beuthert, S. Dehnen, Y. M. Eggeler, F. Breher, W. Klopper, C. Feldmann, *Small* **2025**, *in revision*.
- [7] S. Riegsinger, R. Popescu, D. Gerthsen, C. Feldmann, *Chem. Mater.* **2024**, *36*, 10496-10503.

P 006:

Low-Temperature Liquid-Phase Synthesis of Ultra-Small, Uniform Niobium Nanoparticles

Klaus Beier¹, Alexander Egeberg¹, Lara-Pauline Faden¹ and Claus Feldmann¹

¹Institute of Inorganic Chemistry (AOC), Karlsruhe Institute of Technology (KIT), Engesserstraße 15, 76131

Karlsruhe, Germany, klaus.beier@kit.edu, claus.feldmann@kit.edu

Introduction

Niobium and its alloys are extensively studied, with applications in engineering as durable, high-temperature-resistant materials and in electronics as superconductors or capacitor components. Nanoscale niobium materials are barely explored, but hold promise for further expanding the range of applications. As an example, Nb sheets with a thickness on the nanoscale and surface-adsorbed Au nanoparticles were found to increase the transition temperature for superconductivity [1]. Generally, the increased amount of surface-allocated atoms in nanoparticles is expected to enhance chemical reactivity and open up surface-critical applications such as heterogenous catalysis or hydrogen storage. However, the synthesis of nanoparticulate niobium metal is still a challenge, particularly in regard of precise control of particle size and size distribution. Established methods face difficulties to achieve particle sizes below 10 nm and are typically associated with broad size distributions [2,3]. Here, we present a low-temperature, liquid-phase synthesis capable of obtaining very small uniform Nb(0) nanoparticles (2.1 ± 0.4 nm) with high purity [5].

Materials and Methods

For the bottom-up synthesis of Nb(0) particles, NbCl₅ (99%, Sigma-Aldrich) was dissolved in pyridine (99%, abcr) and reduced by lithium pyridinyl at room temperature. This can be achieved via a one-pot synthesis by adding NbCl₅ and lithium (99%, Riedel-de-Haën) directly into pyridine. Alternatively, a two-step synthesis may be employed, wherein lithium was pre-dissolved in pyridine and thereafter added to a separate solution of NbCl₅ pyridine. The particles were purified by washing redispersion/centrifugation (25 000 RPM, 55 200 × g) in/from pyridine and toluene (99%, Sigma-Aldrich). Due to high reactivity of the nanoparticles, synthesis and purification were conducted under inert argon atmosphere using typical Schlenk techniques or glove boxes. Used solvents were thoroughly dried by refluxing over CaH2 (92%, abcr) for pyridine or sodium (99%, Sigma-Aldrich) for toluene and freshly distilled under argon. The deep black Nb(0) nanoparticles can easily redispersed in pyridine or dried in vacuum to obtain powder samples. Optional sintering was performed at under Ar/H₂ atmosphere at 900 °C.

The nanoparticles were characterized using high-resolution transmission electron microscopy (HR-TEM), X-ray powder diffraction and Fourier-transform infrared (FT-IR) spectroscopy. TEM and high-resolution transmission electron microscopy HR-TEM were conducted with a FEI Osiris microscope operating at 200 kV. TEM samples of the Nb(0) nanoparticles were prepared by evaporating suspensions on amorphous carbon films suspended on copper grids. X-ray powder diffraction of powder was performed on a STOE STADI-MP diffractometer operating with Ge-monochromatized Cu-K α -radiation (λ = 1.54178 Å). Nb(0) powder samples were diluted with dried glass spheres (9-13 μ m, Sigma-Aldrich) to reduce the X-ray absorption of the nanoparticles and filled into glass

capillaries under argon atmosphere. FT-IR spectra of the Nb nanoparticles were recorded in transmission mode using a Bruker Vertex 70 spectrometer. The nanoparticle sample was embedded in KBr (IR-spectroscopy grade, Merck) at a weight percentage of 1.5 % and pressed into a clear pellet under a load of 50 kN within an argon-filled glove box. C/H/N elemental analysis was performed with an Elementar Vario Microcube device at a temperature of 1100 °C.

Results and Discussion

Deep black colloidally stable suspensions of very small, highly uniform Nb nanoparticles were obtained by liquid phase synthesis [5]. TEM overview images show uniform, nonagglomerated nanoparticles with diameters of 1-3 nm (Fig. 1a,b). A statistical evaluation of > 100 nanoparticles on the TEM images resulted in an average diameter of 2.1 ± 0.4 nm (Fig. 1c). HR-TEM images revealed locally ordered atom configurations with parallel lattice fringes (Fig. 1d). The observed lattice fringe distance of 2.3 Å is well in agreement with cubic bulk-niobium (d_{110} with 2.3 Å) [4]. The presence and purity of the Nb(0) nanoparticles was further validated by X-ray powder diffraction (XRD) analysis. Here, the as-prepared nanoparticles do not show any Bragg peaks, which can be ascribed to the small particle size. After sintering of the powder samples at 900 °C in an Ar/H₂ atmosphere, XRD analysis resulted in the characteristic Bragg peaks of bulk niobium (Fig. 2). Sintering in Ar/H₂ atmosphere was performed to avoid a reaction of the metal at elevated temperatures with pyridine adhered on the particle surface. Thus, sintering in Ar/H₂ resulted in the crystalline metals, whereas sintering in Ar only led to the formation of carbides. Although the metals are of course not nanosized after sintering, the absence of impurity phases points to the purity of the as-prepared Nb(0). Fourier-transform infrared spectroscopy (FT-IR) was performed to evaluate the surface of the as-prepared Nb(0) nanoparticles. Due to the synthesis in pyridine the adhesion of solvent molecules on the nanoparticle surface is naturally to be expected. By comparison with pure pyridine as a reference the observed low-intensity vibrations can be indeed related to pyridine. Moreover, elemental analysis (C/H/N analysis) results in 52.0 wt% C, 4.4 wt% H, 11.9 wt% N, and a residue of 31.7 wt%, which can be ascribed to Nb. When considering the nitrogen amount to originate from pyridine, the expected carbon and hydrogen amounts can be calculated as 51.0 and 4.3 wt%, respectively. Thus, the C/H/N amounts confirm pyridine to be adsorbed on the particle surfaces. The total amount of 68.3% reflects the small particle size and high surface of the Nb nanoparticles and is in the expected range. These results were published in literature [5].

The formation of very small nanoparticles with diameters of > 4 nm is in accordance with the LaMer-Dinegar model [6]. Thus, the instantaneous reduction of the dissolved NbCl $_5$ with lithium pyridinyl and the insolubility of the zerovalent metals in pyridine result in a high supersaturation, which promotes a fast nucleation, and consequently, the formation of very small nanoparticles. In the future, we aim at using these fast kinetics of nanoparticle formation to prepare nanoparticular Niobium bimetal phases, which would not be stable in thermodynamically controlled alloy systems.

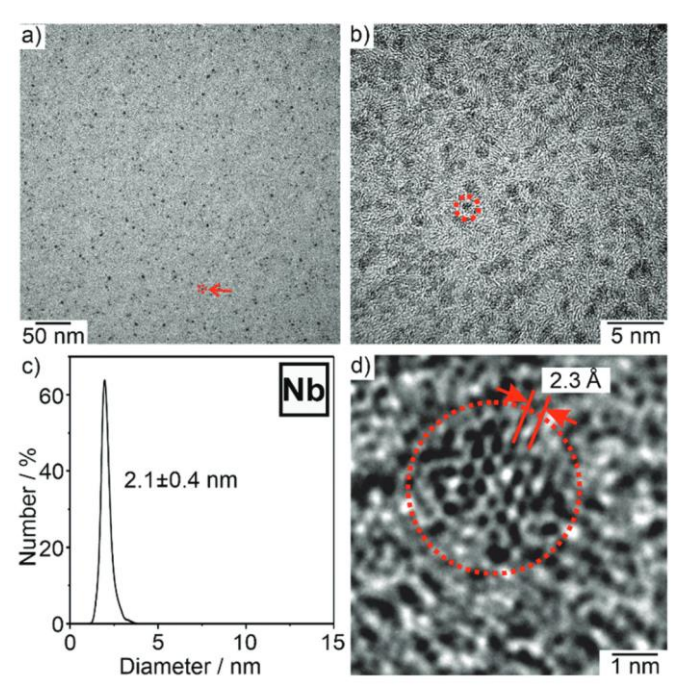


Fig. 1: Particle size, particle shape, and particle size distribution of the as-prepared Nb(0) nanoparticles: (a, b) overview TEM images at different levels of magnification, (c) size distribution based on the statistical evaluation of > 100 nanoparticles on the TEM images, and (d) the HRTEM image of the selected nanoparticles [5].

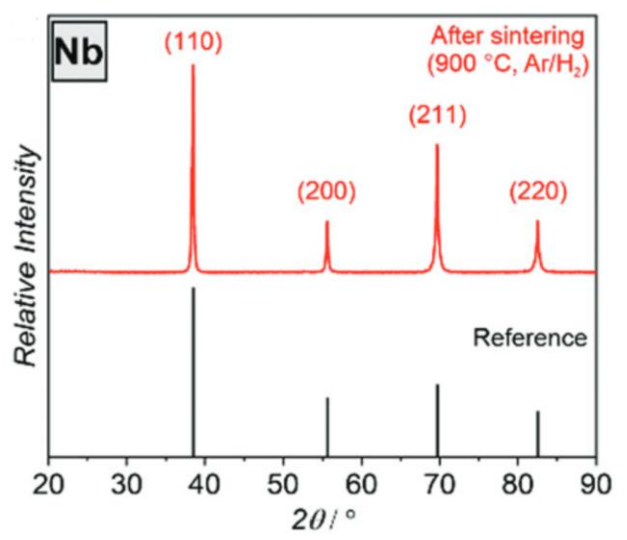


Fig. 2: XRD analysis of Nb(0) nanoparticles after sintering in comparison to a bulk Nb metal reference (ICDD-No. 00-035-0789).

- [1] E. Katzir, S. Yochelis, F. Zeides, N. Katz, Y. Kalcheim, O. Millo, G. Leitus, Y. Myasodeyoov, B. Y. Shapiro, Physical Review Letters. **2012**, 108, 107004.
- [2] N. Wang, K. Huang, J. Hou, H. Zhu, Rare Metals. 2012, 31, 621-626.
- [3] D. Malyshev, F. Boscá, C.-O. L. Crites, G. L. Hallett-Tapley, J. C. Netto-Ferreira, E. I. Alarcon, J. C. Scaiano, Dalton Transactions. **2013**, 42, 14049-14052.
- [4] N. Terao, Japanese Journal of Applied Physics. 1963, 2, 156–174.
- [5] A. Egeberg, L.-P. Faden, A. Zimina, J.-D. Grunwaldt, D. Gerthsen, C. Feldmann, Chemical Communications. **2021**, 57, 3648-3651.
- [6] V. K. La Mer, R. H. J. Dinegar, Journal of the American Chemical Souciety. **1950**, 72, 4847-4854.

P 008:

Microstructural Stability Enhancement and Mechanical Reinforcement of TLP-Bonded Cu/Sn-3.5Ag/Cu Microbumps under Multiple Reflow Cycles through Zn Alloying and Ni Substrate Integration

Yin-Ku Lee¹, Ping-Ling Lin², and Jenq-Gong Duh³,

1Department of Materials Science and Engineering, National Tsing Hua University,
No. 101, Sec. 2, Kuang-Fu Road, Hsinchu, Taiwan 3001. E-mail: h12502212652@gmail.com
2Department of Materials Science and Engineering, National Tsing Hua University,
No. 101, Sec. 2, Kuang-Fu Road, Hsinchu, Taiwan 3001. E-mail: 2001ginalin@gmail.com
3Department of Materials Science and Engineering, National Tsing Hua University,
No. 101, Sec. 2, Kuang-Fu Road, Hsinchu, Taiwan 3001. E-mail: jgd@mx.nthu.edu.tw.

Introduction

Microbumps are essential for high-density interconnections in advanced 2.5D/3D IC packaging. The TLP bonding process enables multiple reflow cycles without remelting, improving yield [1, 2]. However, microbump miniaturization increases IMC formation, phase transformations, and void formation due to volume shrinkage and interdiffusion-driven Kirkendall pores [3].

The η -Cu₆Sn₅ \rightarrow η '-Cu₆Sn₅ phase transformation at ~186–189°C causes ~2% volume expansion, leading to stress and defects [4-7]. Stabilizing η -Cu₆Sn₅ is crucial. Ni (4–9 at%) and Zn (0.8–2.1 at%) effectively inhibit this transformation and nonlinear thermal expansion [5,6, 7]. Optimizing microbump architecture, such as a Cu/Ni/Cu/Sn-1.8Ag configuration, also prevents Cu₆Sn₅ \rightarrow Cu₃Sn transformation [8].

This study explores Cu-15Zn/Sn-3.5Ag/Ni microbumps to enhance IMC stability in TLP bonding under multiple reflows. The brass substrate restricts Cu flux, while Ni promotes Cu_6Sn_5 nucleation and Zn-rich phase precipitation [9]. Microstructure evolution, phase stability, and mechanical properties of sub-10 μ m TLP-bonded microbumps are analyzed.

Materials and Methods

Sandwiched structures were fabricated using Cu, Ni, and Cu-15Zn plates with Sn-3.5Ag solder balls (\emptyset =250 μ m). The plates (2mm × 2mm × 0.4mm) were pickled, fluxed, and bonded under 1.6 MPa, followed by reflow at 221–260°C for 350 seconds per cycle. Bonding height was ~5.5 ±1 μ m.

Nine sample sets—Cu/Sn-3.5Ag/Cu, Cu/Sn-3.5Ag/Ni, and Cu-15Zn/Sn-3.5Ag/Ni—underwent 1, 3, or 5 reflows, with the latter placed at the hot end. Microstructure evolution was analyzed using BEI and FE-EPMA, with detailed grain and elemental distribution examined via TEM/EDS. Phase identification was based on EPMA, TEM/EDS, and TEM-SAD. Cu-Sn IMC grain orientation and sizes were assessed via EBSD in FE-SEM. Hardness was measured using a nano-indenter at a 250 nm depth.

Results and Discussion

The study investigates void formation in Cu/Sn-3.5Ag/Cu and Cu/Sn-3.5Ag/Ni joints after multiple reflow cycles. Voids in Cu/Sn-3.5Ag/Cu joints are primarily caused by volume shrinkage during phase transformations and interdiffusion, with a significant portion attributed to vacancy migration within pre-grown Cu_6Sn_5 . After several reflows, vacancies accumulate, and residual flux gases exacerbate void formation, especially at Cu6Sn5/Cu3Sn interfaces.

In Cu/Sn-3.5Ag/Ni joints, voids predominantly form near the Cu side, driven by Cu-Sn interdiffusion, vacancy migration, and volume shrinkage. Additionally, insufficient Ni presence prevents stabilization of the Cu₆Sn₅ phase, causing higher nonlinear expansion and internal stress. This results in larger voids with increasing reflow cycles.

Cu-15Zn/Sn-3.5Ag/Ni joints exhibit fewer voids due to the formation of a Zn-rich layer that limits Cu-Sn interdiffusion and vacancy migration. The Zn-rich layer stabilizes the IMC structure, reducing the occurrence of Cu3Sn phase transformation and promoting a uniform chemical stability throughout the joint. The Zn diffusion mechanism maintains a stable microstructure during reflow cycles.

Grain refinement in Cu/Sn-3.5Ag/Ni and Cu-15Zn/Sn-3.5Ag/Ni configurations improves shear strength and toughness, with finer grains and more random orientations in the Cu-15Zn/Sn-3.5Ag/Ni configuration. This is attributed to Zn-rich clusters acting as nucleation sites and altering diffusion pathways. The Zn-rich CuZn phase inhibits Cu diffusion, preventing Cu₃Sn formation and enhancing joint stability.

Mechanical analysis reveals that Ni and Zn doping increases hardness, but the balance between elastic recovery and plastic deformation (Er/H ratio) remains consistent, ensuring stable mechanical properties even as hardness increases.

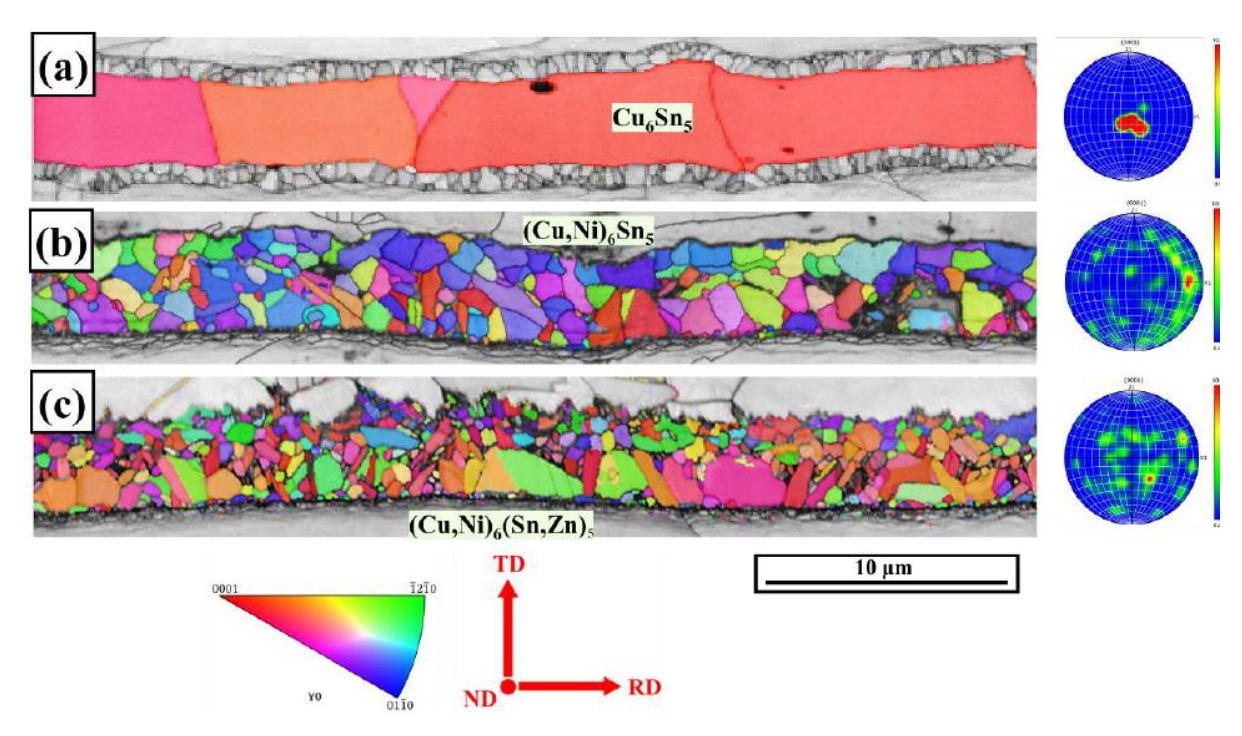
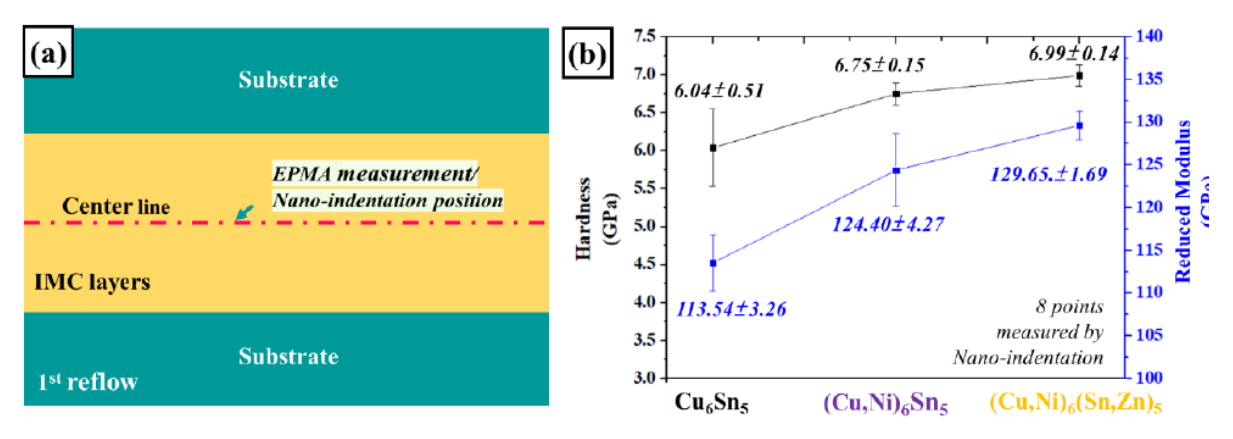


Fig. 1. The orientation maps, and pole figures of hexagonal η -Cu₆Sn₅ in different configurations after the 1st reflow:(a) Cu/Sn-3.5Ag/Cu, (b) Cu/Sn-3.5Ag/Ni, (c) Cu-15Zn/Sn-3.5Ag/Ni.



EPMA quantitative measurement by 10 points along the center line of IMC layers (At. %)

Configuration (1st reflow)	Phase	Cu	Sn	Ni	Zn	Ag
Cu/Sn-3.5Ag/Cu	Cu ₆ Sn ₅	54.88 ± 0.47	45.79 ± 0.39	-	-	0.33±0.02
Cu/Sn-3.5Ag/Ni	$(Cu,Ni)_6Sn_5$	51.43 ± 0.42	43.24 ± 0.42	5.02 ±0.45	-	0.32 ±0.01
Cu-15Zn/Sn-3.5Ag/Ni	(Cu,Ni) ₆ (Sn,Zn) ₅	48.70 ± 0.58	39.48 ± 0.39	6.76 ±0.48	4.73 ±0.35	0.33 ±0.03

Fig. 2. The results of EPMA quantitative analysis and nano-indentation tests along the center line in IMC layers: (a) schematic diagram of tests, (b) hardness and Er.

- [1] Agarwal, Rahul, et al. "Cu/Sn microbumps interconnect for 3D TSV chip stacking." 2010 Proceedings 60th electronic components and technology conference (ECTC). IEEE, **2010**.
- [2] Pawar, Karan, and Pradeep Dixit. "Investigation of Cu-Sn-Cu transient liquid phase bonding for microsystems packaging." Materials and Manufacturing Processes 38.3 (2023): 284-294.
- [3] Chuang, H. Y., et al. "Critical concerns in soldering reactions arising from space confinement in 3-D IC packages." IEEE Transactions on Device and Materials Reliability 12.2 (**2012**): 233-240.
- [4] Zeng, Guang, et al. "Phase stability and thermal expansion behavior of Cu₆Sn₅ intermetallics doped with Zn, Au and In." Intermetallics 43 (**2013**): 85-98.
- [5] Nogita, Kazuhiro, et al. "Effect of Ni on phase stability and thermal expansion of Cu_{6-x}Ni_xSn₅ (X= 0, 0.5, 1, 1.5 and 2)." Intermetallics 26 (**2012**): 78-85.
- [6] Zeng, Guang, et al. "Phase stability and thermal expansion behavior of Cu6Sn5 intermetallics doped with Zn, Au and In." Intermetallics 43 (**2013**): 85-98.
- [7] Yu, Chi-Yang, and Jenq-Gong Duh. "Stabilization of hexagonal Cu6 (Sn, Zn) 5 by minor Zn doping of Sn-based solder joints." Scripta Materialia 65.9 (**2011**): 783-786.
- [8] Xu, Zheqi, et al. "A Cu/Ni/Cu/Sn1. 8Ag Microbump Structure for Void-free Interface under Long Time High-Temperature Storage." Journal of Alloys and Compounds (2024): 176178.
- [9] Yu, Chi-Yang, Kai-Jheng Wang, and Jenq-Gong Duh. "Interfacial Reaction of Sn and Cu-x Zn Substrates After Reflow and Thermal Aging." Journal of electronic materials 39 (2010): 230-237.

P 009:

Powder metallurgical synthesis of ternary intermetallic phases in the V-Si-B system

L. Thielemann¹, G. Hasemann¹, W. Yang², R. Schwaiger^{2,3}, B. Gorr⁴ and M. Krüger¹

¹Otto-von-Guericke University Magdeburg, Institute of Materials, Technologies and Mechanics,
Universitätsplatz, 39106 Magdeburg, Germany, lars.thielemann@ovgu.de, georg1.hasemann@ovgu.de,
manja.krueger@ovgu.de

²Forschungszentrum Jülich GmbH, Institute of Energy Materials and Devices, Structure and Function of Materials (IMD-1), Wilhelm-Johnen-Str., Jülich 52428, Germany, w.yang@fz-juelich.de, r.schwaiger@fz-juelich.de

³Chair of Energy Engineering Materials, Faculty 5, RWTH Aachen University, Templergraben 55, 52056 Aachen, Germany

⁴Institute for Applied Materials – Applied Materials Physics (IAM-AWP), Karlsruhe Institute of Technology, Hermann-von-Helmholtz-Platz 1, 76344 Eggenstein – Leopoldshafen, Germany, bronislava.gorr@kit.edu

Introduction

High-temperature structural materials require a combination of excellent mechanical strength, creep resistance, and oxidation resistance. Vanadium-based alloys are gaining attention as lower-density alternatives to Mo- and Nb-based systems offering promising mechanical properties [1]. However, conventional vanadium alloys, such as V-4Cr-4Ti, suffer from poor oxidation resistance at elevated temperature, which can be mitigated by the addition of elements like Si and B [2]. Intermetallic phases in the V-Si-B system, such as V_3Si , V_5Si_3 and V_5SiB_2 (T2), offer the potential to enhance the mechanical strength and oxidation resistance of vanadium-based alloys [3,4]. Recent research has focused on developing and characterizing these alloys. A key discovery in this system is the ternary intermetallic phase V₈SiB₄. Initial studies suggest that V₈SiB₄ forms at lower temperatures and may transform into the B-rich T2 phase at elevated temperatures [5]. However, the phase stability, solubility range, and mechanical properties of the V₈SiB₄ phase remain largely unknown. A better understanding of these characteristics is crucial for assessing its role in the V-Si-B system and its potential implications for high-temperature applications. This study focuses on synthesizing and characterizing near-single-phase alloys containing either the V₈SiB₄ or the T2 phase, with the goal of understanding their stability and microstructural evolution for potential high-temperature applications.

Materials and Methods

Four alloy compositions (#1 - #4), see Fig. 1., were produced by mechanical alloying (MA) with a milling time of 1 h to 50 h. These powders were vacuum heat-treated at 1400 °C for 10 h. Rietveld analysis of these heat-treated powders was carried out and two alloys were selected for compaction via field-assisted sintering technology (FAST) at 1600 °C for 15 min. Subsequently, the sintered alloys were heat-treated in vacuum at 1400 °C for 100 h to reach equilibrium. The oxygen and nitrogen content as well as chemical and phase composition were controlled where necessary. The phase fraction was studied by X-ray diffraction (XRD) and analysed using the Rietveld method. The microstructure was analysed using scanning electron microscopy, electron backscatter diffraction (EBSD) and energy dispersive X-ray spectroscopy (EDS).

Results and Discussion

Using XRD analysis, it was determined that a milling time of 20 h was the most suitable, as it resulted in a supersaturated solid solution. Extending the milling process further led

to excessive powder welding to the milling vessel wall, therefore leading to a significant reduction of the loose powder fraction for subsequent investigations. Of the four alloys produced, two alloys were selected that had the highest fraction of T2 or V_8SiB_4 in the annealed state. The alloy V-12.5Si-25B (#2), corresponding to the stoichiometric composition of T2, exhibited a phase fraction of 90 % of the desired T2 phase. The second alloy, V-7.5Si-25B (#3), contained approximately 60 % of the desired V_8SiB_4 phase and 40 % of the T2 phase. Alloy #1 did not have any V_8SiB_4 phase, and alloy #4 had approximately 40% V_8SiB_4 phase after the above-mentioned annealing procedure. Therefore alloy #1 and #4 were not further investigated.

According to EBSD analysis after sintering, alloy #3 exhibited a nearly equal distribution of T2 and V_8SiB_4 phase, whereas alloy #2 is primarily composed of the T2 phase (~ 90 vol.%) and about 10 % of the VB phase, as shown in Fig. 2. SEM imaging revealed a fine-grained microstructure with well-defined grain boundaries as a result of the powder metallurgical processing route. Despite following the same MA and FAST parameters, the grain sizes of alloys #2 and #3 differed. In alloy #3, the average grain size of the V_8SiB_4 phase is approximately 5.5 µm and 2.6 µm for the T2 phase, respectively. The average grain size of the T2 phase in alloy #2 is approximately 1.3 µm, which is half the size compared to that in alloy #3.

These findings provide new insights into the microstructural control and phase stability of V-Si-B alloys, with implications for their use in high-temperature applications. Subsequent investigation will focus on the mechanical characterization of the alloys, including compression and creep testing, whereas nanoindentation will be carried out on the individual phases T2 and V_8SiB_4 .

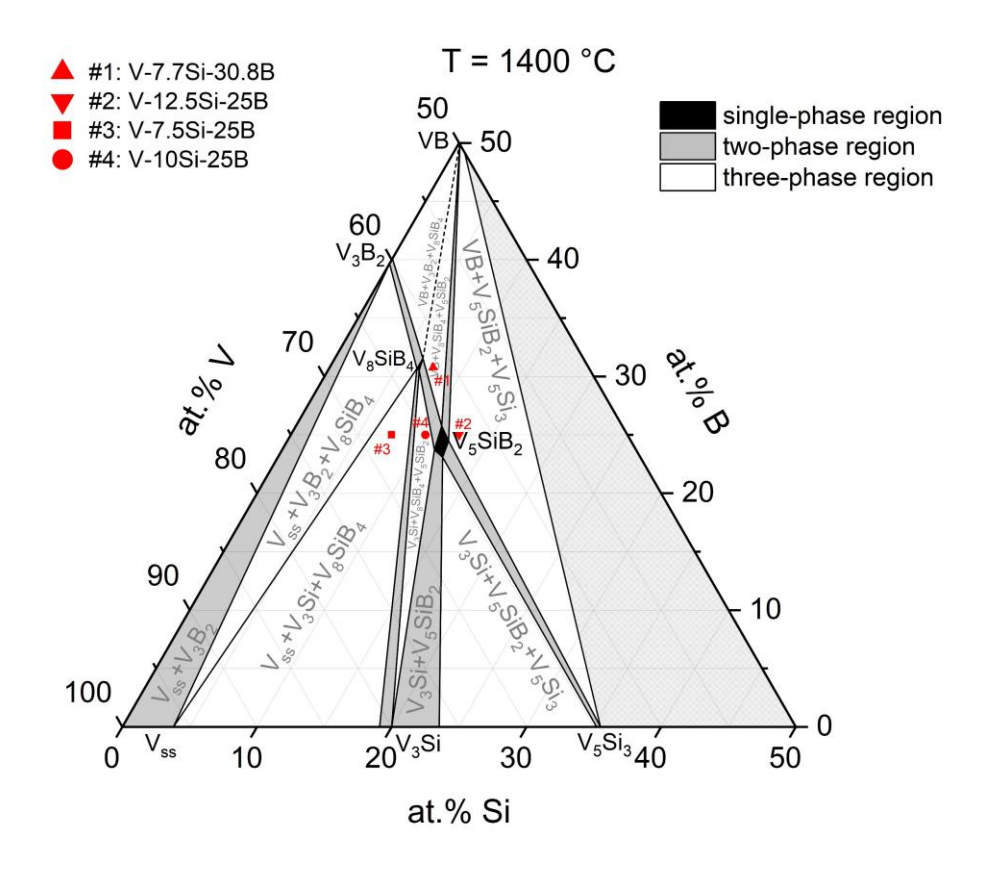


Fig. 1: Isothermal section at 1400 °C of the vanadium rich corner of the V-Si-B ternary system, alloys produced are marked with #1 - #4; diagram modified based on [6].

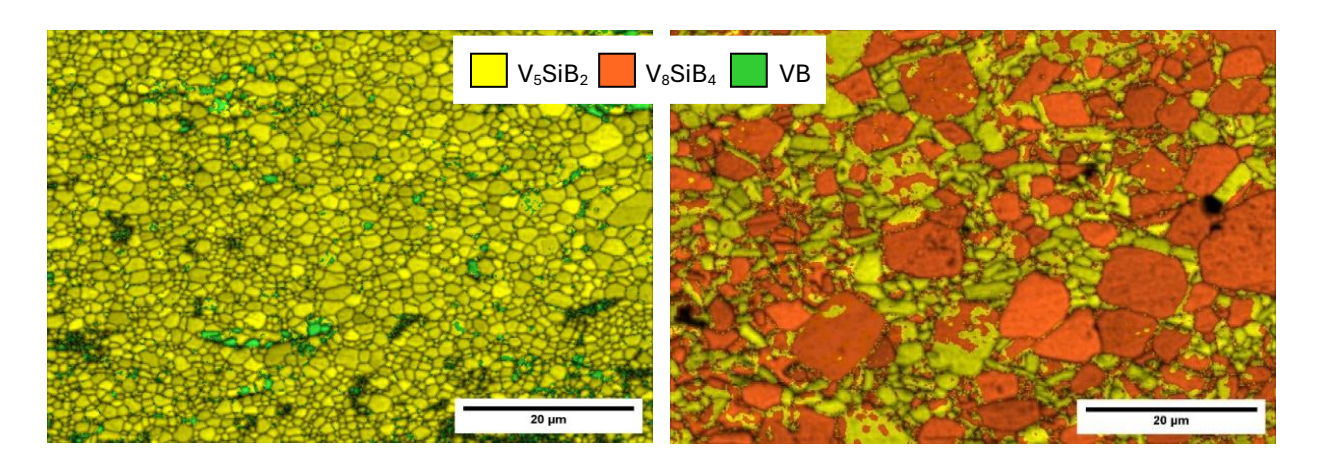


Fig. 2: EBSD phase map (including image quality) of the alloys V-12.5Si-25B (#2, left) and V-7.5Si-25B (#3, right) after FAST, yellow: T2, orange: V_8 SiB₄, green: VB.

- [1] M. Krüger. Habilitation: Innovative Ansätze zur Entwicklung neuer metallischer Hochtemperaturwerkstoffe, Otto-von-Guericke University Magdeburg, **2017**.
- [2] J. Williams, M. Akinc: Oxidation behavior of V5Si3 based materials, Intermetallics, 6, **1998**, 269–275.
- [3] M. Krüger: High temperature compression strength and oxidation of a V-9Si-13B alloy, Scripta Materialia, 121, **2016**, 75–78.
- [4] G. Hasemann, C. Müller, D. Grüner, E. Wessel, M. Krüger: Room temperature plastic deformability in V-rich V–Si–B alloys, Acta Materialia, 175, **2019**, 140–147.
- [5] W.G. Yang, R.S. Touzani, G. Hasemann, M. Yazlak, M. Ziegner, B. Gorr, R. Schwaiger, M. Krüger: V8SiB4 A new ternary phase in the V–Si–B system, Intermetallics, 151, **2022**, 107691.
- [6] W. Yang, G. Hasemann, M. Carrion Saldaña, B. Gorr, R. Schwaiger, M. Krüger: Phase Equilibria in the V-Rich Region of the V-Si-B System at 1400 °C, J. Phase Equilib. Diffus., 46, **2025**, 151–169

P 010:

Experimental assessment of the phase equilibria in system Nb – Mo – Zr (Niobium – Molybdenum – Zirconium) at the 1073K and 1223K isotherms

Cláudio G. Schön¹, Ana K. G. Lagares de Oliveira, Thais K. Y. Ito, Ingrid B. A. de Oliveira and Nathanael W. S. Morais²

Introduction

Uranium metallic fuels are alloyed either with Mo or Nb – Zr in order to stabilize the BCC γ phase, as such, developing a thermodynamic database of the quaternary U – Nb – Mo – Zr system is desirable for optimizing compositions and temperatures. As part of theis effort, the equilibria in system Nb – Mo – Zr needto to be experimentally assessed, and this is the aim of the present work

Materials and Methods

Eight compositions (Table 1), designed to (A) map the BCC miscibility gaps and (B) the equilibria involving the Laves phases, were arc meted in a copper crucible under Argon atmosphere. The obtained samples were analyzed both in the "as cast" condition and after solubilization. The heat treatment was performed in sealed quartz ampules with a low pressure Argon atmosphere in two conditions, first the samples were solubilized at 1223K for 500 hours to achieve equilibrium, the samples were divided in two parts, one part was analyzed to obtain the equilibria at this isotherm, while the second part was reencapsulated and submitted to additional 500 hours at 1073 K, to achieve equilibrium involving the $\alpha\text{-}Zr$ phase.

Table 1 – Nominal compositions of the samples synthetized in the present

Sample	% wt. Nb	% wt. Mo	% at. Nb	% at. Mo
A1	0.5	4	0.49	3.8
A2	3	0.5	2.95	0.48
A3	4	15	3.96	14.4
A4	30	20	29.9	19.3
A5	20	30	20	29.1
В0	0	67.8	0	66.7
B5	4.93	62.8	5	61.7
B10	9.88	57.8	10	56.7

Results and Discussion

Figure 1 shows the microstructure of the A5 sample submitted to 500h solubilization at 1223K. A complex microstructure which can be interpreted as a three phase equilibrium at the heat treatment temperature between the Mo_2Zr Laves phase (C15) and two BCC phases, one rich in Zr and the other rich in Zr and Zr has shows an inner

¹Universidade de São Paulo Escola Politécnica, Department of Metallurgical and Materiais Engineering, São Paulo-SP, Brazil, schoen@usp.br

²Center of Science and Technology of Materials, Instituto de Pesquisas Energéticas e Nucleares – IPEN, São Paulo-SP, Brazil

structure resulting from either partial or total transformation in α -Zr during quenching, probably by a martensitic mechanism. Figure 2 shows the microstructure of sample B5 after solubilization for 500h at 1223K, the matrix is Laves phase (C15+C14) and the particles are α -Mo, present due to a small deviation of the ideal stoichiometry of the C14 phase.

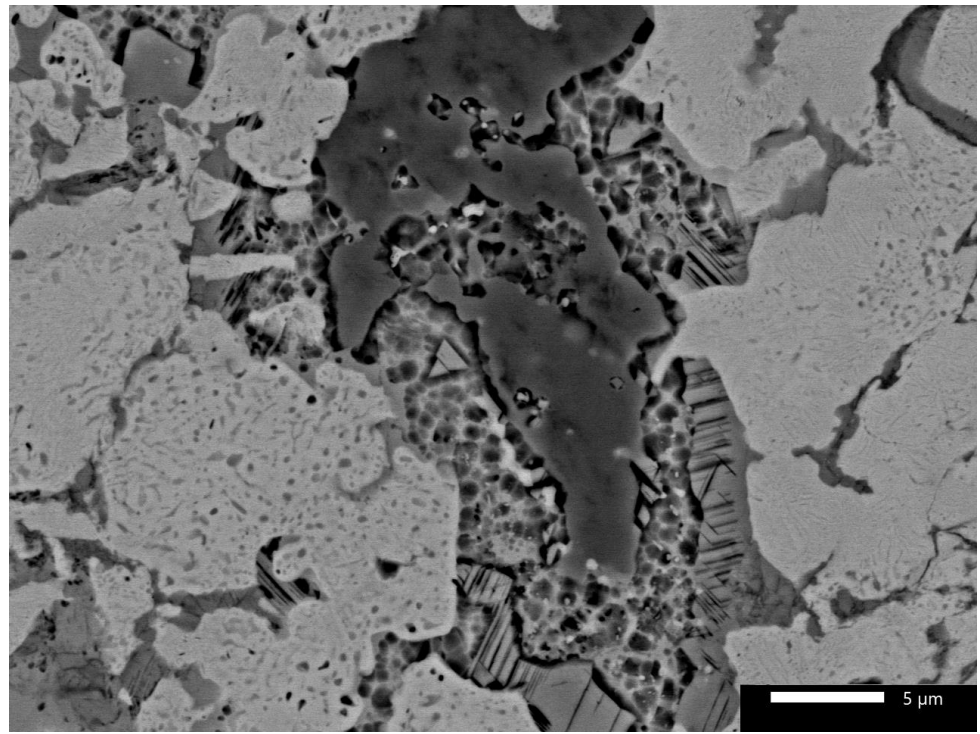


Figure 1 – Sample A5 after solubilization at 1223K for 500 h, Mo_2Zr C15 (dark gray), β -Zr (mottled gray, transformed into α -Zr during cooling) and Nb – Mo rich BCC (light gray).

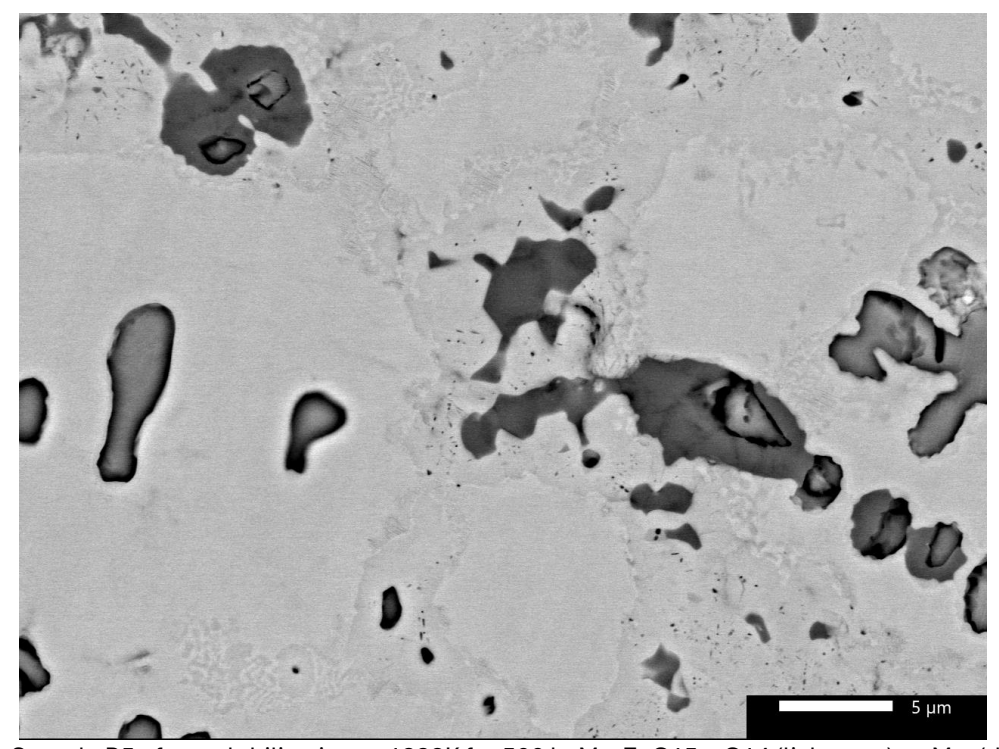


Figure 2 – Sample B5 after solubilization at 1223K for 500 h, Mo_2Zr C15 + C14 (light gray), α -Mo (dark gray).

P 011:

Study of Intermetallic Formation Resulting from Friction Stir Welding of AA5052 Aluminum and DP600 Steel

Giovanni Brandi Cirillo Yazigi¹, Cláudio Geraldo Schön², Nathanael Wagner Sales Morais² and Isolda Costa¹

¹Instituto de Pesquisas Energéticas e Nucleares – IPEN – Centro de Ciências e Tecnologia de Materiais, Av. Prof. Lineu Prestes, 2242 - Butantã, São Paulo - SP, 05508-000. <u>brandigiovanni2@gmail.com</u>

²Departamento de Engenharia Metalúrgica e Materiais. Av. Professor Mello Moraes, 2463 - Butantã, São Paulo - SP, 05508-030. shoen@usp.br

Introduction

The increasing demand for lighter and more efficient vehicles has driven the use of advanced materials in the automotive industry. DP600 steel is widely used due to its high mechanical strength and has been combined with the AA5052 aluminum alloy, which offers lower density and excellent corrosion resistance. The joining of these materials enables vehicle weight reduction without compromising structural safety, making it a promising alternative for enhancing automotive performance.

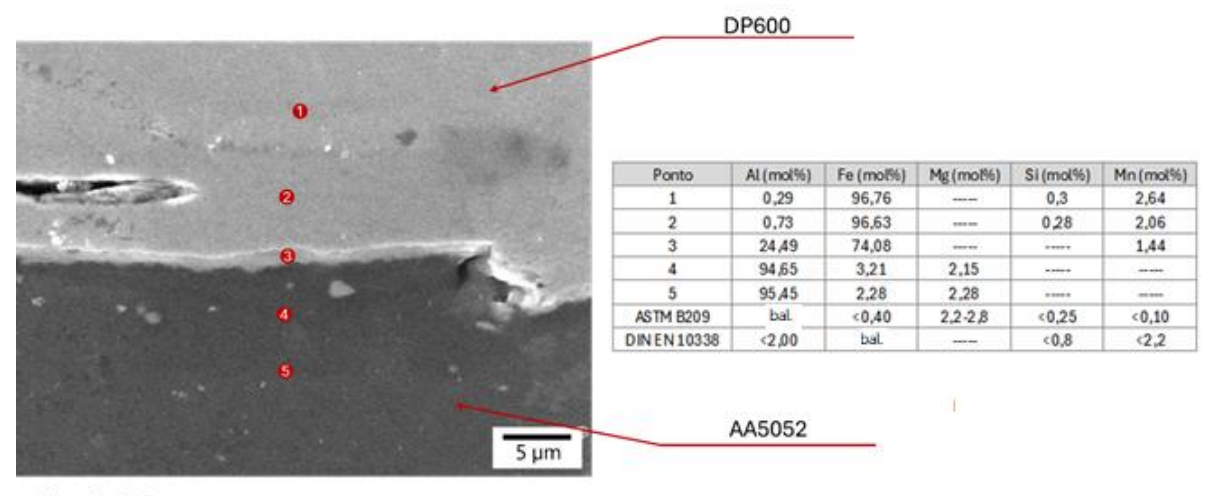
Among the joining techniques, Friction Stir Welding (FSW) stands out because it allows the welding of dissimilar materials without melting, consequently reducing crack formation and thermal embrittlement. However, this process can alter the microstructure of the materials and lead to the formation of intermetallic compounds, which may cause cracking and decrease mechanical strength. Thus, the objective of this study is to evaluate the effects of FSW on the formation of intermetallics between DP600 steel and the AA5052 alloy.

Materials and Methods

The FSW joining was performed using a hardened H13 steel on clockwise rotation speed

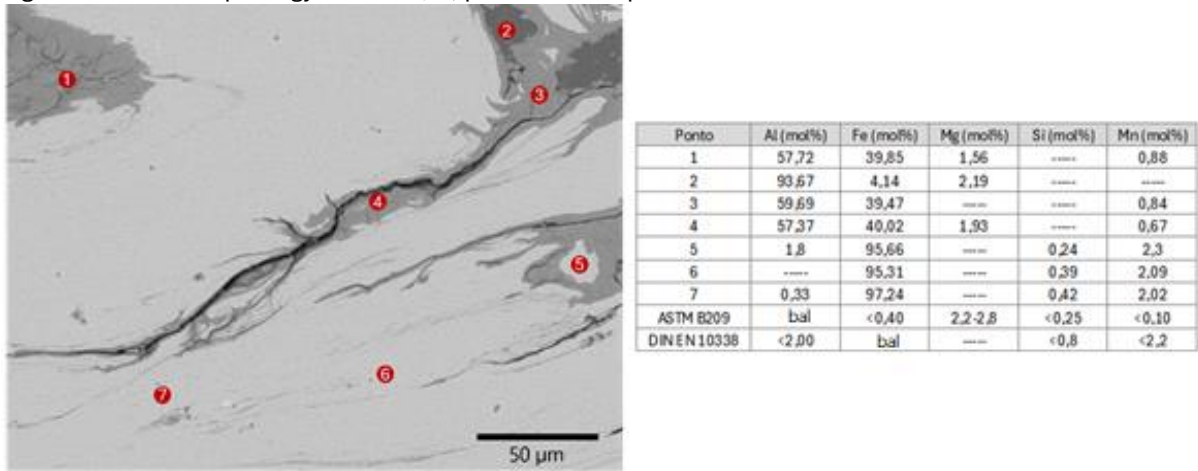
Results and Discussion

The microstructural characterization presented two types of intermetallics: the Fe $_3$ Al [1] and the FeA [1]l. The Fe $_3$ Al is present on the interface between the DP600 and the AA 5052 in a thin discontinuous layer morphology. Some pieces of steels were cladded by AA 5052 generating a system with a 3 phase particle in the AA 5052 matrix: an external layer of Fe $_3$ Al covering a FeAl treads that expands in a steel particle matrix. The presence of these intermetallics were not previously reported in the literature.



Signal SED Landing Voltage 15.0 kV

Fig. 1: Thin film morphology of the Fe₃Al, present in the point 3



Signal BED Landing Voltage 15.0 kV

Fig. 2: FeAl morphology: points 1, 3 and 4. The FeAl acts like a crackpath

[1] ASM handbook 3 – Alloy Phase Diagrams – ASM International – **2016** – ISBN 978-1-62708-070-5

P 012:

Magnetocaloric Performance in Sustainable Ni-Mn-Sn-Based Heusler Alloys by Electron-Beam Additive Manufacturing

Hamed Shokri¹, Silja-Katharina Rittinghaus², Natalia Shkodich³, Enrico Bruder⁴, Michael Farle⁵, Bilal Gökce⁶

- ¹ Materials Science and Additive Manufacturing, School of Mechanical Engineering and Safety Engineering, University of Wuppertal, Gaußstr. 20, 42119 Wuppertal, Germany, shokri@uni-wuppertal.de
 ² Materials Science and Additive Manufacturing, School of Mechanical Engineering and Safety Engineering, University of Wuppertal, Gaußstr. 20, 42119 Wuppertal, Germany, rittinghaus@uni-wuppertal.de
- ³ Faculty of Physics and Center of Nanointegration (CENIDE), University of Duisburg-Essen, Lotharstr. 1, 47057 Duisburg, Germany, natalia.shkodich@uni-due.de
- ⁴ Physical Metallurgy, Institute of Materials Science, Technical University of Darmstadt, Peter- Grünberg-Straße 2, 64287 Darmstadt, Germany <u>e.bruder@phm.tu-darmstadt.de</u>
- ⁵ Faculty of Physics and Center of Nanointegration (CENIDE), University of Duisburg-Essen, Lotharstr. 1, 47057 Duisburg, Germany, michael.farle@uni-due.de
 - ⁶ Materials Science and Additive Manufacturing, School of Mechanical Engineering and Safety Engineering, University of Wuppertal, Gaußstr. 20, 42119 Wuppertal, Germany, goekce@uniwuppertal.de

Introduction

Magnetic refrigeration is a promising green alternative technology to conventional cooling systems. Theoretically, it offers higher energy efficiency, and lower mechanical noise and vibrations compared to traditional cooling methods [1,2]. The technique is based on the magnetocaloric effect (MCE) in which the application or removal of an external magnetic field causes a magnetic entropy change (ΔS) that leads to a temperature change (ΔT) near the magnetic transition temperature [1,3].

The MCE is observable in several magnetic materials containing rare earth elements. To overcome the environmental and geopolitical limitations associated with rare earth materials, research has turned to alternatives such as Ni-Mn-Sn-based Heusler alloys. Ni-Mn-Sn based Heusler alloys with conceptual magnetocaloric properties and with a tunable transition temperature are considered as a low-cost candidate [4,5]. A desirable Curie temperature close to room temperature, significant entropy change, and good mechanical properties depending on the application make them promising for this purpose.

The traditional manufacturing process of these materials has been limited to arc melting [5,6], and powder metallurgy [7] which faces challenges in shaping to suit specific applications and machining after fabrication is inevitable [8]. Additive manufacturing (AM) has overcome the challenge of machining by enabling direct part production with the ability to create complex designs, where components are developed using computer-aided design software and then built from a raw powder in a layer-by-layer fashion [9]. Among the various methods in AM, electron beam powder bed fusion (PBF-EB/M) opens new avenues for the manufacturing of crack-free Ni-Mn-Sn-based Heusler alloys, a breakthrough recently demonstrated for this material system [10]. The oxygen-free manufacturing process, deep energy penetration other additive manufacturing methods, and intrinsic high temperature pre- and post-heating of each layer control thermal gradients and minimize residual stresses, thus mitigating crack formation.

Materials and Methods

To assess the influence of chemical composition on the magnetic entropy change, prealloyed gas-atomized NiMnSn, NiMnSnCr, and NiMnSnCrCo powders were used. The powders (D90~70µm) were provided by VTT, Finland. A FreemeltOne PBF-EB/M machine was used to build various geometries of samples. A random spot melting scanning strategy was employed to reduce stress and minimize porosity, achieving low segregation and evaporation. Preheating was conducted for each deposited layer by a graphite plate to homogenize heat transfer. An annealing heat treatment was carried out for microstructure homogenization. The consolidated material was investigated using LM, SEM, EDS, XRD and PPMS.

Results and Discussion

Crack-free samples with high relative density were produced from the using NiMnSn powder batch. Similarly dense parts were produced with NiMnSnCoCr using the same process parameters. However, using the same parameters, the NiMnSnCr composition did not result in the production of dense, single-piece parts with comparable density properties. This issue was significantly resolved by increasing the volume energy density. Analysis of the built parts with ICP-OES showed a negligible amount of Mn-loss due to evaporation during the process. Characteriation of bulk hardness demonstrated an increase in mechanical strength upon adding elements to NiMnSn in thin-wall-shaped samples. Reducing the thickness decreased elemental migration in NiMnSn samples and increased the mechanical strength due to a higher cooling rate.

The equiaxed grain microstructure of NiMnSn slightly changed to a longitudinal dendritic structure due to the incorporation of Co and Cr. A dual-phase structure containing austenite and martensite was determined by XRD measurements.

The EDS mapping indicated good elemental distribution in NiMnSn and NiMnSnCoCr asbuilt samples. In contrast, the NiMnSnCr samples showed Chromium segregation to grain boundaries which could be moderated to some extent by heat treatment.

Applying a 5T external magnetic field significantly increases the magnetic entropy change compared to previous similar work [10] on NiMnSn Heusler alloys. Our results underscore that optimizing process parameters and heat treatment synergistically engineers the desired magnetic properties by refining the microstructure, while simultaneously enabling the successful production of crack-free components in various near-net shapes.

Acknowledgments

This research was funded by DFG via CRC/TRR 270, project ID 405553726, GO 2566/10-1-(Project-ID 445127149) and INST 218/90-1 (Project-ID 510085108).

- [1] V. Franco, J.S. Blazquez, B. Ingale, A. Conde, Annual Review of Materials Research. **2012**, *42*, *305-342*.
- [2] V. Chaudhary, X. Chen, R.V. Ramanujan, Progress in Materials Science. **2019**, *100*, 64-98.
- [3] V. Franco, J.S. Blazquez, J.J. Ipus, J.Y. Law, L.M. Moreno-Ramirez, A. Conde, Progress in Materials Science. **2018**, 93, 112-232.
- [4] S.Y. Dan'kov, A.M. Tishin, V.K. Pecharsky, K.A. Gschneidner, Physical Review B. **1998**, *57, 3478*.

- [5] P. Shamba, N.A. Morley, O. Cespedes, I.M. Reaney, W.M. Rainforth, Applied Physics A. **2016**, *122*, *1-9*.
- [6] Z. Zhong, S. Ma, D. Wang, Y. Du, Journal of Materials Science & Technology. **2012**, *28*, 193-199.
- [7] A.E.-M.A. Mohamed, B. Hernando, Ceramics International. **2018**, *44*, *17044-17049*.
- [8] J.D. Moore, D. Klemm, D. Lindackers, S. Grasemann, R. Träger, J. Eckert, L. Löber, S. Scudino, M. Katter, A. Barcza, K.P. Skokov, O. Gutfleisch, Journal of Applied Physics. **2013**, *114*, *043907*.
- [9] T. DebRoy, H.L. Wei, J.S. Zuback, T. Mukherjee, J.W. Elmer, J.O. Milewski, A.M. Beese, A. Wilson-Heid, A. De, W. Zhang, Progress in materials science. **2018**, *92*, *112-224*.
- [10] S.-K. Rittinghaus, H. Shokri, N. Shkodich, E. Bruder, M. Farle, B. Gökce, Additive Manufacturing Letters. **2023**, *7*, *100159*.

P 013:

Creep of precipitation-strengthened A2-B2 refractory alloys

Liu Yang¹; Sandipan Sen¹; Daniel Schliephake¹; Raja J. Vikram¹; Stephan Laube¹; Aparajita Pramanik²; Ankur Chauhan²; Steffen Neumeier³; Martin Heilmaier¹; Alexander Kauffmann*

¹ Institute for Applied Materials (IAM-WK), Karlsruhe Institute of Technology (KIT), Engelbert-Arnold-Str. 4, 76131 Karlsruhe, Germany, <u>liu.yang@partner.kit.edu</u>, <u>sandipan.sen@kit.edu</u>, <u>daniel.schliephake@kit.edu</u>, <u>raja.vikram@partner.kit.edu</u>, <u>stephan.laube@kit.edu</u>, <u>martin.heilmaier@kit.edu</u>, <u>alexander.kauffmann@kit.edu</u>

² Extreme Environments Materials Group, Department of Materials Engineering, Indian Institute of Science, Bengaluru, Karnataka 560012, India, paparajita@alum.iisc.ac.in, ankurchauhan@iisc.ac.in
³ Friedrich-Alexander-Universität Erlangen-Nürnberg, Department of Materials Science & Engineering, Institute I: General Materials Properties, Martensstraße 5, 91058 Erlangen, Germany,

steffen.neumeier@fau.de

Introduction

Short after the idea of high entropy alloys (HEAs) became popular, the concept was extended to refractory high entropy alloys (RHEAs) by the seminal work of Senkov et al. [1] to develop novel high temperature materials. RHEAs are composed of refractory elements and exhibit usually high melting points beyond 2000 °C leading to excellent mechanical strength even up to 1600 °C. However, all refractory elements and most of their alloys suffer from catastrophic oxidation which preclude their immediate application in oxidative atmosphere. Accordingly, potentially passivating elements like Al, Cr. etc. were added to RHEAs to improve their oxidation resistance. Particularly, RHEAs containing Ta, Cr and Ti were identified to provide a strategy to achieve oxidation resistance by the formation of a slowly growing rutile type oxide scale [2]. When synthesized in close to equimolar composition and homogenized condition, many of the alloys from the Ta-Mo-Nb-Cr-Ti-Al system form single-phase material with disordered, body centered cubic (BCC) A2 (Strukturbericht designation) or ordered B2 crystal structure [3]. While mechanical strength of such alloys and microstructural conditions were intensively studied and proved the principle promise regarding high temperature application, little is reported on the creep resistance thus far. Gadelmeier et al. [4] and Liu et al. [5] for example systematically studied the single-phase A2, equimolar TiZrHfNbTa as one of the important model alloys among the A2 RHEAs that are ductile at room temperature. In summary, the studies reveal inferior creep resistance as compared to state-of-the-art, single-crystal Ni-based superalloys, like CMSX-4. Accordingly, the recent development trends to obtain precipitation-strengthened alloys with A2 matrix and B2 precipitates came into focus in research. Thus, the present contribution provides detailed mechanical and microstructural insights into the creep of 27.3Ta-27.3Mo-27.3Ti-8Cr-10Al (in at. %, abbreviated by TMT-8Cr-10Al in what follows) [6]. This particular alloy was previously developed to form A2-B2 microstructures via an anticipated precipitation reaction like in Ni-based super alloys.

Materials and Methods

TMT-8Cr-10Al was synthesized by arc melting under Ar atmosphere from high purity raw elements. Homogenization was performed at 1600 °C for 20 h with a cooling rate of

^{*} Institute for Applied Materials (IAM-WK), Karlsruhe Institute of Technology (KIT), Engelbert-Arnold-Str. 4, 76131 Karlsruhe, Germany and Chair Materials Science and Engineering (LWW), Institute for Materials (IM), Ruhr University Bochum (RUB), Universitätsstr. 150, 44801 Bochum, alexander.kauffmann@rub.de

100 K/h under continuous Ar flow. The slow cooling rate allows for the precipitation of the B2 phase from the A2 matrix. After standard metallographic preparation, scanning electron microscopy (SEM) was performed to obtain backscatter electron contrast images (SEM-BSE) and analytical information by electron backscatter diffraction (SEM-EBSD) and energy dispersive X-ray spectroscopy (SEM-EDS). Additionally, transmission electron microscopy (TEM) was performed on focused ion prepared lift-out specimens. The Compression creep tests were conducted on an electro-mechanical universal testing machine equipped with a vacuum furnace. The test temperatures ranged from 1000 - 1070 °C and true stresses of 50 - 175 MPa were applied. For comparison purposes, long-term heat treatments under the same conditions without external mechanical load were also performed.

Results and Discussion

The polycrystalline refractory high entropy alloy TMT-8Cr-10Al features a nanoscaled, two-phase microstructure with a disordered A2 matrix and ordered B2 precipitates after homogenization and slow cooling. In this condition, it is demonstrating promising creep resistance at high temperatures. Compared to other polycrystalline, single-phase A2 and B2 RHEAs (see Fig. 1), TMT-8Cr-10Al shows significantly higher creep resistance, with differences in creep rate amounting to about three to four orders of magnitude at comparable stresses and temperatures. TMT-8Cr-10Al exhibits similar minimum creep rates to CMSX-4 in the stress range of 75 to 125 MPa and temperatures between 1000 and 1030 °C, making it competitive with state-of-the-art, single-crystalline A1-L12 alloys. This comparable creep resistance is noteworthy given that TMT-8Cr-10Al is polycrystalline, unlike the single-crystalline CMSX-4. Furthermore, TMT-8Cr-10Al is tested closer to its solvus temperature of 1060 to 1070 °C compared to CMSX-4's solvus temperature of 1280 °C. Due to the proximity to the solvus temperature during testing and the relatively low volume fraction of B2, the strengthening contribution under creep conditions remains considerably smaller compared to state-of-the-art Ni-base superalloys. Therefore, future alloy developments should aim to increase the solvus temperature and volume fraction of B2 precipitates. The further guided development of Ta-Mo-Ti-Cr-Al+X RCCA with improved precipitate volume fraction and solvus temperature requires enhancements to the existing thermodynamic models as the relevant temperatures of phase separation and ordering are not well captured by current simulations. Directional coarsening or rafting of the precipitate microstructure of TMT-8Cr-10Al is observed after creep at 1000 (see Fig. 2) and 1030 °C. The combination of positive lattice misfit and compression loading causes N-type rafting of the microstructure in grains with the (100) direction parallel to the loading direction, consistent with established theories on the formation of rafted microstructures in Ni- and Co-based superalloys.

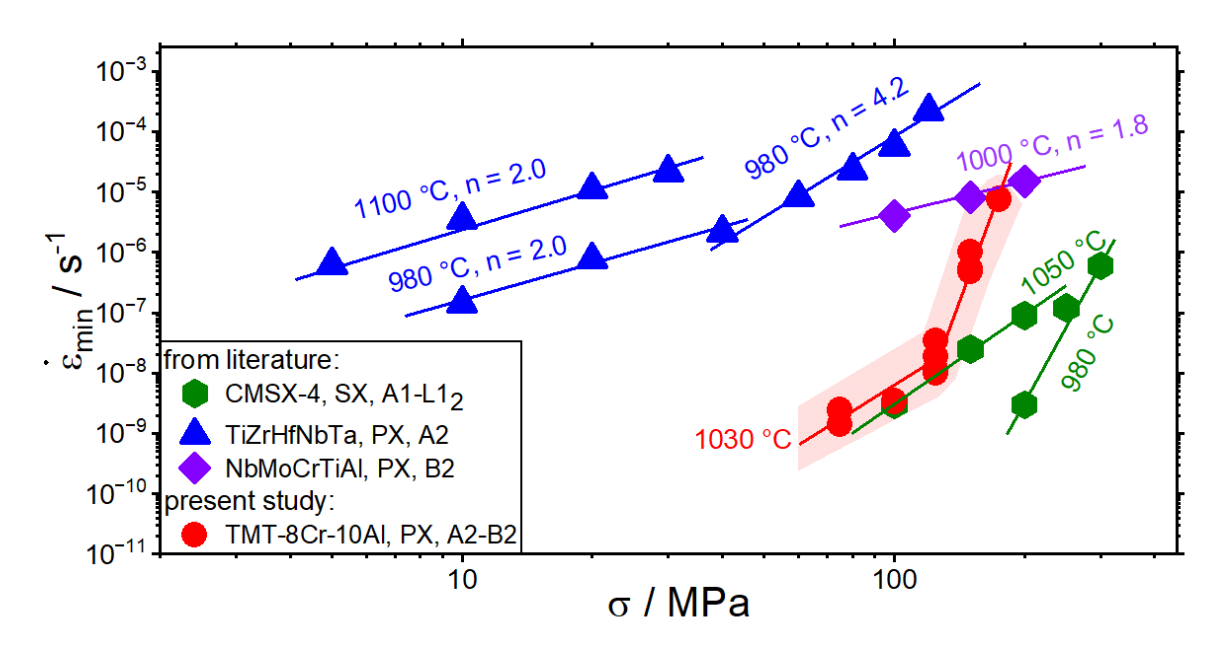


Fig. 1: Comparison of strain rate vs. applied stress for the investigated polycrystalline (PX), A2+B2 TMT-8Cr-10Al and PX, single-phase B2 NbMoCrTiAl, PX, single-phase A2 TiZrHfNbTa [4] as well as for the single-crystalline (SX) Ni-based superalloy CMSX-4 with A1-L1₂ microstructure.

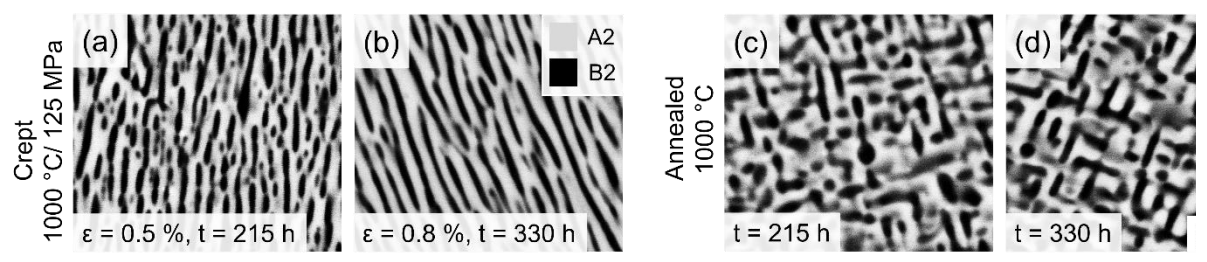


Fig. 2: SEM-BSE micrographs showing microstructure evolution of TMT-8Cr-10Al alloy after creep tests at 1000 °C with a stress of 125 MPa and strains of: (a) 0.5 % and (c) 0.8 % as well as heat treatments at 1000 °C for: (c) 215 h and (d) 330 h. The grains in the crept condition are selected to visualize the rafting.

- [1] O.N. Senkov, G.B. Wilks, D.B. Miracle, C.P. Chuang, P.K. Liaw, Intermetallics 18 (**2010**) 1758–1765.
- [2] B. Gorr, S. Schellert, F. Müller, H.-J. Christ, A. Kauffmann, M. Heilmaier, Adv Eng Mater 23 (**2021**) 2001047.
- [3] H. Chen, A. Kauffmann, S. Seils, T. Boll, C.H. Liebscher, I. Harding, K.S. Kumar, D.V. Szabó, S. Schlabach, S. Kauffmann-Weiss, F. Müller, B. Gorr, H.-J. Christ, M. Heilmaier, Acta Materialia 176 (**2019**) 123–133.
- [4] C. Gadelmeier, Y. Yang, U. Glatzel, E.P. George, Cell Reports Physical Science 3 (2022) 100991.
- [5] C.-J. Liu, C. Gadelmeier, S.-L. Lu, J.-W. Yeh, H.-W. Yen, S. Gorsse, U. Glatzel, A.-C. Yeh, Acta Materialia 237 (**2022**) 118188.
- [6] L. Yang, S. Sen, D. Schliephake, R.J. Vikram, S. Laube, A. Pramanik, A. Chauhan, S. Neumeier, M. Heilmaier, A. Kauffmann, Acta Materialia 288 (**2025**) 120827.

P 014:

Defects in Off-stoichiometric Laves Phases: Atomic Arrangements in Dislocation Locks and Planar Defects

Gang Liu¹, Sharvan Kumar², Christian H. Liebscher³, Gerhard Dehm¹ and Frank Stein¹

¹Max Planck Institute for Sustainable Materials, Max-Planck-Straße 1, 40237 Düsseldorf, Germany, g.liu@mpi-susmat.de, g.dehm@mpie-susmat.de, f.stein@mpi-susmat.de

²Brown University, Providence, RI, USA, sharvan_kumar@brown.edu

³Ruhr University Bochum, Bochum, Germany, christian.liebscher@ruhr-uni-bochum.de

Introduction

Laves phases are intermetallic compounds with an AB_2 stoichiometry and an either cubic (C15 type) or hexagonal (C14 and C36 type) crystal structure, which differ only in the sequence of stacking of a four-layer fundamental structural unit that consists of alternating pure A and B atom planes. Similar to the simple fcc and hcp structures with their abcabc- and abab-type of stacking of the close packed planes, the respective stacking of the four-layer units results in the cubic or hexagonal Laves phase types (see, e.g. [1,2]). As a result of this structural similarity, the energy difference between the stable and unstable structural variants is small. Therefore, the frequent occurrence of stacking faults and twins in Laves phases is not surprising. In addition, these phases often have extended homogeneity ranges. The deviations from the AB₂ stoichiometry are accommodated mainly by antisite atoms. However, also other types of defects play an important role, particularly at the edges of the composition range with the most offstoichiometric compositions. Luo et al. [3] found widely extended stacking faults and an increase in the dislocation density by one order of magnitude near the edges of the composition range of C15 NbCo₂ Laves phase. Studies on the atomic structure of planar defects in an off-stoichiometric Nb-rich hexagonal C14 NbFe₂ Laves phase alloy showed that particular Nb-enriched atomic arrangements occur with atomic motifs resembling those also existing in the crystal structure of μ phases [4].

The present work aims to systematically investigate the atomic arrangements in dislocation locks and planar defects in cubic C15 Laves phase and their dependence on composition/stoichiometry. It also determines whether such μ -phase-like atomic arrangements, as observed in the Nb-rich hexagonal NbFe₂ Laves phase, can only be present where the μ phase coexists as a true equilibrium phase adjacent to the Laves phase (as is the case in the binary Fe-Nb system), or whether this is a more general phenomenon. An ideal system to perform this kind of investigations is the Cr-Nb system, in which no such μ phase exists and the only intermetallic phase is the cubic C15 Laves phase NbCr₂. Therefore, three single-phase cubic C15 NbCr₂ Laves phase alloys with different compositions (Nb-rich, near stoichiometric, and Cr-rich) were produced and analyzed by scanning transmission electron microscopy (STEM).

Materials and Methods

Cr-rich, near-stoichiometric, and Nb-rich cubic $C15 \, \text{NbCr}_2$ Laves phase alloys containing 30, 33, and 35 at.% Nb were synthesized by arc-melting from the pure metals. After a heat treatment at 1200°C for 96 h, the alloys were slowly cooled (5°C/min) to room temperature. Microstructure and chemical composition were checked by scanning electron microscopy (SEM) and electron microprobe analysis (EPMA), respectively, and the cubic $C15 \, \text{crystal}$ structure was confirmed by X-ray diffraction (XRD) analyses. The

presence of dislocations and different kinds of planar faults was verified by conventional TEM, and the characterization of their atomic structure was conducted by high-angle annular dark field (HAADF) STEM using a probe-corrected Titan Themis 60-300 from Thermo Fisher Scientific, operated at 300 kV and coupled with energy dispersive spectroscopy (EDS).

Results and Discussion

Microstructural examination and XRD analyses together revealed that all samples heattreated at 1200°C were single-phase C15 Laves phase. It is important to mention that in the as-cast state, the samples contained not only the equilibrium cubic C15 phase but also a significant amount of metastable hexagonal Laves phase. This hexagonal Laves phase results from the rapid cooling process from the liquid state and is not an equilibrium phase, as has already been frequently and controversially discussed in the literature [5]. A resulting effect is that the heat-treated samples contain a large number of (intrinsic as well as extrinsic) stacking faults and retained C36-ordered domains in the cubic C15 matrix. The present experiments show for the first time different characteristic lock structures defined by the chemical composition and the type and orientation of the reacting stacking faults, see Fig. 1 and ref. [6]. By analogy with concepts for simple fcc alloys, there are two types of Lomer–Cottrell locks (<110> stair-rod partials, 'Lock 1' and 'Lock 2') and two types of Hirth locks (<001> stair-rod partials, 'Lock 3' and 'Lock 4'), as is illustrated in the figure. A pronounced compositional dependence is evident for each type of lock structure, except for 'Lock 2'. For example, in the case of 'Lock 1', the STEM image of the Nb-rich alloy exhibits a bright spot in the center of the lock, corresponding to a Nb antisite column, while the lock core in the Cr-rich alloy adopts a completely different configuration. Another remarkable feature is that in the Cr-rich alloy, in the case of 'Lock 3' and 'Lock 4', nanoscale cracks appear starting from the lock centers, which could be due to the high level of stress generated during the lock formation. In contrast, for the same lock structures in the Nb-rich alloy, the Nb enrichment gives rise to another particular atomic configuration, which appears to be able to effectively accommodate these stresses and thereby suppresses crack initiation.

In the Nb-rich alloy, we also observe well-defined C36/C15 incoherent interface structures with regularly arranged, characteristic atomic motifs [7]. Both this result and the dislocation locks described above will be presented in the poster. Moreover, the observation of individual confined planar defects containing structural elements characteristic of the μ phase will also be discussed in the poster.

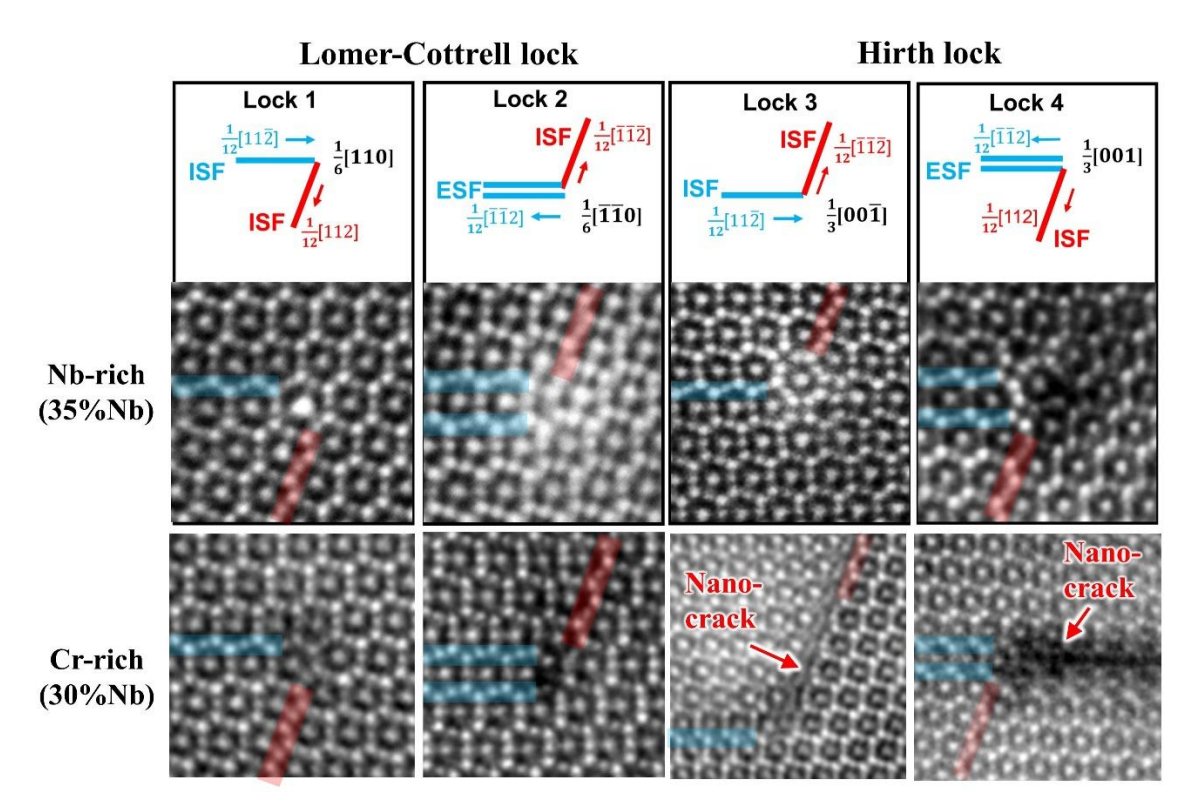


Fig. 1: Composition-dependent dislocation lock structures (ISF: intrinsic stacking fault, ESF: extrinsic stacking fault)

- [1] D.J. Thoma, in: K.H.J. Buschow, R.W. Cahn, M.C. Flemmings, B. Ilschner, E.J. Kramer, S. Mahajan (Eds.): Encyclopedia of Materials: Science and Technology. Elsevier, Amsterdam, The Netherlands, **2001**, 4205-4213.
- [2] K.S. Kumar, P.M. Hazzledine, Intermetallics. **2004**, *12*, 763-770.
- [3] W. Luo, C. Kirchlechner, J. Li, G. Dehm, F. Stein, J. Mater. Res. **2020**, *35(2)*, 185-195.
- [4] M. Šlapáková, A. Zendegani, C.H. Liebscher, T. Hickel, J. Neugebauer, T. Hammerschmidt, A. Ormeci, J. Grin, G. Dehm, K.S. Kumar, F. Stein, Acta Mater. **2020**, *183*, 362-376.
- [5] A. Leineweber, F. Stein, Mater. Des. **2024**, *247*, 113373
- [6] G. Liu, S.-H. Lee, C.H. Liebscher, S. Zhang, X. Zhou, J.S. Lee, S. Wei, M. Vega-Paredes, P. Schweizer, S. Korte-Kerzel, G. Dehm, Z. Xie, F. Stein, *submitted*, **2025**
- [7] G. Liu, C.H. Liebscher, P. Schweizer, F. Stein, G. Dehm, submitted, 2025

P 015:

Effects of Si and B additions on the high-temperature oxidation behavior and room-temperature fracture toughness of Mo-50Ti alloys

<u>Daiki Kubota</u>, Xinyu Yan, Takahiro Kaneko, Nobuaki Sekido, Kyosuke Yoshimi
Department of Materials Science, Graduate School of Engineering, Tohoku University, 980-8579 Sendai,
Japan, kubota.daiki.s4@dc.tohoku.ac.jp, yan.xinyu.a4@tohoku.ac.jp, takahiro.kaneko.e7@tohoku.ac.jp,
nobuaki.sekido.b7@tohoku.ac.jp, kyosuke.yoshimi.d1@tohoku.ac.jp

Introduction

Molybdenum (Mo) -based alloys are considered promising candidates for advanced heat-resistant materials due to their excellent high-temperature strength. However, their practical application is severely limited by poor oxidation resistance, primarily caused by the sublimation of MoO3 [1]. Although MoSi2 and Mo5SiB2 (T2) have demonstrated improved oxidation resistance, their room-temperature fracture toughness remains extremely low [2,3]. Therefore, critical challenges remain in realizing Mo-based alloys as structural materials, and thus enhancing the oxidation resistance of the Mo solid solution (Moss) phase is essential to simultaneously achieve the oxidation resistance and fracture toughness of Mo-based alloys.

Recently, Hatakeyama et al. reported that macro-alloying with titanium (Ti) in Moss of MoSiBTiC alloys—up to a composition ratio of Mo:Ti \approx 1:1—dramatically enhances oxidation resistance [4]. However, these alloys exhibited low room-temperature fracture toughness due to solid solution strengthening by Ti and the presence of a large volume fraction of intermetallic compounds. This study focuses on the Mo-50Ti solid solution as the matrix phase, owing to its inherent ductility and potential for improved oxidation resistance. To improve oxidation resistance, we add silicon (Si), which facilitates the formation of a protective oxide scale, and boron (B), which reduces the viscosity of the amorphous SiO2 [5,6].

Therefore, this study aims to investigate the effects of Si and B additions on the solubility limit, microstructure evolution including the formation of Ti5Si3 and/or Mo5SiB2, high-temperature oxidation behavior, and room-temperature fracture toughness of Mo-50Ti alloys.

Materials and Methods

The (Mo-50Ti)-xSi alloys (x = 0,2,3,5,7 at.%; denoted as 0Si,2Si,3Si,5Si,7Si) and (Mo-50Ti)-5Si-yB alloys (y = 1,3,5 at.%; denoted as 5Si1B,5Si3B,5Si5B) alloys were fabricated by arc melting. All alloys were subsequently homogenized at 1500° C for 24 hours in an Ar atmosphere. Microstructural characterization, phase identification, and volume fraction analysis of the constituent phases were carried out using FE-SEM, SEM-EDS, XRD, and ImageJ. Oxidation behavior was evaluated via isothermal oxidation tests at 800° C for 24 hours under atmospheric conditions. Fracture toughness was assessed via four-point bending tests at room temperature, using Chevron-notched specimens with half the dimensions specified in ASTM C1421-10 [7,8]. The initial applied strain rate was $1.5 \times 10^{-3} \, \text{s}^{-1}$. Fracture toughness values at room temperature were calculated based on Young's modulus and Poisson's ratio obtained by the electromagnetic acoustic resonance (EMAR) method using Irwin's similarity equation.

Results and Discussion

The 0Si alloy consisted of a single-phase Moss. The 2Si, 3Si, 5Si, and 7Si alloys exhibited a two-phase microstructure of Moss and Ti5Si3, with the volume fraction of Ti5Si3 increasing with increasing Si content. In contrast, the 5Si1B, 5Si3B, and 5Si5B alloys exhibited a three-phase microstructure consisting of Moss, Ti5Si3, and T2. With increasing B content, the volume fractions of the Moss and Ti5Si3 phases decreased, while that of the T2 phase increased.

Fig. 1 shows the oxidation curves obtained from isothermal oxidation tests conducted at 800°C for 24 hours. All samples exhibited weight loss; however, the weight loss decreased with increasing Si content, with the exception of the 7Si alloy, which showed a slight increase. These results indicate that an increased volume fraction of Ti5Si3 effectively suppresses the weight loss of the alloys during oxidation. However, when a large amount of Ti5Si3 precipitates, the Moss phase becomes Mo-rich, which may lead to a reduction in oxidation resistance. In contrast, the weight loss showed little change with increasing B content. This behavior would be attributed to the poor fluidity of borosilicate at 800°C [9].

Fig. 2 shows the room-temperature fracture toughness values calculated from the four-point bending tests conducted at room temperature. All specimens exhibited fracture toughness values below the target value of 15 MPa·m $^{1/2}$ [10]. The fracture toughness decreased with increasing Si and B content, due to the increased volume fraction of the Ti5Si3 and/or T2 phases. In addition, microcracks in Ti5Si3 and the precipitation of Ti(O,N) at the grain boundaries of the Moss phase may have further contributed to the reduction in fracture toughness.

- [1] E.A.Gulbransen, K.F.Andrew, F.A.Brassart, J.Electrochem.Soc. **1963**, 110, 952-959.
- [2] I.Jawed, D.C.Nagle, Mat.Res.Bull. 1986, 21, 1391.
- [3] K.Yoshimi, S.Nakatani, T.Suda, S.Hanada, H.Habazaki, Intermetallics. **2002**, 10, 407-414.
- [4] Tomotaka Hatakeyama, Shuntaro Ida, Nobuaki Sekido, Kyosuke Yoshimi, Corrosion Science. **2020**, 176, 108937.
- [5] N.Birks, Introduction to high temperature oxidation of metals. **1988**, p57.
- [6] F.A.Rioult, S.D.Imhoff, R.Sakidja, J.H.Perepezko, Acta Materialia. **2009**, 57, 4600-4613.
- [7] T.Moriyama, K.Yoshimi, M.Zhao, T.Masnou, T.Yokoyama, J.Nakamura, H.Katsui, T.Goto, Intermetallics. **2017**, 84, 92-102.
- [8] ASTM C1421-10, ASTM International, **2014**.
- [9] T.A.Parthasarathy, M.G.Mendiratta, D.M.Dimiduk, Acta Materialia. **2002**, 50, 1857-1868.
- [10] R.Mitra, Inter.Mater.Rev. 2006, 51.

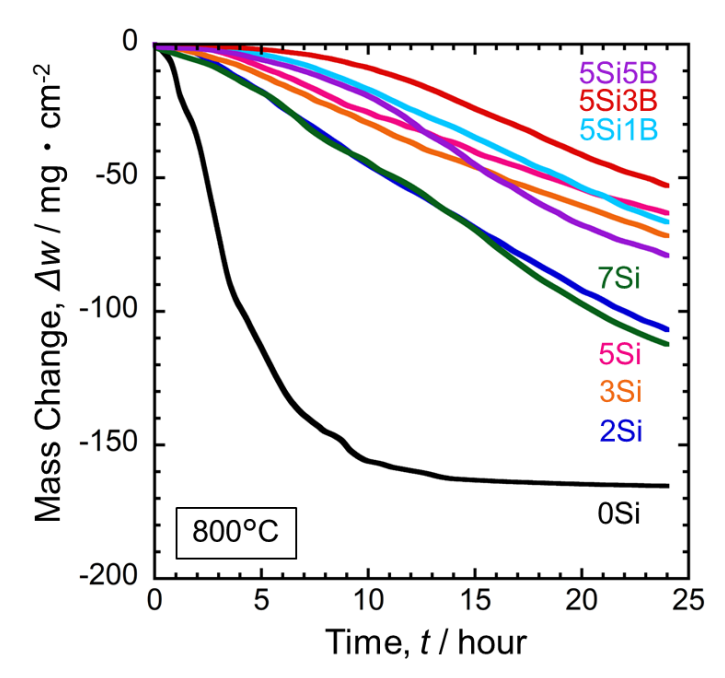


Fig.1 Oxidation curves of the alloys obtained by isothermal oxidation tests at 800°C.

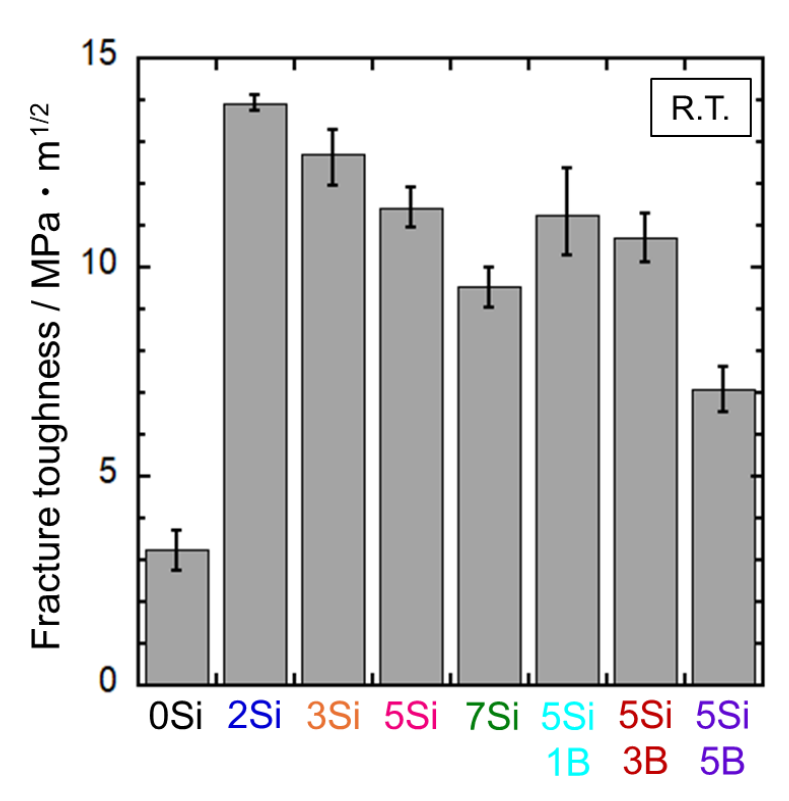


Fig. 2 Fracture toughness of the alloys obtained by four-point bending tests and EMAR method at room temperature.

P 016:

C-doped Molybdenum – Dense and crack-free Molybdenum-alloy manufactured by PBF-LB – an alternative to TZM?

Benedikt Distl¹, Lukas Kaserer², Jakob Braun², Peter Singer¹, Bernhard Mayr-Schmölzer¹, Gerhard Leichtfried²

¹Plansee SE, Metallwerk-Planseestraße 74, 6600 Reutte, Austria, benedikt.distl@plansee.com ²University of Innsbruck, Faculty of Engineering Sciences, Department of Mechatronics, Materials Science, Innrain 52, 6020 Innsbruck, Austria

Introduction

With a small processing window and demanding requirements on the powder quality and process conditions, additive manufacturing (AM) of defect-free refractory metals (RM) such as pure molybdenum (Mo) by Powder Bed Fusion – Laser Beam (PBF-LB) is challenging [1]. A ductile brittle transition temperature (DBTT) above 300 °C [2] and rapid solidification results in the formation of hot- and cold-cracks when manufactured on standard PBF-LB equipment. In addition, small amounts of oxygen impurities will weaken the grain boundaries (GB) [3-5] as solubility for oxygen is low and segregation to the GB occurs where Mo-oxide-particles will form [3,4,6]. Furthermore, the likelihood of defect formation (e.g. pores) is increased by the presence of impurities [1,7]. By combining i) elevated build-plate temperature (above DBTT), ii) alloying strategy to engineer the grain boundaries and segregations, and iii) a low oxygen content in the powder and build chamber, defect free, dense samples can be manufactured [1,8-13].

Especially carbon-doped Mo has shown great potential resulting in comparable mechanical (bending and tensile strength) and physical properties (heat capacity (cp), thermal conductivity, coefficient of thermal expansion (CTE)) when compared to powder metallurgically (PM) manufactured Mo and TZM (Mo-Ti-Zr-C alloy). Combining these properties with the advantages of AM will enable the development of new products and improvement of existing ones.

Materials and Methods

For this study, pure Mo powder supplied by Global Tungsten &Powders (AM WD 200) was doped with carbon at Plansee SE to achieve a carbon content of 0.45 wt.% (hereafter denoted MoC0.4). This powder was used to manufacture samples using an AMCM M290-2 having build-plate heating and two 1kW Yb-fiber lasers (1070 nm wavelength). The parameters used were 400 W and 600 mm/s using a laser spot size of 80 μ m and a layer thickness of 30 μ m with a hatch distance of 100 μ m. The build jobs were run in argon atmosphere with an oxygen level below 20 ppmv.

The properties of the additively manufactured MoC0.4 samples were compared with those of stress-relieved TZM samples, which were conventionally manufactured by sintering and forging. Cylindrical samples with the diameter of 5.0 and 12.7 mm were manufactured to investigate physical properties. The heat capacity and thermal conductivity were measured using Netzsch LFA (Laser Flash Analysis) 457 with measurements taken at RT, 200, 400, 600, 800, and 1000 °C. The linear CTE was measured by a push-rod dilatometer 402 Expedis Select from Netzsch operated in the temperature range from room temperature (RT) to 1200 °C with measurements taken in an interval of 1 °C.

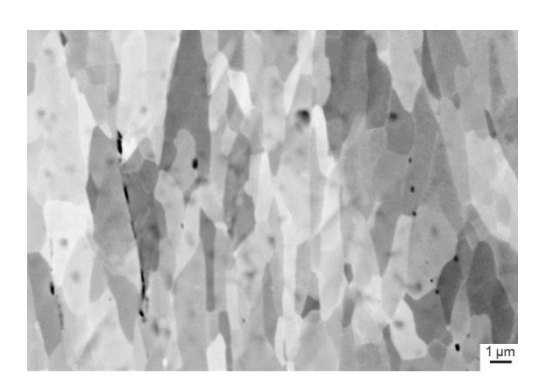
Bending samples for 3-point bending tests were manufactured and tested according to EN ISO 3325:2002-06 (at RT) and DIN EN ISO 7438 (at elevated temperatures) with a span of 200 mm and testing rate of 5 mm/min. Round tensile samples were manufacture according to sample geometry B defined in DIN 50125:2022-08 with a measurement length of 20 mm and a diameter of 4 mm. Testing was done according to EN ISO 6892-2:2018 with a testing rate of $25x10^{-5}$ 1/s.

Results and Discussion

MoC0.4 and TZM show similar thermal expansion, while the heat capacity is about 5 % higher and the thermal conductivity about 10 % lower for MoC0.4 compared to TZM. The electrical conductivity of MoC0.4 is approximately 50% lower than in TZM. These differences are a result of the unique microstructure of MoC0.4. (Fig. 1).

Compared to conventionally manufactured Mo and TZM, MoC0.4 exhibits equal or superior bending strength (Fig.2)

The bending strength of MoC0.4 at RT is approximately 1800 MPa at a bending angle of 8°, while the vales for TZM are 1400 MPa/57°. As displayed in Fig.2, the bending strength of MoC0.4 (2000 MPa, 86°) is double that of TZM at 300 °C. Stress relieved TZM shows higher plasticity at room temperature than MoC0.4 manifesting in a higher bending angle, which equalizes at elevated temperatures. Furthermore, MoC0.4 displays higher bending strength over the entire tested temperature range.



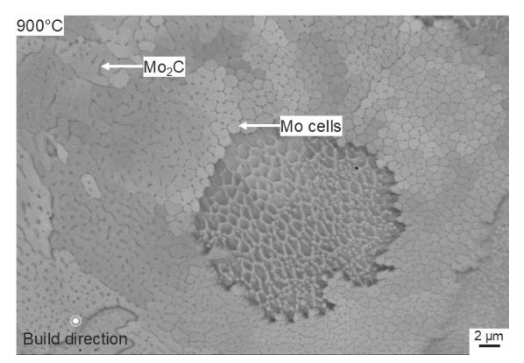


Fig. 1: Microstructure of TZM (left) and additively manufactured MoC0.4 (right)

Similar observations are made when comparing the tensile strength (Fig. 3), however, the differences between MoC0.4 and TZM are not as pronounced as for the bending strength. MoC0.4 shows a brittle material response at RT compared to 15 % uniform elongation of TZM. The difference in UTS at RT is about 50 MPa. At elevated temperatures, the UTS of MoC0.4 and TZM are close together with the elongation at break of MoC0.4 being 5-10 % below that of TZM. Nevertheless, the tensile properties are promising making MoC0.4 a candidate to substitute TZM in certain applications.

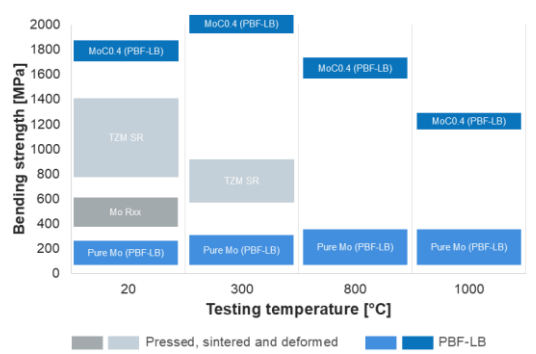


Fig. 2: Comparison of bending strength of MoC0.4 (PBF-LB), TZM SR, Mo Rxx, and pure Mo (PBF-LB) at RT, 300, 800, and 1000 °C

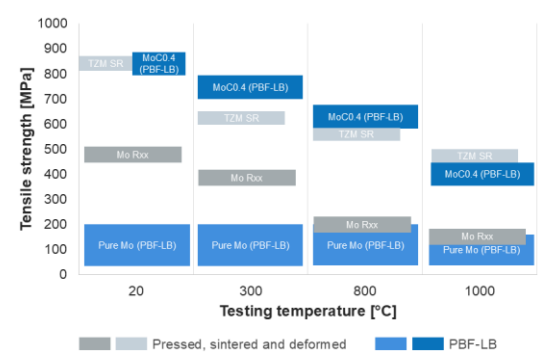


Fig. 3: Comparison of tensile strength of MoC0.4 (PBF-LB), TZM SR, Mo Rxx, and pure Mo (PBF-LB) at RT, 300, 800, and 1000 °C

- [1] J. Braun, L. Kaserer, J. Stajkovic, K.-H. Leitz, B. Tabernig, P. Singer, P. Leibenguth, C. Gspan, H. Kestler, G. Leichtfried, Int. J. Refract. Met. Hard Mater. **2019**, 84, 104999
- [2] G. Leichtfried, J.H. Schneibel, M. Heilmaier, Metall. Mater. Trans. A. **2006**, 37, 2955-2961
- [3] J.L. Bartlett, X. Li, Additive Manufacturing. **2019**,27, 131-149
- [4] S. Patel, M. Vlasea, Materialia. 2020, 9, 100591
- [5] Y. Huang, T.G. Fleming, S.J. Clark, S. Marussi, K. Fezza, J. Thiyagalingam, C.L.A. Leung, P.D. Lee, Nature Communications. **2022**, 13, 1170
- [6] M. Higashi, T. Ozaki, Material & Design. 2020, 191, 108588
- [7] C.L.A. Leung, S. Marussi, M. Towrie, R.C. Atwood, P.J. Withers, P.D. Lee, Acta Mat. **2019**, 166, 294-305
- [8] A. Ivekovic, N. Omidvari, B. Vrancken, K. Lietaert, L- Thijs, K. Vanmeensel, J. Vleugels, J.-P. Kruth, Int. J. Refract. Met. Hard Mater. **2018**, 72, 27-32
- [9] J. Braun, L. Kaserer, I. Letofsky-Papst, K.-H. Leitz, H. Kestler, G. Leichtfried, Int. J. Refract. Met. Hard Mater. **2020**, 92, 105283
- [10] L. Kaserer, J. Braun, J. Stajkovic, K.-H. Leitz, P. Singer, I. Letofsky-Papst, H. Kestler, G. Leichtfried, Int. J. Refract. Met. Hard Mater. **2020**, 93, 105369
- [11] J. Braun, L. Kaserer, J. Stajkovic, H. Kestler, G. Leichtfried, Material & Design Vol. **2022**, 215, 110507
- [12] L. Kaserer, D. Brennsteiner, J. Braun, V. Goettgens, I. Letofsky-Papst, B. Mayr-Schmölzer, B. Distl, G. Leichtfried, Int. J. Refract. Met. Hard Mater Vol. 2025, 130, 107156
- [13] L. Kaserer, D. Brennsteiner, J. Braun, V. Goettgens, I. Letofsky-Papst, P. Singer, H. Kestler, W. Schafbauer, G. Leichtfried, Int. J. Refract. Met. Hard Mater. 2023, 117, 106384

P 017:

How rapid quenching and heating cycles influence phase transformations in advanced γ-TiAl alloys

Andreas Stark, Marcus W. Rackel and Florian Pyczak
Helmholtz-Zentrum Hereon, 21502 Geesthacht, Germany, andreas.stark@hereon.de,
marcus.rackel@hereon.de, florian.pyczak@hereon.de

Introduction

During the last decade, intermetallic γ-TiAl based alloys have been successfully introduced as structural materials for low-pressure turbine blades in civil aero engines [1]. A possibility to expand the range of their use is the introduction of novel production methods like additive manufacturing (AM) [2]. However, a challenge of the AM processes are the very fast cooling and heating rates that cause the formation of microstructures far away from chemical and thermodynamic equilibrium or lead to high internal stresses. With conventional characterization and analysis methods the AM parts can only be studied after processing. Thus, all findings are based on the resulting final microstructures and properties. In contrast, *in situ* high-energy X-ray diffraction (HEXRD) experiments using synchrotron radiation enable a highly time-resolved and direct observation of the evolution of phases, strains, and texture of the material during this dynamic process [3].

Materials and Methods

We used a quenching dilatometer DIL 805 A/D to simulate and study the intrinsic quenching-heating cycles, which occur in the already solidified material below the top layer during an AM process. The dilatometer was slightly modified to work in the HEMS synchrotron radiation beamline P07 (fig. 1a) operated by Hereon at the PETRA III storage ring at DESY (Hamburg, Germany) [4]. Two alloy compositions, namely Ti-43.5Al-4Nb-1Mo-0.1B and Ti-48Al-2Nb-2Cr (all compositions in at. %). were subjected to the same thermal cycles. First, the samples were heated to 1300 °C to produce a similar high temperature start condition. Then they were cyclic quenched and heated with rates of 200 °C·s⁻¹ between a low simulated powder bed temperature (700 °C and 1000 °C) and a high simulated layer temperature. The layer temperature was stepwise reduced from 1300 to 1100 °C in order to simulate the decreasing layer temperature with increasing distance to the surface and the heat source during an AM process (fig. 1b).

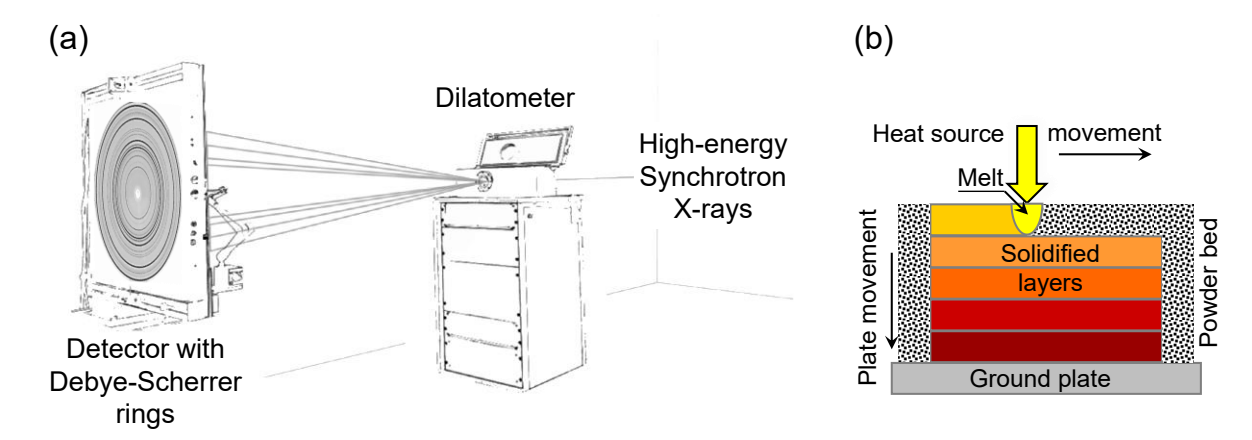


Fig. 1: (a) Sketch of the experimental setup at the synchrotron beamline HEMS. (b) Sketch of the AM process. With increasing distance to the surface and the heat source, the temperature in the solidified layers decreases.

During cycling the diffraction rings were recorded on a Perkin Elmer XRD 1621 flat panel detector with a rate of 10 Hz. The Debye-Scherrer rings were azimuthally integrated using the program Pydidas [5] and phase fractions and lattice parameters were calculated from the resulting diffraction pattern with the Rietveld refinement program MAUD [6]. These *in situ* experiments allow to determine the influence of the cooling rate and a chosen powder bed temperature on lattice parameters and phase fractions, and to observe changes in the crystal structure and atom site occupancy for all phases present, namely α/α_2 , β/β_0 and γ/γ_m .

Results and Discussion

Figure 2 shows the evolution of the diffraction pattern for both alloys during the same temperature program with a simulated powder bed temperature of 1000 °C. While Ti-43.5Al-4Nb-1Mo-0.1B cycles between the two-phase field ($\alpha+\beta$) and the three-phase field ($\alpha+\beta+\gamma$), Ti-48Al-2Nb-2Cr cycles within the two-phase field ($\alpha+\gamma$) almost during the complete temperature program. During the low temperature plateaus the phase fractions still continue to transform in both experiments. This phenomenon is clearly visible e.g. for γ 200 and γ 002 in figure 2a or for α_2 200 in figure 2b especially after quenching from the higher simulated layer temperatures.

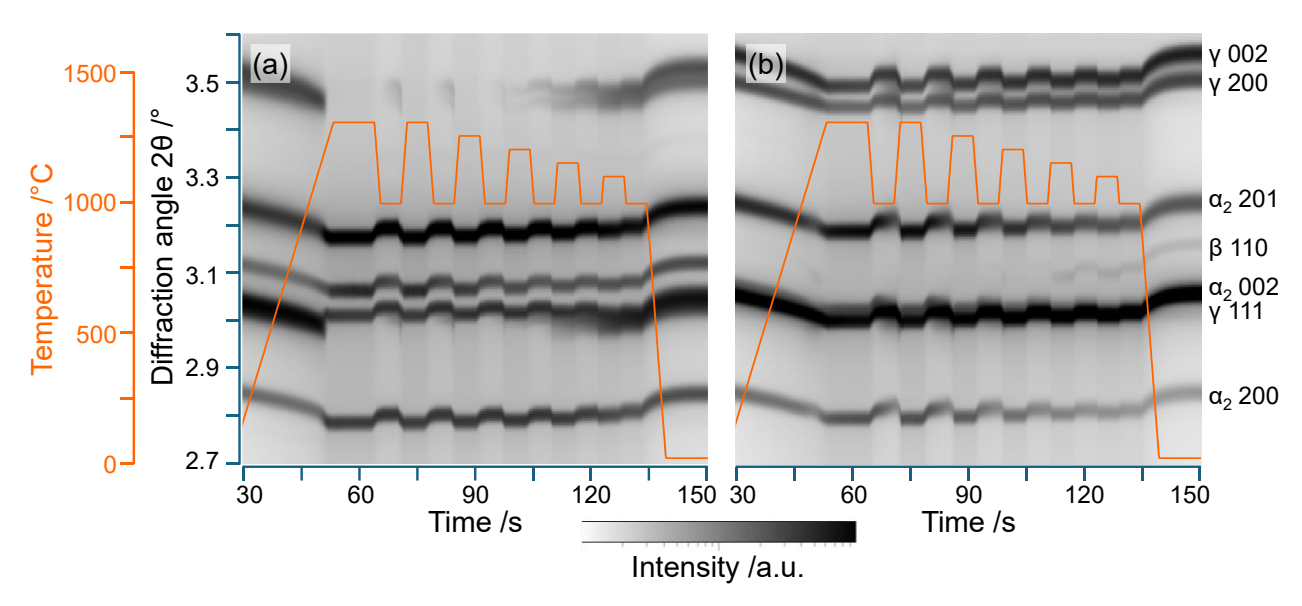


Fig. 2: Evolution of the diffraction pattern during thermal cycling for (a) Ti-43.5Al-4Nb-1Mo-0.1B and (b) Ti-48Al-2Nb-2Cr. The diffraction patterns are overlaid with the temperature profile of the experiments. On the left side, the peaks are assigned to the different phases.

Even if the applied quenching and heating rates ($200 \, ^{\circ}\text{C} \cdot \text{s}^{-1}$) do not reach the rates of real AM processes, the experiments allow to measure the highly dynamic process *in situ*. The phase transformation kinetics cannot follow the applied cooling rates. Strong deviations between the measured phase fractions and the phase fractions in thermodynamic equilibrium occur. Depending on the simulated powder bed temperature, the transformation comes to a virtual standstill or continues, but at different rates depending on the temperature difference between layer and powder bed.

- [1] B. P. Bewlay, S. Nag, A. Suzuki, M. J. Weimer, Materials at High Temperatures 33 (2016) 549-559, doi:10.1080/09603409.2016.1183068.
- [2] Silja-Katharina Rittinghaus, Janett Schmelzer, Marcus Willi Rackel, Susanne Hemes, Andreas Vogelpoth, Ulrike Hecht, Andreas Weisheit, Materials 13 (**2020**) 4392, doi:10.3390/ma13194392.
- [3] Gloria Graf, Jan Rosigkeit, Erwin Krohmer, Peter Staron, Raimund Krenn, Helmut Clemens, Petra Spoerk-Erdely, Advanced Engineering Materials 23 (**2021**)2100557, doi:10.1002/adem.202100557.
- [4] N. Schell, A. King, F. Beckmann, T. Fischer, M. Müller, A. Schreyer, Materials Science Forum 772 (**2014**) 57–61, doi:10.4028/www.scientific.net/MSF.772.57.
- [5] M. Storm, Python Diffraction Data Analysis Suite (2024) https://doi.org/10.5281/zenodo.7568610.
- [6] Luca Lutterotti, Roman Vasin, Hans-Rudolf Wenk, Powder Diffraction 29 (**2014**) 76 84, doi:10.1017/S0885715613001346.

P 018:

In-situ MgO strengthening of spark plasma sintered vanadium alloy

<u>levgen Solodkyi</u>¹, Georg Hasemann², Fabian Lanoy², Mathias Galetz² and Manja Krüger¹

Otto-von-Guericke-Universität Institut für Werkstoffe, Technologien und Mechanik (IWTM)

Universitätsplatz 2, 39106 Magdeburg, Germany, <u>levgen.solodkzi@ovgu.de</u>, <u>georg1.hasemann@ovgu.de</u>, <u>manja.krueger@ovgu.de</u>

²DECHEMA-Forschungsinstitut, Theodor-Heuss-Allee 25, 60486 Frankfurt am Main, Germany, fabian.lanoy@dechema.de, galetz@dechema.de

Introduction

Vanadium alloys present an attractive alternative to high-strength steels, nickel-based alloys, and titanium-based materials for use as structural high-temperature materials. With a density of approximately 6 g/cm³, they offer significant potential as lightweight structural materials [1]. Additionally, vanadium's high melting point (1910°C) allows for applications at elevated temperatures, providing an advantage over nickel-based materials due to the combination of high thermal resistance and low density. However, the strength of vanadium and low-alloy vanadium materials declines significantly at temperatures above 600°C. Furthermore, the formation of liquid oxides at around 700°C necessitates additional protective measures to ensure the alloy's stability at these temperatures.

Powder metallurgy techniques enable the production of fine-grained structures, which enhance strength at elevated temperatures compared to traditionally melted alloys. In most cases, the successful application of powder metallurgy relies on the use of homogeneous powder mixtures, followed by forming and/or sintering. However, achieving uniform dispersion can be challenging when one component is nano-sized, as conventional mixing methods often fail to ensure the required homogeneity. This issue can potentially be addressed through the in-situ synthesis of dispersed MgO particles on the surface of vanadium powder, followed by spark plasma sintering (SPS) of the resulting composite material. Therefore, the primary objective of this study was to investigate the effect of in-situ MgO reinforcement on the high-temperature strengthening of the alloy and its influence on the oxidation resistance of vanadium-based materials.

Materials and Methods

To ensure a uniform distribution of vanadium oxide particles within the material, insitu synthesis was performed within a porous vanadium matrix. Billets with a porosity of 45–47% were impregnated with a 0.2 M/L–0.6 M/L solution of magnesium nitrate hexahydrate and urea, followed by heat treatment in air at 400–600°C for two hours. Powder compacts with varying MgO content, designated as V-xMgO (x = 0, 1, 2.5, 5 wt.%), were then sintered using spark plasma sintering (SPS) at 1300°C under a load of 50 MPa for 5 minutes. The microstructure, chemical composition, and phase composition were analyzed. Additionally, compressive strength and the potential for plastic deformability was tested at both room temperature and 600°C, while oxidation stability was evaluated at 600°C.

Results and Discussion

The study of the phase composition of porous samples after in-situ synthesis of MgO at 400-600 °C heat treatment showed that at a temperature of 400 °C, MgO is synthesized

and no vanadium oxidation occurs. An increase in the synthesis temperature to 500 °C leads to saturation of vanadium with nitrogen and the formation of a solid solution of $V_{16}N_{1.5}$, the amount of which increases with an increase in the synthesis temperature to 600 °C. At the same time, at a synthesis temperature of 500 °C, the formation of vanadium oxide was not recorded, while at a temperature of 600 °C, vanadium oxide VO_2 appeared.

The microstructures of V-xMgO composites after SPS are shown in Fig. 1. It can be observed that MgO is evenly distributed along the boundaries of the vanadium grains. Notably, the SPS process resulted in an almost fully dense structure. Moreover, increasing the vanadium oxide content did not negatively impact the densification of the samples or lead to residual porosity.

At the same time, the presence of MgO on the surface of vanadium powder particles acted as a limiting factor, preventing structural coarsening through recrystallization. As indicated by the yellow arrows in Fig. 1, grains that were not coated with MgO were more prone to recrystallization during SPS. Microstructural analysis (Fig. 1) suggests that the primary densification mechanisms are surface diffusion and viscous flow.

The addition of MgO also slowed the formation of oxide scales on vanadium surfaces during oxidation tests at 600°C. After 30 hours of testing, samples of pure vanadium and those with the lowest MgO concentration (1 wt%) were completely converted into oxide scale. In contrast, samples containing 2.5 wt% and 5 wt% MgO exhibited oxidation behavior consistent with a parabolic rate law. The reduced oxidation rate is likely due to grain refinement, as fine-grained materials generally exhibit greater oxidation resistance than coarse-grained counterparts [2,3]. After SPS, the grain size of vanadium ranged from 5 to 75 μ m (Fig. 1).

In both cases, oxidation followed a parabolic rate law. Based on these findings, it can be concluded that the addition of dispersed MgO particles enhances the oxidation resistance of vanadium, an effect that can be further improved by refining the grain size. The results of the compression tests showed that increasing the MgO particle content to 5 wt% enhanced the yield strength of the composite to 2.18 ± 0.07 GPa. Prior to fracture, plastic deformation was observed in the range of 0.1–0.22%. Fracture occurred exclusively through a brittle mechanism. During testing, longitudinal cracks along the compression axis were recorded, indicating minimal plastic deformation. Notably, sintered vanadium exhibited a yield strength nearly ten times higher than that of commercially pure vanadium tested at room temperature. For the V-5MgO composite, the yield strength increased from 0.3 GPa to 0.35 GPa during testing at 600°C. In contrast, pure vanadium exhibited dynamic strain aging at 600°C, whereas this effect was absent in V-xMgO composites. The reason for this difference remains unclear and requires further investigation.

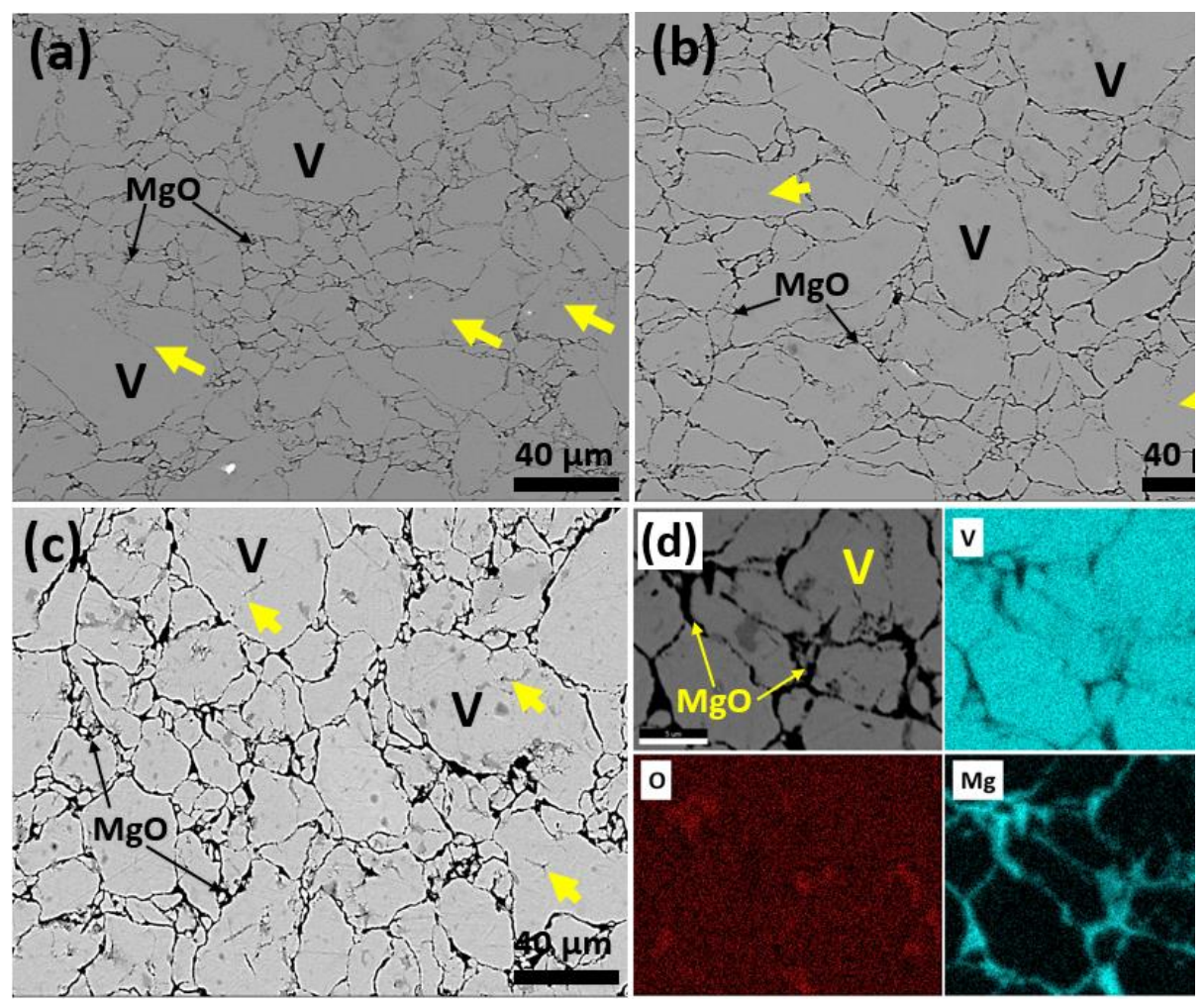


Fig. 1: SEM images of sintered specimens with different MgO concentration: (a) 1 wt.%; (b) 2.5 wt.%; (c) 5 wt.% and (d) elemental mapping of the V-5MgO.

- [1] M. Krüger, V. Bolbut, F. Gang, G. Hasemann. JOM **2016**, 68, 2811–2816.
- [2] P. Martin, C. Aguilar, J.M. Cabrera, Journal of Materials Research and Technology, **2024**, 30, 1900-1928.
- [3] X. Wang, J.A. Szpunar, 752 (2018) 40, Journal of Alloys and Compounds. 2018, 752, 40.

Acknowledgements

We acknowledge the DFG for funding this project (funding nb. 494809307).

P 019:

Microstructure formation of eutectic V-9Si-6.5B alloys observed by in-situ HE-XRD during directional solidification

Roja Rani Korrayi¹, Zahra Sabeti², Andreas Stark¹, Georg Hasemann², Florian Pyczak¹

¹Helmholtz-Zentrum Hereon, Institute of Materials Physics, Max-Planck-Str. 1, 21502 Geesthacht, Germany, Roja.Korrayi@hereon.de, andreas.stark@hereon.de, florian.pyczak@hereon.de ²Otto-von-Guericke University Magdeburg, Institute of Materials, Technologies and Mechanics, Universitätsplatz 2, 39106 Magdeburg, Germany, zahra.sabeti@ovgu.de, georg1.hasemann@ovgu.de.

Introduction

Ni-base super alloys are the established metallic high temperature material due to their temperature capability of up to 1150 °C. Above this temperature the strengthening capacity of y'-phase is lost and they lose their high temperature strength and creep resistance. Directionally solidified Ni-base superalloys proved that minimizing the amount of grain boundaries perpendicular to external loads can further improve creep resistance. As an alternative to Ni-base superalloys, directionally solidified eutectic alloys of intermetallic systems have shown continuous, better aligned, and fine lamellar microstructure and offer a potential for higher temperature capability [1]. Refractory Mo-, Nb-, and V-silicides, often with the addition of boron, were identified as attractive candidates for such eutectic systems and have a potential to be applied in aerospace, gas-turbines and VIth generation of nuclear reactors [2]. Among them, V-silicides gain increasing attention due to their combination of high melting point and low-density. However, several issues like improving oxidations resistance still have to be addressed before this system can be seen as a viable option for a high temperature structural material.

The aim of the present study is to investigate the underlying mechanisms of phase -, microstructure - and texture formation of ternary eutectic V-Si-B alloy during directional solidification which are not completely understood, yet.





Fig. 1. Images of (a) button shape ingot and (b) cylindrical shape V-9Si-6.5B alloy

Materials and Methods

Rod-shaped samples of the eutectic V-9Si-6.5B alloy for in-situ directional solidification experiments, were produced by melting pure V (99.9%), Si (99.9999%), and B (99.4%) into a 120-gram button using a vacuum arc melting furnace as shown in figure (1-a). To achieve a homogeneous distribution of all elements, each button was flipped and remelted more than 7 times. Subsequently, the prepared buttons are drop-cast into a cylindrical copper mold with a length of 134 mm and a diameter of 11.75 mm as shown in figure (1-b) and machined to 10 mm diameter. A zone melting device with induction heating was used for the directional solidification process. During this process, high energy X-rays with 100.5 keV (λ =0.123 Å) are used to transmit the rod at different positions with respect to the melt pool to collect diffraction data [3]. The in-situ experiments were conducted at the P07 High Energy Materials Science (HEMS) beamline, operated by Helmholtz-Zentrum Hereon Geesthacht at PETRA III (DESY) in Hamburg, Germany.

Results and Discussion

This study investigates the microstructure formation in an eutectic V-9Si-6.5B alloy [4] through in-situ high-energy X-ray diffraction (HE-XRD) characterisation during directional solidification. The research focuses on understanding the microstructural evolution and phase transformation under controlled solidification conditions such as withdrawal speed and rotational speed of the feed and seed rod. The directional solidification process was systematically varied using withdrawal rates between 0.5 to 5 mm/min with a rotation speed of 20 rpm. These parameters are used to evaluate their impact on eutectic lamellar spacing, interphase boundary alignment and resulting mechanical properties. Utilizing HE-XRD, real-time data was collected during directional solidification at different positions such as in the solid phase before and after directional solidification, at the solidification front, and in the liquid phase as shown in figure (2). From the collected data, dynamic changes in phase fraction, microstructure, and crystallographic texture were seen at different processing parameters. It was found that the withdrawal rate had a significant influence whether texture occurred or not favouring texture formation for higher withdrawal rates. The findings will be used to understand the solidification of V-Si-B based alloys and optimize their directional solidification process.

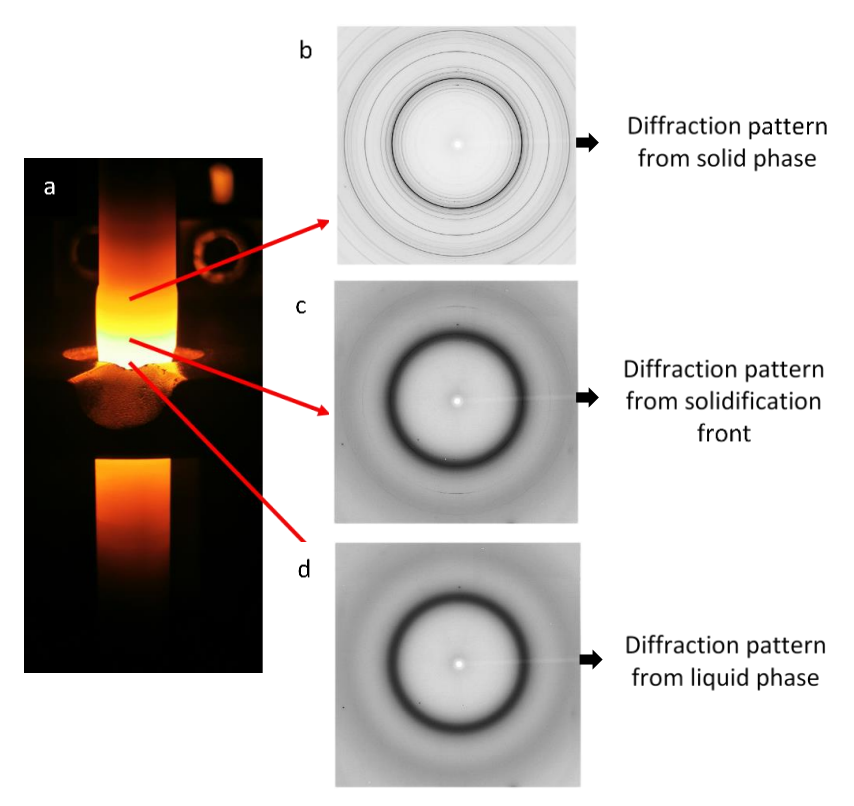


Fig. 2. In-situ HE-XRD data at different positions during (a) directional solidification processing. Images in (b), (c), and (d) are Debye-Scherrer diffraction rings at different positions such as at sold phase, solidification front, and at liquid phase respectively

- [1] Gang, F., Heilmaier, M. Influence of Directional Solidification on the Creep Properties of a Binary NbSi Eutectic Alloy. JOM 66, 1908–1913 (**2014**).
- [2] Silva, AAAP Da., Chaia, N., Ferreira, F., Carvalho Coelho, G., Fiorani, JM., David, N., Vilasi, M., Nunes, CA. Thermodynamic modeling of the V-Si-B system. Calphad **2017**, 59, 199-206.
- [3] Gombola, C., Hasemann, G., Kauffmann, A., Sprenger, I., Laube, S., Schmitt, A., Gang, F., Bolbut, V., Oehring, M., Blankenburg, M., Schell, N., Staron, P., Pyczak, F., Krüger, M., Heilmaier, M. A zone melting device for the in-situ observation of directional solidification using high-energy synchrotron X-rays. Review of Scientific Instruments **2020**, 91, 093901-1 093901-9.
- [4] Yang, W. G.; Hasemann, G.; Gorr, B.; Schwaiger, R.; Krüger, M. V₈SiB₄—A New Ternary Phase in the V–Si–B System. Intermetallics **2022**, 151, 107691.

P 020:

Extension of thermodynamic and thermophysical data for TiAlbased alloys using CALPHAD

Yang Yang, Martin Xing, Reza Naraghi, Anders Engström Thermo-Calc Software AB, Råsundavägen 18, 169 67 Solna, Sweden yang@thermocalc.com

Titanium aluminide (TiAl) based alloys represent a superior class of lightweight structural materials that are promising candidates for aerospace and automotive applications [1, 2]. TiAl-based alloys exhibit advantageous specific strength-temperature properties compared with steels, Ni-based superalloys and conventional titanium alloys particularly in the temperature range of 600 to 800 °C [3]. The development of advanced TiAl alloys with more demanding properties for aerospace applications attracts considerable attentions. The microstructure, phase constituents of TiAl alloys and their properties strongly depend on the composition and manufacturing procedure. The phase constituents of TiAl-based alloys are highly susceptible to small changes in the alloy's chemistry and heat treatment procedure. In a general manner, the conventional processing routes like casting might restrict the use of titanium alloys to simple shapes and moderate dimensions due to processing defects. Therefore, alternative manufacturing routes including additive manufacturing are being investigated with the aim of producing complex-shaped TiAl components achieving the desired geometrical, technical and functional properties.

To achieve accurate performance predictions of components and optimize materialspecific requirements, we need to be able to analyze and replicate the changes in materials properties during processing. To achieve this, it is essential to understand the process-structure-property relationships of the materials. A challenge is that the properties of materials depend on both their chemical composition and processing conditions. Handbook data and data repositories alone tend to be limited in the scope of materials covered (their compositions), the temperature range (processing conditions), or the lack of time dependence. The CALPHAD approach captures the composition and temperature dependence of properties, as well as their temporal evolution, which makes it possible to cover gaps in the measured data. The usefulness of CALPHAD simulations depends on the quality and scope of the database being used. In recent years we have successfully extended traditional thermodynamic CALPHAD databases by incorporating thermophysical properties, such as molar volume, electrical resistivity, thermal conductivity, viscosity and surface tension of liquid, in the spirit of the CALPHAD approach. In addition, transport properties such as diffusivities or atomic mobilities have been modeled to improve the accuracy of microstructure evolution predictions. Fig. 1 shows the calculated tracer diffusivities of some elements in α₂ phase (Ti₃Al) while Fig. 2 presents the calculated thermal conductivity of y phase (TiAl). In this presentation, we will discuss the recent development on extending thermodynamic and thermophysical data for TiAl alloys. Besides, the applications in alloy design and process optimization will also be demonstrated.

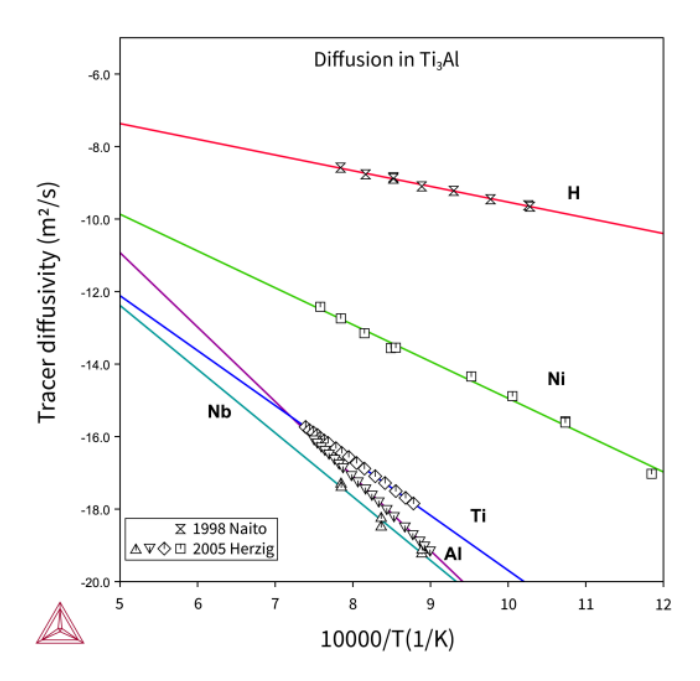


Fig. 1: The calculated tracer diffusivities of Ni, Ti, Al, Nb, H in Ti₃Al (experimental data from [4, 5]).

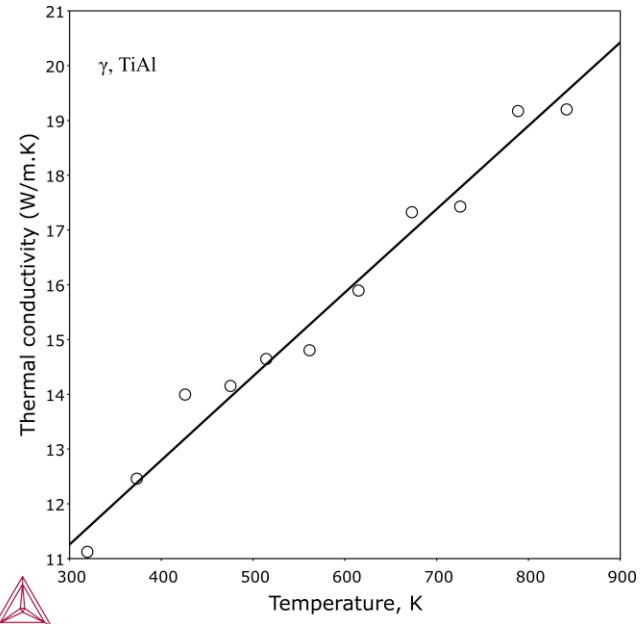


Fig. 2: The calculated thermal conductivity of γ phase (Ti-34 wt% Al) (experimental data from [6]).

- [1] H. Clemens, H. Kestler, Adv. Eng. Mater. 2 (2000) 551-570.
- [2] T. Noda, Current Status of Mass Production of Gamma Titanium Aluminide Alloy Turbine Rotors in Turbochargers and Future Challenges, in: Structural Aluminides for Elevated Temperature Applications: Gamma Titanium and Other Metallic Aluminides, New Orleans, USA, (2008) 7-8.
- [3] H. Clemens, W. Smarsly, V. Güther, S. Mayer, Advanced intermetallic titanium aluminides, 13th World Titanium Conference Proceeding, San Diego, USA, (2015) 1189-1200.
- [4] S. Naito, M. Yamamoto, M. Doi, M. Kimura, J. Electrochem. Soc. 145 (**1998**) 2471–2475. [5] C. Herzig, S. Divinski, Bulk and Grain Boundary Diffusion in Intermetallic Compounds, in Diffusion Processes in Advanced Technological Materials, Elsevier/William Andrew Publishing, (**2005**) 173–238.
- [6] A. Sugawara, I. Takahashi, Netsu Bussei. 5 (1991) 184-189.

P 021:

Heat capacities for several ordered intermetallic phases in the system Al-Fe-Mn-Ni-Ti

Mario J. Kriegel¹, Alexander Walnsch² and Andreas Leineweber³

¹TU Bergakademie Freiberg, Institute of Materials Science, Gustav-Zeuner-Str. 5, 09599 Freiberg,

Germany, mario.kriegel@iww.tu-freiberg.de

²TU Bergakademie Freiberg, Institute of Materials Science, Gustav-Zeuner-Str. 5, 09599 Freiberg, Germany,

Present address: GTT-Technologies, Kaiserstr. 103, 52134 Herzogenrath, Germany, aw@gtt-technologies.de

³TU Bergakademie Freiberg, Institute of Materials Science, Gustav-Zeuner-Str. 5, 09599 Freiberg, Germany, andreas.leineweber@iww.tu-freiberg.de

Introduction

Thermodynamic data, such as the isobaric heat capacity (c_p), is essential for establishing reliable thermodynamic databases, which serve as the foundation for computer-based materials development methods. Moreover, heat capacity data is crucial for high-temperature applications where heat transfer plays a significant role, as it heavily affects thermal conductivity. The development of CalPhaD (Calculation of Phase Diagrams) databases, which can describe thermodynamic functions of bulk phases down to 0 K in a physically meaningful manner, also known as " 3^{rd} generation CalPhaD databases", is becoming increasingly important [1,2]. The thermodynamic functions of phases in higher-order systems are typically described by the Neumann-Kopp rule, which relates the Gibbs energy of an intermediate phase to the individual pure end-member elements [3]. However, this approach often overestimates the heat capacity of the intermetallic compound [4]. Therefore, experimental data is necessary to compensate for these differences and enable the modeling of realistic material behavior.

Intermetallic materials have attracted the attention of scientists for more than one decade [5] because their fields of application range from, e.g., high-temperature structural materials, shape-memory alloys, permanent magnets and hydrogen-storage materials. The focus is placed on intermetallic phases, which are ordered superstructures derived from disordered FCC (A1, Cu, $Fm\overline{3}m$), BCC (A2, W, $Im\overline{3}m$) and HCP (A3, Mg, $P6_3/mmc$) solid solutions. One of these intermetallic phases is the $L1_0$ ordered TiAl phase (γ-TiAl), which is mainly used in high-temperature structural applications such as gas-turbine blades. The Ni-based L12-ordered phases Ni3Mn and Ni₃Fe are also important for this type of application, since Fe and Mn can occur as trace elements in multicomponent Ni-based superalloys, where they affect the formation of γ 'precipitates. L₁₀-NiMn is another rather versatile phase, which can be applied in functional applications as an antiferromagnetic layer material with high magnetic anisotropy energy. Moreover, L10-NiMn has also a severe impact on structural Ni–Fe–Mn maraging alloys, where it is formed as a grain boundary strengthening phase. The intermetallic phases in the Ni–Fe–Ti system, especially those connected to the B2-NiTi phase are of considerable interest, due to their vast applicability as shape-memory alloys. The Fe-containing B2-based phases are of particular importance for the thermodynamic modeling of the binary B2-NiTi phase, since due to the martensitic transformation occurring in the binary alloy, the low-temperature heat capacity is not directly accessible by experimental investigation. However, by extrapolating the lowtemperature c_p data of the B2-(Ni,Fe)Ti phase, the corresponding temperature dependent c_p below the martensite start temperature of the binary NiTi end-member can be reliably estimated.

Materials and Methods

The alloys were prepared using a high purity metal mixture of aluminum, iron, manganese, nickel and titanium (Al: 99.9995 %, Fe: 99.99 %, Mn: 99.95 %, Ni: 99.995 %, Ti: 99.995 %, Alfa Aesar/Thermo Fisher GmbH, Germany). Afterwards, an additional heat treatment at 1273 K for 24 h was executed to ensure the homogeneity of the alloys. Their chemical composition was checked by means of electron-probe microanalysis with wavelength-dispersive X-ray spectroscopy (EPMA/WDS). In addition, scanning-electron microscopy (SEM) and X-ray diffraction (XRD) was used to determine the spatial distribution of each phase in the alloy and to perform the phase identification, respectively. For the heat-capacity determination, the alloy rods were cut into discs and analyzed using differential-scanning calorimeter (DSC) devices. Applying the classical three-step continuous method, a DSC 8000 (PerkinElmer, USA) was used in the temperature range from 110 K to 570 K, and a DSC Pegasus 404C (Netzsch, Germany) in the range from 520 K to 870 K. The alloy discs were measured in a Pt/Rh crucible with an Al₂O₃ inlet under an Ar flow (20 ml/min) at a heating rate of 10 K/min. Certified standard sapphire discs with a mass approximately equal to the mass of the sample were used for calibration purposes. Additionally, enthalpy increment measurements of the alloys were performed using a MHTC 96 drop calorimeter (SETARAM/KEP Technologies, France) under isothermal conditions between 680 and 890 K. The alloys were dropped at ambient temperature into an Al₂O₃ crucible with an Al₂O₃ powder bed inside the calorimeter under Ar atmosphere.

Results and Discussion

The microstructures of the heat-treated alloys were first examined to assess their homogeneity and to ensure their suitability for subsequent heat-capacity measurements. The SEM/BSE micrograph of the NiTi alloy showed a very fine needle like microstructure, indicating the presence of a solid-state phase transformation upon cooling. This was confirmed by the XRD measurements, which showed the presence of significant amounts of the martensitic phase B19'-NiTi along with some retained B2 austenite. In order to determine the heat capacity of B2-NiTi, preliminary DSC measurements were performed to determine the characteristic martensite temperatures and thus limit the temperature range investigated. Based on these measurements, the minimum temperature for subsequent heat-capacity measurements was set to 400 K for this particular alloy.

The experimentally derived c_p values were used, together with c_p data from literature, to describe the temperature dependent heat capacities of the respective phases using an Extended-Einstein model (EE-model). The EE-model is currently widely adopted in the development of novel multicomponent thermodynamic descriptions (3rd generation databases) using the CalPhaD approach [1,2]. The major part of the EE-model follows the classical Einstein model [6] to describe the harmonic vibrations of the atoms. Moreover, to account for electronic contributions and low-order anharmonic effects, two additional parameters a and b were included as follows:

$$c_{\mathrm{p}}^{\mathrm{EE}} = 3 \cdot \mathrm{R} \cdot \left(\frac{\theta_{\mathrm{E}}}{T}\right)^{2} \cdot \frac{\exp\left(\frac{\theta_{\mathrm{E}}}{T}\right)}{\left[\exp\left(\frac{\theta_{\mathrm{E}}}{T}\right) - 1\right]^{2}} + a \cdot T + b \cdot T^{2},$$

(1)

where θ_E is the Einstein temperature and R is the gas constant. Exemplarily, the experimentally determined heat capacities of the binary NiTi and TiAl phases are shown, together with literature data and the temperature dependent heat capacities described by the EE-model, in Fig. 1. Since for the binary NiTi phase, the low-temperature range was not accessible experimentally, due to the occurring martensitic transformation at approx. 325 K, the corresponding contribution from harmonic lattice vibrations, mainly described by the Einstein temperature (θ_E), was derived from a linear extrapolation of θ_E from the ternary phases Ni_{0.25}Fe_{0.75}Ti, Ni_{0.5}Fe_{0.5}Ti and Ni_{0.75}Fe_{0.25}Ti. Hereby, it was found that with decreasing Fe-content, θ_E decreases, leading to an extrapolated value for NiTi of θ_E = 236 K.

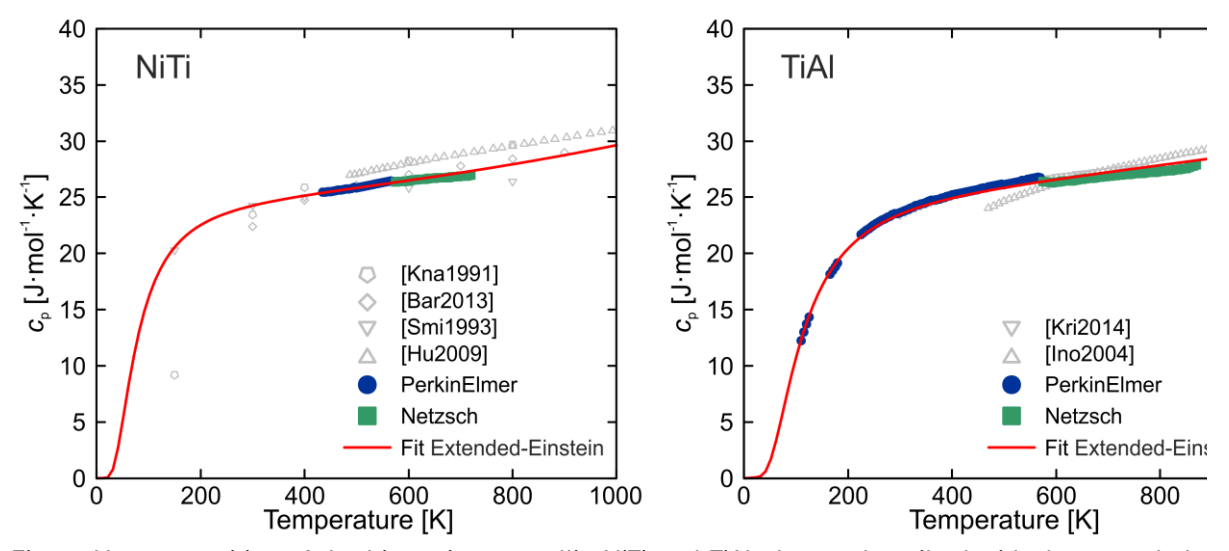


Fig. 1: Heat capacities of the binary intermetallic NiTi and TiAl phases described with the extended Einstein model together with experimental and literature data.

- [1] Q. Chen, B. Sundman, Journal of Phase Equilibria. 2001, 22, 631-644.
- [2] M.W. Chase, I. Ansara, A. Dinsdale, G. Eriksson, G. Grimvall, L. Hoglund, H. Yokokawa, Calphad: Computer Coupling of Phase Diagrams and Thermochemistry. **1995**, *19*, 437–447.
- [3] H. Kopp, T. Graham, Philosophical Transactions of the Royal Society of London. **1865**, *155*, 71–202.
- [4] J.-M. Joubert, B. Kaplan, M. Selleby, Calphad: Computer Coupling of Phase Diagrams and Thermochemistry. **2023**, *81*, 102562.
- [5] W. Rosenhain, Nature. 1923, 112, 832-834.
- [6] A. Einstein, Annalen der Physik. **1907**, *327*, 180–190.

P 022:

Fe-Al-Si-X based intermetallic alloys

Pavel Hanus¹, Martin Švec², Věra Vodičková³, Petra Pazourková Prokopčáková⁴, Adam Hotař⁵, Šárka Vávrová⁶

- ¹ Technical University of Liberec, Faculty of Engineering, Department of Material Science, Studentská 1402/2, Liberec, 46117, Czech Republic, pavel.hanus@tul.cz
 - ²Technical University of Liberec, Faculty of Engineering, Department of Engineering Technology, Studentská 1402/2, Liberec, 46117, Czech Republic, martin.svec@tul.cz
- ³ Technical University of Liberec, Faculty of Engineering, Department of Material Science, Studentská 1402/2, Liberec, 46117, Czech Republic, vera.vodickova@tul.cz
- ⁴ Technical University of Liberec, Faculty of Engineering, Department of Material Science, Studentská 1402/2, Liberec, 46117, Czech Republic, petra.prokopcakova@tul.cz
- ⁵ Technical University of Liberec, Faculty of Engineering, Department of Material Science, Studentská 1402/2, Liberec, 46117, Czech Republic, adam.hotar@tul.cz
 - ⁶Technical University of Liberec, Faculty of Engineering, Department of Engineering Technology, Studentská 1402/2, Liberec, 46117, Czech Republic, sarka.vavrova@tul.cz

Introduction

Iron aluminides have been investigated for decades as an excellent replacement for highalloy steels and cast irons for high-temperature applications [1]. The intermetallic group at TUL set itself the task of describing and testing the properties of the new Fe-Al-Si base [2], which was also modified by small additions of the elements Mo, Ti, B, V, W and Nb [3]. The structure of the prepared alloys was investigated in both the as-cast state and after heat treatment at 800°C/100h. Observation of the structure showed that the strengthening mechanism is associated with solid solution strengthening, a combination of solid solution strengthening and individual incoherent precipitates, and solid solution and incoherent precipitates arranged in a eutectic. Mechanical compression tests were performed for the as-cast and heat treatment states to determine the yield strength for room temperature and temperatures in the range of 600 - 800°C. To get a better idea of the applicability of alloys as structural materials, thermal expansion tests were performed on samples in the state after heat treatment of 800°C/100h, which is important for assemblies of structural units operating at high temperatures.

Materials and Methods

The alloys based on Fe-28Al-Si were prepared by vacuum induction melting and casting – from raw iron with carbon content lower than 0.2 at.%. As the fourth micro alloying elements, Mo, Ti, B, V, W, and Nb were used, see Tab. 1. Alloys were analysed in the ascast state and in the state after heat treatment performed in the furnace without a protective atmosphere 800°C/100h. Metallographic samples were prepared by the common metallographic method, and as the final step, the oxide polishing was used. The structure of the materials was examined by light optical microscopy (Nikon Epiphot 200) and by scanning electron microscopy with an EBSD detector (Tescan Mira). For the measurement of Thermal expansion, the quench dilatometer DIL 805L was used.

Tab. 1: All tested compositions.	. Marking of fine-grained allovs -	- green and alloys with large grains - red.

Alloy [at. %]	Αl	Si	В	V	w	Ti	Мо	Nb
Fe28Al5Si	28	5	-	-	-	-	-	-
Fe28Al15Si	28	15	-	-	-	-	-	-
Fe28Al5Si2Ti	28	5	-	-	-	≤2	-	-
Fe28Al15Si2Ti	28	15	-	-	-	≤2	-	-
Fe28Al5Si2Mo	28	5	-	-	-	-	≤2	-
Fe28Al15Si2Mo	28	15	-	-	-	-	≤2	-
Fe28Al5Si1B	28	5	1	-	-	-	-	-
Fe28Al5Si2Ti1B	28	5	1	-	-	≤2	-	-
Fe28Al5Si2Mo1B	28	5	1	-	-	-	≤2	-
Fe28Al5Si1V	28	5	-	1	-	-	-	-
Fe28Al5Si2Mo1V	28	5	-	1	-	-	≤ 2	-
Fe28Al5Si1W	28	5	-	-	1	-		-
Fe28Al5Si2Mo1W	28	5	-	-	1	-	≤2	-
Fe28Al5Si2Nb	28	5	-	-	-	-	-	≤2

Results and Discussion

The presented set of alloys can be divided into two groups in terms of grain size - with fine grains up to 250 μ m and large grains in the range of 300 - 750 μ m. In the group with fine grains, the alloy Fe28Al15Si2Mo stands out, which has an average grain size of 50 μ m in the as-cast state, and after heat treatment, the grains are coarsened to an average size of 120 μ m (see Tab. 1 – green and red groups).

High temperature tests for yield stress determination were performed at 600, 700, 800°C, and were supplemented with room temperature values. For measurements at 600°C, the yield stress range is from 340 - 960 MPa, where the best alloys were Fe28Al15Si2Mo "as cast" and Fe28Al5Si2Ti "as cast" (both fine-grained).

For practical use, the temperature of 700°C is intended, where the yield stress is from 160 to 520 MPa, where the best alloys were Fe28Al5Si1W "as cast" and Fe28Al5Si2Mo1V "as cast" (both coarse-grained).

Finally, for measurements at 800°C, the yield stress range is from 80 to 220 MPa, where the best alloys were Fe28Al15Si2Mo (both states) and Fe28Al5Si2Ti1B "as cast" (both fine-grained).

Measurement of the coefficient of thermal expansion of alloys after heat treatment at 800°C/100h shows linear curves for all alloys. Alloys Fe28Al15Si2Mo and Fe28Al5Si have better lower values of the coefficient of thermal expansion, especially up to 800°C.

Acknowledgements

This work was supported by the Ministry of Education, Youth and Sports of the Czech Republic and the European Union - European Structural and Investment Funds in the frames of Operational Programme Research, Development and Education - project Hybrid Materials for Hierarchical Structures (HyHi, Reg. No. CZ.02.1.01/0.0/0.0/16_019/0000843) and by the Institutional Endowment for the Long

Term Conceptual Development of Research Institutes, as provided by the Ministry of Education, Youth and Sports of the Czech Republic in the year 2025.

- [1] S. C. Deevi, V. K. Sikka, Nickel and iron aluminides: An overview on properties, processing, and applications. Intermetallics, 4(5), **1996**, 357–375.
- [2] M. Švec, V. Vodičková, V. Keller, P. Hanus, The effect of chromium addition and heat treatment on phase composition of cast fealsi alloys. Manufacturing Technology, 18(6), **2018**, 1029–1033.
- [3] V. Vodičková, M. Švec, P. Hanus, P. Novák, A. Záděra, V. Keller, P.P. Prokopčáková, The effect of simultaneous Si and Ti/Mo alloying on high-temperature strength of Fe3Al-based iron aluminides. Molecules, 25(18), **2020**, 4268.

P 023:

Effect of heat-treatment on the structure of Fe -28Al -15Si-X alloys

Pavel Hanus¹, Věra Vodičková², Martin Švec³ and Petra Pazourková Prokopčáková⁴
¹ Technical University of Liberec, Faculty of Engineering, Department of Material Science, Studentská
1402/2, Liberec, 46117, Czech Republic, pavel.hanus@tul.cz

- ² Technical University of Liberec, Faculty of Engineering, Department of Material Science, Studentská 1402/2, Liberec, 46117, Czech Republic, vera.vodickova@tul.cz
 - ³Technical University of Liberec, Faculty of Engineering, Department of Engineering Technology, Studentská 1402/2, Liberec, 46117, Czech Republic, martin.svec@tul.cz
- ⁴ Technical University of Liberec, Faculty of Engineering, Department of Material Science, Studentská 1402/2, Liberec, 46117, Czech Republic, petra.prokopcakova@tul.cz

Introduction

Iron-aluminium intermetallic alloys are considered to be promising candidates for structural applications, primarily due to their excellent resistance to oxidation and sulfidation. In addition, their density is significantly lower compared to steels [1]. The high-temperature mechanical properties of Fe₃Al based alloys can be improved by solid solution hardening by adding elements (Cr, V, Mo, Ti, ...) soluble in Fe₃Al matrix, increase of crystallographic order (Fe-Al-Ti system), coherent precipitates – most effective for strengthening in Fe-Al-Ta and Fe-Al-Ni system and incoherent precipitates – formed by elements with low solubility (Zr, Ta, Nb, ...) in Fe₃Al matrix or carbide and boride precipitates [2,3].

Si addition improves high-temperature tensile strength, creep, and oxidation resistance in the whole range of iron aluminides compositions [4,5]. An addition of Mo or Nb in combination with a small amount of Zr dramatically improves the creep-rupture strength of binary Fe_3Al [6].

The high-temperature mechanical properties of these alloys can be improved not only by optimal chemical composition but also by optimal heat treatment. Therefore, several types of heat treatments were tested to improve the initial as-cast structure, that can be inhomogeneous and with internal stresses after casting.

Materials and Methods

Two alloys based on Fe-28Al-15Si were prepared by vacuum induction melting and casting – from raw iron with carbon content lower than 0.2 at.%. The first alloy was alloyed with a small amount of zirconium (0.2 at. %) and the second one was alloyed 2 at. % of molybdenum. Both alloys were analysed in the as-cast state and in several states after heat treatment performed in the furnace without protective atmosphere (800°C/100h, 1000°C/24h, 1200°C/2h).

Metallographic samples were prepared by the common metallographic method, and as the final step, the oxidical polishing was used. The structure of the materials was examined by light optical microscopy (Nikon Epiphot 200) and by scanning electron microscopy (Zeiss Ultra Plus). And subsequently the hardness measurements were performed using Vickers method with 30 kg load (30HV), Struers Duramin 40.

Results and Discussion

Fe-28Al-15Si alloy with Zr addition had a homogeneous structure with irregular grains. The most of Si content was dissolute in the matrix. The particles of secondary phase, based on complex (Fe, Si, Zr) carbides, were observed on grain boundaries. Any of

accomplished types of heat treatment had no effect on the structure or the hardness of this alloy.

Fe-28Al-15Si alloy with Mo addition has a fine grained structure with regular grains. The most of content both of Si and Mo was dissolute in the matrix. The rest of Si and Mo reacted with Fe and C forming complex carbides (Fe, Si, Mo). Precipitates of the secondary phase were in form of very fine particles densely distributed both in the grains an on the grains boundaries.

After long annealing at 800°C for 100 hours, coarsening of precipitates at the grain boundaries occurred. Inside the grains, a large volume of new very fine precipitates Fig. 1 (similar to those observed after annealing at 1000°C for 24h, but in much greater quantity) formed and were distributed in the form of dispersion. Around the coarse precipitates at the grain boundaries, the matrix became depleted of impurities, resulting in a narrow zone devoid of secondary particles. The resulting structure is a prerequisite for good (high) temperature mechanical properties, which was confirmed during hardness measurements. Fe-28Al-15Si2Mo alloy after this type of heat treatment shows a hardness of nearly 600HV. This is more than 60HV higher than in other states of the alloy and is comparable to hardened steels.

After annealing the alloy at 1200°C for 2 hours, there is an even more pronounced coagulation of precipitates at the grain boundaries and their significant coarsening. The precipitates from the grains were completely dissolved Fig. 2. The effect of the transition of molybdenum from the matrix to the precipitates was even more evident after this type of annealing than after annealing at 1000°C – according to EDX analysis, the presence of molybdenum in the matrix was not detected at all, while the molybdenum content in the precipitates increased to approximately 23 at. %. The silicon content remained without significant changes.

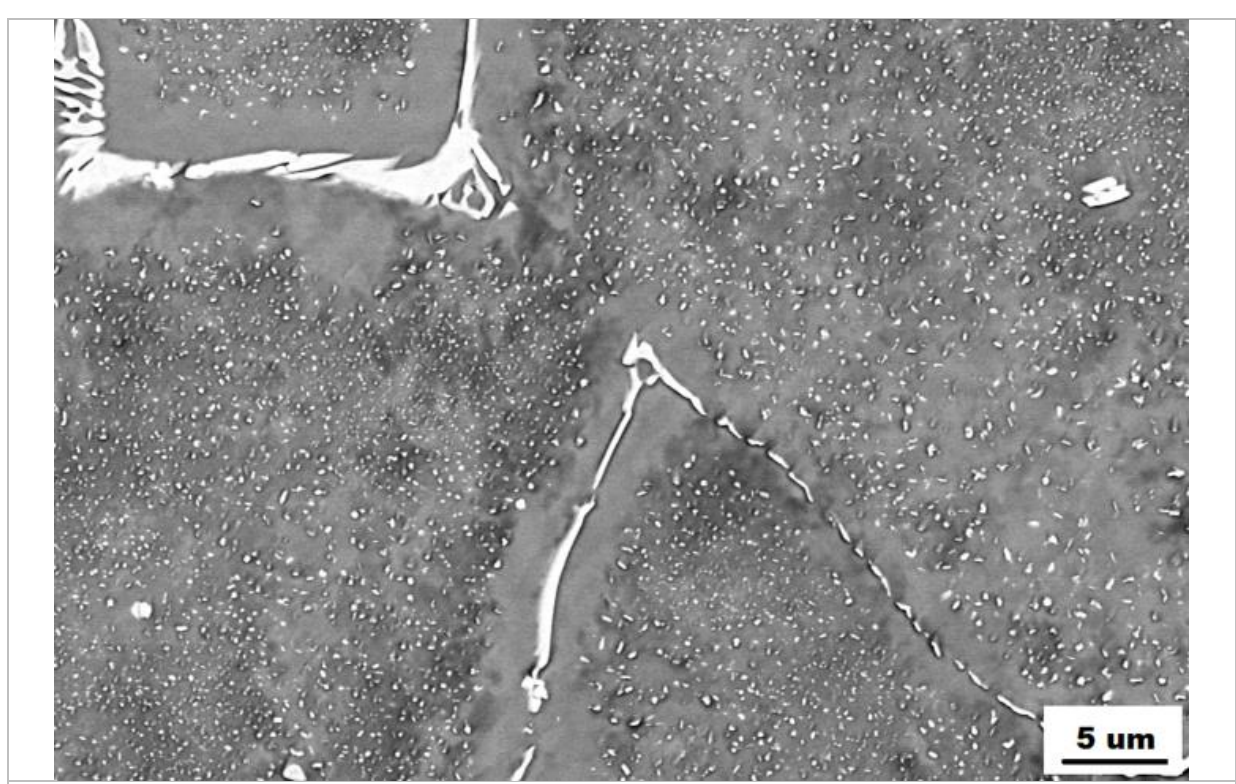


Fig. 1: Fe-28Al-15Si2Mo alloy after HT 800°C/100h. Inside the grains, a large volume of new very fine precipitates formed and were distributed in the form of dispersion.

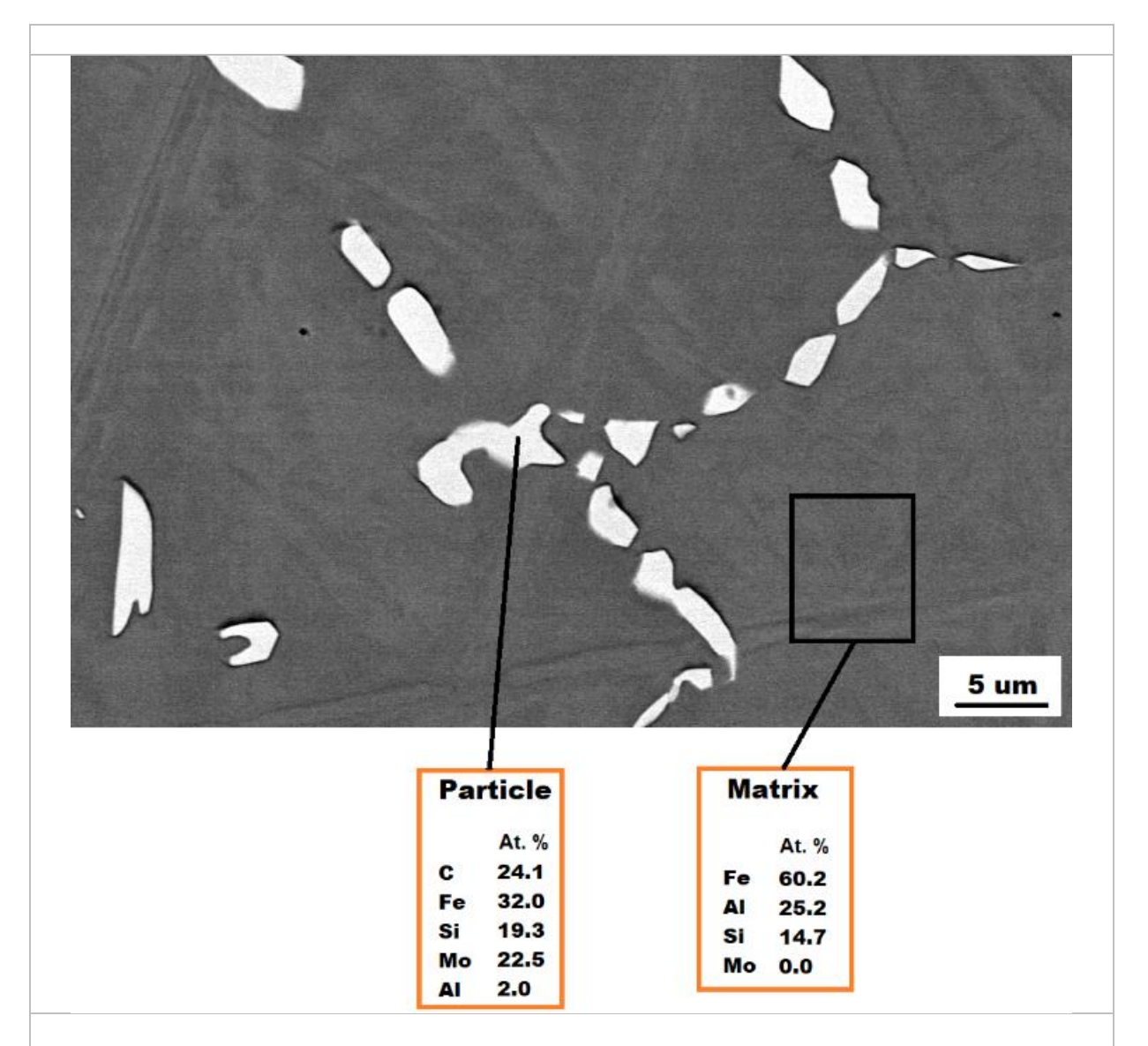


Fig. 2: Fe-28Al-15Si2Mo alloy after HT 1200°C/2h. There is an even more pronounced coagulation of precipitates at the grain boundaries and their significant coarsening.

Acknowledgements

This work was supported by the Ministry of Education, Youth and Sports of the Czech Republic and the European Union - European Structural and Investment Funds in the frames of Operational Programme Research, Development and Education - project Hybrid Materials for Hierarchical Structures (HyHi, Reg. No. CZ.02.1.01/0.0/0.0/16_019/0000843) and by the Institutional Endowment for the Long Term Conceptual Development of Research Institutes, as provided by the Ministry of Education, Youth and Sports of the Czech Republic in the year 2025.

- [1] M. Palm, Concepts derived from phase diagram studies for the strengthening of Fe–Al-based alloys. Intermetallics. [online]. **2005**, 13(12), 1286-1295.
- [2] P. Kratochvíl, M. Švec, R. Král, J. Veselý, P. Lukáč, et al., The Effect of Nb Addition on the Microstructure and the High-Temperature Strength of Fe3Al Aluminide.

- Online. Metallurgical and Materials Transactions A. [online]. **2018**, 49 (5), 1598-1603.
- [3] P. Kejzlar, P. Kratochvíl, R. Král, V. Vodičková, Phase Structure and High-Temperature Mechanical Properties of Two-Phase Fe-25Al-xZr Alloys Compared to Three-Phase Fe-30Al-xZr Alloys. Metallurgical and Materials Transactions A. [online]. **2014**, 45(1), 335-342.
- [4] V. Vodičková, M. Švec, P. Hanus, P. Novák, A. Záděra, V. Keller, P.P. Prokopčáková, The effect of simultaneous si and ti/mo alloying on high-temperature strength of fe3al-based iron aluminides. Molecules, **2020**, 25(18), 4268.
- [5] A. Hotař, V. Vodičková, P. Pazourková Prokopčáková, M. Švec, P. Hanus, S. Daniš, Oxidation behaviour of Fe-28Al-5Si at. % alloyed with Ti and Mo. JOM, **2024**, 76(11), 6152–6166.
- [6] P.J. Masziasz, C.G. McKamey, Microstructural characterization of precipitates formed during high-temperature testing and processing of iron aluminide alloys, Mater. Sci. Eng. A 152 (1992) 322-334

Intermetallics 2025



ISBN: 978-3-948023-57-7